Advanced Methods, Models, and Algorithms for Multi-Rate Co-Simulation of Power System Transients

by

Rupasinghe Arachchige Tharinda
Janesh Kumar Rupasinghe

A Thesis submitted to the Faculty of Graduate Studies of

The University of Manitoba

in partial fulfilment of the requirements for the degree of

DOCTOR OF PHILOSOPHY

Department of Electrical and Computer Engineering

University of Manitoba

Winnipeg, Manitoba, Canada

Abstract

This thesis develops advanced methods, models, and algorithms for next generation co-simulation engines for electromagnetic transient (EMT) type simulations by combining the benefits of dynamic phasors (DPs), frequency adaptive simulation of transients, parallel processing, multi-rate simulation, and accuracy of EMT simulators. The thesis addresses a number of important aspects of power system co-simulation including (i) conditions for numerical stability and their reliance on the interface topology, (ii) dynamic phasor extraction methods and their capabilities to represent typical power system phenomena, (iii) adaptive time-step adjustments when the simulated time-horizon includes varying harmonic contents, and (iv) layered electromagnetic transient, dynamic phasor, and transient stability (TS) simulations. The research develops industrial-grade prototypes for co-simulation with EMT and DP-based solvers, and multi-layered co-simulation of EMT, TS, and DP-based solvers based upon novel algorithms. It also implements a large number of component models and interfacing mechanisms for such systems as electric machines, transformers, and advanced converter systems. Illustrative examples are included to demonstrate the thesis' findings, and validate the accuracy and computational benefits of the developed methods, models, and algorithms.

Use of Copyright Material

Acknowledgement

I would like to convey my sincere gratitude to several individuals and institutions without the support of whom this thesis would not have become a reality.

First, I would like to thank my academic advisor, Prof. Shaahin Filizadeh, for his constant encouragement and guidance throughout the research. His expertise in the relevant research area and the faith shown in my abilities made this work possible.

A special thanks must be conveyed to Prof. Aniruddha Gole and Prof. Kai Strunz for sharing their knowledge and for their inputs to enhance the values of this research.

I would also like to acknowledge the insights and technical support I received from Dr. Darshana Muthumuni and Dr. Rohitha Jayasinghe during my internship in Manitoba HVDC Research Center. I extend my gratitude to the staff of the institution for their continuous support.

I must thank Mitacs Accelerate program, Manitoba HVDC Research Center, and Natural Science and Engineering Research Council (NSERC) of Canada for fulfilling the financial needs of this research.

A special mention must be given to Mr. Shrimal Koruwage for his technical assistance throughout the research. Furthermore, I thank the staff of the Department of Electrical and Computer Engineering, Faculty of Graduate studies of the University of Manitoba, and all the colleagues and friends, whom I shared this wonderful experience with.

Last but not least, I would like to pay tribute to each and everyone, who either shared their knowledge and experience or encouraged me in the process of accomplishing this endeavour.

Janesh Rupasinghe

Contents

List of Figures

List of Tables

Acronyms

AC	alternative current
BFDP	base-frequency dynamic phasor
BFAST	base-frequency dynamic phasors for frequency adaptive simulation of transients
DC	direct current
DP	dynamic phasor
EMT	electromagnetic transient
ENI	electrical network interface
FACTS	flexible alternating current transmission system
HVDC	high voltage direct current
IEEE	the institute of electrical and electronics engineers
MATE	multi-area Thévenin equivalent
MMC	modular multilevel converter
PCC	point of common coupling
PLL	phase-locked loop
SFA	shifted frequency analysis
SM	submodule
SMIB	single machine-infinite bus
TS	transient stability

Symbols

x	a scalar quantity
$\underline{\mathbf{x}}$	a vector quantity
$\mathbf{X}$	a matrix quantity
$\vec{\mathrm{X}}$	a phasor
$\hat{\mathbf{I}}$	identity matrix
$\left\langle x \right\rangle_{\mathrm{h}}$	Fourier coefficient of h^{th} order harmonic of x
$\left\langle \mathrm{X} \right\rangle_{\mathrm{B}}$	base-frequency dynamic phasor of x
$\mathrm{j} = \sqrt{-1}$	imaginary unit
$\mathfrak{Re}\{\}$	real part of a complex number
$\mathfrak{Im}\{\}$	imaginary part of a complex number
ω	angular frequency
Δt	simulation time-step

Chapter 1

Introduction

1.1 General Background

Technological advancements in high-power semiconductor devices, sophisticated control and protection schemes, and renewable energy sources have ushered a tremendous growth in HVDC transmission, flexible ac transmission systems, and converter-tied distributed power generation. These advancements, together with increasing power demand, have created complications in design, analysis, and operation of modern power systems due to the unprecedented complexity of sub-systems involved.

Transient studies of power systems are carried out usually by means of simulation tools such as transient stability (TS), also known as RMS-type, and electromagnetic transient (EMT) type solvers to circumvent the practical limitations of conducting actual experiments. These simulation tools use diverse numerical techniques and solution algorithms to model electromechanical and electromagnetic variations of currents and voltages following switching events and disturbances in a power system. The level of accuracy provided by each simulator generally has a commensurate influence on its computational complexity and speed.

Conventional transient stability simulations sacrifice such details as harmonics and non-linearities of the network to focus on steady-state operation and relatively slow phenomena such as slow electromechanical transients that occur in tens of milliseconds. Therefore, TS simulators offer the benefit of large simulation time-steps in the range of milliseconds, and hence, can readily perform simulations of large-scale networks of tens of thousands of buses. Furthermore, they assume balanced operation of the system, thus, model the networks only with positive-sequence components. This reduces the number of algebraic and differential equations to be solved by the simulator easing a great amount of numerical computations.

EMT simulators, on the other hand, are designed to represent fast transients over a wide frequency range with great precision. They use detailed models to represent non-linearities and fast switching transients that take place in power systems. As such, these simulators require small simulation time-steps in the range of microseconds. Presently they are considered as the most detailed and accurate power system simulation tools.

1.2 Problem Definition

The complexity and involvement of fast-acting devices and control schemes in modern power systems impose practical limitations to conduct simultions using the transient stability approach due to its negligence of detailes of rapid transients. As such, the role of EMT-type simulators has become more prominent in simulating such systems. However, given the small time-step sizes employed, their computational burden rapidly increases with the network size and complexity, which implies that EMT simulation of large networks comprising thousands of buses and a large number of switching devices rapidly becomes prohibitively difficult.

This is not a limitation merely during transients; certain systems and operating conditions - for example, power electronic converters and transformer saturation studies - require small simulation time-steps even during normal operation while the rest of the system may require small time-steps only during transients. With conventional single-rate (fixed time-step) EMT algorithms, the entire network needs to be simulated with a small time step even if high frequency components and events are confined to small areas within the network. This together with the need for handling excessively large matrices renders conventional EMT-type simulations of large networks computationally inefficient and time-consuming.

1.3 Thesis Motivation

Various modeling and simulation techniques have given rise to a number of approaches that extend the applicability of EMT simulations to the study of large networks. Parallel processing, where the network is divided into multiple subsystems each assigned to a distinct processor is one of such techniques used to speed-up simulations [1–3]. Parallel processing alone is still computationally expensive, and requires specialized hardware, thus, has limitations to simulate large systems. Dynamic equivalents where the system or parts thereof is represented with reduced-order models (and hence reduce the size of the nodal admittance matrix) are also used [4–6]. They are often cumbersome to derive and need re-derivation if the network undergoes a change. The accuracy of the simulation is entirely dependent upon the correctness of the equivalent, which may be limited particularly in the presence of non-linearities.

The concept of dynamic phasors (DPs) [7–9] has received much interest in contemporary literature as an alternative to conventional steady-state phasors to model and simulate power systems and components in frequency domain. Compared to steady-state phasors, dynamic phasors allow to retain a considerable amount of dynamics associated with waveforms without compromising the advantage of a large time-step size. Therefore, they are successfully employed in many power system and power electronic modeling and simulation applications [10–12].

In [13], a concept, referred to as frequency-adaptive simulation of transients (FAST), is proposed for simulation of a system in both time and frequency domains within a single solver. In this method, the simulator switches between the detailed EMT solution with a small time-step and the phasor solution with a large time-step by changing a simulation parameter, known as the shift-frequency. This method is unique for its ability to capture fast transients and to accelerate the simulation. The challenge in this context is the limitation of frequency shifting in the presence of continuously-occurring fast phenomena such as those in power electronic converters, and non-linear elements such as arresters and saturable reactors as these force the solver to operate in time-domain for the majority of the simulation.

Co-simulation (or hybrid simulation) combines two or more solvers to perform simulations of a single network by segmenting it to several subsystems and assigning them to distinct solvers based on the transient properties of each subsystem [14–17]. This method generally marries the accuracy of an EMT solver with the computational efficiency of a less detailed solver (e.g., a TS solver) and enables simulation of large-scale power systems. Co-simulators often use features such as parallel processing and multi-rate techniques [18–20] to accelerate their computations. However, this will have many complications in many aspects including the interfacing topology and interactions between solvers, which need to be addressed properly.

Recent developments in co-simulations are reported in EMT-TS co-simulation [21–27], EMT-DP co-simulation [28–30], and EMT-DP-TS co-simulation [31–33]. It is understood that common problems associated with these models and algorithms include, but are not limited to, (i) reduced accuracy of the overall simulation when disturbances occur near the interface, (ii) possibility of one time-step interaction delay between decoupled systems, (iii) inaccuracies of interaction in the presence of high-frequency waveforms, and (iv) lack of control of the computational burden and speed during the simulation.

Development and incorporation of latest techniques into simulation tools is critical as the nature of modern power systems has changed and conventional dynamic simulation algorithms that were developed for traditional power systems are no longer adequate. Modern power systems require modern and drastically more capable simulation programs. The research reported in this thesis creates a rich set of methods, models, and algorithms for the next generation of co-simulation engines for EMT-type simulations.

1.4 Thesis Objectives

This thesis aims at developing a co-simulation platform, which combines the benefits of dynamic phasors, FAST, multi-rate simulation, parallel processing, and EMT solvers for detailed and accelerated transient simulations of large power systems. The primary objectives of the thesis are enumerated as follows.

1. Development of a novel adaptive dynamic phasor-based solver for EMT-type simulations of large power systems.
   (a) To devise procedures for adaptive variation of simulation time-step when the simulated time-horizon includes varying frequency contents.
   (b) To address the crucial task of converting signals between EMT and dynamic phasor solvers, in particular the task of extracting the equivalent dynamic phasors from time-domain EMT samples.
   (c) To develop a library of power system components for the simulator and a suitable interfacing mechanism so that custom-developed model can be easily interfaced to the simulator engine.
2. Development of multi-rate co-simulation platforms in which conventional EMT and TS simulators are interfaced with the adaptive dynamic phasor solver.

(a) To carry out an extensive study of various explicit network partitioning and coupling techniques used in literature based upon which suitable method(s) will be selected to facilitate multi-rate co-simulations.

(b) To assess the influence of the interface topology and interaction methods for stability and convergence properties of interfaced simulators.

(c) To extend the platform to multi-layer co-simulations in which a large network is partitioned into several layers, from detailed EMT to dynamic phasor and to steady-state phasor portions.

1.5 Thesis Organization

Following the introductory material presented in this chapter, the rest of the thesis is organized as follows. Chapter 2 provides a review of power system co-simulations and different network partitioning techniques. In Chapter 3, several types of dynamic phasor modeling and extraction techniques used in co-simulation applications are discussed. Their applicability to represent general power system signals are also compared in this chapter. Then, a comprehensive stability analysis of interfaced simulations is presented in Chapter 4 highlighting the influence of time-delays and the interaction method. Chapter 5 develops a novel dynamic phasor solver for frequency-adaptive simulations of transients using a specialized dynamic phasor technique. The thesis then shows in Chapter 6 the development of a novel co-simulator in which the external system is simulated with two time-steps in the context of the novel dynamic phasor solver while the detailed system is simulated in an EMT solver. This co-simulation engine is extended to combine and co-simulate several solvers in Chapter 7. Finally, conclusions and contributions of the thesis, and proposed directions for future work are given in Chapter 8.

Chapter 2

A Review of Power System Co-Simulations

Co-simulation is an effective solution to the problem of modeling and simulation of large networks. This chapter provides an extensive literature review of power system transient co-simulations along with conventional transient solution methods and several types of explicit and implicit network partitioning and coupling techniques that are beneficial for the construction of the rest of the thesis.

2.1 Conventional Transient Solution Methods

Transients in a power system can be broadly categorized into electromechanical and electromagnetic types. Electromechanical transients, as implied by the name, are caused by the interaction of the mechanical energy of rotating machines and the electrical energy of the network while the electromagnetic transients are caused by the interactions between magnetic fields of inductors and electric fields of capacitors caused by numerous disturbances and dynamic conditions [34]. These transients differ in their time scale and frequency range; thus, distinct solution methods are used to represent each in simulation engines.

2.1.1 Transient Stability (TS) Solution Method

Any current or voltage in an AC-excited linear circuit operating in steady-state is a sinusoidal signal, which can be characterized by its magnitude and phase angle, on a common frequency that is equal to the frequency of the excitation source. As such, TS solvers model power systems with phasor quantities (also referred to as the frequency-domain representation) wherein natural signals are represented using their magnitude and phase angle with the aim of gaining computational convenience and efficiency [11, 35].

Consider a time-domain sinusoidal signal $x(t)$ with a frequency of ω_0, magnitude of $\sqrt{2}A$, and phase angle of δ as follows.

$$x(t) = \sqrt{2}A\cos(\omega_0 t + \delta) \tag{2.1}$$

Using Euler's representation one can represent this signal as

$$\begin{aligned} x(t) &= \sqrt{2}\,\mathfrak{Re}\Big\{A\mathrm{e}^{\mathrm{j}(\omega_0 t+\delta)}\Big\} \\ &= \sqrt{2}\,\mathfrak{Re}\Big\{\vec{\mathrm{X}}\mathrm{e}^{\mathrm{j}\omega_0 t}\Big\} \end{aligned} \tag{2.2}$$

where $\vec{\mathrm{X}} = A\mathrm{e}^{\mathrm{j}\delta}$ is called the "*phasor*" corresponding to the sinusoidal signal $x(t)$. Note that $\vec{\mathrm{X}}$ is a time-invariant complex quantity that embodies the same magnitude and phase angle of the natural signal. The frequency of the signal is not directly included in its phasor; therefore, the conventional phasor analysis applies only when the frequency of the system is constant or varies so slightly around the nominal value that may be considered to be essentially constant. Under such conditions, all voltages and currents in a linear circuit are assumed to be sharing the same frequency. This notion is referred to as the *quasi-steady-state* assumption.

One of the main benefits of phasor representation is that the time-domain differential equations that describe the behaviour of elements such as inductors and capacitors become algebraic equations in the frequency-domain. This is due to the following relationship between a time-domain signal and its phasor representation:

$$\frac{\mathrm{d}}{\mathrm{d}t}x(t) \longleftrightarrow \mathrm{j}\omega_0\vec{\mathrm{X}} \tag{2.3}$$

which shows that the phasor corresponding to the derivative of a sinusoid is related to the phasor of the sinusoid via a complex multiplier. As a result, in transient stability programs, inductors and capacitors are modeled as constant, albeit complex, admittances as depicted in Table 2.1

Table 2.1: TS models of basic circuit elements

Element	**Phasor Equivalent**	
Resistor 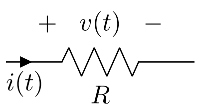 $v(t) = Ri(t)$		$y = \frac{1}{R}$
Inductor 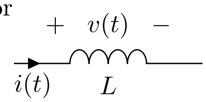 $\frac{\mathrm{d}}{\mathrm{d}t}i(t) = \frac{1}{L}v(t)$	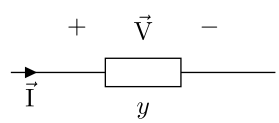 $\vec{\mathrm{I}} = y\vec{\mathrm{V}}$	$y = \frac{1}{\mathrm{j}\omega_0 L}$
Capacitor 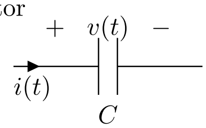 $\frac{\mathrm{d}}{\mathrm{d}t}v(t) = \frac{1}{C}i(t)$		$y = \mathrm{j}\omega_0 C$

In the meantime, the TS solver models rotating machines in the network as a set of algebraic and first-order differential equations, and solves them separately to find machines' variables [36,37]. The machines are then represented as dynamic current sources connected to the network as below.

$$\begin{aligned} \dot{x} &= f(x, \vec{\mathrm{V}}) \\ \vec{\mathrm{I}} &= h(x, \vec{\mathrm{V}}) \end{aligned} \tag{2.4}$$

The positive sequence model of the the transient stability network is built as a constant nodal admittance matrix, and then the network's node voltages (positive sequence only) are calculated in each time-step by solving the following algebraic equation.

$$\mathbf{Y}\,\underline{\vec{\mathbf{V}}} = \underline{\vec{\mathbf{I}}} \tag{2.5}$$

where $\mathbf{Y}$, $\underline{\vec{\mathbf{V}}}$, and $\underline{\vec{\mathbf{I}}}$ are nodal admittance matrix, the frequency-domain node voltage vector, and the frequency-domain current source vector, respectively. In this solution method, the network and rotating plants exchange data at each time-step, and iterations are typically used till convergence is achieved [16]. In a different approach, rotating machines are represented as set of algebraic equations and the entire system is solved at once iteratively using a method such as Newton-Raphson [38].

2.1.2 Electromagnetic Transient (EMT) Solution Method

An EMT solver involves, at least in part, computing the solution of a set of first-order differential equations that characterizes the dynamic behaviour of network elements. Difference equation-based nodal analysis methods have become the generally accepted EMT-type simulation engine in discrete-time computer simulations due to their simplicity and flexibility to acquire a generalized solution to a given network. In such a method, discrete equivalents of network elements are developed using Dommel's discretization technique [39], and then the resultant network is solved using the nodal analysis method. The Dommel's discretization process involves developing a set of difference equations to a given network and representing each difference equation as a Norton equivalent. The implicit trapezoidal integration rule is employed as the general technique of discretization due to its simplicity and the ability to provide an accurate solution with preserved stability (guaranteed for linear systems) [39, 40].

If a first-order differential equation is written as,

$$\frac{dx}{dt} = f(x(t), t) \tag{2.6}$$

where t is the time and x is corresponding to the current through an inductor or the voltage across a capacitor, then the solution at time t using trapezoidal rule with a time-step of Δt is computed as

$$x(t) = x(t - \Delta t) + \frac{\Delta t}{2}\Big(f(x(t), t) + f(x(t - \Delta t), t - \Delta t)\Big) \tag{2.7}$$

Rearranging (2.7) yields

$$x(t) = \frac{\Delta t}{2} f(x(t), t) + \left(x(t - \Delta t) + \frac{\Delta t}{2}[f(x(t - \Delta t), t - \Delta t)]\right) \tag{2.8}$$

It is apparent from (2.8) that a solution at time t can be found by a term corresponding to the time t and a historic term calculated at time $(t - \Delta t)$. Note that in EMT algorithms, it is common practice to represent network elements using their Norton equivalents wherein the historic term of each element is simulated as a current source. As such, one must be careful to rearrange (2.7) in such a way that each term of (2.8) resembles a current. Table 2.2 illustrates the discretized EMT equivalents of basic circuit elements.

Once the discretized Norton equivalents of all the components are obtained as in (2.8), a set of nodal equations are found in the form of

$$\mathbf{G}\,\underline{\mathbf{v}} = \underline{\mathbf{i}} + \underline{\mathbf{i}}_{\text{his}} \tag{2.9}$$

where $\mathbf{G}$, $\underline{\mathbf{v}}$, $\underline{\mathbf{i}}$, and $\underline{\mathbf{i}}_{\text{his}}$ are the nodal conductance matrix, the vector of node voltages, the vector of external current sources associated with each node, and the vector of current sources representing the history terms, respectively. The time-varying vectors $\underline{\mathbf{i}}$ and $\underline{\mathbf{i}}_{\text{his}}$ are updated at each time-step. Then the system described by (2.9) is solved in each time-step to find the unknown node voltages $\underline{\mathbf{v}}$ until the end of simulation is reached.

Table 2.2: EMT models of basic circuit elements

Element	**Discretized Equivalent**	
Resistor 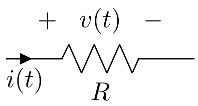 $v(t) = Ri(t)$	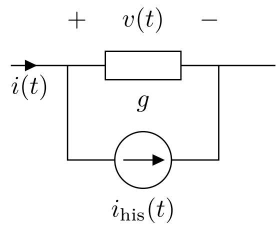 $i(t) = g\,v(t) + i_{\text{his}}(t)$	$g = \dfrac{1}{R}$ $i_{\text{his}}(t) = 0$ (No history term)
Inductor 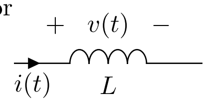 $\dfrac{\mathrm{d}}{\mathrm{d}t}i(t) = \dfrac{1}{L}v(t)$		$g = \dfrac{\Delta t}{2L}$ $i_{\text{his}}(t) = i(t-\Delta t) + g\,v(t-\Delta t)$
Capacitor 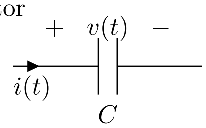 $\dfrac{\mathrm{d}}{\mathrm{d}t}v(t) = \dfrac{1}{C}i(t)$		$g = \dfrac{2C}{\Delta t}$ $i_{\text{his}}(t) = -i(t-\Delta t) - g\,v(t-\Delta t)$

The solution of (2.9) involves the inversion of the nodal admittance matrix whose size corresponds to the number of nodes of the network being simulated. This matrix may be time-dependent since it must account for possible topological changes, for example due to switching events and faults, of the network. In such an event, the matrix must be reformed and re-inverted every time a topological change takes place, which is extremely computationally demanding.

Typical applications of EMT simulations include determination of component ratings, insulation coordination, study of over-voltages due to switching surges and circuit breaker operations, explanation of equipment failures, and study of system dynamics and switching transients caused by power electronic devices and controllers [34, 41].

2.2 Power System Co-Simulation

TS solvers ignore fast dynamics associated with network components to model them in frequency-domain while EMT solvers use a difference equation-based approach taking their dynamics into account; therefore, EMT simulators are generally computationally much more expensive than TS solvers. The size and the complexity of modern power systems impose practical limitations to either type of solvers. This incentivizes the development of muti-rate co-imulators in order to bring a trade off between the accuracy and the speed of simulations. The first such development is reported in [42].

2.2.1 Introduction to Co-Simulation

Simulating a single electrical network by coupling two or more solvers is referred to as power system "*co-simulation*" or "*hybrid simulation*" [16, 43]. A co-simulation algorithm segments a large network into several subsystems and assigning them to distinct solvers based on the transient properties of each subsystem. The *detailed subsystems* (or the *EMT subsystems*) wherein major dynamic information lies are assigned to an EMT solver; these subsystems are often confined to small areas within a large network. The *external subsystem* (rest of the large system), where retention of details is not critical, is assigned to a solver with better computational efficiency than an EMT solver. This is illustrated in Figure 2.1. The electric network is partitioned to subsystems at the boundary buses while the interface provides the connection between subsystems as well as a means to exchange data between two simulators.

There are several aspects in power system co-simulations that need careful consideration. Network partitioning and interfacing topology are two of them, which are further discussed in section 2.3. Use of solvers in different domains forces co-simulators to implement data conversion

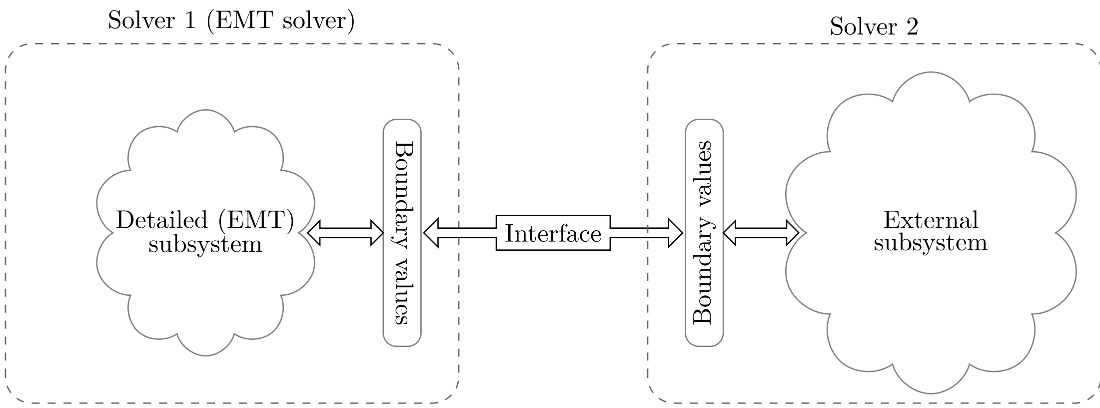

Figure 2.1: Co-simulation model of a large power system

methods to transform interface variables from one domain to another. Conventional TS-EMT hybrid simulators use techniques such as curve fitting [15, 44] and Fast Fourier Transform (FFT) [45] to extract phasors from instantaneous EMT values. However, these methods are difficult to implement when frequency-domain waveforms contain intricate dynamics, and hence, are not often seen in DP-EMT co-simulations. Chapter 3 provides a comprehensive analysis of prominent dynamic phasor extraction techniques. Another crucial aspect of co-simulation is the data interaction between solvers. This is reviewed at length in section 2.4.

2.2.2 Multi-Rate Simulation

The external subsystem in a typical co-simulation is modeled to capture slow dynamics and steady state operation, and is segmented in such a way that switching devices and disturbance locations are placed far from the interfacing locations. This allows the solver that is employed to simulate the external subsystem to use a much larger simulation time-step than the EMT solver. The practice of simulating subsystems using different time-steps is termed as *multi-rate* (or multiple sampling rate) simulation [18, 19].

Use of multiple time-steps greatly enhances computational efficiency, and consequently the speed of the simulation. However, this will have many complications in the interaction of subsystems at the interface, particularly in the presence of dynamics, since the granularity of data samples of each side is dissimilar. In order to balance the number of data samples at the interface, methods such as interpolation or iterations have been used.

2.3 Network Partitioning and Interfacing

Co-simulation starts with partitioning a large network into small subsystems. The partitioning and interfacing topology will have implications on several aspects of simulation including accuracy, speed, and stability. Also of importance are whether or not they could be implemented at arbitrary places within a network and capability to ease the multi-rate simulations. It is observed that discontinuities that occur close to interface buses cause severe distortions and imbalances in co-simulation waveforms. As a solution, the interfacing location may be moved deeper in the external system, but it comes at the expense of simulating a larger portion of the network in the EMT solver, which poses computational burden.

In an explicitly partitioned environment, information of interface variables from one subsystem is available to the other side via the interface only after the solution of that particular subsystem for the present time-step is obtained; therefore, they can only be used in the next time-step solution of the other subsystem. As a result, network partitioning may introduce a time delay for the solution. Numerical instabilities and phase errors might occur in co-simulation environments if this delay is not properly addressed [46, 47]. An analytical insight to this aspect is shown in Chapter 4.

Interfacing mechanisms can be categorized as *internal interfacing* (implicit coupling) and *external interfacing* (explicit coupling) [48]. An internal interface can only be used when the user has access to the algorithms of the solvers. External interfaces uses power system elements (e.g., transmission lines) to form the interface; therefore, they eliminate difficulties in internal methods and allow to implement and solve subsystems independently. This type of interfacing mechanism can be rapidly implemented and is flexible to make changes; therefore, they can be readily used to interface externally developed algorithms to standalone software. Several network partitioning and coupling mechanisms used in co-simulation applications are explained next.

2.3.1 Current Source-Voltage Source Interface

This is the simplest form of explicit technique used to segment networks. In this approach, subsystems are portrayed in the opposite subsystems using a dependent voltage or current source whose values are updated using the latest values of the other side's interface bus voltage or the branch current as illustrated in Figure 2.2. In order to prevent any numerical instability, a fixed shunt admittance and a series resistance may be connected to the current source and the voltage source, respectively.

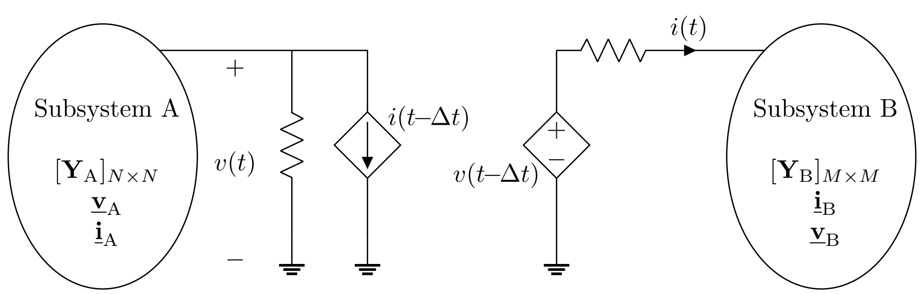

Figure 2.2: Current source-voltage source interface

This means of partitioning directly inserts a time-step delay to the interaction between subsystems, and hence, could introduces significant phase errors and a risk of a numerically unstable solution. Nevertheless, they are proved to be sufficiently stable and accurate in many applications [49–51]. Applications such as synchronous machine-EMT interface use the same model with compensation sources to make up for mismatches due to added resistive elements, and with high frequency dampers to retain stability [34].

Co-simulation application such as [33, 52] uses extrapolation to predict boundary values as a compensation mechanism to the time-step delay. However, the accuracy of predicted values only holds under the assumption that the prediction interval is kept as small as possible; therefore, they are vulnerable in transients and multi-rate methods. Accuracy and stability of this type of interfacing are improved by implicit interfacing methods such as frequency-dependant network equivalent (FDNE) [5] and dynamic Norton-Thévenin equivalents [22, 24] to represent subsystems. These representations are dynamic in nature and require run-time updating to the equivalents whenever a subsystem undergoes a change. For this reasons, they are still not established in industry. Dynamic interfacing mechanisms are not further discussed in this thesis.

2.3.2 Transmission Line Interface

Wave propagation from one node to another node through a transmission line involves a delay. Therefore, a network partitioning done at a transmission line, whose wave propagation time is used to compensate for the time delay caused by the partitioning, does not insert an additional time delay to the solution, and hence, forms an accurate and robust interface. Figure 2.3 shows the Bergeron model [34] of a lossless transmission line between nodes K and M,

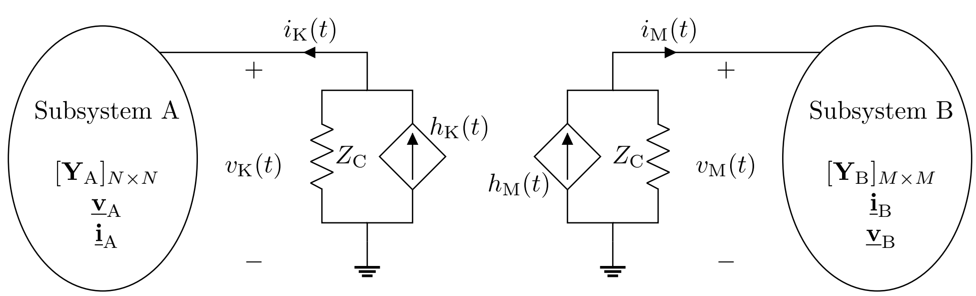

Figure 2.3: Lossless transmission line interface

where Z_{C} is the surge impedance of the line. If the wave propagation delay of the transmission line is τ, then current injections are given as below.

$$h_{\mathrm{M}}(t) = \frac{2v_{\mathrm{K}}(t-\tau)}{Z_{\mathrm{C}}} - h_{\mathrm{K}}(t-\tau) \tag{2.10}$$

$$h_{\mathrm{K}}(t) = \frac{2v_{\mathrm{M}}(t-\tau)}{Z_{\mathrm{C}}} - h_{\mathrm{M}}(t-\tau) \tag{2.11}$$

The transmission line interface is a well-established explicit coupling method in co-simulation applications [21, 28]. The main restraint of this interface is the maximum time delay that can be compensated, which is equal to the wave travel time through the line and is limited by its length. For example, a minimum 300 km long transmission line is required to use a simulation time-step as large as 1 ms (approximately 50-μs per 15 km).

2.3.3 Multi-Area Thévenin Equivalents

The idea of splitting a sparse network to dense subsystems connected by few linking branches was introduced by G. Kron in his *Diakoptics* method [53]. The Multi-Area Thévenin Equivalents (MATE) concept [54] extends this notion and provide a way to obtain paralleled solution of subsystems by representing each subsystem by a Thévenin Equivalent.

Consider the two subsystems that are connected by linking branches as displayed in Figure 2.4. Each linking branch is represented using an impedance and a voltage source as a general case. Note that any component in the system, for example, RLC elements, voltage source or switch, can become a link connecting the subsystems.

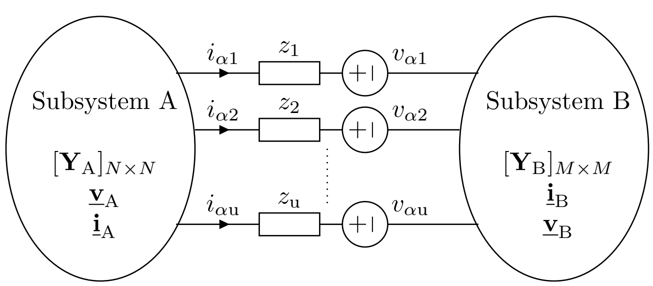

Figure 2.4: Two subsystems connected via linking branches

Assume that the subsystems A and B consist of N and M number of nodes, respectively, and subsystem are connected by u number of branches. The network equations of the entire system can be written using modified nodal analysis in the form of

$$\begin{pmatrix} \mathbf{Y}_{\mathrm{A}} & \mathbf{0} & \mathbf{P} \\ \mathbf{0} & \mathbf{Y}_{\mathrm{B}} & \mathbf{Q} \\ \mathbf{P}^{\mathrm{T}} & \mathbf{Q}^{\mathrm{T}} & -\mathbf{Z} \end{pmatrix} \begin{pmatrix} \underline{\mathbf{v}}_{\mathrm{A}} \\ \underline{\mathbf{v}}_{\mathrm{B}} \\ \underline{\mathbf{i}}_{\alpha} \end{pmatrix} = \begin{pmatrix} \underline{\mathbf{h}}_{\mathrm{A}} \\ \underline{\mathbf{h}}_{\mathrm{B}} \\ \underline{\mathbf{v}}_{\alpha} \end{pmatrix} \tag{2.12}$$

where $\mathbf{Z}$, $\underline{\mathbf{i}}_{\alpha}$, and $\underline{\mathbf{v}}_{\alpha}$ are the matrix of link impedance, vector of link currents, and vector of link voltages, respectively. They have dimensions of $u \times u$, $u \times 1$, and, $u \times 1$, respectively. Matrices $\mathbf{P}$ and $\mathbf{Q}$ are the connectivity arrays of link currents to each subsystem, and $N \times u$ and $M \times u$ in size, respectively. Link connectivity arrays are constructed based on the direction of current flow through the linking branches. If the current flow of a particular branch is out of the node, then it is assigned a '+1' and if the flow is into the node, then it is assigned a '-1'. If there is no connectivity to a node, it is assigned a value of '0'.

Rearranging (2.12) gives the following.

$$\begin{pmatrix} \hat{\mathbf{I}} & \mathbf{0} & \mathbf{A} \\ \mathbf{0} & \hat{\mathbf{I}} & \mathbf{B} \\ \mathbf{0} & \mathbf{0} & \mathbf{Z}_{\alpha} \end{pmatrix} \begin{pmatrix} \underline{\mathbf{v}}_{\mathrm{A}} \\ \underline{\mathbf{v}}_{\mathrm{B}} \\ \underline{\mathbf{i}}_{\alpha} \end{pmatrix} = \begin{pmatrix} \underline{\mathbf{e}}_{\mathrm{A}} \\ \underline{\mathbf{e}}_{\mathrm{B}} \\ \underline{\mathbf{e}}_{\alpha} \end{pmatrix} \tag{2.13}$$

where

$\mathbf{A} = \mathbf{Y}_{\mathrm{A}}^{-1}\mathbf{P}$, $\qquad \mathbf{B} = \mathbf{Y}_{\mathrm{B}}^{-1}\mathbf{Q}$,

$\underline{\mathbf{e}}_{\mathrm{A}} = \mathbf{Y}_{\mathrm{A}}^{-1}\underline{\mathbf{h}}_{\mathrm{A}}$, $\qquad \underline{\mathbf{e}}_{\mathrm{B}} = \mathbf{Y}_{\mathrm{B}}^{-1}\underline{\mathbf{h}}_{\mathrm{B}}$,

$\mathbf{Z}_{\alpha} = \mathbf{Z}_{\mathrm{th\_A}} + \mathbf{Z}_{\mathrm{th\_B}} + \mathbf{Z}$,

$\underline{\mathbf{e}}_{\alpha} = \underline{\mathbf{e}}_{\mathrm{th\_A}} + \underline{\mathbf{e}}_{\mathrm{th\_B}} + \underline{\mathbf{v}}_{\alpha}$,

and $\hat{\mathbf{I}}$ denotes the identity matrix. $\mathbf{Z}_{\mathrm{th\_A}}$ and $\mathbf{Z}_{\mathrm{th\_B}}$ represent the Thévenin impedance matrices and $\underline{\mathbf{e}}_{\text{th\_A}}$ and $\underline{\mathbf{e}}_{\text{th\_B}}$ represents the Thévenin voltage vectors of corresponding subsystems. They are calculated as

$$\mathbf{Z}_{\text{th\_A}} = \mathbf{P}^{\mathrm{T}}\mathbf{A}, \qquad \mathbf{Z}_{\text{th\_B}} = \mathbf{Q}^{\mathrm{T}}\mathbf{B}, \tag{2.14}$$

$$\underline{\mathbf{e}}_{\text{th\_A}} = \mathbf{P}^{\mathrm{T}}\underline{\mathbf{e}}_{\mathrm{A}}, \qquad \underline{\mathbf{e}}_{\text{th\_B}} = \mathbf{Q}^{\mathrm{T}}\underline{\mathbf{e}}_{\mathrm{B}} \tag{2.15}$$

Note that in (2.13), each subsystem is decoupled, and the individuality of them are preserved; thus, it allows simultaneous solution of subsystems. The MATE solution procedure is as follows.

First, the Thévenin voltage vectors and Thévenin impedance matrices of subsystems are calculated usinng (2.14) and (2.15) considering subsystems as independent. The requirement of re-computation of a Thévenin impedance matrix arises only if the configuration of the subsystem is changed. Then, the branch currents are found by solving

$$\underline{\mathbf{i}}_{\alpha} = \mathbf{Z}_{\alpha}^{-1}\underline{\mathbf{e}}_{\alpha} \tag{2.16}$$

The final solution is obtained by injecting calculated link currents, $\underline{\mathbf{i}}_{\alpha}$, to corresponding nodes and solving each subsystem independently. This procedure must be continued in each time-step until the end of simulation is reached.

The MATE solution procedure does not insert a time-step delay to the solution, but involves more steps than the conventional EMT solution procedure. This drawback is insignificant as MATE provides advantages such as a reduced-size admittance matrices, multi-rate simulation, and parallel solution for subsystems [55, 56].

2.4 Interaction Protocols

The *interaction protocol* in co-simulation predefines the sequence of actions required for data exchange between solvers. The objectives of a interaction protocol are twofold: (i) deciding which simulator to run at a given time, and (ii) assigning a sequence for data exchange. Therefore, interaction protocols found in literature are primarily divided into two categories, namely *serial protocols* and *parallel protocols* [16].

2.4.1 Serial Interaction Protocols

At a given instant in a serial protocol, only one of the simulators solves its subsystem while the other one(s) remain idle. Data exchange between the two solvers is executed at a common point in time, which generally coincides with the time-step of the external solver. Figure 2.5 illustrates an example case of a serial protocol used in conventional TS-EMT co-simulations.

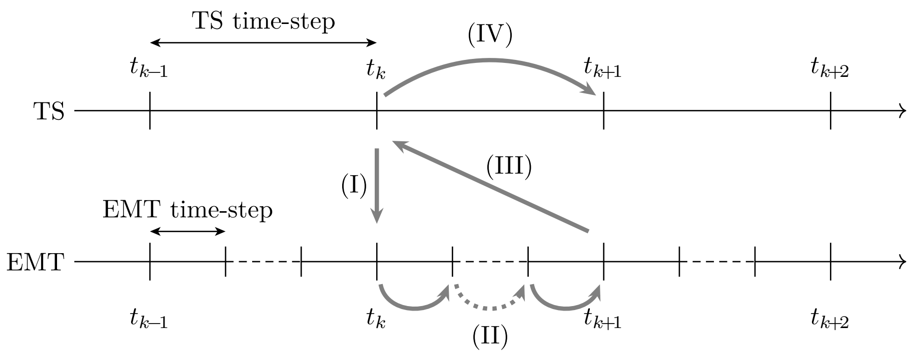

Figure 2.5: An example of a serial interaction protocol

In this example, the boundary of the EMT subsystem is updated using transferred values from the TS solver at $t = t_k$. Then, the solution for the EMT subsystem is obtained at every EMT time-step until $t = t_{k+1}$ while the TS solver is idle. Based on EMT solutions at this period, the TS boundary is updated and then the TS subsystem's solution for $t = t_{k+1}$ is performed (including iterations) while the EMT solver remains inactive. This is repeated until the end of the simulation is reached.

Idling durations of simulators means that this interaction protocol does not achieve high computational efficiency; therefore, it does not greatly comply with the main purpose of co-simulations. Applications of this protocol can be found in [22, 24, 45].

2.4.2 Parallel Interaction Protocols

In the parallel interaction protocol, all simulators execute at the same time solving subsystems simultaneously; therefore, this protocol offers the highest advantage in terms of simulation speed. However, these types of interactions are somewhat complex and harder to implement than a serial interaction. Figure 2.6 illustrates an example of a parallel interaction protocol implemented in a TS-EMT co-simulation.

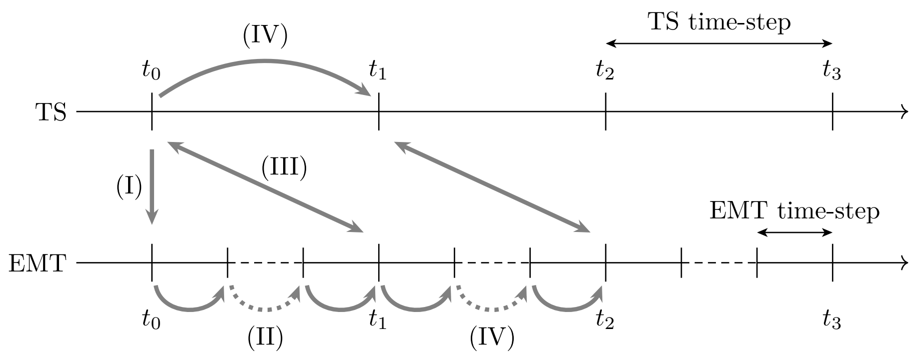

Figure 2.6: An example of a parallel interaction protocol

When solvers are executed in parallel, the TS simulator does not have data for its initial iteration. Therefore, in the example shown in Figure 2.6, the EMT solver performs its simulation using approximated boundary data until $t = t_1$ (or when current and voltages are stabilized) while the TS solver stays idle. Then boundary values of both subsystems are exchanged. Using updated values, the TS solver is executed from $t = t_0$ to $t = t_1$ while the EMT solver is executed for each EMT time-step from $t = t_1$ to $t = t_2$ simultaneously. The step (III) and (IV) of this procedure are repeated until the simulation ends. Applications of parallel interaction protocols can be found in [21, 57, 58]. Interactions described in [23, 25] use combined methods of serial and parallel protocols.

2.5 Summary

This chapter examined several aspects of power system transient co-simulations in detail. The topics discussed under this chapter included conventional transient solution methods, the concepts of power system co-simulation and multi-rate simulation, network partitioning and interfacing techniques, and interaction protocols. The contents of this chapter, as well as the review of existing literature (see the summary on section 1.3) show that there are important gaps in the knowledge that support the motivations of this thesis.

Chapter 3

Assesment of Dynamic Phasor Extraction Techniques

Section 2.1.1 showed that the conventional phasor analysis represents periodic sinusoidal signals using their magnitude and phase angle on a common frequency base. For example, a time-domain signal $x(t) = \sqrt{2}A\cos(\omega_0 t + \delta)$ is represented as $\vec{\mathrm{X}} = A\mathrm{e}^{\mathrm{j}\delta}$ in frequency domain. Due to their numerous mathematical advantages, phasors were used in the early analyses of power system transients under quasi steady-state assumptions wherein dynamic variations much slower than the system's base frequency prevail. This assumption was able to deliver satisfactorily accurate results; it is, however, no longer adequate for modern power systems where fast acting phenomena such as those observed in HVDC systems, FACTS, renewables, and in sub-synchronous oscillation have resulted in transients with much wider frequency spectrum

The notion of *dynamic phasors* (at times referred to as time-varying phasors), which was originated to improve the frequency bandwidth of phasor-based transient simulations, is a much more contemporary concept. Even though this concept existed in other fields for decades [59], it was in the 1990's that dynamic phasors took a first appearance in power system engineering [8,60], and power electronic modeling applications [7,61]. The most notable feature of a dynamic phasor is that it provides a low-pass, frequency-domain representations of a real-valued, band pass signal, which is significant in terms of computational efficiency in long-term, discrete-time simulations as it relieves the requirement of sampling at a high rate; hence, it permits to use large solution time-steps while retaining accuracy within the frequency range of waveforms being simulated.

Conversion of time-domain EMT signals to dynamic phasors and vice versa is one of the essential requirements of any DP-EMT hybrid application. While conversion of a dynamic phasor to an time-domain EMT signal may be straightforward, extracting dynamic phasors from instantaneous samples produced by EMT simulations is not so. The task involves creating a phasor, or a series of phasors if harmonics are included, to represent the time-domain waveform or a meaningful subset of its harmonics. Earlier investigations have shown that several elegant methods for this crucial task are available; however, additional work is necessary to understand the application range of those techniques and devise methods to improve their harmonic selectivity and computational efficiency.

This chapter provides an in-depth look into the dynamic phasor principles and extraction techniques currently used in power system modeling and simulation applications. A detailed assessment is made to determine the applicability and the effectiveness of each technique when extracting dynamic phasors from instantaneous samples of time-domain signals consisting of a wide range of typical power system conditions.

3.1 Fast Time-Varying Phasors

A concept referred to as "*fast time-varying phasors*" was introduced by V. Venkatasubramanian in [8, 60, 62] to analyse time-domain signals by transforming them to low bandwidth dynamic phasors. This was a significant improvement to the conventional quasi-stationary phasors as it extended the applicable frequency-range of phasor analysis by accommodating transients up to the base-frequency of power system signals. The following provides the mathematical background of this dynamic phasor principle.

3.1.1 Phasor Transformation

Consider an arbitrary three-phase balanced voltage or current signal $\underline{\mathbf{x}}(t)$ with a time-varying amplitude and a time-varying phase angle at a carrier frequency of ω_0 as in (3.1).

$$\underline{\mathbf{x}}(t) = \begin{pmatrix} \sqrt{2}A(t)\cos(\omega_0 t + \delta(t)) \\ \sqrt{2}A(t)\cos(\omega_0 t + \delta(t) - 2\pi/3) \\ \sqrt{2}A(t)\cos(\omega_0 t + \delta(t) + 2\pi/3) \end{pmatrix} \tag{3.1}$$

The fast time-varying phasors for $x(t)$ is defined as below [62].

$$\vec{\mathrm{X}}(t) = A(t)\mathrm{e}^{\mathrm{j}\delta(t)} \tag{3.2}$$

The definition in (3.2) for fast time-varying phasors is directly based on the traditional stationary phasor definition. However, transforming a signal to a time-varying phasor is not a trivial task as the magnitude and the phase angle of the time-domain signal are varying. Therefore, a mathematical transformation to extract phasors from time-domain signals is also introduced. For this, the three-phase signal $\underline{\mathbf{x}}(t)$ is rewritten in the following form:

$$\underline{\mathbf{x}}(t) = \sqrt{3}\,\mathbf{B}(t) \begin{pmatrix} A(t)\cos(\delta(t)) \\ A(t)\sin(\delta(t)) \\ 0 \end{pmatrix} \tag{3.3}$$

where,

$$\mathbf{B}(t) = \sqrt{\frac{2}{3}} \begin{pmatrix} \cos(\omega_0 t) & -\sin(\omega_0 t) & 1/\sqrt{2} \\ \cos(\omega_0 t - 2\pi/3) & -\sin(\omega_0 t - 2\pi/3) & 1/\sqrt{2} \\ \cos(\omega_0 t + 2\pi/3) & -\sin(\omega_0 t + 2\pi/3) & 1/\sqrt{2} \end{pmatrix} \tag{3.4}$$

is the inverse *Blondel-Park transformation* matrix [63]. Then a phasor transformation operator $\mathcal{P}(.)$, which maps the time-domain balanced three-phase signals, $\underline{\mathbf{x}}(t)$, to the time-varying phasor,

$\vec{\mathrm{X}}(t)$, is defined as follows.

$$\mathcal{P}\Big(\underline{\mathbf{x}}(t)\Big) = \frac{1}{\sqrt{3}}\begin{pmatrix}1 & \mathrm{j} & 0\end{pmatrix}\mathbf{B}^{-1}(t)\underline{\mathbf{x}}(t) \tag{3.5}$$

Using (3.1), (3.4), and (3.5) it is readily seen that

$$\mathcal{P}\Big(\underline{\mathbf{x}}(t)\Big) = \vec{\mathrm{X}}(t) = A(t)\mathrm{e}^{\mathrm{j}\delta(t)} \tag{3.6}$$

The phasor transformation in (3.5) provides the expected dynamic phasor only when the input signal, $\underline{\mathbf{x}}(t)$, is a balanced three-phase quantity. When the three-phase system is unbalanced, the transformation produces a non-zero, real-valued zero sequence component in addition to the time-varying phasor. If included, this increases the complexity of phasor analysis; therefore, applications of this concept are essentially tied with balanced three-phase systems.

Although (3.5) uses the Blondel transformation matrix to map the time-domain three-phase signals to a corresponding phasor, it is possible to use alternative transformations as well. For example, in [30], a three-phase transformation referred to as $\alpha\beta$-transformation, which is based on Clark's transformation [63], is used to produce dynamic phasors.

3.1.2 Time-Varying Phasor Properties

The following properties of fast time-varying phasors prove to be useful in applying them to the analysis of dynamical systems.

1. Linearity: The phasor operator $\mathcal{P}(\cdot)$ is a linear transformation. That is

$$\mathcal{P}\Big(\underline{\mathbf{x}}(t) + \underline{\mathbf{y}}(t)\Big) = \mathcal{P}\Big(\underline{\mathbf{x}}(t)\Big) + \mathcal{P}\Big(\underline{\mathbf{y}}(t)\Big) \tag{3.7}$$

$$\mathcal{P}\Big(\alpha\underline{\mathbf{x}}(t)\Big) = \alpha\mathcal{P}\Big(\underline{\mathbf{x}}(t)\Big) \tag{3.8}$$

2. Differentiation: The phasor transformation of the time-derivative of a signals has the following relationship.

$$\mathcal{P}\left(\frac{\mathrm{d}}{\mathrm{d}t}\underline{\mathbf{x}}(t)\right) = \frac{\mathrm{d}}{\mathrm{d}t}\mathcal{P}\Big(\underline{\mathbf{x}}(t)\Big) + \mathrm{j}\omega_0\mathcal{P}\Big(\underline{\mathbf{x}}(t)\Big) \tag{3.9}$$

3. The phasor operator $\mathcal{P}(\cdot)$ is bijective. That is, each time-domain signal is paired with a unique time-varying phasor, and vice versa.

It is readily seen from (3.9) that the conventional phasor in (2.3) is a subclass of dynamic phasors wherein the derivative term on the right-hand side of (3.9) is not present because it is either zero or negligibly small.

3.2 Generalized Averaging Method

"*Generalized (state space) averaging method*", which was introduced in the early 1990's, is based on the notion that a time-domain signal can be represented by a series of time-varying Fourier coefficients with arbitrary accuracy assuming quasi-periodicity of the signal [7, 61]. The primary intention of introducing this concept was to model the dynamics of power electronic systems, which normally comprise many harmonics.

3.2.1 Mathematical Background

Consider an arbitrary time-domain signal, $x(t)$, with a fundamental period of T over the time window $(t-T, t)$. The Fourier series of the signal at a particular time in this window is as follows.

$$x(t-T+s) = \sum_{k=-\infty}^{+\infty} \Big\langle x \Big\rangle_k (t)\mathrm{e}^{\mathrm{j}k\omega_0(t-T+s)} \tag{3.10}$$

where $s \in (0, T]$, k is the harmonic order, and $\omega_0 = 2\pi/T$ is the fundamental angular frequency. The k^{th} Fourier coefficient of $x(t)$ is

$$\Big\langle x \Big\rangle_k (t) = \frac{1}{T}\int_0^T x(t-T+s)\mathrm{e}^{-\mathrm{j}k\omega_0(t-T+s)}\mathrm{d}s \tag{3.11}$$

The coefficient $\left\langle x \right\rangle_k(t)$ is a time-dependent complex value and referred to as the dynamic phasor of the k^{th} harmonic of $x(t)$. Contrary to the fast time-varying phasor representation, this method provides a way to model all harmonics including dc component of the time-domain waveform. As such, models developed using generalized averaging method may be used to simulate the entire time-domain dynamics, and hence are used in EMT-type simulations as well [51, 64].

The generalized averaging method may be computationally expensive when modeling the overall dynamics of a system with many frequency components as it requires to model each coefficient individually using (3.11). This should be weighed, however, against the selectivity of this method to include or exclude any number of frequency components based on the desired level of accuracy. This is a noteworthy advantage as it provides control over the accuracy and the efficiency of simulation waveforms. Therefore, it is in common practice that the infinite series given in (3.10) is truncated to a finite number of coefficients depending on the accuracy requirement of the application. Owing to this fact, this notion of a dynamic phasor is used in many power system and power electronic modeling and simulation applications where several frequency components exist [10, 12, 65, 66].

3.2.2 Extracting Dynamic Phasor Coefficients

The definition in (3.11) provides a straightforward way of extracting dynamic phasor coefficients from a time-domain signal by using instantaneous samples over window of length T of the signal. This window then slides along the time axis - in discrete steps when calculations are done numerically - to calculate the new coefficients. Assuming that the signal consist of N samples per window, (3.11) can be readily discretized as:

$$\left\langle x \right\rangle_k(t) = \frac{1}{N} \sum_{i=0}^{N-1} x(t - i\Delta t)\mathrm{e}^{-\mathrm{j}k\omega_0(t-i\Delta t)} \tag{3.12}$$

which needs at least N additions and N multiplications to extract a single coefficient at a given time. This is an inefficient process as the same computation has to be repeated every time the window is moved to the next sample, until the end of the simulation. However, one can calculate these coefficients much more efficiently if the overlap of the windows is properly utilized when moving from one sample point to the next as illustrated in Figure 3.1.

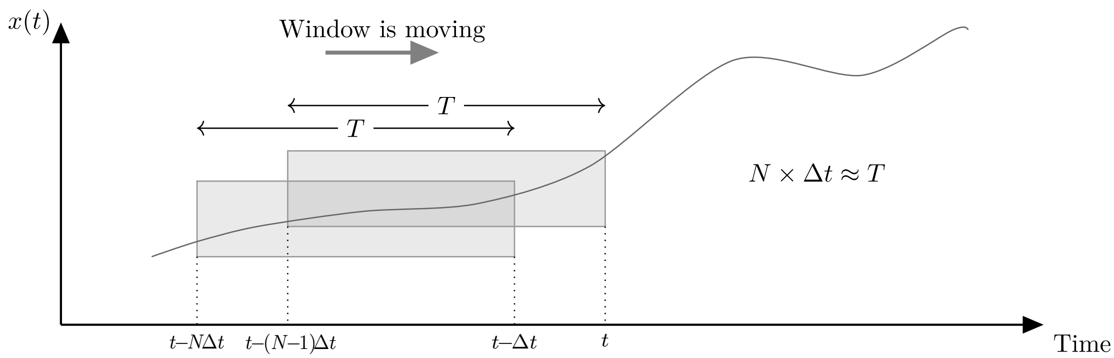

Figure 3.1: Coefficient extraction using generalized averaging method

Assume that the dynamic phasor coefficient at $t = t - \Delta t$ is previously calculated and known. Then, the dynamic phasor coefficient for the present time, t, can be derived as

$$\left\langle x\right\rangle_k(t) = \left\langle x\right\rangle_k(t-\Delta t) + \frac{1}{N}\left(x(t)\mathrm{e}^{-\mathrm{j}k\omega_0 t} - x(t-N\Delta t)\mathrm{e}^{-\mathrm{j}k\omega_0(t-N\Delta t)}\right) \tag{3.13}$$

which requires only two additions and two multiplications.

3.2.3 Generalized Averaging Method Properties

Several properties of generalized averaging method that are useful in dynamic phasor modeling and simulation applications are listed below.

1. Differentiation: The time-derivative of k^{th} Fourier coefficient is as follows.

$$\frac{\mathrm{d}}{\mathrm{d}t}\left\langle x\right\rangle_k(t) = \left\langle \frac{\mathrm{d}}{\mathrm{d}t}x\right\rangle_k(t) - \mathrm{j}k\omega_0\left\langle x\right\rangle_k(t) \tag{3.14}$$

2. Convolution: Consider two time-domain signals $x(t)$ and $y(t)$; the dynamic phasors of the product of the two signals can be expressed as an explicit function of the individual coefficients using the following convolution relationship.

$$\left\langle xy \right\rangle_k (t) = \sum_{i=-\infty}^{+\infty} \left\langle x \right\rangle_{k-i} \left\langle y \right\rangle_i \tag{3.15}$$

3. Conjugate: Although the Fourier series is defined using both positive and negative frequencies, extraction of positive frequency coefficients is adequate since any negative-frequency coefficient is the complex conjugate of the positive-frequency coefficient of the same order; i.e.,

$$\left\langle x \right\rangle_{-k} (t) = \left\langle x \right\rangle_k^* (t) \tag{3.16}$$

where * denotes the complex conjugate.

In addition to the above, the generalized averaging method preserves the all the properties of dynamic phasors discussed in Section 3.1.2

3.3 Analytic Signals and Shifted-Frequency Analysis

The relationship between "*analytic signals*" (also referred to as complex signals) derived by means of Hilbert transformation and dynamic phasors for power system signals is described in [67] by S. Henschel and later formalized by J. R. Marti when introducing the "*shifted-frequency analysis*" (SFA) solution framework [9, 11, 68] for power system simulations.

3.3.1 Mathematical Background

Power system waveforms in general are band-pass signals centered around frequencies ω_0 and $-\omega_0$. They can be represent in terms of two low-pass signals and two sinusoidal carrier signals using Fourier decomposition as:

$$x(t) = u_{\mathrm{I}}(t)\cos(\omega_0 t) - u_{\mathrm{Q}}(t)\sin(\omega_0 t) \tag{3.17}$$

where u_{I} and u_{Q} are referred to as *in-phase* and *quadrature* components of $x(t)$, respectively [67]. These two low-pass signals provides all the information relating to $x(t)$ with a frequency-spectrum shifted down by ω_0 to around to zero. Therefore, the dynamic phasor of signal $x(t)$ is described as follows.

$$\mathcal{D}\Big[x(t)\Big] = u_{\mathrm{I}}(t) + \mathrm{j}u_{\mathrm{Q}}(t) \tag{3.18}$$

Another representation of $x(t)$ is using its analytic signal, which is defined as

$$z(t) = \mathcal{D}\Big[x(t)\Big]\mathrm{e}^{\mathrm{j}\omega_0 t} \tag{3.19}$$

Substituting (3.18) in (3.19) and further simplifying yields:

$$\begin{aligned} z(t) &= \Big[u_{\mathrm{I}}(t) + \mathrm{j}\,u_{\mathrm{Q}}(t)\Big]\Big[\cos(\omega_0 t) + \mathrm{j}\sin(\omega_0 t)\Big] \\ &= \Big[u_{\mathrm{I}}(t)\cos(\omega_0 t) - u_{\mathrm{Q}}(t)\sin(\omega_0 t)\Big] + \mathrm{j}\Big[u_{\mathrm{I}}(t)\sin(\omega_0 t) + u_{\mathrm{Q}}(t)\cos(\omega_0 t)\Big] \\ &= x(t) + \mathrm{j}\mathcal{H}\Big[x(t)\Big] \end{aligned} \tag{3.20}$$

where

$$\mathcal{H}\Big[x(t)\Big] = \frac{1}{\pi}\int_{-\infty}^{\infty}\frac{x(\tau)}{t-\tau}\,\mathrm{d}\tau \tag{3.21}$$

is the *Hilbert transformation* [69] of $x(t)$. The significance of the analytic signal is that the time-domain signal is retained in the real part of it while the dynamic phasor can be readily extracted from by applying a single phasor transformation. The concept of shifted-frequency analysis is established on this outcome in order to provide a general framework to unify the notion of dynamic phasors. It can be presented using the following steps [11].

I. The frequency spectrum obtained by Fourier decomposition ($\mathscr{F}[\cdot]$) of a general power system signal, $x(t)$, is symmetric with respect to the vertical axis; thus, it provides two frequency bands around $-\omega_0$ and ω_0 as shown in Figure 3.2a.

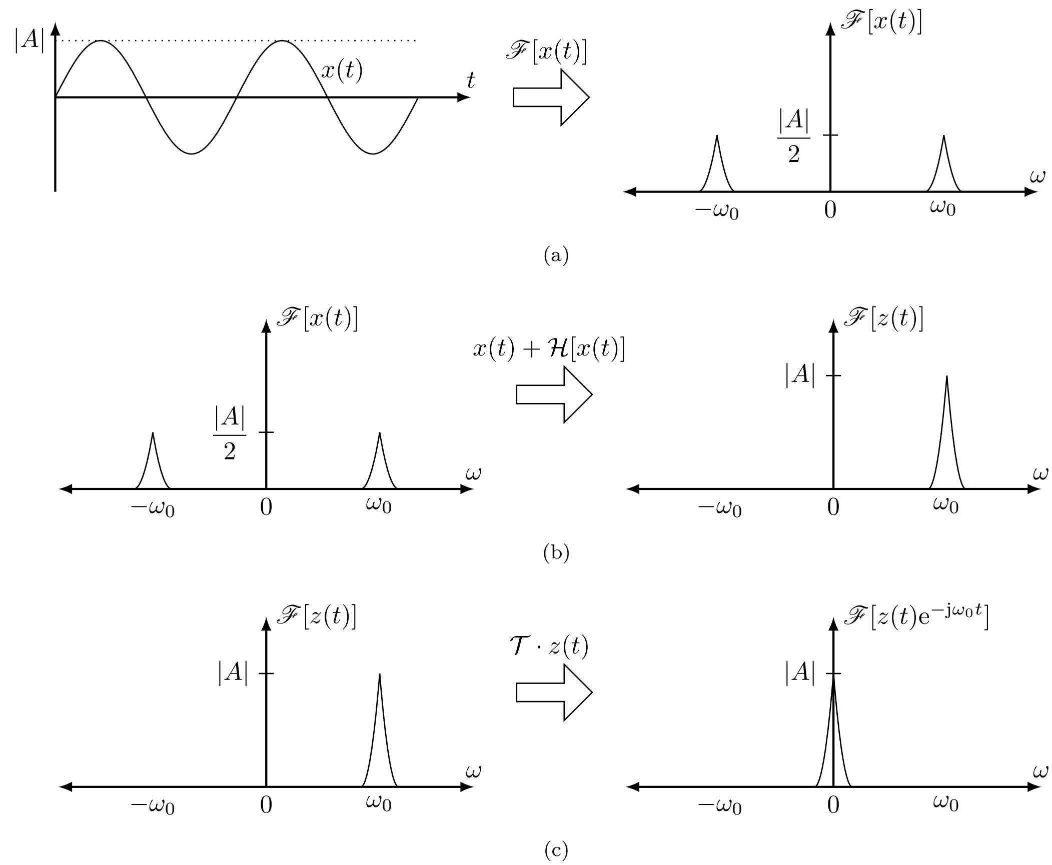

Figure 3.2: Shifted-frequency analysis illustration: (a) real signal Fourier decomposition, (b) yielding analytic signal (c) frequency shifting

II. The analytic signal, $z(t)$, of $x(t)$ is derived by applying the Hilbert transformation as defined in (3.20). This is graphically equivalent to ignoring the negative frequency term and multiplying the positive frequency magnitude by two as depicted in Figure 3.2b. Analytic signal extraction of power system signals is explain in section 3.3.2.

III. The frequency bandwidth of $z(t)$ is still around the carrier frequency of the system. Therefore, a frequency-shifting transformation is defined as:

$$\mathcal{T} = \mathrm{e}^{-\mathrm{j}\omega_0 t} \tag{3.22}$$

application of which brings the frequency band of analytic signal to around zero creating a low pass signal - in other words, dynamic phasor of $x(t)$ as,

$$\mathcal{D}\Big[x(t)\Big] = \mathcal{T} \cdot z(t) = z(t)\mathrm{e}^{-\mathrm{j}\omega_0 t} \tag{3.23}$$

The graphical representation of frequency shifting is shown in Figure 3.2c.

3.3.2 Extracting Analytic Signals

The Hilbert transformation, which forms the imaginary part of the analytic signal, is generally applied to known signals [69, 70]. However, in power system simulations, all signals are unknown at the beginning as it is generated during the course of the simulation. As such, the Hilbert transformation of the signal has to be computed in a causal manner, which is not always an easy task unless necessary assumptions are made.

Reference [67] explains how to apply Hilbert transformation to power system signals starting from steady-state initial conditions and system equations assuming that all signals are sinusoidal and have only the fundamental frequency at steady-state, as is the case virtually in all AC power system simulations. Based on this assumption, the following relationship can be written using the real-valued Fourier series for an arbitrary time-domain signal.

$$x(t) = a_1 \cos(\omega t) + b_1 \sin(\omega t) \tag{3.24}$$

where a_1 and b_1 are real Fourier coefficients at the fundamental frequency. The analytic signal of $x(t)$, can be derived as follows.

$$\begin{aligned} z(t) &= x(t) + \mathrm{j}\mathcal{H}\Big[x(t)\Big] \\ &= x(t) + \mathrm{j}\mathcal{H}\Big[a_1 \cos(\omega t) + b_1 \sin(\omega t)\Big] \\ &= x(t) + \mathrm{j}\, a_1 \sin(\omega t) - \mathrm{j}\, b_1 \cos(\omega t) \end{aligned} \tag{3.25}$$

This is a straightforward computation, which can be used with any arbitrary number of signals or phases. Since vast majority of power system applications are three-phase, the following explains a method that can be used to extract analytic signals from three-phase AC signals using a single transformation.

Consider a three-phase signal $\underline{\mathbf{x}}_{\text{abc}} = [x_{\text{a}}, x_{\text{b}}, x_{\text{c}}]'$. Denote the corresponding analytic signal as $\underline{\mathbf{z}}_{\text{abc}} = [z_{\text{a}}, z_{\text{b}}, z_{\text{c}}]'$ and the signal in $dq0$-domain as $\underline{\mathbf{x}}_{\text{dq0}} = [x_{\text{d}}, x_{\text{q}}, x_0]'$. It is given in the definition of analytic signal that

$$\mathfrak{Re}\{\underline{\mathbf{z}}_{\text{abc}}\} = \underline{\mathbf{x}}_{\text{abc}} \tag{3.26}$$

$$\mathfrak{Im}\{\underline{\mathbf{z}}_{\text{abc}}\} = \mathcal{H}\Big[\underline{\mathbf{x}}_{\text{abc}}\Big] = \mathcal{H}\Big[\mathfrak{Re}\{\underline{\mathbf{z}}_{\text{abc}}\}\Big] \tag{3.27}$$

Take the original signal to the $dq0$-domain as follows:

$$\underline{\mathbf{x}}_{\text{dq0}} = \mathbf{K}(t)\,\underline{\mathbf{x}}_{\text{abc}} \tag{3.28}$$

where

$$\mathbf{K}(t) = \frac{2}{3}\begin{pmatrix} \cos(\omega_0 t) & \cos(\omega_0 t - 2\pi/3) & \cos(\omega_0 t + 2\pi/3) \\ \sin(\omega_0 t) & \sin(\omega_0 t - 2\pi/3) & \sin(\omega_0 t + 2\pi/3) \\ 1/2 & 1/2 & 1/2 \end{pmatrix} \tag{3.29}$$

and

$$\mathbf{K}^{-1}(t) = \begin{pmatrix} \cos(\omega_0 t) & \sin(\omega_0 t) & 1 \\ \cos(\omega_0 t - 2\pi/3) & \sin(\omega_0 t - 2\pi/3) & 1 \\ \cos(\omega_0 t + 2\pi/3) & \sin(\omega_0 t + 2\pi/3) & 1 \end{pmatrix} \tag{3.30}$$

Combining (3.26) and (3.28) yields the following relationship.

$$\mathfrak{Re}\{\underline{\mathbf{z}}_{\text{abc}}\} = \underline{\mathbf{x}}_{\text{abc}} = \mathbf{K}^{-1}(t)\underline{\mathbf{x}}_{\text{dq0}} \tag{3.31}$$

or

$$\begin{aligned} \mathfrak{Re}\Big\{z_{\text{a}}\Big\} &= x_{\text{a}} = \cos(\omega_0 t)\,x_{\text{q}} + \sin(\omega_0 t)\,x_{\text{d}} + x_0 \\ \mathfrak{Re}\Big\{z_{\text{b}}\Big\} &= x_{\text{b}} = \cos(\omega_0 t - 2\pi/3)\,x_{\text{q}} + \sin(\omega_0 t - 2\pi/3)\,x_{\text{d}} + x_0 \\ \mathfrak{Re}\Big\{z_{\text{c}}\Big\} &= x_{\text{c}} = \cos(\omega_0 t + 2\pi/3)\,x_{\text{q}} + \sin(\omega_0 t + 2\pi/3)\,x_{\text{d}} + x_0 \end{aligned} \tag{3.32}$$

In steady-state, x_d and x_q are constants. Assuming that the signal consists of only the fundamental component in steady-state, the Hilbert transformation of $\underline{\mathbf{x}}_\mathrm{abc}$ can be derived as:

$$\begin{aligned}
\mathfrak{Im}\Big\{z_\mathrm{a}\Big\} &= \mathcal{H}\Big[\mathfrak{Re}\Big\{z_\mathrm{a}\Big\}\Big] = \sin(\omega_0 t)\,x_\mathrm{q} - \cos(\omega_0 t)\,x_\mathrm{d} \\
\mathfrak{Im}\Big\{z_\mathrm{b}\Big\} &= \mathcal{H}\Big[\mathfrak{Re}\Big\{z_\mathrm{b}\Big\}\Big] = \sin(\omega_0 t - 2\pi/3)\,x_\mathrm{q} - \cos(\omega_0 t - 2\pi/3)\,x_\mathrm{d} \\
\mathfrak{Im}\Big\{z_\mathrm{c}\Big\} &= \mathcal{H}\Big[\mathfrak{Re}\Big\{z_\mathrm{c}\Big\}\Big] = \sin(\omega_0 t + 2\pi/3)\,x_\mathrm{q} - \cos(\omega_0 t + 2\pi/3)\,x_\mathrm{d}
\end{aligned} \tag{3.33}$$

which also can be written in the following matrix form.

$$\mathfrak{Im}\Big\{\underline{\mathbf{z}}_\mathrm{abc}\Big\} = \begin{pmatrix} \sin(\omega_0 t) & -\cos(\omega_0 t) & 0 \\ \sin(\omega_0 t - 2\pi/3) & -\cos(\omega_0 t - 2\pi/3) & 0 \\ \sin(\omega_0 t + 2\pi/3) & -\cos(\omega_0 t + 2\pi/3) & 0 \end{pmatrix} \underline{\mathbf{x}}_\mathrm{qd0} \tag{3.34}$$

Note that the Hilbert transformation of a constant is zero; thus, the zero-sequence component is canceled out in (3.33). The analytic signal can be written as

$$\begin{aligned}
\underline{\mathbf{z}}_\mathrm{abc} &= \mathfrak{Re}\Big\{\underline{\mathbf{z}}_\mathrm{abc}\Big\} + \mathrm{j}\,\mathfrak{Im}\Big\{\underline{\mathbf{z}}_\mathrm{abc}\Big\} \\
&= \underline{\mathbf{x}}_\mathrm{abc} + \mathrm{j} \begin{pmatrix} \sin(\omega_0 t) & -\cos(\omega_0 t) & 0 \\ \sin(\omega_0 t - 2\pi/3) & -\cos(\omega_0 t - 2\pi/3) & 0 \\ \sin(\omega_0 t + 2\pi/3) & -\cos(\omega_0 t + 2\pi/3) & 0 \end{pmatrix} \underline{\mathbf{x}}_\mathrm{qd0} \\
&= \underline{\mathbf{x}}_\mathrm{abc} + \mathrm{j} \begin{pmatrix} \sin(\omega_0 t) & -\cos(\omega_0 t) & 0 \\ \sin(\omega_0 t - 2\pi/3) & -\cos(\omega_0 t - 2\pi/3) & 0 \\ \sin(\omega_0 t + 2\pi/3) & -\cos(\omega_0 t + 2\pi/3) & 0 \end{pmatrix} \mathbf{K}(t)\,\underline{\mathbf{x}}_\mathrm{abc}
\end{aligned} \tag{3.35}$$

Substituting $\mathbf{K}(t)$ and further simplifying (3.35) yields.

$$\underline{\mathbf{z}}_\mathrm{abc} = \Big[\hat{\mathbf{I}} + \mathrm{j}\frac{1}{\sqrt{3}}\mathbf{M}\Big]\,\underline{\mathbf{x}}_\mathrm{abc} \tag{3.36}$$

where $\hat{\mathbf{I}} = \begin{pmatrix} 1 & 0 & 0 \\ 0 & 1 & 0 \\ 0 & 0 & 1 \end{pmatrix}$ is the identity matrix and $\mathbf{M} = \begin{pmatrix} 0 & 1 & -1 \\ -1 & 0 & 1 \\ 1 & -1 & 0 \end{pmatrix}$ is a constant matrix.

It is observable from (3.36) that the three-phase analytic signal is a multiplication of the time-domain signal and a constant transformation matrix. At this point the frequency band of the analytic signal, $\underline{\mathbf{z}}_{\mathrm{abc}}$, can be shifted by multiplying it by $\mathrm{e}^{-\mathrm{j}\omega_0 t}$ to form dynamic phasors.

Shifted-frequency analysis provides a framework to analyse real signals with bandwidths around their fundamental frequency, in shifted-frequency domain. This concept can be extended to signals consisting of multiple harmonics by computing respective Fourier coefficients as described in section 3.4.

3.4 Base-frequency Dynamic Phasors

"*Base-frequency dynamic phasor*" (BFDP) is a novel technique established on the notion that all dynamic phasor coefficients of generalized averaging method (see section 3.2) can be combined to represent the entire frequency range of a time-domain signal including the dc component using a single dynamic phasor coefficient defined in the frame of the fundamental frequency [28]. This method, similar to the SFA method explained in section 3.3, produces a low bandwidth dynamic phasor signal through shifting each frequency component of the time-domain signal to a lower frequency by its carrier frequency. The following shows the theory underlying this method and techniques to extract BFDP from a time-domain signal.

3.4.1 Mathematical Background

The generalized averaging method provides the main foundation for this technique. The derivation of BFDPs can be commenced with rewriting the Fourier series in (3.10) as a series of explicit real values in the following form.

$$x(t-T+s) = \left\langle x \right\rangle_0(t) + \mathfrak{Re}\left\{ 2\sum_{k=1}^{+\infty} \left\langle x \right\rangle_k(t)\mathrm{e}^{\mathrm{j}k\omega_0(t-T+s)} \right\} \tag{3.37}$$

Equation (3.37) represents each harmonic with a distinct coefficient. They can be brought to frame of the fundamental frequency to yield a single dynamic phasor quantity as:

$$x(t-T+s) = \mathfrak{Re}\left\{\left\langle \mathrm{X}\right\rangle_{\mathrm{B}}(t)\mathrm{e}^{\mathrm{j}\omega_0(t-T+s)}\right\} \tag{3.38}$$

where

$$\left\langle \mathrm{X}\right\rangle_{\mathrm{B}}(t) = \left(\left\langle x\right\rangle_{0}(t) + 2\sum_{k=1}^{+\infty}\left\langle x\right\rangle_{k}(t)\mathrm{e}^{\mathrm{j}k\omega_0(t-T+s)}\right)\mathrm{e}^{-\mathrm{j}\omega_0(t-T+s)} \tag{3.39}$$

is termed as the base-frequency dynamic phasor and represents the entire frequency range of time-domain signal $x(t)$. As such, this method offers both efficiency and accuracy when extracting dynamic phasors from a time-domain signal and can be readily applied to single- and multi-phase quantities. It ensures that the network needs to be modeled only for its base frequency rather than modeling and solving for each harmonic, as is the case with generalised averaging method. Furthermore, BFDP preserves selectivity as any frequency component can be readily excluded from $\left\langle \mathrm{X}\right\rangle_{\mathrm{B}}(t)$ if need to be.

3.4.2 Base-Frequency Dynamic Phasor Extraction

Although $\left\langle \mathrm{X}\right\rangle_{\mathrm{B}}(t)$ is a sole complex quantity, it is clear from (3.39) that its computation still requires the knowledge of all Fourier coefficients, which may be computationally expensive if calculated directly. Two algorithms that extract BFDPs from any arbitrary real signal may be used as follows.

Method-I

A straightforward way of yielding BFDP is to extract the coefficients correspond to positive frequency and dc components of the signal individually and then merge them in a later stage before shifting the frequency spectrum down by its fundamental frequency. This is depicted in Figure 3.3.

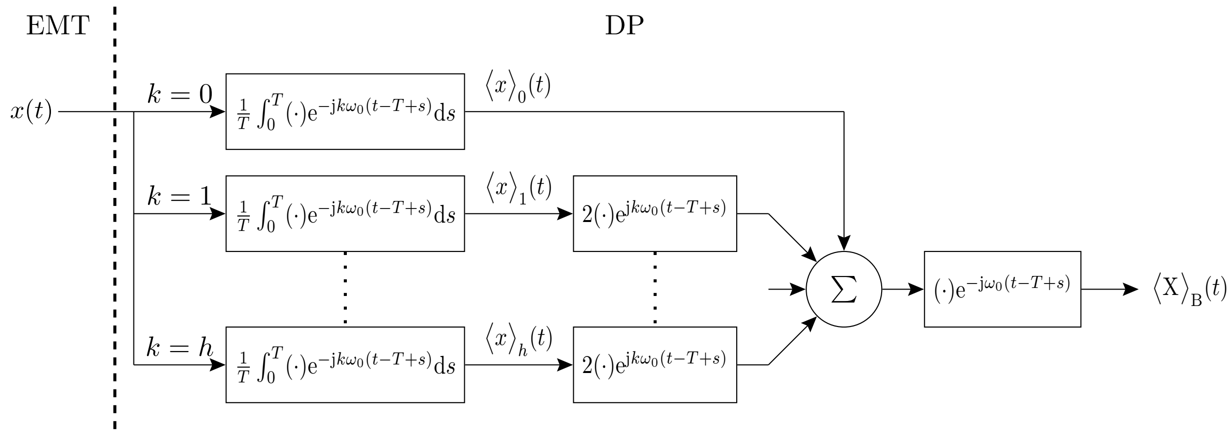

Figure 3.3: BFDP extraction: method-I

The recursive integration to obtain each coefficients can be efficiently done using (3.13). However, the drawback of this method is that the frequency contents of the time-domain waveform is unknown before the simulation, which may cause difficulties when deciding the number of coefficients required to achieve decent level of accuracy.

Method-II

Consider the series given in (3.37). One can express the same series in the following form separating the fundamental component from the signal [28]:

$$x(t-T+s) = \mathfrak{Re}\left\{2\left\langle x\right\rangle_1(t)\mathrm{e}^{\mathrm{j}\omega_0(t-T+s)}\right\} + \sum_{\substack{k=-\infty \\ k\neq -1,1}}^{+\infty} \left\langle x\right\rangle_k(t)\mathrm{e}^{\mathrm{j}k\omega_0(t-T+s)} \tag{3.40}$$

which can be further simplified as:

$$x(t-T+s) = \mathfrak{Re}\left\{2\left\langle x\right\rangle_1(t)\mathrm{e}^{\mathrm{j}\omega_0(t-T+s)}\right\} + \mathrm{X_h}(t)\mathrm{e}^{\mathrm{j}\omega_0(t-T+s)} \tag{3.41}$$

where

$$\mathrm{X_h}(t) = \sum_{\substack{k=-\infty \\ k\neq -1,1}}^{+\infty} \left\langle x\right\rangle_k(t)\mathrm{e}^{\mathrm{j}(k-1)\omega_0(t-T+s)} \tag{3.42}$$

is a composite complex signal, which comprises all harmonic contents of $x(t)$ except the fundamental component. The steps for extracting BFDP can be described using (3.41) as follows. The same procedure is illustrated in Figure 3.4.

First, the fundamental component, $\left\langle x \right\rangle_1(t)$, is calculated employing (3.11) with $k = 1$. It is then used to form the first term on the right-hand side of (3.41), which is then subtracted from the original signal. This yields the second term on the right-hand side of (3.41), from which $\mathrm{X_h}(t)$ is readily obtained. Finally, the BFDP is computed as:

$$\left\langle \mathrm{X} \right\rangle_{\mathrm{B}}(t) = 2\left\langle x \right\rangle_1(t) + \mathrm{X_h}(t) \tag{3.43}$$

While this extraction method (method-II) provides both efficiency and accuracy, in an event of the network consists of higher order harmonics, it shifts negative frequency components of $\mathrm{X_h}(t)$ further away from the imaginary axis, generating a high oscillating complex signal, which is undesirable in large time-step simulations. This problem does not arise for networks with frequencies up to the power system's base-frequency as the dynamic phasor coefficient for the base frequency is extracted separately. Therefore, for systems with multiple harmonics, it is recommended to calculate BFDPs using method-I by amalgamating the coefficients, which are calculated using (3.13), as in (3.39) if the Fourier series can be truncated to a small enough subset of coefficients.

The benefits of BFDPs are used in DP-EMT co-simulation applications [28,71] when mapping real EMT signal to dynamic phasors in order to model the network in a single frequency frame, and in [51] when interfacing a dynamic-phasor power electronic converter model to an EMT solver with a high degree of accuracy.

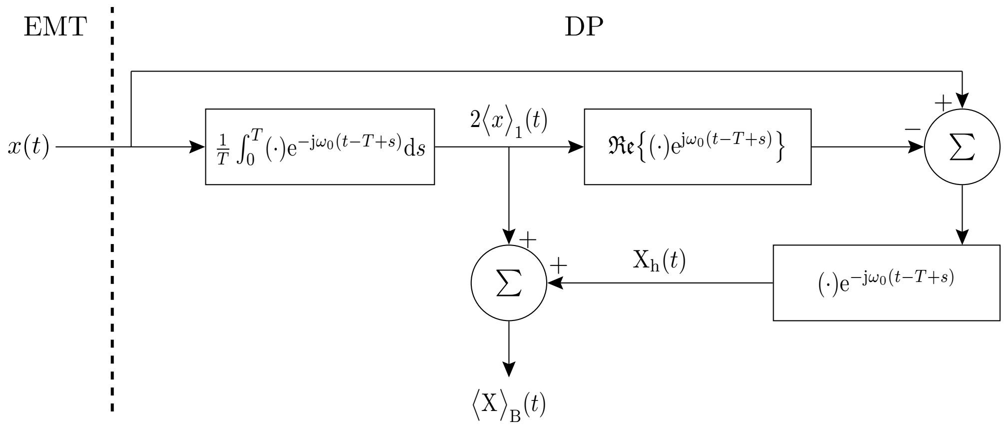

Figure 3.4: BFDP extraction: method-II

3.5 Illustrative Comparison of Dynamic Phasors

This section is intended to demonstrate and compare the performances of each dynamic phasor extraction method discussed in this chapter when representing generic power system signals in frequency-domain. Firstly, time-domain signals representing wide range of typical power system scenarios such as (i) electromechanical oscillations, (ii) higher order harmonics, (iii) dc offsets, (iv) un-balanced operation, (v) change of amplitudes, and (vi) frequency variations are defined. Then a comparison of the dynamic phasors waveforms and the frequency-spectra is carried out emphasizing the strengths and limitations of each method. For followings, each dynamic phasor waveform is extracted iteratively; i.e. only using present and past values of the time-domain signal, at each time-step, as is the case with power system simulations.

3.5.1 Representing General Power System Signals

Case I - Electromechanical Oscillations

One of the most common scenarios in power systems is electromechanical oscillations, which typically befall in the frequency range of 0.1 Hz-3 Hz. These are much slower compared to the fundamental power system frequency (e.g., 60 Hz) and appear in large networks mostly due to inter-area oscillations. This type of signal can be represented as:

$$x(t) = (A(t) + A_{\mathrm{e}}(t)\cos(2\pi f_{\mathrm{e}} t))\cos(\omega_0 t + \delta) \tag{3.44}$$

where A and A_{e} (typically functions of time) are magnitudes of fundamental component and the electromechanical component, respectively. ω_0 is the fundamental angular frequency, f_{e} is the frequency of the slowly-varying component, and δ is the initial phase angle.

Figure 3.5 displays the frequency-domain representations of this type of signal (or the corresponding balanced three-phase signal) with a decaying electromechanical component using respective dynamic phasor extraction methods. The parameters used to construct $x(t)$ are $A = 20$, $A_{\mathrm{e,max}} = 15$, $f_{\mathrm{e}} = 3$ Hz, and $\delta = \pi/6$ rad.

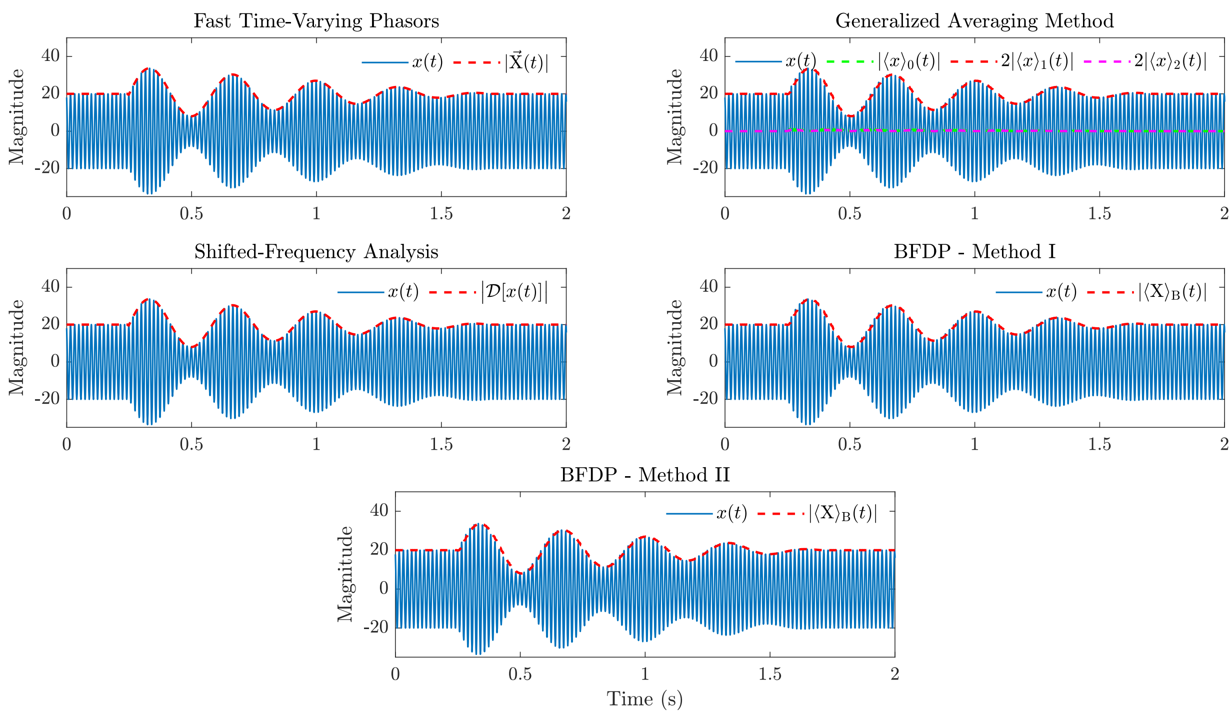

Figure 3.5: Dynamic phasor representations of a real signal consisting of electromechanical frequencies

For a signal with a frequency bandwidth around its fundamental component f_0 $(= \omega_0/2\pi)$, all phasor extraction methods produce essentially identical representations of the envelop waveform. For the generalized averaging method several frequency components are computed, which are unnecessary in this case as slow dynamics are attributed to the fundamental dynamic phasor coefficient. It is clear from the frequency-spectra given in Figure 3.6 that the frequency band of $x(t)$, which is originally in $f_0 \pm f_e$ and $-f_0 \pm f_e$ are now shifted to $0 \pm f_e$ yielding a low-pass signal in dynamic phasor-domain.

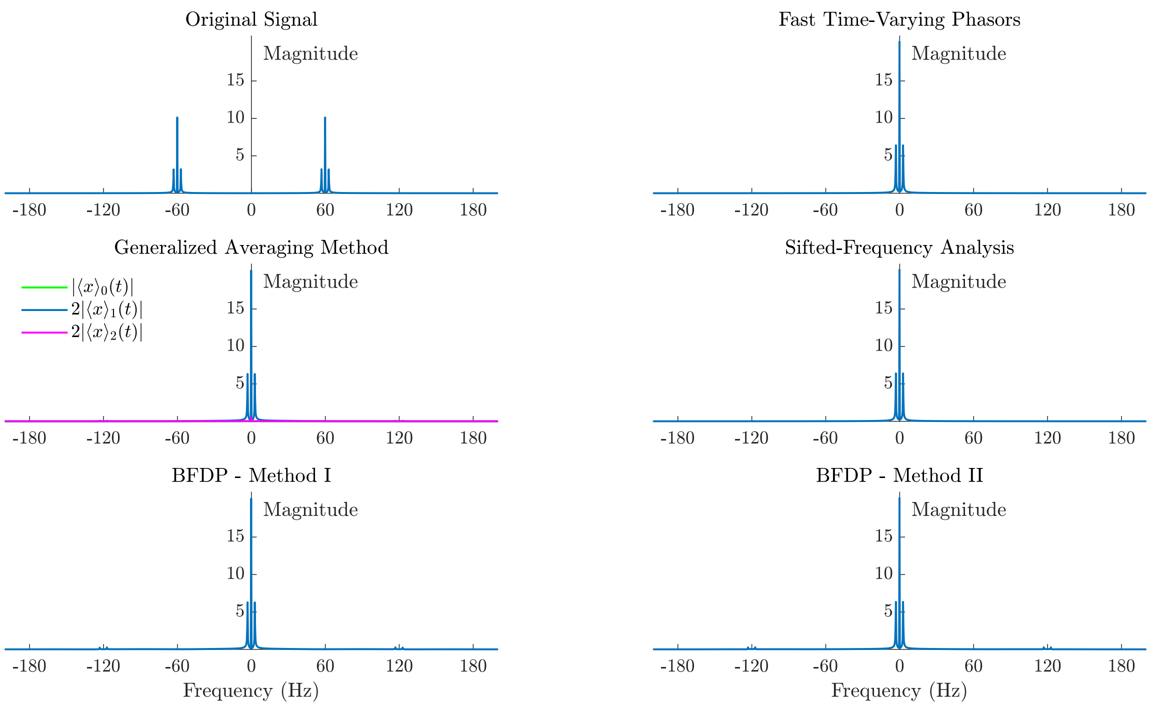

Figure 3.6: Frequency spectrum of DPs when the real signal consists of electromechanical frequencies

Case II - Higher Order Harmonics

Consider a second order harmonic component of magnitude A_h added to the fundamental-frequency signal to signify harmonics in a system. This takes the following form.

$$x(t) = A(t)\cos(\omega_0 t + \delta) + A_h(t)\cos(2\omega_0 t) \tag{3.45}$$

The phasor representations of (3.45) are given in Figure 3.7, for A_h of 10. It is observed that phasor extraction from this signal using each method produces a different representation, which can be explained using the harmonic spectrum of the signal provided in Figure 3.8.

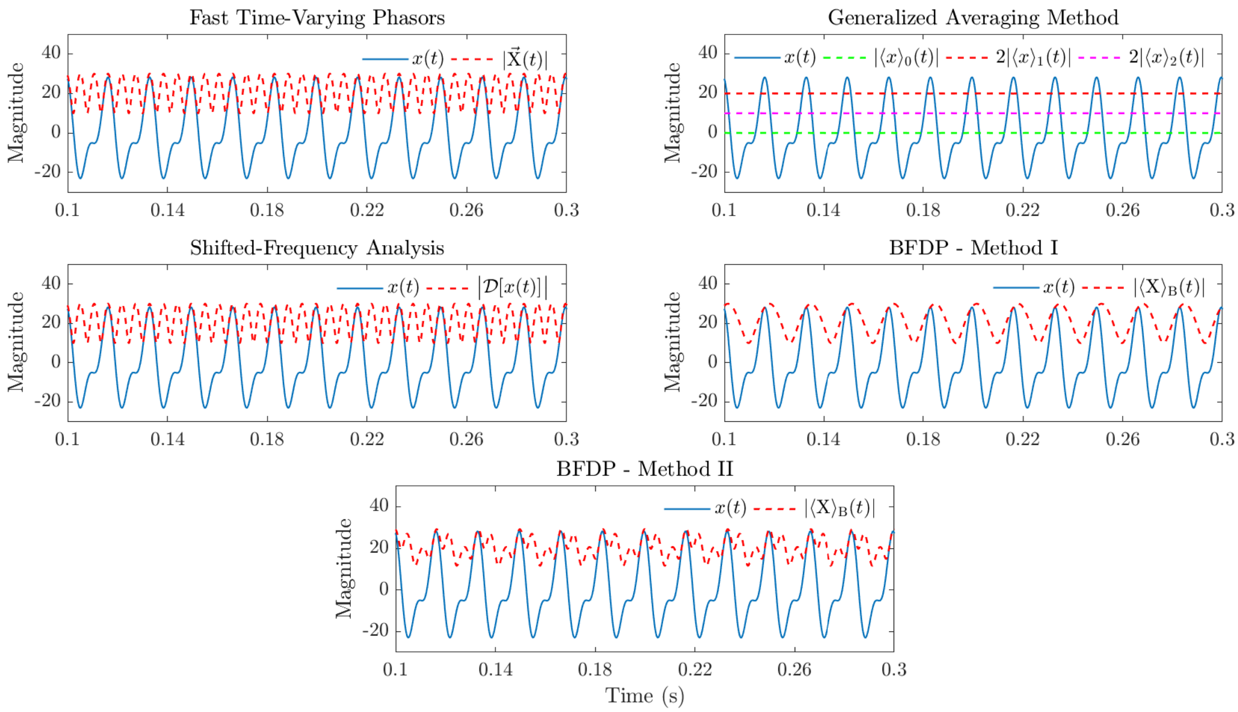

Figure 3.7: Dynamic phasor representations of a real signal consisting of harmonics

Fast time-varying phasor, by its definition, is tied with positive sequence three-phase signals; thus, it faces difficulties when the signal comprises harmonic components with different phase sequences. For example, in a general three-phase signal, the second order harmonics has a negative phase sequence while the third harmonics creates a zero-sequence component. Therefore, it is accurate to say that fast time-varying phasors are not suitably defined to model signals with higher order harmonics.

The generalized averaging method, on the other hand, shifts all its harmonic components to around zero, which makes it superior for modeling power electronic systems wherein the waveforms are made of multiple harmonics. However, each frequency component must be evaluated solely,

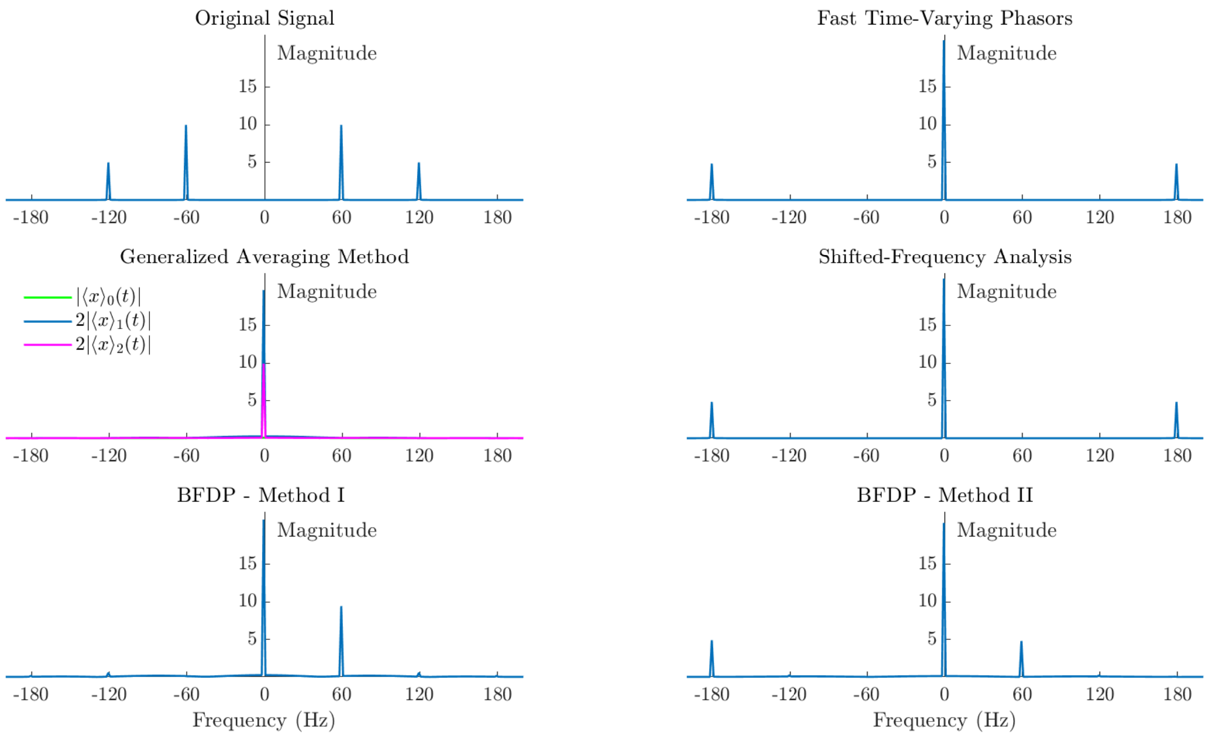

Figure 3.8: Frequency spectrum of dynamic phasors when the original signal consists of harmonics

which makes it a trying method when the solver's requirement is to model the entire network in a single-frequency frame.

The analytic signal in (3.36) is derived under the assumption that the signal is a fundamental-frequency sinusoid at steady state; therefore, it has a positive-frequency spectrum only when the natural signal is a periodic fundamental-frequency sinusoid. For other signals, it may generates negative-frequency components as well. Note that (3.36) is used to practically generate the analytic signal during a simulation in iterative manner, and is only an approximation to (3.20). As such, this method is only appropriate to represent frequencies up to the fundamental frequency.

As expected, the BFDPs in method-I shifted both the fundamental and the second order harmonic components by 60 Hz to zero and 60 Hz, respectively. This method uses only the positive-frequency coefficients; therefore, the frequency shifting process always creates a low-pass spectrum in frequency-domain compared to the real signal, and does not yield any negative frequency component, thus, making it a favourable method for large time-step simulation of harmonic rich systems in the fundamental frequency frame.

In the BFDP method-II, the frequency shifting process of $\mathrm{X_h}$ (see (3.42)) creates a third-order harmonic component of the dynamic phasor envelop since it shifts the -120 Hz component of the real signal further by 60 Hz to -180 Hz. Similarly, the positive frequency band of the second-order term is shifted down to 60 Hz.

Case III - DC Components:

DC components are common in most power electronic applications and can be expected even in a general power system waveforms, especially during abnormal circumstances such as line to ground faults. This type of signal can be represented as:

$$x(t) = A_0(t) + A(t)\cos(\omega_0 t + \delta) \tag{3.46}$$

where A_0 is the dc offset, which may be a function of time. The dynamic phasor waveforms and the frequency spectrum of each method for a signal with $A_0 = 5$ are given in Figure 3.9 and Figure 3.10, respectively.

A dc components results in a zero sequence component in symmetrical component decomposition; thus, the time-varying phasors, which focuses only on the positive sequence, completely ignores the dc part and generates an envelope waveform corresponding to the fundamental component. In the generalized averaging method, the dc component is readily captured by calculating the coefficient corresponding to $k = 0$. The shifted-frequency method and both BFDP methods are also able to capture the dc offset; however, small oscillations in the envelope waveform are observed that can be explained as follows.

With a non-zero dc component, the frequency shifting process shifts the dc component of the original signal to the frame of the fundamental component (a shift of $-f_0$) to include it as part

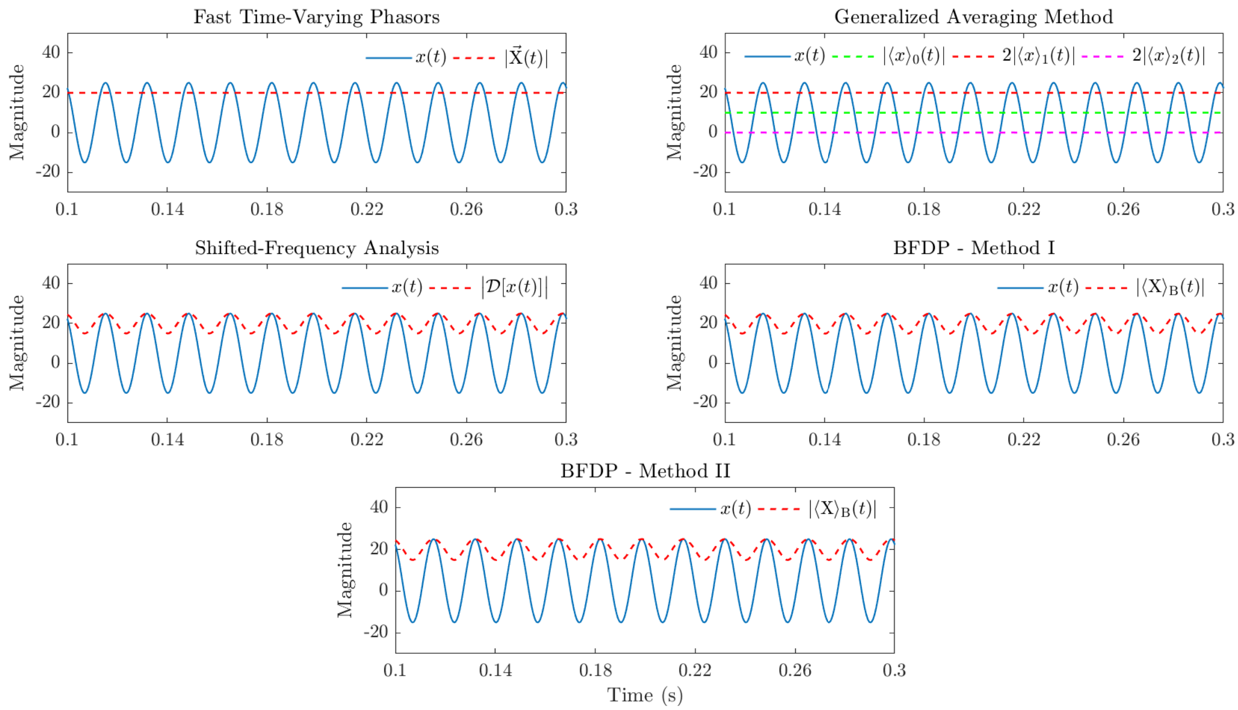

Figure 3.9: Dynamic phasor representations of a real signal consisting of a dc component

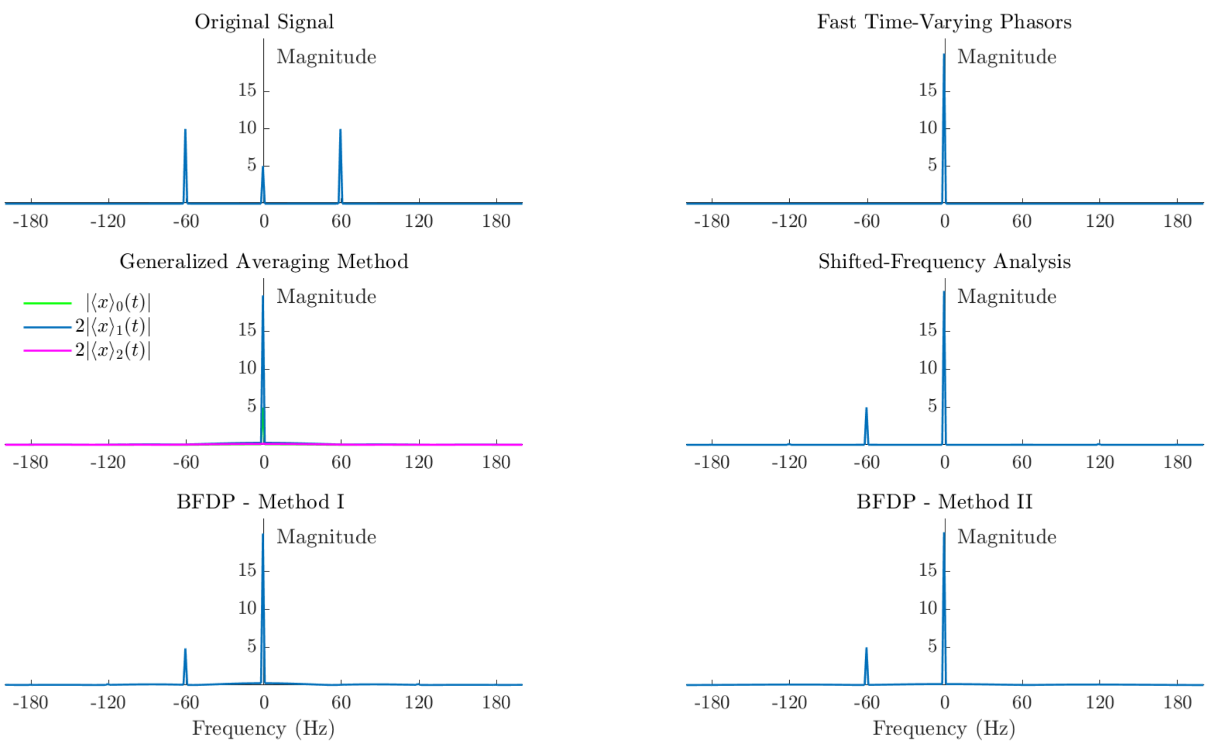

Figure 3.10: Frequency Spectrum of dynamic phasors when the real signal consists of dc component

of the dynamic phasor. Therefore, a dc component of magnitude $A_0(t)$ in time-domain, results in $A_0(t)\mathrm{e}^{-j\omega_0 t}$ in phasor domain; hence, it brings about visible oscillations at the fundamental frequency in the envelope waveform as it can be observed from Figure 3.9.

Case IV - Unbalanced Operation:

Unbalanced operation produce negative- and zero-sequence components in addition to the positive-sequence component in three-phase signals. The fast time-varying phasor method ignore the zero component of the three–phase phasor transformation; therefore, it is not readily applicable to unbalanced system representations. On the contrary, all other methods are defined to use with any arbitrary number of phases. As such, they are capable of accurately replicating any unbalanced condition associated with three-phase signal in frequency domain.

3.5.2 Representing Power System Transients

Dynamic phasors enable the use of frequency-domain representation to analyse various dynamic conditions where the conventional phasors fail. It is important to investigate the capabilities of each extraction method when replicating such conditions in phasor-based power system simulations to decide on the best technique(s) for the application at hand.

Change in Magnitude:

Consider a fundamental-frequency (60 Hz) signal whose magnitude is modulated as given in (3.44). Initially the signal has only the fundamental component with magnitudes, $A = 20$, which is then changed to 10 at $t = 0.2$ s. After $t = 0.25$ s, the magnitude is modulated with a slow varying 3 Hz component with $A_{\mathrm{e}} = 4$. Figure 3.11 shows how each phasor extraction method captures these changes in the real signal. The accuracy is examined by reconstructing the real signal using the extracted dynamic phasors as illustrated in the Figure 3.12.

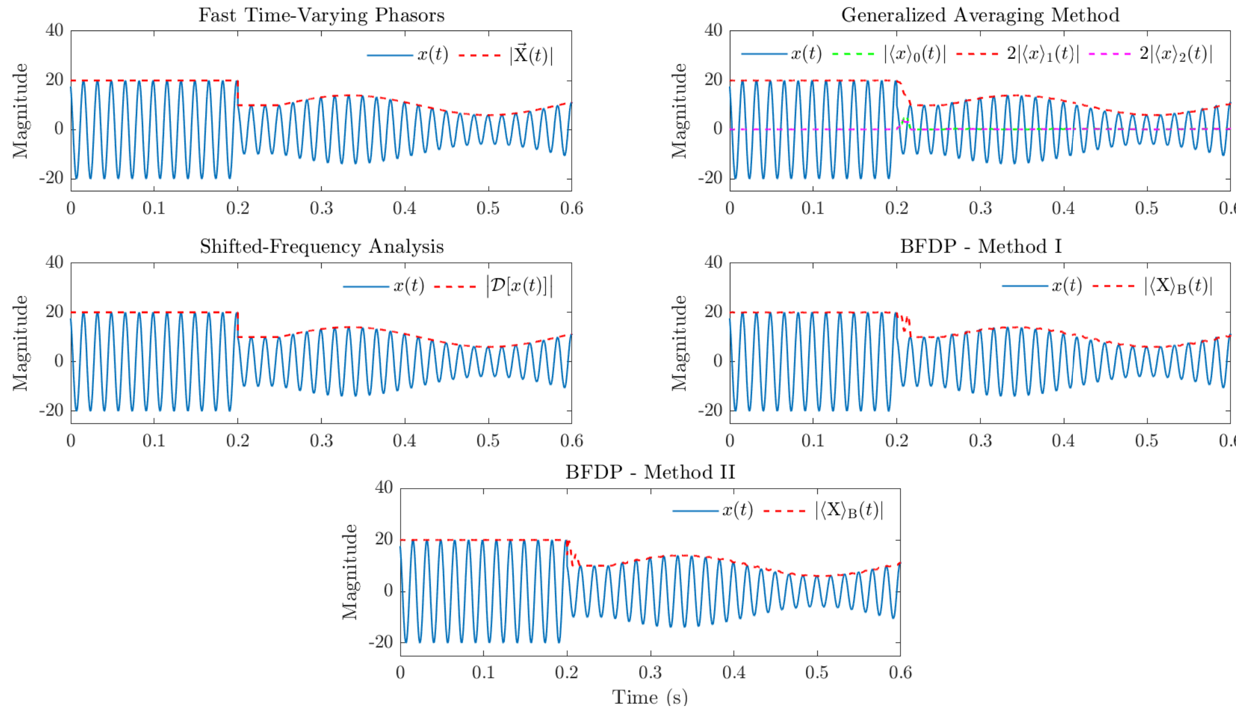

Figure 3.11: Dynamic phasor representations when the original signal undergoes a step change of magnitude

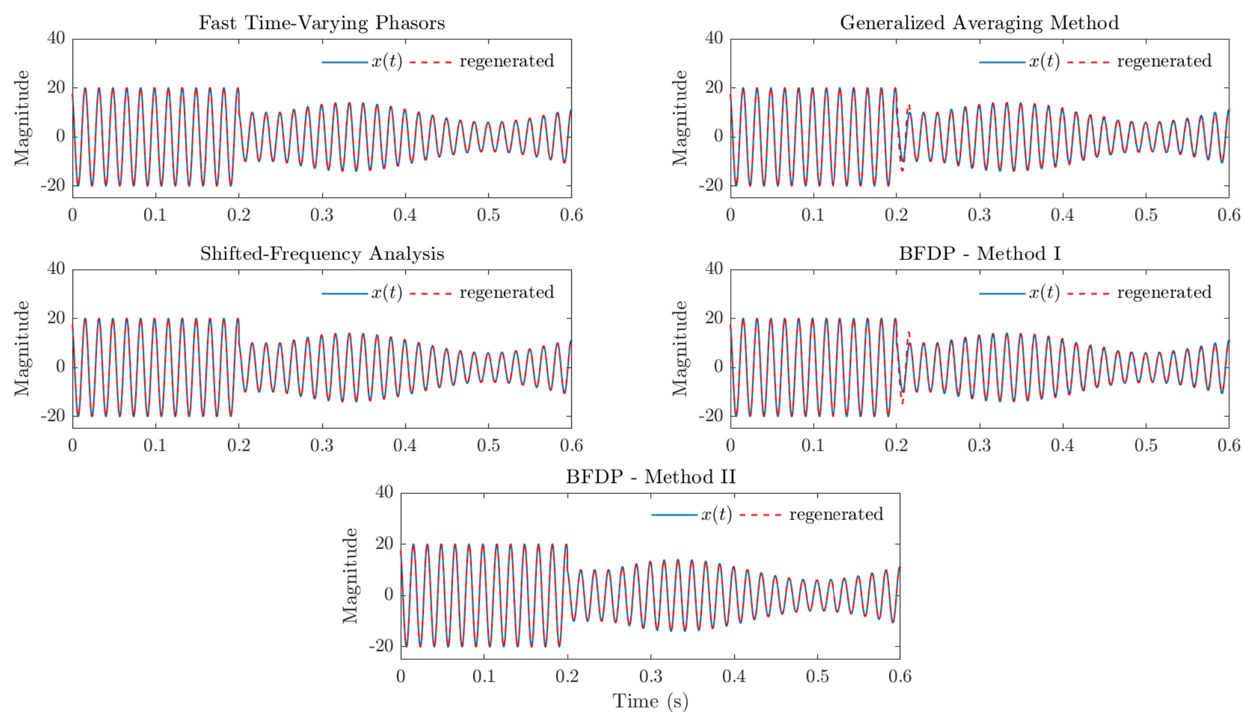

Figure 3.12: A comparison between the real signal and the recreated time-domain waveforms from dynamic phasors

Fast time-varying phasors and shifted-frequency analysis exactly follow the envelope of the signal amid the step change and slow variations of magnitude as they are extracted from instantaneous values of the signal associated with the present time-step. The conformity of $x(t)$ and the reconstructed waveforms implies that these two methods provide a high degree of accuracy during magnitude changes as long as $x(t)$ has a steady-state spectrum around its fundamental frequency.

The generalized averaging method and the BFDP-I closely follow the envelope; however, there appears to be a visible delay during magnitude changes. This takes place due to the fact that the coefficients are extracted by averaging instantaneous values over a previous cycle, which has implications on the envelope waveform. Nevertheless, it can be observed from the regenerated waveforms that they provide high accuracy when representing transients. Small discrepancies during changes are due to the unaccounted frequencies when the Fourier series is truncated to a finite series. The number of Fourier coefficients to include in each method is a decision the user has to make in order to realize an acceptable level of accuracy.

Similar to BFDP-I, BFDP-II also exhibits a delay in the envelope during step-change as the fundamental-frequency coefficient is extracted using values of the previous cycle. Barring that, the computation of $\mathrm{X}_{\mathrm{h}}(t)$ (see (3.42)) involves only present time-step values, and it accounts for all the frequencies of the real signal. Consequently, BFDP-II is able to deliver an exact replica of $x(t)$ both during steady state and transients. This can be understood by observing the regenerated waveform.

Change in Frequency:

In dynamic phasors, any change in the frequency of the real signal can be seen as a phase shift to the dynamic phasor obtained in the frame of its carrier frequency. Consider the following signal with a time-varying amplitude and phase angle at the frequency of $\omega_0 + \Delta\omega$.

$$x(t) = A(t)\cos((\omega_0 + \Delta\omega)t + \delta(t)) \tag{3.47}$$

The dynamic phasor at its carrier frequency can be written as:

$$\begin{aligned} \vec{\mathrm{X}}'(t) &= A(t)\mathrm{e}^{\mathrm{j}(\delta(t)+\Delta\omega t)} \\ &= A(t)\mathrm{e}^{\mathrm{j}\delta(t)}\mathrm{e}^{\mathrm{j}\Delta\omega t} \\ &= \vec{\mathrm{X}}(t)\mathrm{e}^{\mathrm{j}\Delta\omega t} \end{aligned} \tag{3.48}$$

which proves that waveform that may undergo frequency changes can still be represented with dynamic phasors at a fixed frequency.

Frequency changes are regular occurrences in power systems due to imbalances between the generation and load and sometimes due to abnormal conditions such as tripping of a machine. The system inertial and frequency control schemes disallow step changes in frequency; as such a frequency change, in general, may be represented as a ramp.

Consider the signal given in (3.49), where m denotes the slope of the frequency ramp.

$$x(t) = A(t)\cos(\omega_0 t + \delta(t) + m\pi t^2) \tag{3.49}$$

Let $m = -0.5$ for $0.2 < t < 0.4$ and $m = 0$ otherwise. The real and imaginary parts of the dynamic phasor representations of this signal are revealed in Figure 3.13 to identify the phase-angle change during the frequency ramp. It can be seen that all along the period of change, i.e., $t \in (0.2, 0.4)$, the real and imaginary parts of each method's phasor change their magnitudes to imitate the frequency change as a phase different. Note that despite the changes in the phase angle, the absolute value of each dynamic phasor remains constant since the magnitude of $x(t)$ is a constant in (3.49).

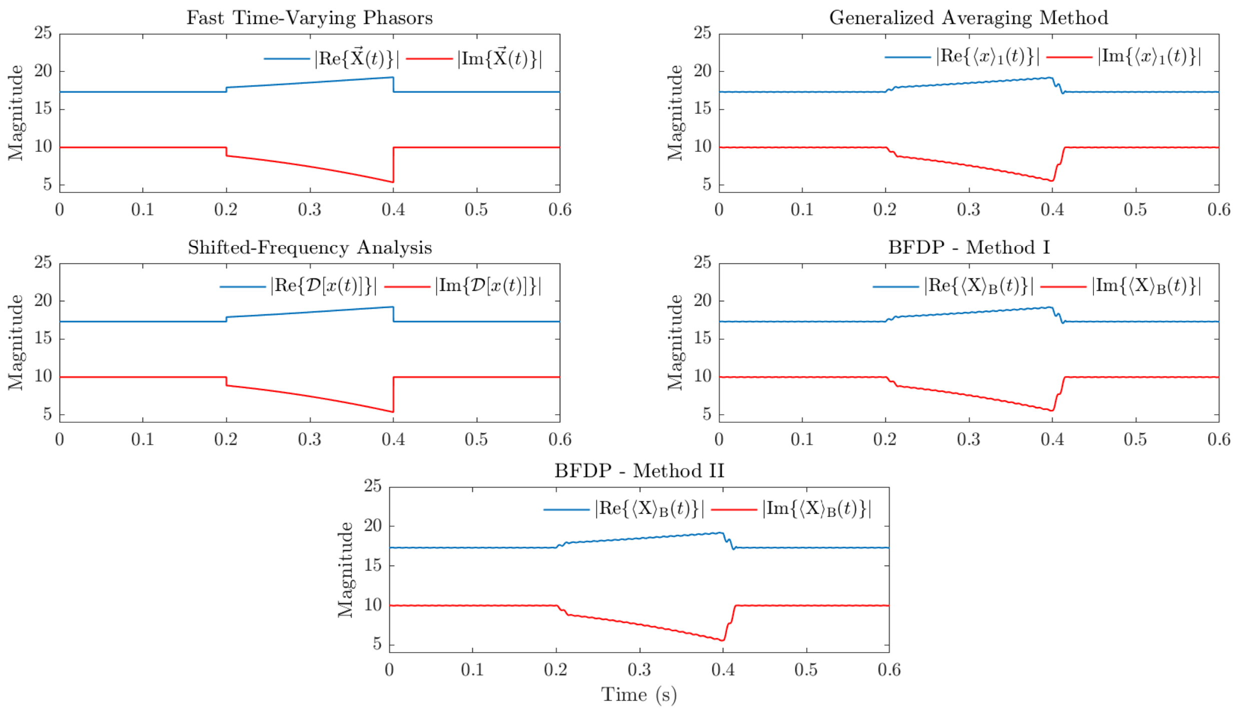

Figure 3.13: Dynamic phasor representations when the real signal undergoes a frequency ramp

3.6 Benefits of Using Dynamic Phasors

In discrete-time simulations, the computational burden on the simulator is proportional to the number of sample points for which the system solution has to be obtained. The intent of dynamic phasor representation is to reduce the size of samples, hence the number of computations and the overall solution time required to analyse an electric network by relocating the frequency spectrum of power system signals to a lower band. This can be further explained using the *Nyquist frequency.*

Nyquist frequency is the highest frequency that can be captured in a waveform at a given sampling rate [72]. If the sampling interval (also referred to as the time-step) is selected as Δt, then the sampling rate of the signal is given by $1/\Delta t$. The Nyquist frequency is equal to one-half the sampling rate; i.e.,

$$f_{\mathrm{Ny}} = \frac{1}{2\Delta t} \tag{3.50}$$

However, for higher accuracy in power system simulations, it is common practice to choose the time-step in such a way that the maximum frequency being simulated is at least five times less than the Nyquist frequency. Therefore, the following relationship can be obtained.

$$f_{\max} = \frac{f_{\mathrm{Ny}}}{5} = \frac{1}{10 \cdot \Delta t} \longrightarrow \Delta t = \frac{1}{10 \cdot f_{\max}} \tag{3.51}$$

This implies that shifting the frequency spectrum of a band-pass signal to a lower band allows to use larger time-steps in circuit solutions. For example, a perfect 60 Hz signal, which is shifted to 0 Hz by dynamic phasors allows to use a theoretical infinitely large time-step according to (3.51). In a more realistic scenario in which the power frequency changes between 58-62 Hz, dynamic phasors yield a band-pass signal between -2 Hz to 2 Hz; for that a 50-ms maximum time-step can be used. This is a large gain of the simulation speed compared to the time-domain analysis, which endures a maximum time-step of 1.61 ms.

3.7 Summary of Contributions and Conclusions

This chapter investigated a number of methods widely used in power system modeling and transient simulation applications for extracting dynamic phasors from samples of natural waveforms that are generated using EMT simulators. The contribution in this chapter is an in-depth assessment of each extraction method based on its ability to replicate general power system signals including electromechanical frequencies, dc and harmonic components, imbalances, and transient conditions such as magnitude and frequency variations. Simulation results were presented to demonstrate any limitations of these methods and to assess the resulting harmonic spectra of the phasors.

Fast time-varying phasors and the method explained for shifted-frequency analysis provide simple means to represent time-domain power system signals as long as their frequency spectrum is around the power system carrier frequency. However, fast time-varying phasors focus on the positive-sequence of those signals and, therefore, are applicable only to three-phase balanced systems. No such limitation exists for the shifted-frequency analysis.

The generalized averaging method uses time-varying Fourier coefficients as dynamic phasors at each frequency; therefore, it permits to model any number of harmonics in the system. However, the network at each frequency must be modeled and solved separately; hence, this method has drawbacks if the simulation is running at a single frequency frame.

Base-frequency dynamic phasors are developed by combining time-varying Fourier coefficients in the generalized averaging method to solve systems in fundamental frequency frame. This chapter suggested two methods to extract BFDPs from a real signal. Method-I computes a finite number of positive Fourier coefficients and brings them to fundamental-frequency frame by a frequency shifting transformation. The accuracy of this method greatly depends on the number of Fourier coefficients used to yield BFDPs. The extraction method-II uses a distinctive algorithm to do the same. Although this algorithm provides a great deal of accuracy, it generates undesirable higher frequency components of the BFDPs at the presence of higher order harmonics.

The findings of this chapter are instrumental in enabling an in-depth, quantitative analysis of various phasor extraction methods that form the underlying component of EMT-DP co-simulations of large electric networks.

Chapter 4

Stability Analysis of Interfaced Simulations

Interfacing different solvers under one simulation platform has implications on the stability of the simulation results. In other words, spurious numerical instabilities may occur due to interfacing that are otherwise absent in an actual un-partitioned system. These instabilities result from several factors including signal distortion due to conversion, time-delays in information exchange due to interface or partition topology, and the surrounding circuits.

Signal conversion methods that can be used in a DP-EMT co-simulation interface and their applicability in different power system scenarios are presented and discussed in Chapter 3. In section 2.3, it is noted that the physical structure, i.e., the circuit topology, of the interface has strong connections to the time-delay inserted in interface values. For example, a transmission line interface and MATE do not have such problems at the interface, whereas direct coupling with dependent sources always introduces a delay of one time-step to the solution. Understanding the impact of this delay on the stability of the overall solution is far reaching as it may be beneficial in coming up with suitable interface topologies or devising new instability mitigation schemes.

The objective of this chapter is to assess the stability and convergence properties of interfaced simulations to get a perspective on the most suited method(s) that can be used in DP-EMT co-simulation. Factors that are taken into account in this analysis are the structure of the surrounding circuit, time-delays caused by interface, and the sequence (sequential or simultaneous) of the solutions of the interfaced subsystems.

4.1 An Introduction to z-Domain Stability Analysis

4.1.1 z-Transformation

The *z-transformation* maps a discrete-time signal into a complex frequency domain, which is typically referred to as the z-domain, signal. It changes real or complex difference equations into z-domain algebraic equations, thus, making easier to evaluate the discrete-time system. The definition of the z-transformation of a discrete signal, $x[n]$, is given in as follows:

$$X(z) = \sum_{n=-\infty}^{\infty} x[n]z^{-n} \tag{4.1}$$

where z is a complex variable in what is called the z-plane [73]. The $[n]$ denotes the normalized time in which the discrete signal exists only for samples at $t = n\Delta t$ where n is an integer and Δt is the sample interval (referred to as the time-step). The definition given in (4.1) indicates the *bilateral z-transformation*. In cases where $x[n]$ is defined only for $n \geq 0$, the *unilateral z-transformation* is used wherein the support interval of n in (4.1) is changed to $[0, \infty)$. More details including the inverse z-transformation are not discussed in this thesis, but can be found in [73]. Some properties of z-transformation that are needed to build the theory in this chapter are given in Table 4.1.

Table 4.1: Useful properties of z-transformation

	Time-domain	z-domain
Linearity:	$a_1 x_1[n] + a_2 x_2[n]$	$a_1 X_1(z) + a_2 X_2(z)$
Time-delay:	$x(n-k)$; $k > 0$	$z^{-k} X(z)$
Convolution:	$x_1[n] * x_2[n]$	$X_1(z) X_2(z)$

4.1.2 z-Domain Stability

Consider a discrete-time system in the z-domain as given below.

$$Y(z) = H(z)\, X(z) \tag{4.2}$$

where $X(z)$, $Y(z)$, and $H(z)$ are the input signal, the output signal, and the transfer function of the system, respectively. The transfer function can be written as a ratio of two polynomials as:

$$H(z) = \frac{P(z)}{Q(z)} \tag{4.3}$$

wherein the roots of $P(z)$ and $Q(z)$ are referred to as the *zeros* and *poles* of the transfer function, respectively. As it is clear from (4.3), when z approaches a pole of the system, the magnitude of $H(z)$ approaches infinity. Therefore, the stability criteria for a discrete-time system are given based on the location of system poles in the z-plane as follows [73].

- A discrete system is *asymptotically stable* if and only if all the poles of $H(z)$ are within the unit circle in the z-plane. The poles may be repeated or simple (poles of order one).

- A discrete system is *marginally stable* if and only if there are no poles of $H(z)$ outside the unit circle, and there are some simple poles on the unit circle.

- A discrete system is *unstable* if and only if (i) at least one pole of $H(z)$ is outside the unit circle; or (ii) there are repeated poles of $H(z)$ on the unit circle.

An asymptotically stable system is one whose solution always converges to an equilibrium. A marginally stable system will not blow up and give an unbounded output, but neither will settle in an equilibrium. Simply put, a stable system has all its poles within the unit circle of the z-plane as depicted in Figure 4.1.

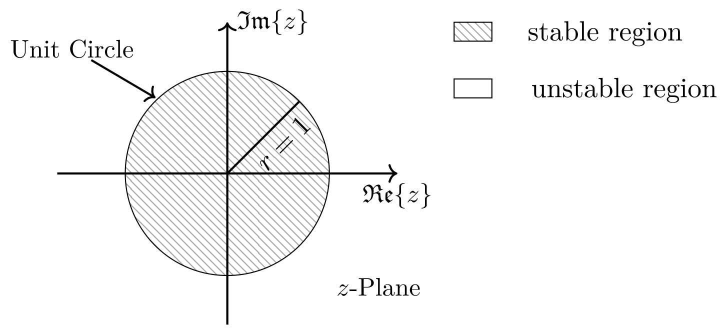

Figure 4.1: System stability based on pole locations in z-plane

4.2 Interface Stability of Resistive Networks

Digital computer-based simulators use discretization techniques, for example, the Dommel's method explained in section 2.1.2, to build the network's model as a set of difference equations, and then solve them iteratively for each time-step. In such a method, the admittance or the impedance matrix of the network is a function of the solution time-step. This, however, is not the case with entirely resistive networks as characteristic of such networks are not described by difference equations. This section derives the necessary stability criterion for interfacing two resistive subsystems. Then methods are devised to improve the stability of the interface if the solution is found to be unstable.

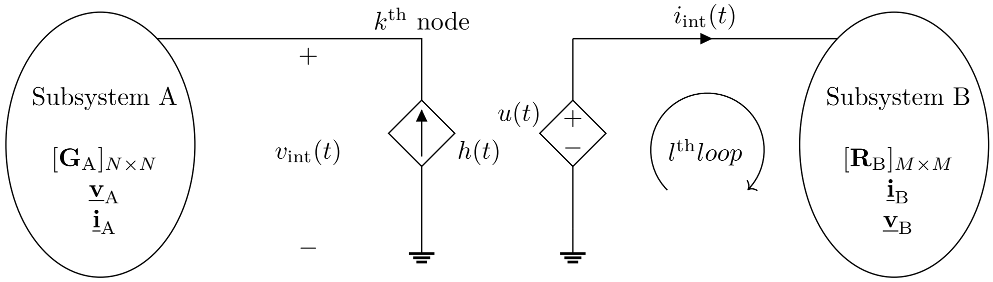

Figure 4.2: Two coupled resistive subsystems

Consider a resistive and stable network that is partitioned into two subsystems as shown in Figure 4.2. Although the figure shows one interface, the subsystems may be interfaced at more than one location. The anaylsis that follows next is based upon a general case of multiple interfaces. The nodal equations for subsystem A are as follows.

$$\mathbf{G}_{\text{A}}\underline{\mathbf{v}}_{\text{A}} = \underline{\mathbf{i}}_{\text{A}} + \underline{\mathbf{h}} \tag{4.4}$$

$$\underline{\mathbf{v}}_{\text{A}} = \mathbf{G}_{\text{A}}^{-1}\underline{\mathbf{i}}_{\text{A}} + \mathbf{G}_{\text{A}}^{-1}\underline{\mathbf{h}} \tag{4.5}$$

where $\mathbf{G}_{\text{A}}$, $\underline{\mathbf{v}}_{\text{A}}$, $\underline{\mathbf{i}}_{\text{A}}$, and $\underline{\mathbf{h}}$ are nodal conductance matrix, nodal voltage vector, nodal current source vector, and interface current source vector of subsystem A, respectively. Similarly, mesh equations of subsystem B can be given as:

$$\mathbf{R}_{\text{B}}\underline{\mathbf{i}}_{\text{B}} = \underline{\mathbf{v}}_{\text{B}} + \underline{\mathbf{u}} \tag{4.6}$$

$$\underline{\mathbf{i}}_{\text{B}} = \mathbf{R}_{\text{B}}^{-1}\underline{\mathbf{v}}_{\text{B}} + \mathbf{R}_{\text{B}}^{-1}\underline{\mathbf{u}} \tag{4.7}$$

where $\mathbf{R}_{\text{B}}$, $\underline{\mathbf{i}}_{\text{B}}$, $\underline{\mathbf{v}}_{\text{B}}$, and $\underline{\mathbf{u}}$ are mesh resistance matrix, mesh current vector, mesh voltage source vector, and interface voltage source vector of subsystem B, respectively.

The k^{th} node voltage of subsystem A is used to update the interface voltage source in the l^{th} loop of subsystem B; therefore, the following relationship is obtained for the interface voltage to match the length of $\underline{\mathbf{v}}_{\text{int}}$ and $\underline{\mathbf{u}}$ vectors.

$$\underline{\mathbf{v}}_{\text{int}} = \mathbf{S}_{\text{v}}\underline{\mathbf{v}}_{\text{A}} \tag{4.8}$$

where

$$\underline{\mathbf{v}}_{\text{int}} = \begin{array}{cl} \begin{pmatrix} 0 \\ \vdots \\ v_{\text{int}} \\ \vdots \\ 0 \end{pmatrix} & \begin{array}{l} \\ \\ \leftarrow l^{\text{th}} \text{ row} \\ \\ \\ M \times 1 \end{array} \end{array} \tag{4.9}$$

is a $M \times 1$ vector with zeros in all rows except l^{th} row and

$$\mathbf{S}_{\text{v}} = \begin{array}{cl} \begin{array}{c} \, k^{\text{th}} \text{ column} \\ \downarrow \end{array} & \\ \begin{pmatrix} 0 & \cdots & 0 & \cdots & 0 \\ \vdots & \ddots & \vdots & \ddots & \vdots \\ 0 & \cdots & +1 & \cdots & 0 \\ \vdots & \ddots & \vdots & \ddots & \vdots \\ 0 & \cdots & 0 & \cdots & 0 \end{pmatrix} & \begin{array}{l} \\ \\ \leftarrow l^{\text{th}} \text{ row} \\ \\ \\ M \times N \end{array} \end{array} \tag{4.10}$$

On the same ground, the relationship between the interface current and the mesh current vector of subsystem B is acquired as given in (4.11) since interface current source connected to the k^{th} node of subsystem A is updated using the l^{th} loop current of subsystem B.

$$\underline{\mathbf{i}}_{\text{int}} = \mathbf{S}_{\text{i}}\underline{\mathbf{i}}_{\text{B}} \tag{4.11}$$

where

$$\underline{\mathbf{i}}_{\text{int}} = \begin{array}{cl} \begin{pmatrix} 0 \\ \vdots \\ -i_{\text{int}} \\ \vdots \\ 0 \end{pmatrix} & \begin{array}{l} \\ \\ \leftarrow k^{\text{th}} \text{ row} \\ \\ \\ N \times 1 \end{array} \end{array} \tag{4.12}$$

is a $N \times 1$ vector with zeros in all rows except k^{th} row and

$$\mathbf{S}_{\mathrm{i}} = \begin{array}{cc} \begin{array}{ccccc} & & l^{\mathrm{th}}\text{ column} & & \\ & & \downarrow & & \end{array} & \\ \begin{pmatrix} 0 & \cdots & 0 & \cdots & 0 \\ \vdots & \ddots & \vdots & \ddots & \vdots \\ 0 & \cdots & -1 & \cdots & 0 \\ \vdots & \ddots & \vdots & \ddots & \vdots \\ 0 & \cdots & 0 & \cdots & 0 \end{pmatrix}_{N \times M} & \begin{array}{l} \\ \\ \leftarrow k^{th}\text{ row} \\ \\ \\ \end{array} \end{array} \tag{4.13}$$

As explained in Chapter 2, network coupling introduces a time-step delay when exchanging information between subsystems. This delay can be represented using appropriate values to update the current source and voltage source of the Figure 4.2 based on the sequence of subsystem solutions.

4.2.1 Interface Stability with Sequential Solutions

Assume that subsystems A and B are solved in series and that the solution of subsystem A is obtained first. Since subsystem B is yet to be solved for the present time-step, previous time-step values of subsystem B are used to update the interface current source of subsystem A. Once subsystem A is solved for the present time-step, those values can be used to update the interface voltage source of subsystem B. Therefore, the following relationship exists.

$$\underline{\mathbf{h}}(t) = \underline{\mathbf{i}}_{\mathrm{int}}(t - \Delta t) \tag{4.14}$$

$$\underline{\mathbf{u}}(t) = \underline{\mathbf{v}}_{\mathrm{int}}(t) \tag{4.15}$$

Combining (4.5), (4.8), and (4.14) one can obtain the following relationship for the interface voltage at a given time, t.

$$\underline{\mathbf{v}}_{\mathrm{int}}(t) = \mathbf{S}_{\mathrm{v}}\mathbf{G}_{\mathrm{A}}^{-1}\underline{\mathbf{i}}_{\mathrm{A}}(t) + \mathbf{S}_{\mathrm{v}}\mathbf{G}_{\mathrm{A}}^{-1}\underline{\mathbf{i}}_{\mathrm{int}}(t - \Delta t) \tag{4.16}$$

Similarly, the interface current for the sequential solution can be derived by combining (4.7), (4.11), and (4.15) as below.

$$\underline{\mathbf{i}}_{\text{int}}(t) = \mathbf{S}_{\text{i}}\mathbf{R}_{\text{B}}^{-1}\underline{\mathbf{v}}_{\text{B}}(t) + \mathbf{S}_{\text{i}}\mathbf{R}_{\text{B}}^{-1}\underline{\mathbf{v}}_{\text{int}}(t) \tag{4.17}$$

It is evident from (4.16) and (4.17) that the interface current and the interface voltage are dependent on one another; as such, a stability criterion for the overall solution can be derived by examining the dynamic behaviour of one of those variables. For this reason, the following expression is derived by substituting (4.17) in (4.16).

$$\underline{\mathbf{v}}_{\text{int}}(t) = \mathbf{S}_{\text{v}}\mathbf{G}_{\text{A}}^{-1}\underline{\mathbf{i}}_{\text{A}}(t) + \mathbf{S}_{\text{v}}\mathbf{G}_{\text{A}}^{-1}\mathbf{S}_{\text{i}}\mathbf{R}_{\text{B}}^{-1}\underline{\mathbf{v}}_{\text{B}}(t-\Delta t) + \mathbf{S}_{\text{v}}\mathbf{G}_{\text{A}}^{-1}\mathbf{S}_{\text{i}}\mathbf{R}_{\text{B}}^{-1}\underline{\mathbf{v}}_{\text{int}}(t-\Delta t) \tag{4.18}$$

Before applying the z-transformation, (4.18) must be written with normalized time (see the definition of z-transformation given in (4.1)) as,

$$\underline{\mathbf{v}}_{\text{int}}[n] = \mathbf{S}_{\text{v}}\mathbf{G}_{\text{A}}^{-1}\underline{\mathbf{i}}_{\text{A}}[n] + \mathbf{S}_{\text{v}}\mathbf{G}_{\text{A}}^{-1}\mathbf{S}_{\text{i}}\mathbf{R}_{\text{B}}^{-1}\underline{\mathbf{v}}_{\text{B}}[n-1] + \mathbf{S}_{\text{v}}\mathbf{G}_{\text{A}}^{-1}\mathbf{S}_{\text{i}}\mathbf{R}_{\text{B}}^{-1}\underline{\mathbf{v}}_{\text{int}}[n-1] \tag{4.19}$$

from which the z-domain equation can be derived as below, wherein $\hat{\mathbf{I}}$ represents the identity matrix.

$$\underline{\mathbf{v}}_{\text{int}}(z) = \mathbf{S}_{\text{v}}\mathbf{G}_{\text{A}}^{-1}\underline{\mathbf{i}}_{\text{A}}(z) + z^{-1}\mathbf{S}_{\text{v}}\mathbf{G}_{\text{A}}^{-1}\mathbf{S}_{\text{i}}\mathbf{R}_{\text{B}}^{-1}\underline{\mathbf{v}}_{\text{B}}(z) + z^{-1}\mathbf{S}_{\text{v}}\mathbf{G}_{\text{A}}^{-1}\mathbf{S}_{\text{i}}\mathbf{R}_{\text{B}}^{-1}\underline{\mathbf{v}}_{\text{int}}(z) \tag{4.20}$$

$$\left[\hat{\mathbf{I}} - z^{-1}\mathbf{S}_{\text{v}}\mathbf{G}_{\text{A}}^{-1}\mathbf{S}_{\text{i}}\mathbf{R}_{\text{B}}^{-1}\right]\underline{\mathbf{v}}_{\text{int}}(z) = \mathbf{S}_{\text{v}}\mathbf{G}_{\text{A}}^{-1}\underline{\mathbf{i}}_{\text{A}}(z) + z^{-1}\mathbf{S}_{\text{v}}\mathbf{G}_{\text{A}}^{-1}\mathbf{S}_{\text{i}}\mathbf{R}_{\text{B}}^{-1}\underline{\mathbf{v}}_{\text{B}}(z) \tag{4.21}$$

Clearly the poles of the transfer function, and hence the dynamics of the solution, depends on the properties of $\mathbf{S}_{\text{v}}\mathbf{G}_{\text{A}}^{-1}\mathbf{S}_{\text{i}}\mathbf{R}_{\text{B}}^{-1}$, which needs to be explored further. Assume that inverses of matrices $\mathbf{G}_{\text{A}}$ and $\mathbf{R}_{\text{B}}$ take following forms.

$$\mathbf{G}_{\text{A}}^{-1} = \left[r_{ij}\right]_{N\times N} \tag{4.22}$$

$$\mathbf{R}_{\text{B}}^{-1} = \left[g_{ij}\right]_{M\times M} \tag{4.23}$$

Then one can readily show that

$$
\mathbf{S}_\mathrm{v}\mathbf{G}_\mathrm{A}^{-1}\mathbf{S}_\mathrm{i}\mathbf{R}_\mathrm{B}^{-1} = \begin{array}{cc}
\begin{array}{cccccc} & & & l^{\text{th}}\text{ column} & & \\ & & & \downarrow & & \end{array} & \\
\begin{pmatrix}
0 & 0 & \cdots & 0 & \cdots & 0 \\
\vdots & \vdots & \ddots & \vdots & \ddots & \vdots \\
-g_{l1}r_{kk} & -g_{l2}r_{kk} & \cdots & -g_{ll}r_{kk} & \cdots & -g_{lM}r_{kk} \\
\vdots & \vdots & \ddots & \vdots & \ddots & \vdots \\
0 & 0 & \cdots & 0 & \cdots & 0
\end{pmatrix}_{M \times M} & \begin{array}{l} \\ \\ \leftarrow l^{\text{th}}\text{ row} \\ \\ \\ \end{array}
\end{array} \tag{4.24}
$$

Multiplying (4.24) by $\underline{\mathbf{v}}_{\text{int}}(z)$, whose elements are zero except in the l^{th} row, yields a similar sparse vector whose l^{th} element is equal to $-g_{ll}r_{kk}\, v_{\text{int}}(z)$. Therefore, one only needs to consider the l^{th} row of (4.21) to find the poles of the system. The l^{th} row of (4.21) is given by

$$
\Big[1 - z^{-1}(-g_{ll}r_{kk})\Big] v_{\text{int}}(z) = r_{kl}\, i_{A_l}(z) - z^{-1} g_{ll}r_{kk}\, v_{B_l}(z) \tag{4.25}
$$

from which the pole of the transfer function can be found as $z = g_{ll}r_{kk}$. Therefore, the criterion for the stability of the interfaced simulation of a partitioned resistive network, while solving subsystems sequentially, is as follows.

$$
|g_{ll}r_{kk}| \leq 1.0 \tag{4.26}
$$

Note that the criterion given in (4.26) is based on single-rate simulation for a system with one interface. In case of a multi-rate simulation, assuming subsystem A uses a larger time-step, the intermediate point may have to interpolated before taking the solution of subsystem B at a given time. A system with multiple interfaces yields a large number of poles in its transfer function of (4.21). Therefore, the easiest way to find a stability criterion is to use a computerized method.

4.2.2 Interface Stability with Simultaneous Solutions

In simultaneous solution, both subsystems are solved in parallel. Therefore, both interface sources in Figure 4.2 must be updated based on the previous time-step values from the corresponding subsystems; i.e.,

$$\underline{\mathbf{h}}(t) = \underline{\mathbf{i}}_{\text{int}}(t - \Delta t) \tag{4.27}$$

$$\underline{\mathbf{u}}(t) = \underline{\mathbf{v}}_{\text{int}}(t - \Delta t) \tag{4.28}$$

For a discrete-time implementation, one can obtain expressions for the interface voltage by combining (4.5), (4.8), and (4.27) and for interface current by combining (4.7), (4.11), and (4.28) as follows.

$$\underline{\mathbf{v}}_{\text{int}}(t) = \mathbf{S}_{\text{v}}\mathbf{G}_{\text{A}}^{-1}\underline{\mathbf{i}}_{\text{A}}(t) + \mathbf{S}_{\text{v}}\mathbf{G}_{\text{A}}^{-1}\underline{\mathbf{i}}_{\text{int}}(t - \Delta t) \tag{4.29}$$

$$\underline{\mathbf{i}}_{\text{int}}(t) = \mathbf{S}_{\text{i}}\mathbf{R}_{\text{B}}^{-1}\underline{\mathbf{v}}_{\text{B}}(t) + \mathbf{S}_{\text{i}}\mathbf{R}_{\text{B}}^{-1}\underline{\mathbf{v}}_{\text{int}}(t - \Delta t) \tag{4.30}$$

The following z-domain expression can be derived for the simultaneous solution by repeating the same steps taken for the sequential solution in section 4.2.1.

$$\left[\hat{\mathbf{I}} - z^{-2}\mathbf{S}_{\text{v}}\mathbf{G}_{\text{A}}^{-1}\mathbf{S}_{\text{i}}\mathbf{R}_{\text{B}}^{-1}\right]\underline{\mathbf{v}}_{\text{int}}(z) = \mathbf{S}_{\text{v}}\mathbf{G}_{\text{A}}^{-1}\underline{\mathbf{i}}_{\text{A}}(z) + z^{-1}\mathbf{S}_{\text{v}}\mathbf{G}_{\text{A}}^{-1}\mathbf{S}_{\text{i}}\mathbf{R}_{\text{B}}^{-1}\underline{\mathbf{v}}_{\text{B}}(z) \tag{4.31}$$

From (4.31), the poles of the transfer function are readily found as $z = \pm\sqrt{g_{ll}r_{kk}}$. Therefore, the stability criterion of an interfaced resistive network for simultaneous solution is given as

$$\sqrt{g_{ll}r_{kk}} \leq 1.0 \tag{4.32}$$

4.2.3 Modifying the Interface for Guaranteed Stability

The findings of the previous section established that the interface of two resistive subsystems is stable as long as particular conditions are satisfied. In [47] it is shown that if the solution is unstable when two subsystems are interfaced using a current source in the first system and a voltage source in the other system with a time-step delay, then the solution is stable if they are interfaced using a voltage source in the first system and a current source in the other system, and vice versa. However, [47] did not account for the time-steps and implications of past values of difference equations; therefore, the validity of the statements made in [47] is limited. This subsection devises a comprehensive method to improve the interface's stability in case the interface induces numerical instabilities in the solution.

Consider the interface shown in Figure 4.3 between two resistive subsystems. The interface current source connected to subsystem A and the interface voltage source connected to subsystem B are augmented by a shunt conductance and a series resistance, respectively. The goal is to find the values (or range of values) for g and r in such a way that the stability of the solution is preserved.

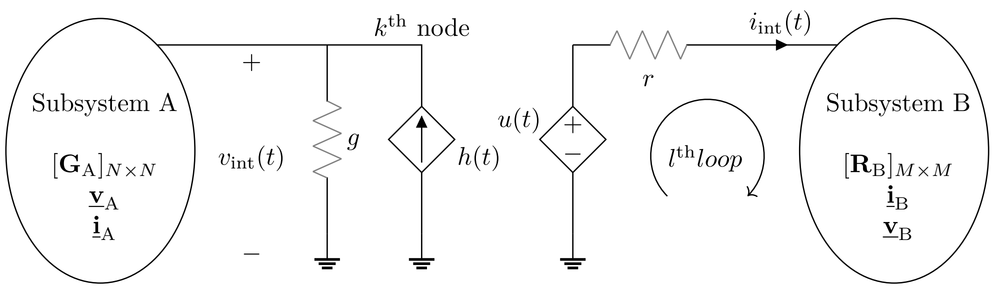

Figure 4.3: Improving the interface stability of resistive subsystems

Note that g and r are externally added elements; i.e., they are not parts of the original system; therefore, they must be appropriately compensated when updating interface sources. This is given in (4.33) and (4.34), which are deduced assuming a sequential solution of subsystems.

$$\underline{\mathbf{h}}(t) = \underline{\mathbf{i}}_{\text{int}}(t - \Delta t) + \mathbf{G}^{'}\underline{\mathbf{v}}_{\text{int}}(t - \Delta t) \tag{4.33}$$

$$\underline{\mathbf{u}}(t) = \underline{\mathbf{v}}_{\text{int}}(t) + \mathbf{R}^{'}\underline{\mathbf{i}}_{\text{int}}(t - \Delta t) \tag{4.34}$$

where

$$
\mathbf{G}^{'} = \begin{array}{cl} \begin{array}{ccccc} & & l^{\text{th}}\text{ column} & & \\ & & \downarrow & & \end{array} & \\ \begin{pmatrix} 0 & \cdots & 0 & \cdots & 0 \\ \vdots & \ddots & \vdots & \ddots & \vdots \\ 0 & \cdots & g & \cdots & 0 \\ \vdots & \ddots & \vdots & \ddots & \vdots \\ 0 & \cdots & 0 & \cdots & 0 \end{pmatrix}_{N \times M} & \begin{array}{l} \\ \\ \leftarrow k^{\text{th}}\text{ row} \\ \\ \\ \end{array} \end{array} \tag{4.35}
$$

and

$$
\mathbf{R}^{'} = \begin{array}{cl} \begin{array}{ccccc} & & k^{\text{th}}\text{ column} & & \\ & & \downarrow & & \end{array} & \\ \begin{pmatrix} 0 & \cdots & 0 & \cdots & 0 \\ \vdots & \ddots & \vdots & \ddots & \vdots \\ 0 & \cdots & -r & \cdots & 0 \\ \vdots & \ddots & \vdots & \ddots & \vdots \\ 0 & \cdots & 0 & \cdots & 0 \end{pmatrix}_{M \times N} & \begin{array}{l} \\ \\ \leftarrow l^{\text{th}}\text{ row} \\ \\ \\ \end{array} \end{array} \tag{4.36}
$$

The compensations provided for supplementary elements g and r appear with a time-step delay in (4.33) and (4.34); hence, it may manifest small inaccuracies in the solution. However, it is unlikely that the delay leads to any numerical instability as it is comprehensively considered for the following derivation.

One can derive expressions by combining (4.5), (4.8), and (4.33) for the interface voltage and by combining (4.7), (4.11), and (4.34) for the interface current as:

$$
\underline{\mathbf{v}}_{\text{int}}(t) = \mathbf{S}_{\text{v}}\mathbf{G}_{\text{A}}^{-1}\underline{\mathbf{i}}_{\text{A}}(t) + \mathbf{S}_{\text{v}}\mathbf{G}_{\text{A}}^{-1}\underline{\mathbf{i}}_{\text{int}}(t-\Delta t) + \mathbf{S}_{\text{v}}\mathbf{G}_{\text{A}}^{-1}\mathbf{G}^{'}\underline{\mathbf{v}}_{\text{int}}(t-\Delta t) \tag{4.37}
$$

$$
\underline{\mathbf{i}}_{\text{int}}(t) = \mathbf{S}_{\text{i}}\mathbf{R}_{\text{B}}^{-1}\underline{\mathbf{v}}_{\text{B}}(t) + \mathbf{S}_{\text{i}}\mathbf{R}_{\text{B}}^{-1}\underline{\mathbf{v}}_{\text{int}}(t) + \mathbf{S}_{\text{i}}\mathbf{R}_{\text{B}}^{-1}\mathbf{R}^{'}\underline{\mathbf{i}}_{\text{int}}(t-\Delta t) \tag{4.38}
$$

which can be readily transformed to z-domain as follows.

$$
\left[\hat{\mathbf{I}} - z^{-1}\mathbf{S}_{\text{v}}\mathbf{G}_{\text{A}}^{-1}\mathbf{G}^{'}\right]\underline{\mathbf{v}}_{\text{int}}(z) = \mathbf{S}_{\text{v}}\mathbf{G}_{\text{A}}^{-1}\underline{\mathbf{i}}_{\text{A}}(z) + z^{-1}\mathbf{S}_{\text{v}}\mathbf{G}_{\text{A}}^{-1}\underline{\mathbf{i}}_{\text{int}}(z) \tag{4.39}
$$

$$
\left[\hat{\mathbf{I}} - z^{-1}\mathbf{S}_{\text{i}}\mathbf{R}_{\text{B}}^{-1}\mathbf{R}^{'}\right]\underline{\mathbf{i}}_{\text{int}}(z) = \mathbf{S}_{\text{i}}\mathbf{R}_{\text{B}}^{-1}\underline{\mathbf{v}}_{\text{B}}(z) + \mathbf{S}_{\text{i}}\mathbf{R}_{\text{B}}^{-1}\underline{\mathbf{v}}_{\text{int}}(z) \tag{4.40}
$$

Then the following expression can be obtained by eliminating $\underline{\mathbf{i}}_{\text{int}}(z)$ from (4.39) and (4.40).

$$\begin{aligned}\left[\hat{\mathbf{I}} - z^{-1}\mathbf{S}_{\text{v}}\mathbf{G}_{\text{A}}^{-1}\mathbf{G}'\right]\underline{\mathbf{v}}_{\text{int}}(z) = \mathbf{S}_{\text{v}}\mathbf{G}_{\text{A}}^{-1}\underline{\mathbf{i}}_{\text{A}}(z) + z^{-1}\mathbf{S}_{\text{v}}\mathbf{G}_{\text{A}}^{-1}\left[\hat{\mathbf{I}} - z^{-1}\mathbf{S}_{\text{i}}\mathbf{R}_{\text{B}}^{-1}\mathbf{R}'\right]^{-1}\mathbf{S}_{\text{i}}\mathbf{R}_{\text{B}}^{-1}\underline{\mathbf{v}}_{\text{B}}(z) \\ + z^{-1}\mathbf{S}_{\text{v}}\mathbf{G}_{\text{A}}^{-1}\left[\hat{\mathbf{I}} - z^{-1}\mathbf{S}_{\text{i}}\mathbf{R}_{\text{B}}^{-1}\mathbf{R}'\right]^{-1}\mathbf{S}_{\text{i}}\mathbf{R}_{\text{B}}^{-1}\underline{\mathbf{v}}_{\text{int}}(z)\end{aligned}$$

$$\begin{aligned}\left[\hat{\mathbf{I}} - z^{-1}\mathbf{S}_{\text{v}}\mathbf{G}_{\text{A}}^{-1}\mathbf{G}' - z^{-1}\mathbf{S}_{\text{v}}\mathbf{G}_{\text{A}}^{-1}\left[\hat{\mathbf{I}} - z^{-1}\mathbf{S}_{\text{i}}\mathbf{R}_{\text{B}}^{-1}\mathbf{R}'\right]^{-1}\mathbf{S}_{\text{i}}\mathbf{R}_{\text{B}}^{-1}\right]\underline{\mathbf{v}}_{\text{int}}(z) = \\ \mathbf{S}_{\text{v}}\mathbf{G}_{\text{A}}^{-1}\underline{\mathbf{i}}_{\text{A}}(z) + z^{-1}\mathbf{S}_{\text{v}}\mathbf{G}_{\text{A}}^{-1}\left[\hat{\mathbf{I}} - z^{-1}\mathbf{S}_{\text{i}}\mathbf{R}_{\text{B}}^{-1}\mathbf{R}'\right]^{-1}\mathbf{S}_{\text{i}}\mathbf{R}_{\text{B}}^{-1}\underline{\mathbf{v}}_{\text{B}}(z)\end{aligned} \tag{4.41}$$

It is clear from (4.41) that the poles of the system are described by

$$\hat{\mathbf{I}} - z^{-1}\mathbf{S}_{\text{v}}\mathbf{G}_{\text{A}}^{-1}\mathbf{G}' - z^{-1}\mathbf{S}_{\text{v}}\mathbf{G}_{\text{A}}^{-1}\left[\hat{\mathbf{I}} - z^{-1}\mathbf{S}_{\text{i}}\mathbf{R}_{\text{B}}^{-1}\mathbf{R}'\right]^{-1}\mathbf{S}_{\text{i}}\mathbf{R}_{\text{B}}^{-1} = 0 \tag{4.42}$$

which can be broken down as follows.

Matrix $\left[\hat{\mathbf{I}} - z^{-1}\mathbf{S}_{\text{i}}\mathbf{R}_{\text{B}}^{-1}\mathbf{R}'\right]$ is diagonal; thus its inverse can be found by replacing each diagonal element with its reciprocal:

$$\left[\hat{\mathbf{I}} - z^{-1}\mathbf{S}_{\text{i}}\mathbf{R}_{\text{B}}^{-1}\mathbf{R}'\right]^{-1} = \begin{array}{cl} \begin{array}{c} k^{\text{th}} \text{ column} \\ \downarrow \end{array} & \\ \begin{pmatrix} 1 & 0 & \cdots & 0 & \cdots & 0 \\ 0 & 1 & \cdots & 0 & \cdots & 0 \\ \vdots & \vdots & \ddots & \vdots & \ddots & \vdots \\ 0 & 0 & \cdots & \dfrac{1}{1 - z^{-1}g_{ll}r} & \cdots & 0 \\ \vdots & \vdots & \ddots & \vdots & \ddots & \vdots \\ 0 & 0 & \cdots & 0 & \cdots & 1 \end{pmatrix} & \begin{array}{l} \\ \\ \\ \leftarrow k^{\text{th}} \text{ row} \\ \\ N \times N \end{array} \end{array} \tag{4.43}$$

Then, it is straightforward to show that

$$\mathbf{S}_{\text{v}}\mathbf{G}_{\text{A}}^{-1}\left[\hat{\mathbf{I}} - z^{-1}\mathbf{S}_{\text{i}}\mathbf{R}_{\text{B}}^{-1}\mathbf{R}'\right]^{-1}\mathbf{S}_{\text{i}}\mathbf{R}_{\text{B}}^{-1} =$$

$$
\begin{array}{c}
l^{\text{th}} \text{ column} \\
\downarrow \\
\begin{pmatrix}
0 & 0 & \cdots & 0 & \cdots & 0 \\
\vdots & \vdots & \ddots & \vdots & \ddots & \vdots \\
\dfrac{-g_{l1}r_{kk}}{1-z^{-1}g_{ll}r} & \dfrac{-g_{l2}r_{kk}}{1-z^{-1}g_{ll}r} & \cdots & \dfrac{-g_{ll}r_{kk}}{1-z^{-1}g_{ll}r} & \cdots & \dfrac{-g_{lM}r_{kk}}{1-z^{-1}g_{ll}r} \\
\vdots & \vdots & \ddots & \vdots & \ddots & \vdots \\
0 & 0 & \cdots & 0 & \cdots & 1
\end{pmatrix}_{M \times M} \leftarrow l^{\text{th}} \text{ row}
\end{array}
\tag{4.44}
$$

and

$$
\mathbf{S}_{\text{v}}\mathbf{G}_{\text{A}}^{-1}\mathbf{G}' =
\begin{array}{c}
l^{\text{th}} \text{ column} \\
\downarrow \\
\begin{pmatrix}
0 & \cdots & 0 & \cdots & 0 \\
\vdots & \ddots & \vdots & \ddots & \vdots \\
0 & \cdots & r_{kk}g & \cdots & 0 \\
\vdots & \ddots & \vdots & \ddots & \vdots \\
0 & \cdots & 0 & \cdots & 0
\end{pmatrix}_{M \times M} \leftarrow l^{\text{th}} \text{ row}
\end{array}
\tag{4.45}
$$

Taking the sparsity of (4.45), (4.44), and $\underline{\mathbf{v}}_{\text{int}}(z)$ in to account, dealing with the l^{th} row of (4.42) is adequate to find the poles of the system. Therefore, the following relationship can be obtained.

$$
1 - z^{-1}r_{kk}g - z^{-1}\left(\frac{-g_{ll}r_{kk}}{1-z^{-1}g_{ll}r}\right) = 0
$$

$$
\boxed{z^2 - \Big(g_{ll}r + r_{kk}g - g_{ll}r_{kk}\Big)z + g_{ll}r_{kk}gr = 0} \tag{4.46}
$$

The roots of the quadratic equation in (4.46) provide the poles of the system. As such, one can choose the values of g and r in such a way that the poles of the system (or the roots of (4.46)) are within the unit circle in the z-plane ($|z| \leq 1$) for a stable solution.

In case of simultaneous solution, the same concept can be applied but with a modification to (4.34) as follows.

$$
\underline{\mathbf{u}}(t) = \underline{\mathbf{v}}_{\text{int}}(t - \Delta t) + \mathbf{R}'\underline{\mathbf{i}}_{\text{int}}(t - \Delta t) \tag{4.47}
$$

This yields the following quadratic equation, from which the values for g and r can be readily chosen to preserve the interface's stability.

$$\boxed{z^2 - \Big(g_{ll} r + r_{kk} g\Big) z + g_{ll} r_{kk} \Big(1 + gr\Big) = 0} \tag{4.48}$$

4.2.4 An Example of Interfaced Simulation of Resistive Networks

A simple test circuit to illustrate the stability of interfaced simulations of resistive networks is given in Figure 4.4. The network is excited by two AC voltage sources.

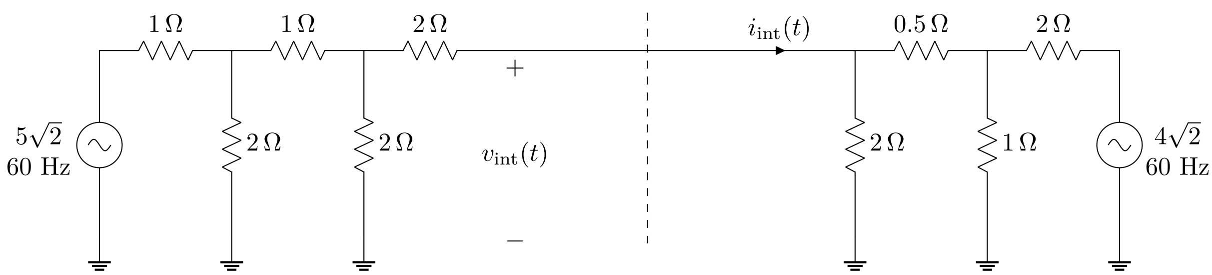

Figure 4.4: Resistive test system to investigate interface stability

The test system is partitioned to two subsystems; they are then coupled using the delay-insertion method as illustrated in Figure 4.5.

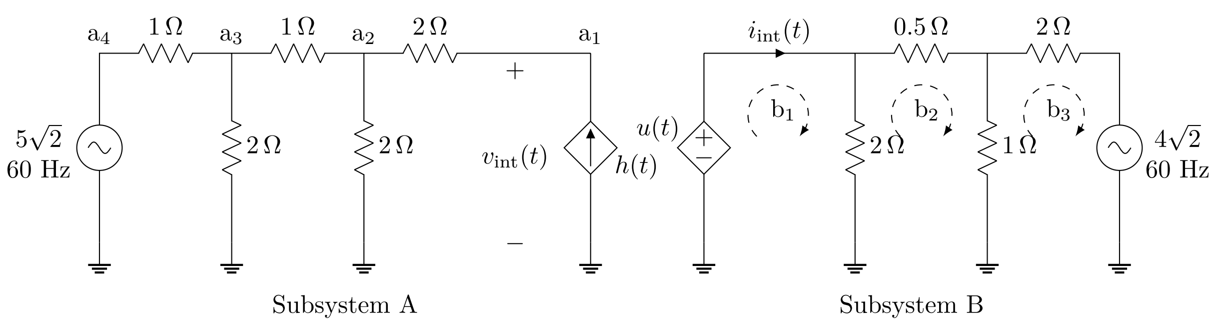

Figure 4.5: Partitioned resistive test system

Once the network is partitioned, the nodal conductance matrix of subsystem A, $\mathbf{G}_{\text{A}}$, and mesh resistance matrix of subsystem B, $\mathbf{R}_{\text{B}}$, are formed as follows.

$$\mathbf{G}_{\mathrm{A}} = \begin{pmatrix} 0.5 & -0.5 & 0 & 0 \\ -0.5 & 2 & -1 & 0 \\ 0 & -1 & 2.5 & -1 \\ 0 & 0 & -1 & 1 \end{pmatrix} \qquad \mathbf{R}_{\mathrm{B}} = \begin{pmatrix} 2 & -2 & 0 \\ -2 & 3.5 & -1 \\ 0 & -1 & 3 \end{pmatrix}$$

The inverses of these two matrices are:

$$\mathbf{G}_{\mathrm{A}}^{-1} = \begin{pmatrix} 3.2 & 1.2 & 0.8 & 0.8 \\ 1.2 & 1.2 & 0.8 & 0.8 \\ 0.8 & 0.8 & 1.2 & 1.2 \\ 0.8 & 0.8 & 1.2 & 2.2 \end{pmatrix} \qquad \mathbf{R}_{\mathrm{B}}^{-1} = \begin{pmatrix} 1.3571 & 0.8571 & 0.2857 \\ 0.8571 & 0.8571 & 0.2857 \\ 0.2857 & 0.2857 & 0.4286 \end{pmatrix}$$

Since the interface is formed at the first node of the subsystem A and the first loop of the subsystem B, r_{kk} and g_{ll} are found as 3.2 and 1.35, respectively. Then, the criteria outlined in (4.26) or (4.32) can be applied to ascertain the stability of the solution based on the solution method. The criterion for the sequential solution is

$$\left| g_{ll} r_{kk} \right| = \left| 1.35 \times 3.2 \right| = 4.32 > 1.0$$

This implies that the interfaced simulation of the partitioned network given in Figure 4.5 is unstable for the sequential solution method. This can be further illustrated by the waveforms given in Figure 4.6 for interface variables, which rapidly diverge with time.

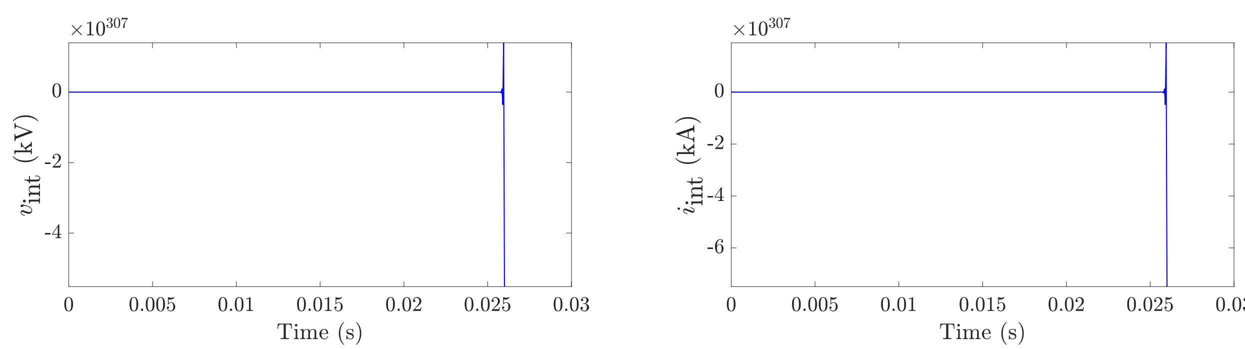

Figure 4.6: Interfaced simulation of the resistive test system

It is clear at this point that the interface needs to be modified for an accurate and stable simulation. As such augmenting elements are added to the interface as shown in Figure 4.7.

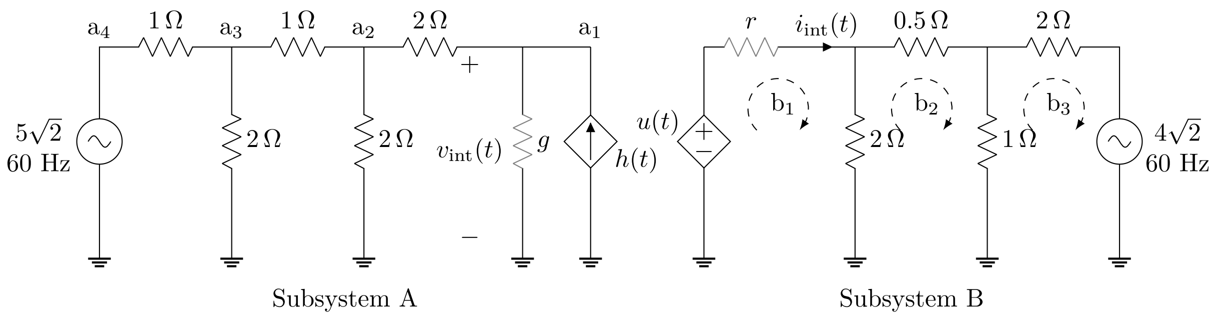

Figure 4.7: Improving interface stability of the resistive test system

The choices of g and r are based on the roots of (4.47), which may have to be found relying on a trial-and-error method as there are three unknowns. For that, the recommended way is to start from small g and r values and keep increasing them until the required conditions are satisfied as smaller values of g and r reduce the error they cause on the overall simulation.

For the system given in Figure 4.7, $g = 0.3$ and $r = 0.25$ are chosen for the sequential solution. This provides poles of the transfer function at $z = -0.7447$ and $z = -0.1666$, which are inside the unit circle. Note that once g and r are added to the network, some elements of the network matrices are changed; therefore, new values of g_{ll} and r_{kk} must be computed before finding the poles. Enhanced stability and great accuracy of the solution can be observed from Figure 4.8, which shows a comparison of waveforms obtained by simulating the unpartitioned system and the partitioned system with the augmented interface.

This example is shown assuming that the subsystems of the network are solved sequentially. A similar analysis can be done for the simultaneous solution to find stability conditions and then ensure the stability in case the conditions are not satisfied.

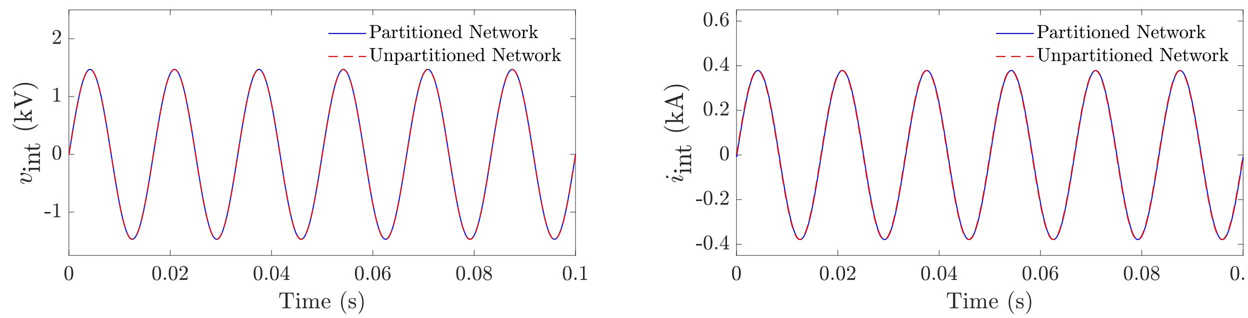

Figure 4.8: Interfaced simulation of the resistive test system with improved stability

4.3 Interface Stability when the Network Consists of Inductors and Capacitors

In the difference equation-based solution method, an inductor or a capacitor is expressed as a companion circuit of the Thévenin or Norton equivalent form; in these companion models the term contributing to the present time-step is a time-step-dependant resistance while the history term is represented as a current or voltage source. Therefore, when a network consisting of inductors and capacitors is partitioned and interfaced, not only does the size of its solution time-step have a direct impact on the stability of the solution, but also the time delay of data exchange caused by interfacing creates implications on the history terms, and hence, the stability of the simulation as well. This can be further explained using simple examples.

4.3.1 An Example of an *RL* Network

Consider a simple RL circuit, which is partitioned and interfaced as depicted in Figure 4.9.

Sequential Solution

For the sequential solution of subsystems A and B, the interface sources are updated as $h(t) = -i_L(t - \Delta t)$ and $u(t) = v_{\text{int}}(t)$. Then, the following expression can be obtained by applying

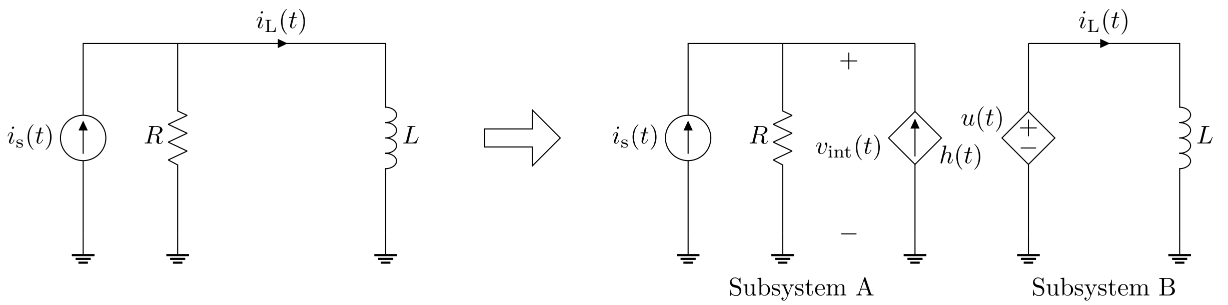

Figure 4.9: Partitioning and interfacing an RL network

Kirchhoff's voltage law to subsystem A.

$$\begin{aligned} v_{\text{int}}(t) &= R\Big(i_s(t) + h(t)\Big) \\ &= R\Big(i_s(t) - i_L(t-\Delta t)\Big) \end{aligned} \tag{4.49}$$

The differential equation for the inductor in subsystem B is:

$$\frac{d}{dt} i_L(t) = \frac{1}{L} u(t) = \frac{1}{L} v_{\text{int}}(t) \tag{4.50}$$

which can be discretized using the trapezoidal rule as:

$$i_L(t) = i_L(t-\Delta t) + \frac{1}{L}\left(\frac{v_{\text{int}}(t) + v_{\text{int}}(t-\Delta t)}{2}\right)\Delta t \tag{4.51}$$

Combining (4.49) and (4.51), the following expression can be obtained for the inductor current.

$$\begin{aligned} i_L(t) &= i_L(t-\Delta t) + \frac{R\Delta t}{2L}\Big(i_s(t) - i_L(t-\Delta t) + i_s(t-\Delta t) - i_L(t-2\Delta t)\Big) \\ &= \left(1 - \frac{R\Delta t}{2L}\right) i_L(t-\Delta t) - \left(\frac{R\Delta t}{2L}\right) i_L(t-2\Delta t) + \left(\frac{R\Delta t}{2L}\right)\Big(i_s(t) + i_s(t-\Delta t)\Big) \end{aligned} \tag{4.52}$$

It can be perceived from (4.52) that the dynamics of the inductor, which is normally characterized by a first-order difference equation, is now described by a second-order one due to the delay introduced by interfacing. Furthermore, the coefficients of (4.52) are functions of the solution time-step, which implies the significance of the size of the solution time-step on the stability of the solution.

The z-domain equation of (4.52) is given by

$$\left(1 - z^{-1}\left(1 - \frac{R\Delta t}{2L}\right) + z^{-2}\frac{R\Delta t}{2L}\right)i_L(z) = \frac{R\Delta t}{2L}\left(1 + z^{-1}\right)i_s(z) \tag{4.53}$$

Therefore, one can determine the stability of the solution by examining whether the roots of the following quadratic equation, i.e., the poles of the system function described in (4.53)), are within the unit circle of the z-plane.

$$z^2 - \left(1 - \frac{R\Delta t}{2L}\right)z + \frac{R\Delta t}{2L} = 0 \tag{4.54}$$

Simultaneous Solution

In the simultaneous solution, the interface sources of Figure 4.9 are updated as $h(t) = -i_L(t - \Delta t)$ and $u(t) = v_{int}(t - \Delta t)$. Carrying out the same steps as in the sequential solution, it can be found that the poles of the system function are the roots of the following cubic equation, from which the stability of the interface can be readily determined.

$$z^3 - z^2 + \left(\frac{R\Delta t}{2L}\right)z + \frac{R\Delta t}{2L} = 0 \tag{4.55}$$

4.3.2 An Example of an *RC* Network

A similar criterion can be derived for a circuit consisting of capacitors as well. Consider the partitioned RC circuit circuit shown in Figure 4.10.

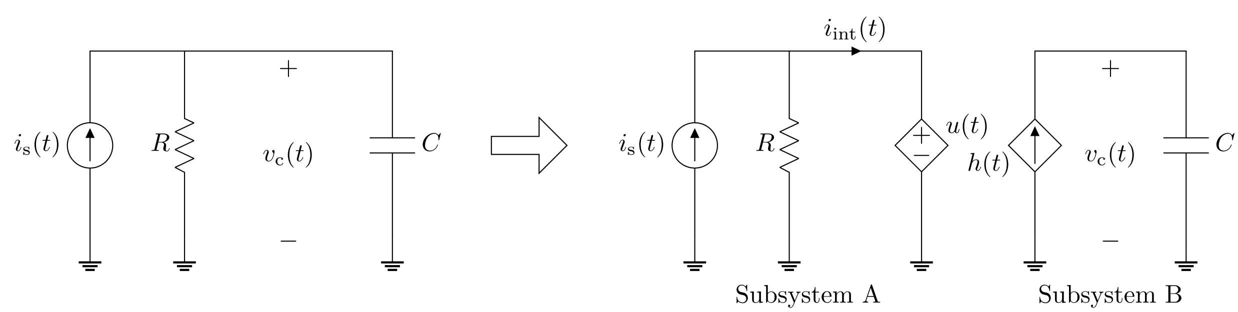

Figure 4.10: Partitioning and interfacing an RC network

Sequential Solution

For the sequential solution of subsystems A and B, the interface sources are updated as $u(t) = v_c(t-\Delta t)$ and $h(t) = i_{\text{int}}(t)$. By applying Kirchhoff's current law, one can obtain the following relationship for subsystem A.

$$\begin{aligned} i_{\text{int}}(t) &= i_s(t) - \frac{1}{R}u(t) \\ &= i_s(t) - \frac{1}{R}v_c(t-\Delta t) \end{aligned} \tag{4.56}$$

The differential equation for the capacitor in subsystem B is:

$$\frac{d}{dt}v_c(t) = \frac{1}{C}h(t) = \frac{1}{C}i_{\text{int}}(t) \tag{4.57}$$

which can be discretized using the trapezoidal rule as:

$$v_c(t) = v_c(t-\Delta t) + \frac{1}{C}\left(\frac{i_{\text{int}}(t) + i_{\text{int}}(t-\Delta t)}{2}\right)\Delta t \tag{4.58}$$

The following expression is obtained for the capacitor voltage by substituting (4.56) in (4.58).

$$\begin{aligned} v_c(t) &= v_c(t-\Delta t) + \frac{\Delta t}{2C}\left(i_s(t) - \frac{v_c(t-\Delta t)}{R} + i_s(t-\Delta t) - \frac{v_c(t-2\Delta t)}{R}\right) \\ &= \left(1 - \frac{\Delta t}{2CR}\right)v_c(t-\Delta t) - \left(\frac{\Delta t}{2CR}\right)v_c(t-2\Delta t) + \left(\frac{\Delta t}{2C}\right)\Big(i_s(t) + i_s(t-\Delta t)\Big) \end{aligned} \tag{4.59}$$

Again, it can be observed from (4.59) that the characterize equation of capacitor voltage has become a second-order difference equation due to the time-step delay caused by interfacing and that the coefficients depend on the solution time-step.

The z-domain version of (4.59) is given in (4.60).

$$\left(1 - z^{-1}\left(1 - \frac{\Delta t}{2CR}\right) + z^{-2}\frac{\Delta t}{2CR}\right)v_c(z) = \frac{\Delta t}{2C}\left(1 + z^{-1}\right)i_s(z) \tag{4.60}$$

It is clear from (4.60) that the poles of the system function are given by the roots of the following quadratic equation.

$$z^2 - \left(1 - \frac{\Delta t}{2CR}\right)z + \frac{\Delta t}{2CR} = 0 \tag{4.61}$$

Simultaneous Solution

The following equation can be derived to find the poles of the system function when the two subsystems in Figure 4.10 are solved simultaneously, wherein the interface sources are updated as $u(t) = v_{\mathrm{c}}(t - \Delta t)$ and $h(t) = i_{\mathrm{int}}(t - \Delta t)$.

$$z^3 - z^2 + \left(\frac{\Delta t}{2CR}\right)z + \frac{\Delta t}{2RC} = 0 \tag{4.62}$$

Then the stability of the overall solution can be determined by examining the locations of the roots of (4.62) in the z-plane.

It is evident from the examples given in sections 4.3.1 and 4.3.2 that the stability of the overall solution of an interfaced network depends on the size of the solution time-step and that the history terms are affected by the time-delay caused by the interfacing, in the presence of capacitors and inductors (elements that are characterized by difference equations). In typical difference equation-based solution methods, the time-step appears in the admittance or the impedance matrix of the system. However, it is challenging to provide a general method to accommodate the influence of the interface time-delay in network history terms when deriving criteria for interface stability as history terms of inductors and capacitors take different forms. Therefore, the generalized method developed to interface a resistive network with preserved stability (see section 4.2.3) may be practiced in a given RLC network by unfolding the required condition from the beginning. However, it is much more complicated to devised a general technique that is pertinent for an arbitrary RLC network.

4.4 Summary of Contributions and Conclusions

This chapter investigated the numerical instabilities that may occur in interfaced simulations due to the physical structure of the surrounding circuit and the time delay of information exchange between the subsystems that are interfaced. Criteria for interfaced stability were derived considering both sequential solution and simultaneous solution of subsystems. It was found that the solution of a coupled network is stable as long as certain conditions are satisfied by the physical structure of the interface, solution time-step, and the nature of surrounding circuits.

For a resistive network, the stability of the interfaced simulation depends only on the values of the admittance or the impedance matrices of subsystems. These matrices are generally time-step independent. Taking advantage of this fact, a generalized method was developed to change specific elements of these matrices by adding companion elements with necessary compensations to the interface in such a way that the solution is assuredly stable and sufficiently accurate.

For a network constituting inductors and capacitors, the aforementioned matrices are constructed as functions of the simulation time-step; therefore, the stability of interfaced simulation of such a system is directly influenced by the size of the time-step. Furthermore, it was shown in this chapter that the time-delay caused by interfacing introduces complications in history values of inductor and capacitor difference equations; therefore, difficulties in alleviating any stability issue may arise.

As a conclusion, time-delays of interfaced simulations are mainly related to the interface circuit topology and the order in which the subsystems are solved. Depending on the circuit structures of coupled subsystems, these delays may cause severe numerical stability issues that may be difficult to remedied by ordinary methods. As a result, despite their limitations, interface topologies that do not insert time-delays to the solution, e.g., transmission line interfaces and multi-area Thévenin equivalents, remain the most reliable and fitting network coupling techniques.

Chapter 5

A BFDP Solver for Frequency-Adaptive Simulation of Transients

In a typical power system simulation, transients where most information of interest lies are often confined to small time-intervals. Outside such intervals, i.e., before and after a transient, the system essentially settles into periodic steady state operation. In sinusoidal steady state, a signal gives no information to the user other than its magnitude and phase at a constant frequency. Even though the information required to characterize the system response in steady state is limited to the magnitude and phase angle of voltages and currents, an EMT simulator requires a fixed and small time-step for the entire simulation.

As it is demonstrated in Chapter 3, a base-frequency dynamic phasor captures both steady-state and high frequency transient regimes by preserving the entire harmonic spectrum. The base-frequency dynamic phasor solver for frequency adaptive simulation of transients (BFAST solver) presented in this chapter exploits these features and adapts its solution method and time-step according to the frequency contents of the waveforms being simulated. During high-frequency transients, it uses a detailed EMT solution with a small time-step and during steady-state or slowly varying dynamics, it reverts to a phasor-based solution with a large time-step.

5.1 Network Modeling with Base-Frequency Dynamic Phasors

The concept of changing the solution time-step during a simulation is built into the ability of the solver to switch between the frequency-domain solution and the time-domain EMT solution. For this purpose, discretised equivalents of basic network components are developed using base-frequency dynamic phasors and the implicit trapezoidal integration rule as explained below.

A first-order differential equation in time-domain may be written as follows.

$$\frac{\mathrm{d}}{\mathrm{d}t}x(t) = f\Big(x(t), t\Big) \tag{5.1}$$

One can transform (5.1) to the base-frequency dynamic phasor frame as:

$$\begin{aligned}\frac{\mathrm{d}}{\mathrm{d}t}\Big\langle \mathrm{X}\Big\rangle_{\mathrm{B}}(t) &= \Big\langle \frac{\mathrm{d}}{\mathrm{d}t}\mathrm{X}\Big\rangle_{\mathrm{B}}(t) - \mathrm{j}\omega_0\Big\langle \mathrm{X}\Big\rangle_{\mathrm{B}}(t) \\ &= \Big\langle f\Big(x(t), t\Big)\Big\rangle_{\mathrm{B}} - \mathrm{j}\omega_0\Big\langle \mathrm{X}\Big\rangle_{\mathrm{B}}(t)\end{aligned} \tag{5.2}$$

where $\Big\langle \mathrm{X}\Big\rangle_{\mathrm{B}}(t)$ denotes the base-frequency dynamic phasor corresponding to $x(t)$. Equation (5.2) can be discetized by applying the integration trapezoidal rule as follows.

$$\begin{aligned}\Big\langle \mathrm{X}\Big\rangle_{\mathrm{B}}(t) &= \Big\langle \mathrm{X}\Big\rangle_{\mathrm{B}}(t-\Delta t) \\ &+ \frac{\Delta t}{2}\Bigg(\Big\langle f\Big(x(t), t\Big)\Big\rangle_{\mathrm{B}} + \Big\langle f\Big(x(t-\Delta t), t-\Delta t\Big)\Big\rangle_{\mathrm{B}} - \mathrm{j}\omega_0\Big(\Big\langle \mathrm{X}\Big\rangle_{\mathrm{B}}(t) + \Big\langle \mathrm{X}\Big\rangle_{\mathrm{B}}(t-\Delta t)\Big)\Bigg)\end{aligned} \tag{5.3}$$

Rearranging (5.3) gives

$$\begin{aligned}\Big\langle \mathrm{X}\Big\rangle_{\mathrm{B}}(t) &= \frac{\Delta t}{2(1+\mathrm{j}\omega_0\Delta t/2)}\Big\langle f\Big(x(t), t\Big)\Big\rangle_{\mathrm{B}} \\ &+ \Bigg(\Big(\frac{1-\mathrm{j}\omega_0\Delta t/2}{1+\mathrm{j}\omega_0\Delta t/2}\Big)\Big\langle \mathrm{X}\Big\rangle_{\mathrm{B}}(t-\Delta t) + \frac{\Delta t}{2(1+\mathrm{j}\omega_0\Delta t/2)}\Big\langle f\Big(x(t-\Delta t), t-\Delta t\Big)\Big\rangle_{\mathrm{B}}\Bigg)\end{aligned} \tag{5.4}$$

which shows that a discretized equivalent for (5.1) in the base-frequency dynamic phasor frame is described by a term related to the present time-step and a term related to the previous time-step.

Discretized base-frequency dynamic phasor equivalents developed for basic circuit elements using this technique are shown in Table 5.1. Note that each element (except for a resistor) is developed as a Norton equivalent for it to be readily applicable to nodal analysis. More details about the development of companion models in frequency-domain may be found in [28, 68, 74].

Table 5.1: Discretized BFDP equivalents of basic circuit elements

Element	Discretized BFDP equivalent	
Resistor 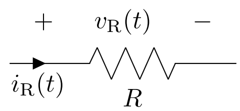 $v_\mathrm{R}(t) = R\, i_\mathrm{R}(t)$	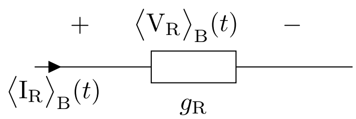	$\langle \mathrm{I_R} \rangle_\mathrm{B}(t) = g_\mathrm{R} \langle \mathrm{V_R} \rangle_\mathrm{B}(t) \quad (5.5)$ where $g_\mathrm{R} = \dfrac{1}{R} \quad (5.6)$
Inductor 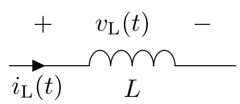 $\dfrac{\mathrm{d}}{\mathrm{d}t} i_\mathrm{L}(t) = \dfrac{1}{L} v_\mathrm{L}(t)$	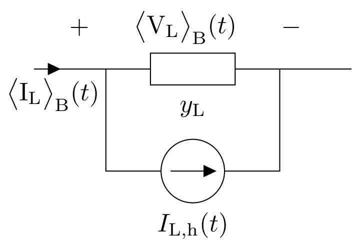	$\langle \mathrm{I_L} \rangle_\mathrm{B}(t) = y_\mathrm{L} \langle \mathrm{V_L} \rangle_\mathrm{B}(t) + I_\mathrm{L,h}(t) \quad (5.7)$ where $y_\mathrm{L} = \dfrac{\Delta t}{2L(1 + \mathrm{j}\omega_\mathrm{s}\Delta t/2)} \quad (5.8)$ $I_\mathrm{L,h}(t) = \left(\dfrac{1 - \mathrm{j}\omega_\mathrm{s}\Delta t/2}{1 + \mathrm{j}\omega_\mathrm{s}\Delta t/2}\right) \langle \mathrm{I_L} \rangle_\mathrm{B}(t - \Delta t)$ $- y_\mathrm{L} \langle \mathrm{V_L} \rangle_\mathrm{B}(t - \Delta t) \quad (5.9)$
Capacitor 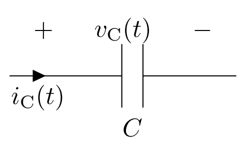 $\dfrac{\mathrm{d}}{\mathrm{d}t} v_\mathrm{C}(t) = \dfrac{1}{C} i_\mathrm{C}(t)$	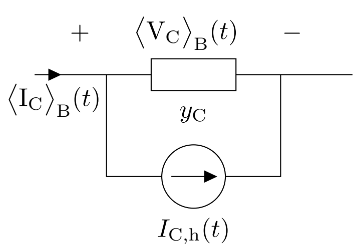	$\langle \mathrm{I_C} \rangle_\mathrm{B}(t) = y_\mathrm{C} \langle \mathrm{V_C} \rangle_\mathrm{B}(t) + I_\mathrm{C,h}(t) \quad (5.10)$ where $y_\mathrm{C} = \dfrac{2C}{\Delta t}\left(1 + \dfrac{\mathrm{j}\omega_\mathrm{s}\Delta t}{2}\right) \quad (5.11)$ $I_\mathrm{C,h}(t) = -\langle \mathrm{I_C} \rangle_\mathrm{B}(t - \Delta t)$ $- y_\mathrm{C}^{*} \langle \mathrm{V_C} \rangle_\mathrm{B}(t - \Delta t) \quad (5.12)$

In these element models, ω_{s} is referred to as the "*shift frequency*" and is equal to the fundamental frequency, ω_0, in base-frequency dynamic phasor domain. However, since it is used as a simulation parameter in the developed BFAST solver, a distinct symbol is given to this variable.

The contribution of each base-frequency dynamic phasor equivalent to the network nodes are added to the corresponding elements of the nodal admittance matrix. Once built, the resulting nodal admittance matrix of the network is a function of the two simulation parameters, i.e. the simulation time-step, Δt, and the shift frequency, ω_{s}:

$$\mathbf{Y}_{\mathrm{B}} = f(\Delta t, \omega_{\mathrm{s}}) \tag{5.13}$$

Furthermore, it is seen from (5.5)-(5.12) that the imaginary part of each BFDP equivalent model includes the shift frequency. Setting the shift frequency to zero ($\omega_{\mathrm{s}} = 0$), which implies no frequency shifting, creates real-valued models that are the same as Dommel's EMT companion models explained in Chapter 2. Setting the shift frequency to the fundamental frequency of the system ($\omega_{\mathrm{s}} = \omega_0$) yields dynamic phasors at that frequency; however, since base-frequency dynamic phasors are used, harmonic information will not be lost, since all frequencies are transferred into the frame of the fundamental frequency component.

The ability of the developed models to be either phasor-domain or time-domain EMT models enables solving the network with either approach in a single solver only by setting the shift frequency ω_{s} and usage an appropriate simulation time-step; this provides a way to adapt the nature of the solver (dynamic phasor vs. EMT) to the nature of the waveforms being simulated. Earlier work in this area has identified this dual-approach possibility [13, 75] albeit in the context of shifted-frequency analysis, which faces practical limitations when the transients are not of a band-pass nature around the system's fundamental frequency.

5.2 Algorithm for Solver Changeover

The task of switching between dynamic phasor and EMT solvers by setting the value of ω_{s} requires determining the correct instant to change the shift frequency and to calculate history current source values in the proper domain using the right time-step prior to the change. An algorithm for doing so in the context of BFAST solver is proposed next. For that, assume that the dynamic phasor and EMT solutions are obtained with a large time-step, Δt_{DP}, and a small time-step, Δt_{T}, respectively.

5.2.1 Changeover from Dynamic Phasor Solution to EMT Solution

Consider a situation where the BFAST solver changes its solution technique from dynamic phasor ($\omega_{\mathrm{s}} = \omega_0$) to EMT ($\omega_{\mathrm{s}} = 0$) at time t_{x} as shown in Figure 5.1.

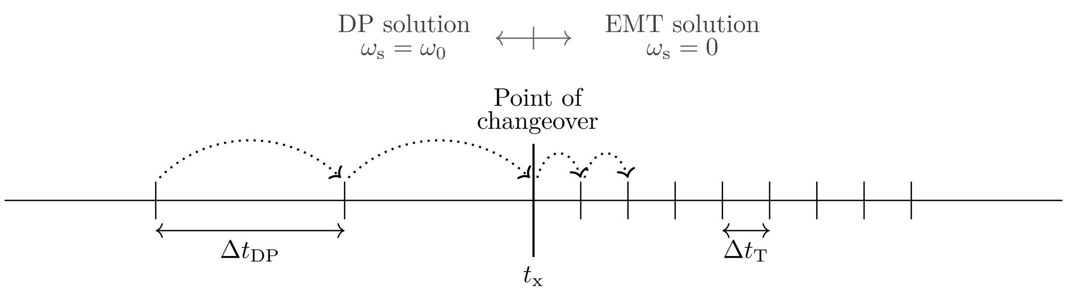

Figure 5.1: Changeover from DP solution to EMT solution

The solution at the first time-step after the changeover, i.e, at $t = t_{\mathrm{x}} + \Delta t_{\mathrm{T}}$, requires computation of history sources that represent values from previous time-step, i.e, $t = t_{\mathrm{x}}$. However, at $t = t_{\mathrm{x}}$, the currents and voltages are already calculated in the phasor domain; therefore, they must be brought to time domain before the solution at the subsequent time-step is obtained. This can be readily done employing (3.38) to each variable as below.

$$x(t_{\mathrm{x}}) = \mathfrak{Re}\left\{\Big\langle \mathrm{X} \Big\rangle_{\mathrm{B}}(t_{\mathrm{x}})\mathrm{e}^{\mathrm{j}\omega_0 t_{\mathrm{x}}}\right\} \tag{5.14}$$

The need for switching to the EMT solution arises only when there is a disturbance in the system. It is common practice to pre-specify the instants of network disturbances before the beginning of the simulation (for example the user can easily pre-specify the instant a fault or switching event takes place). This is then followed by adjustments to the admittance matrix at the onset of the disturbance. Therefore, the changeover instant from dynamic phasor to EMT can be determined either by monitoring the admittance matrix or simply by means of pre-specified instants of network disturbances that are set by the user. The latter is particularly practical when the eventual objective of the development of BFAST solver is to co-simulate with an industrial-grade EMT solver wherein the network matrix may be inaccessible. If the inception point of the disturbance and the DP solution grid do not coincide on the discretized time axise, the solution can be interpolated to the actual inception point before the changeover or the changeover point can be set to the time-step just before the disturbance.

5.2.2 Determining the End of the Transient

Once the solution method is changed to EMT (i.e., with $\omega_s = 0$) reverting to the DP solution is done only after the transient has settled into steady state. For that matter, the solver needs a criterion to automatically determine the end of the transient; this is shown in Figure 5.2.

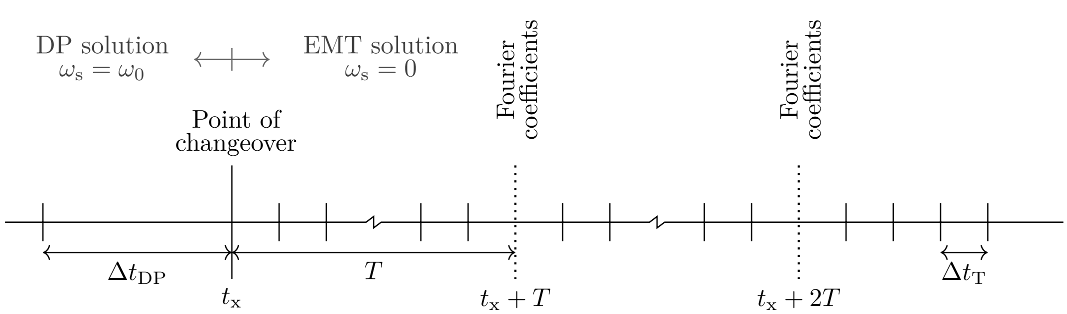

Figure 5.2: Deciding the end of the transient

As soon as dynamic phasor to EMT changeover occurs, the solver begins to calculate the Fourier coefficients of the signals that are affected by the disturbance. These signals are normally confined to small areas of the network where the impact of the transient is most severe. For example, in the event of a fault, the voltages and currents of the buses in the electrical vicinity of the fault's location are often sufficient for this purpose. To avoid calculations at each time-step, Fourier coefficients are only calculated once per fundamental-frequency cycle. As a result, the computational burden of this task is negligible compared with the computations of the actual network solution. If the calculated coefficients match the corresponding coefficients in the previous cycle within a small pre-specified tolerance, then the solver decides that the end of the transient is reached. In following simulation examples, this tolerance is selected empirically based on the duration of the EMT solution after a disturbance. For example, 15% of the base value (current or voltage) is selected to compare the fundamental frequency Fourier coefficients and 10% of the base value for the dc component comparison. Selecting this value to be too small results in the BFAST solver to operate for a longer duration with its EMT solution and a small time-step, and, therefore, lead to computational inefficiency. The number of Fourier coefficients compared is based upon the harmonics present during normal operation of the system; this implies that comparison of the fundamental coefficient is sufficient for most systems as they are expected to be operating at the fundamental frequency in steady state.

5.2.3 Changeover from EMT Solution to Dynamic Phasor Solution

Once the BFAST solver detects that the transient has settled, it begins to extract base-frequency dynamic phasors of each variable from time-domain instantaneous samples. Note that even though the end of transient is reached, the solver is still operating with the EMT solution. Therefore, the dynamic phasor extraction can be readily achieved using one of the BFDP extraction methods explained in section 3.4.2, for that the operation has to be carried over an exact period. As such, the changeover from EMT to dynamic phasor solution is set at $t = t_\mathrm{y}$, which is exactly one cycle from the end of transient detection as illustrated in Figure 5.3. Then, the extracted dynamic phasors are used in values representing history sources for the solution at $t = t_\mathrm{y} + \Delta t_\mathrm{DP}$.

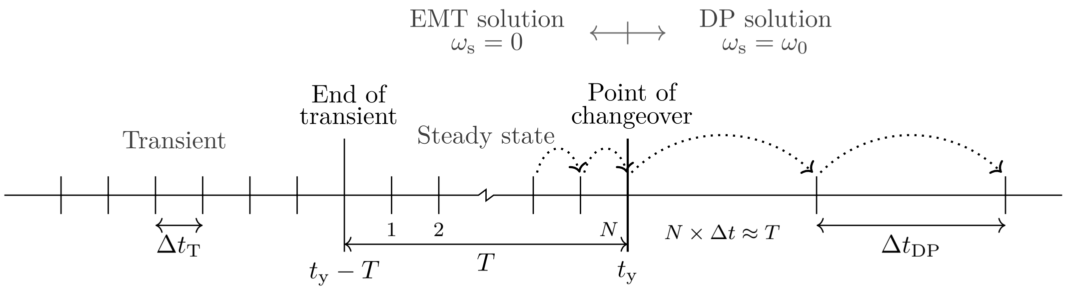

Figure 5.3: Changeover from EMT solution to dynamic phasor solution

5.3 Illustrative Example

The principle of BFAST solver can be demonstrated with an illustrative simulation of the simple circuit shown in Figure 5.4.

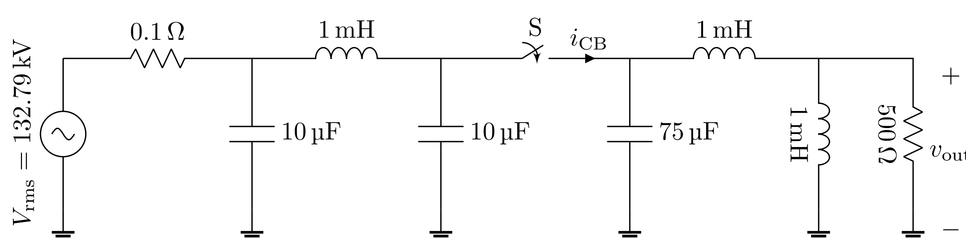

Figure 5.4: Illustrative circuit with basic circuit elements for BFAST simulation

A discretized equivalent of the circuit shown in Figure 5.4 is given as in the Figure 5.5 using the base-frequency dynamic phasor equivalents derived in (5.5)-(5.12). Simulation is carried out using $\Delta t_\mathrm{DP} = 1000\,\mu\mathrm{s}$ and $\Delta t_\mathrm{T} = 10\,\mu\mathrm{s}$ time steps, for which equivalent admittances of discretized circuit models are as given in Table 5.2.

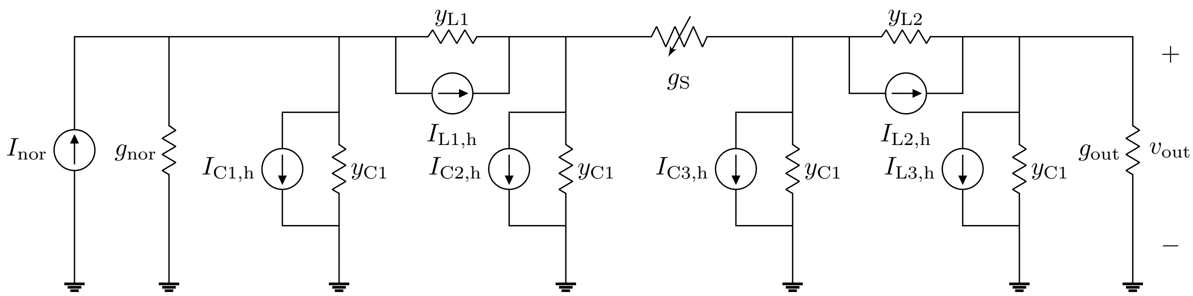

Figure 5.5: Discretized circuit model of the Illustrative circuit in BFAST solver

Table 5.2: Admittances of discretized circuit model of illustrative circuit

	$\omega_{\mathrm{s}} = 60$ Hz, $\Delta t_{\mathrm{DP}} = 1$ ms	$\omega_{\mathrm{s}} = 0$, $\Delta t_{\mathrm{T}} = 10\,\mu$s
g_{nor}	10 S	10 S
g_{o}	0.002 S	0.002 S
y_{L1}, y_{L2}, y_{L3}	0.5 - j0.015 S	0.005 S
y_{C1}, y_{C2}	0.02 + j0.0006 S	2 S
y_{C3}	0.15 + j0.0045 S	15 S

Simulation results of transients due to opening the circuit breaker at $t = 0.3$ s and closing it at $t = 0.6$ s are depicted in Figure 5.6. Waveforms obtained by simulating the same circuit entirely in PSCAD/EMTDC are used as a benchmark to validate the accuracy. The BFAST results include the envelopes of the waveforms (i.e., magnitude of the dynamic phasors) when the dynamic phasor solution is obtained and the natural waveform for the durations where the EMT solution is found.

Figure 5.6 readily shows that the BFAST uses the EMT solution ($\omega_{\mathrm{s}} = 0$) during the start-up transient and circuit breaker transients. Identical transient behaviour is observed in both PSCAD/EMTDC and BFAST solvers. At the end of each transient, which is detected automatically by the simulator, the BFAST simulator switches to the dynamic phasor solution by changing the shift frequency to $\omega_{\mathrm{s}} = 2\pi 60$ rad/s and uses a large solution time-step to accelerate the simulation.

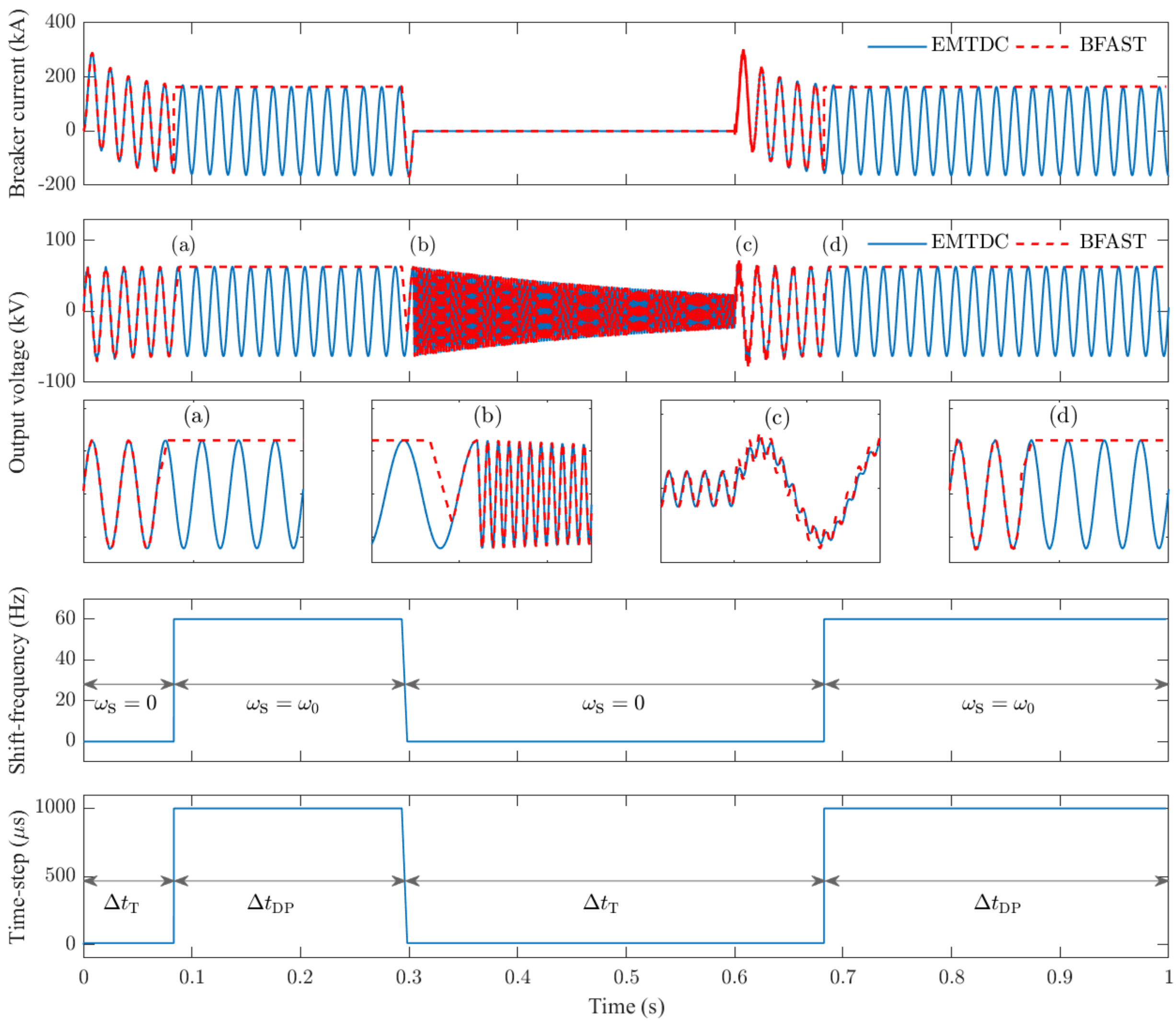

Figure 5.6: Simulation waveform for circuit breaker transients

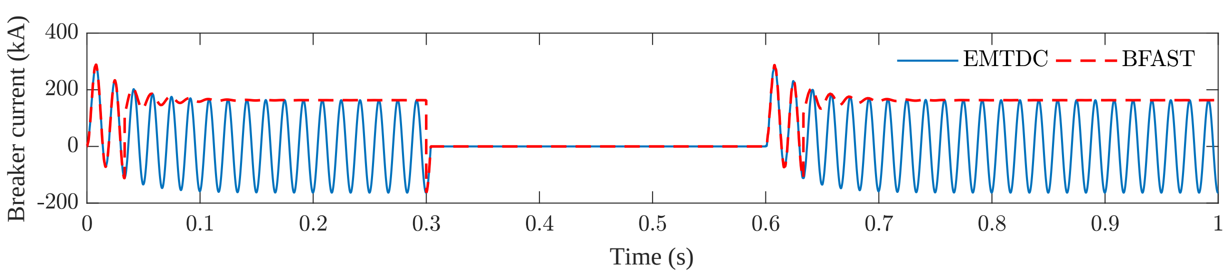

Figure 5.7: Effect of changeover from EMT to dynamic phasor before the end of the transient

In Figure 5.6, the BFAST solver switches from the EMT to the dynamic phasor solution after the transients in the waveforms have settled sufficiently, i.e., around $t = 0.1$ s and $t = 0.7$ s, when the decaying dc component is negligibly small. The importance of correctly detecting the end of a transient is illustrated in Figure 5.7 wherein the breaker current waveform is shown for a solver changeover from EMT to dynamic phasor well before $t = 0.1$ s and $t = 0.7$ s, when the decaying dc component is still present. As seen, the solver is still able to capture the envelope of the settling waveform; however, small oscillations in the captured amplitude are observed that are due to the shifting of the dc component to the frame of the fundamental component.

The BFAST solver yields two admittance matrices (one complex-valued matrix and one real-valued matrix) corresponding to the large time-step and the small time-step during a course of a simulation. They can be built, inverted, and stored before the beginning of the simulation as simulation time-steps are pre-defined; hence, their calculation does not affect the speed of the simulation.

5.4 Representing Power System Components in the BFAST Solver

In order to create a practical simulator capable of simulating realistic networks, a rich library of components and system models needs to be in place. While simple network elements are modeled with ease as discussed in section 5.1, modeling and integrating sophisticated components such as transmission lines, electric machines, transformers, and advanced converter systems in the context of the BFAST solver is a task that requires dedicated attention to ensure accuracy and versatility of the models. The focus in this section is to provide suitable models of general power system components and interfacing mechanisms so that these and future custom-developed model may be easily interfaced to the BFAST simulator engine.

5.4.1 Synchronous Machines

Synchronous machines are an integral part of power systems; therefore, they are indispensable to any transient simulation tool. In difference-equation based nodal analysis, a synchronous machine is represented externally to the electrical network and connects to it via an appropriate interfacing mechanism, which plays a vital role when selecting a proper model in the context of a given simulator [76, 77]. A number of synchronous machine models have been developed to interface with nodal analysis-based simulation tools [34, 78–83]. The objectives of these models vary by such factors as simulation efficiency, transient accuracy, numerical stability, and interfacing ability to the electric network.

Several types of synchronous machine models are considered to interface with the BFAST solver. Machine models developed in the qd-domain [34, 81] may allows large simulation time-steps as stator and rotor dynamic equations yield constant coefficient matrices; however, these models require sophisticated interfacing mechanisms as the network is typically modeled in the phase-domain (abc-domain). The interface to the network in this type of models often causes time-step delays and, hence, severe numerical instability issues in simulations unless special schemes are implemented to improve the interface stability.

Phase-domain models [78, 79], on the other hand, can be directly interfaced with the electrical network without time delays or stability issues. Internal machine phenomena such as internal faults and magnetic saturations can be readily represented in phase-domain model as they represent machine variables in their physical form. The main drawback of this type of models is that they are computationally expensive due to rotor position dependant inductances and the requirement of relatively small simulation time-steps.

Another approach of representing a synchronous machine is to model it as a voltage source behind an impedance [82]. The generic interface equation for a this model is given as

$$\underline{\mathbf{v}}_{\mathrm{abcs}}(t) = \mathbf{R}_{\mathrm{s}}\underline{\mathbf{i}}_{\mathrm{abcs}}(t) + \frac{\mathrm{d}}{\mathrm{d}t}\left[\mathbf{L}''_{\mathrm{abcs}}(\theta_r)\underline{\mathbf{i}}_{\mathrm{abcs}}(t)\right] + \underline{\mathbf{e}}''_{\mathrm{abc}}(t) \tag{5.15}$$

where $\mathbf{R}_{\mathrm{s}}$, $\mathbf{L}''_{\mathrm{abcs}}(\theta_r)$, and $\underline{\mathbf{e}}''_{\mathrm{abc}}$ are the stator resistance matrix, sub-transient inductance matrix, and the sub-transient voltage, respectively. As is understood from (5.15), this model has the ability to directly interface with the network as the stator circuit is represented in the phase-domain. The rotor circuit in this model is developed independently in the qd-domain, therefore, large time-steps are allowed for simulations. However, this synchronous machine model is still computationally demanding as the sub-transient inductance matrix is dependent upon the rotor-position, and needs to be re-calculated in each time-step. In order to cope with this drawback, an implicit approach that ensures a rotor-position independent sub-transient inductance matrix has been proposed by algebraic manipulation of machine equations [83, 84]. As such, the interface equation given in (5.15) is modified to represent the stator interface as:

$$\underline{\mathbf{v}}_{\mathrm{abcs}}(t) = \mathbf{R}_{\mathrm{s}}\underline{\mathbf{i}}_{\mathrm{abcs}}(t) + \mathbf{L}''\frac{\mathrm{d}}{\mathrm{d}t}\underline{\mathbf{i}}_{\mathrm{abcs}}(t) + \underline{\mathbf{e}}''_{\mathrm{abc}}(t) \tag{5.16}$$

wherein the inductance matrix $\mathbf{L}''$ is constant. Due to many benefits offered including numerical robustness, ability to use large simulation time-steps, and ease of interfacing with the electric network, this thesis represents the synchronous machine as a voltage source behind an impedance with a constant-parameter stator interface. A block diagram of the implementation of this model in the context of the BFAST solver is illustrated in Figure 5.8. Details of this model, its interface circuit to the electric network, and transformations required to convert signals among $qd0$-domain, time-domain, and dynamic phasors are provided in Appendix A.

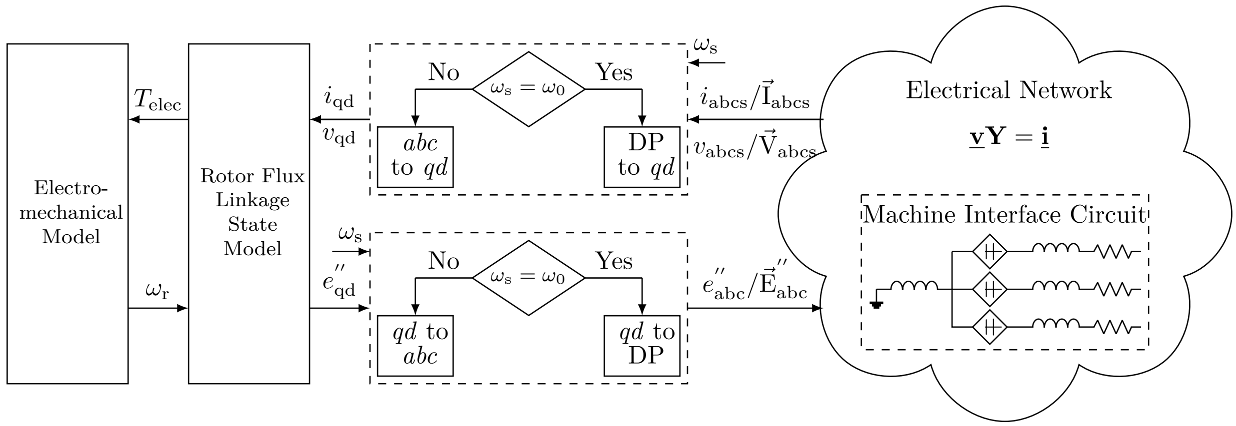

Figure 5.8: Implementation of synchronous machine model in the BFAST solver

5.4.2 Transformers

A transformer model can be readily incorporated in a difference equation-based nodal analysis simulator using its discretized equivalent circuit [34]. Figure 5.9 illustrates the base-frequency dynamic phasor adaptation of the discretized equivalent circuit of the basic transformer model.

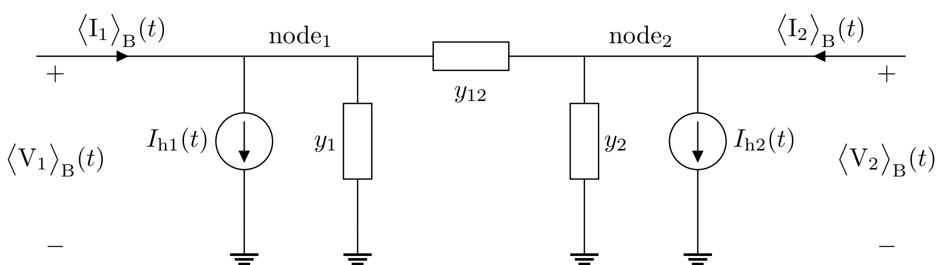

Figure 5.9: Discretized equivalent circuit of basic transformer model with BFDPs

The equivalent admittances in Figure 5.9, i.e., y_1, y_2, and y_{12}, are included in the network's nodal admittance matrix and the current sources $I_{\mathrm{h1}}(t)$ and $I_{\mathrm{h2}}(t)$, which represent previous time-step values, are recalculated and updated in each time-step. Derivation of this model and parameter computations are included in Appendix B.

5.4.3 Transmission Lines

Several types of transmission line models are used in nodal analysis based simulations. They differ from one another based on several aspects such as accuracy, simplicity, and representation of the physical geometry and parameters of transmission lines. As a general rule, the decision of adequacy of a particular model in a transient simulator is split by the size of the simulation time-step and the length of the line [34]. Transmission lines with shorter wave propagation times than the simulation time-step are usually modeled as π-sections while longer lines are implemented using models such as the Bergeron's model [34] or a frequency-dependent line model [85].

In frequency-domain simulations, particularly when the aim is to use large simulation time-steps in the order of milliseconds, more often than not, the time-step size is found to be larger than the wave travel time through transmission lines of real world networks. Therefore, it is common practice to implement transmission lines as π-sections in such simulations. The accuracy of this representation is proved sufficient in studies of slowly varying dynamics [37].

The BFAST solver uses the lumped-parameter π-section transmission line model in order to preserve its ability to use large simulation time-steps, to avoid wave propagation time interpolations, and due to ease of modeling in frequency-adaptive simulations of transients. Therefore, the solver does not account for waveform propagation delays and frequency-dependency of transmission lines. Details of the line model used in this thesis are provided in Appendix C. A π-section transmission line model with distributed-parameters can be found in [86].

5.4.4 Modular Multilevel Converter

Upsurge of HVDC systems and unprecedented penetration of renewable energy sources means the modern power system is rich in high-frequency power converters. Modeling and simulations of such systems are challenging due to the number of switching devices they are built upon and frequent switching events that demand computationally expensive reformation and re-inversion of the nodal admittance matrix during simulations. In order to create a professional-quality frequency-domain simulator capable of simulating converter-heavy systems, methods to model and interface power electronic converters in the context of dynamic phasor simulators needs to be looked at. This will require not only development of alternative models that are suitable for other solver environments, but also invention of ways to model their non-linear control systems with a high degree of accuracy, which is a task that is prohibitively difficult in many non-EMT solvers.

By taking advantage of the computational relief that dynamic phasors provide, this thesis proposes a mechanism to represent and control modular multilevel converters (MMCs) in a dynamic phasor environment. The MMC in the BFAST simulator is represented using the equivalent circuit shown in Figure 5.10.

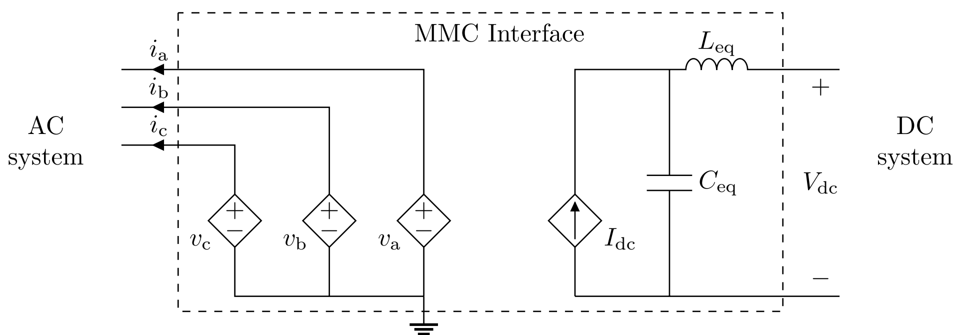

Figure 5.10: MMC representation in the BFAST solver

The MMC in this representation is connected to the ac- and dc-systems via three-phase voltage source and a dc-side equivalent circuit that consists of a current source, an equivalent capacitor, and an equivalent inductance. The equivalent dc-side capacitance represents the effect of energy stored inside the MMC submodules on the dc-side. The dc-side inductance mimics the effect of arm inductance on dc current. The instantaneous values of ac line currents of all three phases and the dc bus voltages are taken at the interfaces; the ac-side source voltages and dc-side source current are calculated and updated in each simulation time-step. The derivation and source value computations of this DP-MMC model [51] are provided in Appendix D.

This model is particularly designed to interface and simulate MMCs in the context of the external subsystem in a co-simulation platform. As such, further details of this model, implementation of controllers, and examples are discussed in Chapter 6. It is expected that similar approaches may be followed in DP solvers to represent other types of power electronic converters.

5.4.5 Simulation Example

The accuracy of the synchronous machine model, transformer model, and the transmission line model in the context of the BFAST solver are validated by simulating a single-machine infinite-bus (SMIB) test system wherein a synchronous generator is connected to an infinite bus through two transmission lines and a step-up transformer as shown in Figure 5.11. Test system specifications and synchronous machine constants are given in Table 5.3.

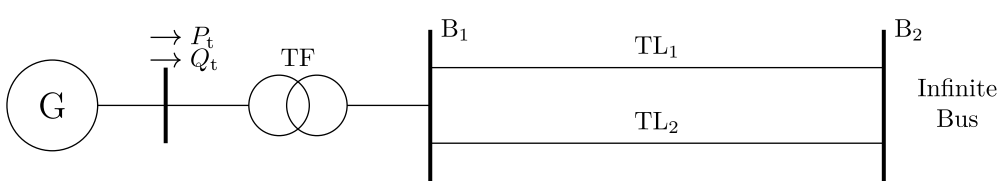

Figure 5.11: Single machine infinite bus test system

In the simulation, the infinite bus is represented using a constant-frequency ac voltage source. The initial conditions of the network are set to feed 0.9 pu of real power from the generator to the network. A disturbance is provided to the SMIB system by applying a solid line-to-ground three-phase fault to bus B_1 at $t = 2$ s for a duration of 0.05 s. BFAST results are compared against standalone EMT simulation waveforms obtained by conducting the same simulation in

Table 5.3: SMIB test system specifications

Component	Specifications
Infinite Bus	230 kV, $0.90081\angle 0°$ pu, 60 Hz
Transmission line 1	2200 MVA, 230 kV, $0.01 + \mathrm{j}0.5$ pu
Transmission line 2	2200 MVA, 230 kV, $0.03 + \mathrm{j}0.93$ pu
Transformer	2200 MVA, 24:230 kV, $X_{\mathrm{l}} = \mathrm{j}0.15$ pu, $I_{\mathrm{m}} = 0.02$ pu
Synchronous machine	2200 MVA, 24 kV, 60 Hz, $P_{\mathrm{t}} = 0.9$ pu, $Q_{\mathrm{t}} = 0.436$ pu
	$X_{\mathrm{d}} = 1.81$ pu, $X_{\mathrm{q}} = 1.76$ pu, $X_{\mathrm{d}}^{'} = 0.3$ pu, $X_{\mathrm{q}}^{'} = 0.65$ pu,
	$X_{\mathrm{d}}^{''} = 0.25$ pu, $X_{\mathrm{q}}^{''} = 0.25$ pu, $X_{\mathrm{l}} = 0.15$ pu, $r_{\mathrm{s}} = 0.003$ pu,
	$T_{\mathrm{d0}}^{'} = 8$ s, $T_{\mathrm{q0}}^{'} = 1$ s, $T_{\mathrm{d0}}^{''} = 0.03$ s, $T_{\mathrm{q0}}^{''} = 0.07$ s, $H = 3.5$, $D = 0$

PSCAD/EMTDC in which the synchronous machine is modeled as a Norton equivalent [81]. Time steps used for the BFAST simulation are $\Delta t_{\mathrm{DP}} = 2$ ms and $\Delta t_{\mathrm{T}} = 50\,\mu$s and for PSCAD/EMTDC is 50 μs. Transient waveforms produced by both simulators are shown in Figure 5.12 and Figure 5.13 for comparison.

In both PSCAD/EMTDC and BFAST simulations, the synchronous machine is started as a fixed voltage source at its terminal with the voltage magnitude ramped up in order to provide space to self-initialize machine's flux linkage variables. Once the system reaches steady state, the voltage source representing the machine is converted to the actual machine model with a constant speed of 1 pu. After the actual machine model is settled, the mechanical model of the rotor is unlocked. In this SMIB network simulation, the actual machine model is connected to the network at $t = 0.5$ s and the rotor is unlocked at $t = 1$ s.

According to Figure 5.12, the waveforms generated by the synchronous machine model in the BFAST solver demonstrate a great compliance to those of PSCAD/EMTDC. The network produces a great deal of high-frequency transients in waveforms during the fault and they are slowly damped out after the fault is cleared. As such, the BFAST simulator produces the natural waveforms during the fault transients. Once the high-frequency content and dc-offsets of post-fault waveforms are cleared, it switches back to the dynamic phasor solution as the frequencies of the

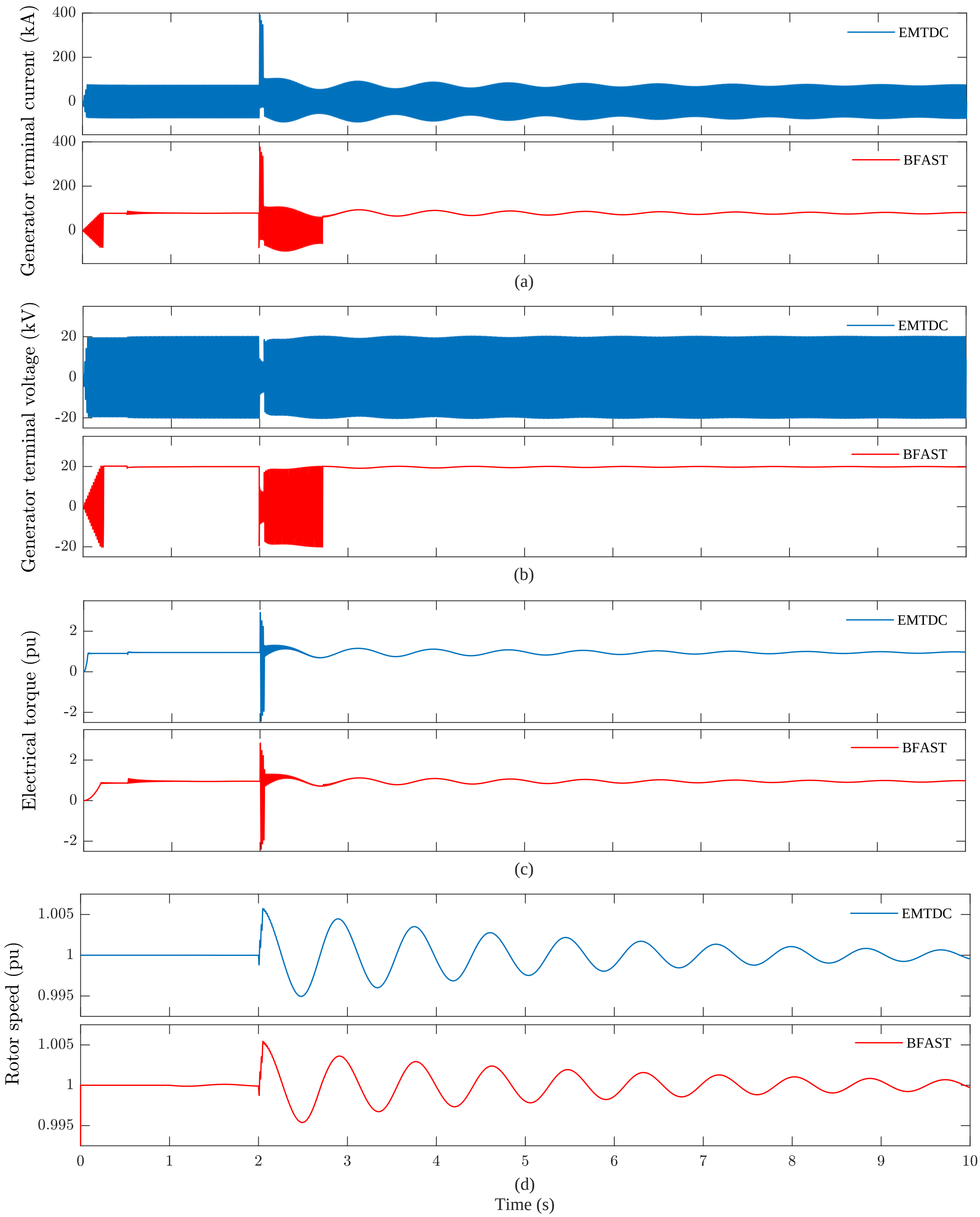

Figure 5.12: Synchronous machine's (a) current, (b), terminal voltage, (c) electrical torque, (d) rotor speed

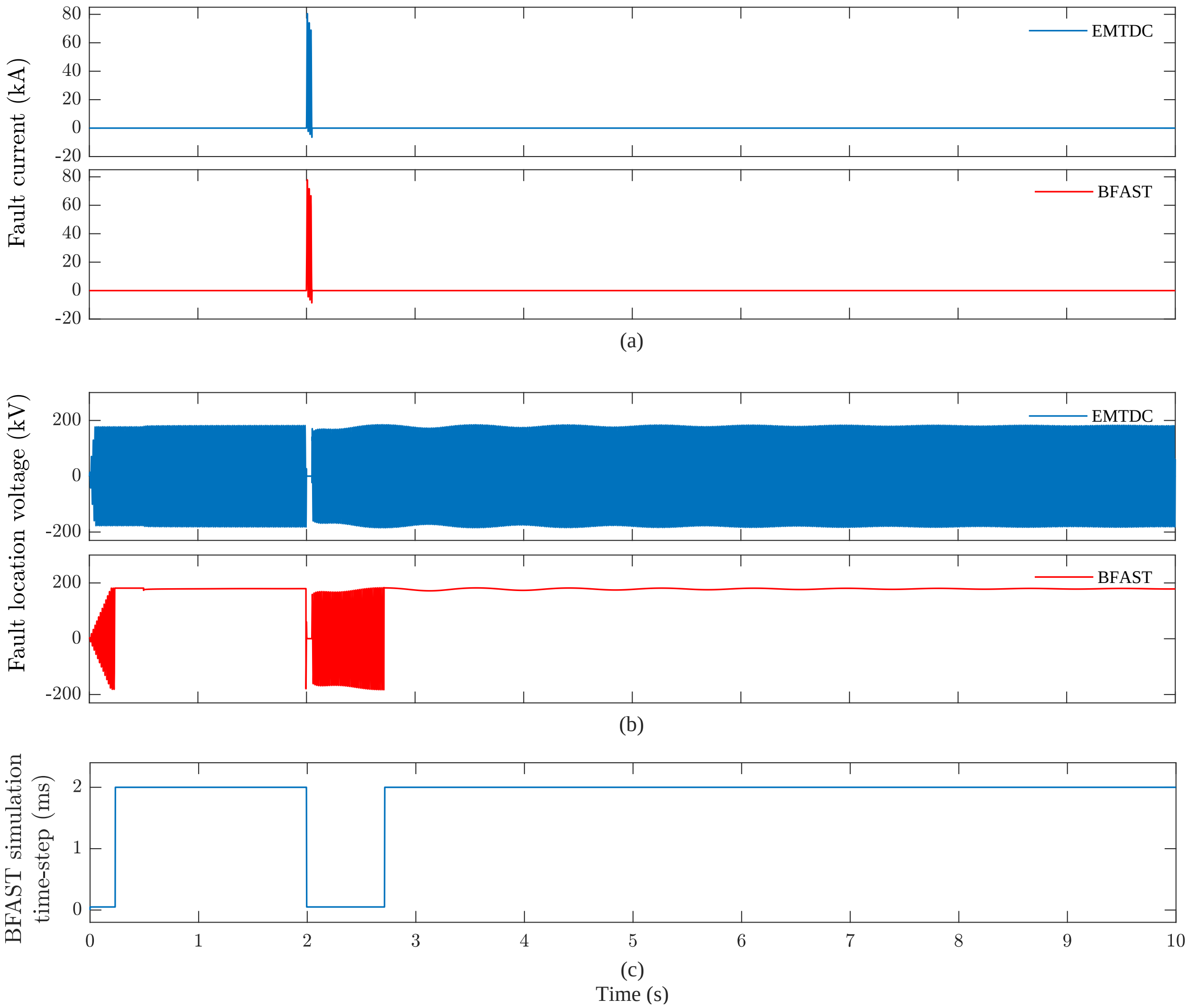

Figure 5.13: SMIB system waveforms for (a) fault current, (b) fault location voltage, (c) BFAST simulation time-step

rest of the transient are much slower than the power system frequency. The envelope of this slow transient is readily captured by the BFAST simulator using a time-step as large as 2 ms. Simulation time-steps of this magnitude are not practical to use in a fixed time-step environment as they cause difficulty in accurately replicating waveforms, especially during transients that constitute many frequencies.

The waveforms of the high-voltage side of the transformer and variation of the BFAST simulation time-step are shown in Figure 5.13. BFAST and PSCAD/EMTDC show similar transient behaviour while the BFAST follows the envelopes of PSCAD/EMTDC waveforms during slow variations and steady state. The BFAST solver operated with the large 2-ms solution time-step for a majority portion of the simulation improving the efficiency of the overall simulation.

5.5 Summary of Contributions and Conclusions

A base-frequency dynamic phasor-based transient simulator (refereed to as the BFAST solver), which can adapt its simulation time-step as well as the solution method according to the frequency contents of waveforms, was developed in this chapter. The simulator alters its solution technique between dynamic phasor and EMT, and simultaneously changes the size of the simulation time-step to capture details of transients of the network being simulated. A novel algorithm is developed to ensure a smooth and accurate transition between two solution techniques.

This chapter also provided a rich library of suitable models of power system components that can be incorporated in the BFAST simulator. This included a synchronous machine model, a transformer model, a transmission line model, and a modular multilevel converter model. Their interfacing circuits to the BFAST simulator and interfacing algorithms were also presented.

Simulation results demonstrated the ability of the novel BFAST solver to capture all the details of transient events, versatility of incorporated power system component models and their interface mechanisms, the ability to accelerate the simulation when slow or no transients are present, and also that the accurate and smooth transition between two solutions methods can be safeguarded by the proposed changeover algorithm. It is expected that the effectiveness of this solver improves with the length of simulations increasing since such simulations operate in steady state or with slow dynamics for long periods for which large simulation time-steps can be used.

Chapter 6

A Novel Multi-Rate Co-simulator Using BFAST and EMT Solvers

6.1 Development of BFAST-EMT Co-Simulator

Although the BFAST simulator can solve a network as a dynamic phasor and an EMT solver, it requires both EMT and dynamic phasor models to represent the entire power system. Dynamic phasor models of many components such as static converters may not be readily available or may need to be developed for specialised operating conditions such as commutation failure or imbalances. This limits the applicability of the solver as a stand-alone platform.

On the other hand, use of multiple simulation time-steps greatly enhances the computational workload, and consequently the speed of a simulation. However, it comes with challenges, especially in interactions at the interface boundaries between the solvers as it generates unequal number of data samples on both sides. Use of numerical methods such as interpolation offer reasonable accuracy and, hence, allow to use large time-step ratios for solutions during steady-state operation of the system since dynamic phasors provide nearly constant values. However, the accuracy of these methods may deteriorate during a network contingency as transmitting transients through the interface forces dynamic phasors to deviate from constant values. It is likely that a transient would disappear within a short period of time; it nonetheless is important to note that the error accumulated during the transient may adversely affect the performance of the co-simulation. This can be readily avoided if the time-steps of both sides of the interface are matched by using a reduced time-step ratio only during transients. It is, therefore, logical and practical to envision a co-simulation platform wherein an existing EMT solver and the BFAST solver are combined.

The underlying objective of the BFAST-EMT co-simulator proposed in this section is to change the BFAST solver's solution method and simulation time-step when transients are transmitted through the interface in order to increase the accuracy of the interaction. It must be noted that the solver changeover between EMT and dynamic phasor follows the same logic outlined in Chapter 5. The variables selected to ascertain the steady-state (compute Fourier coefficients) are the interface voltages and currents; therefore, the algorithm does not add any considerable computational burden as these are only a small subset of system variables.

In the BFAST-EMT co-simulation, the interface algorithm must be properly defined to ensure accurate and efficient interaction between the two solvers, especially when the BFAST solver experiences a time-step change. The proposed co-simulation algorithm can be explained using the illustrative network given in Figure 6.1, for which system parameters are listed in Table 6.1.

6.1.1 Network Partitioning at a Transmission Line

Co-simulation requires partitioning the network into subsystems and forming an interface between them. As explained in Chapter 2, network partitioning for explicit coupling introduces time-delays for data interaction between solvers as information from one subsystem is available to the other side only after the solution of that particular subsystem for the present time-step is obtained.

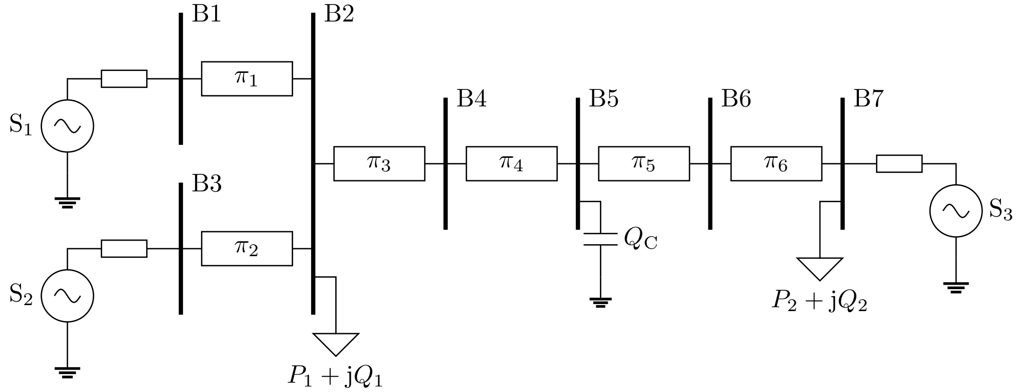

Figure 6.1: Illustrative test system for BFAST-EMT co-simulation

Table 6.1: BFAST-EMT co-simulation test system specifications

Component	Specification (system base: 100 MVA, 230 kV)
S_1, S_2, S_3	$1.01\angle 11.5°$ pu, $1.02\angle 21.5°$ pu, $1.00\angle 0.0°$ pu
π_1, π_5, π_6	$R = 0.00168$ pu; $X = 0.01333$ pu; $B = 0.02770$ pu
π_2, π_4	$R = 0.00336$ pu; $X = 0.03306$ pu; $B = 0.05550$ pu
π_3	$R = 0.00115$ pu; $X = 0.00911$ pu; $B = 0.01830$ pu
Q_C	0.6 pu
$Load_1$, $Load_2$	$1 + j0.25$ pu, $5 + j2.5$ pu

Applications such as [24, 51] ignore this delay when interfacing with external system. However, if not properly compensated, this time delay may cause severe phase errors in waveforms and numerical instabilities in the solution as proved in Chapter 4, particularly when one side uses a large time-step.

There are several time-delay compensating methods in literature, some of which are discussed in Chapter 2. The method proposed in [33, 52] uses extrapolation in order to compensate the time-delay. The accuracy of this method drops when there is a discontinuity in signals or when a large solution time-step is used. The interface used in [87] adopts MATE technique to partition the network. This method avoids any partitioning delay, but at the expense of increased computational steps. The transmission line interface based on the Bergeron's model is a widely-used method to partition a network as it uses the natural wave propagation time through the line [28, 88]. The main restraint of the transmission line interface is that the maximum time delay that can be compensated is equal to the wave travel time through the line and, thus, is limited by its length.

As devising a suitable decoupling method is not a primary objective of this thesis, the transmission line method is used to form the interface considering its simplicity and robustness. Other forms of interface that do not insert time-delays to the solution such as MATE method may also be used with minimal impact on the two solvers.

The network given in Figure 6.1 is partitioned into two subsystems and interfaced via the transmission line-4 (π_4) as shown in Figure 6.2. Partitioning and interfacing subsystems using the transmission line model are discussed in section 2.3.2. The characteristic impedance and the wave travel time of this line are calculated as 400 Ω and 100 μs for this 30 km line, respectively.

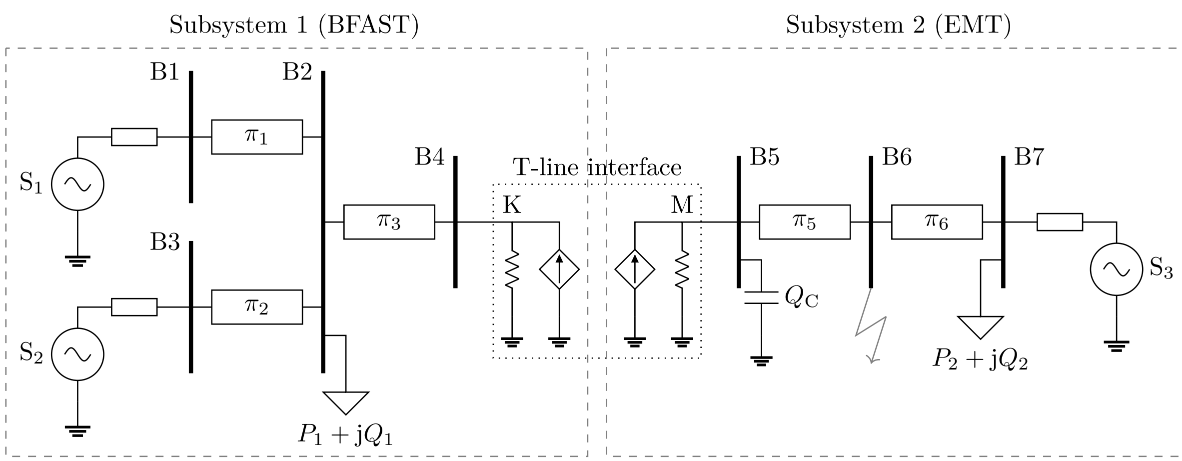

Figure 6.2: Decoupled representation of co-simulation illustrative test system

It is important to note that the interface current source of the BFAST side at node K must now be updated with base-frequency dynamic phasor values. For that, (2.11) needs to be transformed to base-frequency dynamic phasors as follows.

$$\left\langle \mathrm{H_K} \right\rangle_{\mathrm{B}}(t) = \left(\frac{2\left\langle \mathrm{V_M} \right\rangle_{\mathrm{B}}(t-\tau)}{Z_{\mathrm{C}}} - \left\langle \mathrm{H_M} \right\rangle_{\mathrm{B}}(t-\tau) \right) \mathrm{e}^{-\mathrm{j}\omega_{\mathrm{s}}\tau} \tag{6.1}$$

where

$$\left\langle \mathrm{H_M} \right\rangle_{\mathrm{B}}(t) = \left(\frac{2\left\langle \mathrm{V_K} \right\rangle_{\mathrm{B}}(t-\tau)}{Z_{\mathrm{C}}} - \left\langle \mathrm{H_K} \right\rangle_{\mathrm{B}}(t-\tau) \right) \mathrm{e}^{-\mathrm{j}\omega_{\mathrm{s}}\tau} \tag{6.2}$$

Equation (6.1) requires extraction of BFDPs of both the current and voltage from the other side of the interface, which increases the number of computations as well as conversion errors. Extraction of BFDPs of current samples can be readily avoided if (6.1) is rewritten in the following recursive form by substituting $\left\langle \mathrm{H_M} \right\rangle_{\mathrm{B}}(t)$.

$$\left\langle \mathrm{H_K} \right\rangle_{\mathrm{B}}(t) = \left(\frac{2\left\langle \mathrm{V_M} \right\rangle_{\mathrm{B}}(t-\tau)}{Z_{\mathrm{C}}} - \left(\frac{2\left\langle \mathrm{V_K} \right\rangle_{\mathrm{B}}(t-2\tau)}{Z_{\mathrm{C}}} - \left\langle \mathrm{H_K} \right\rangle_{\mathrm{B}}(t-2\tau) \right) \mathrm{e}^{-\mathrm{j}\omega_{\mathrm{s}}\tau} \right) \mathrm{e}^{-\mathrm{j}\omega_{\mathrm{s}}\tau} \tag{6.3}$$

6.1.2 BFAST-EMT Interaction Algorithm

Assume that the simulation time-step of the EMT solver is Δt_{EMT}. Understandably the smallest time-step belongs to the EMT simulator; therefore, one can choose BFAST solver's time-steps as,

$$\begin{aligned} \Delta t_{\mathrm{T}} &= N_1 \Delta t_{\mathrm{EMT}} \\ \Delta t_{\mathrm{DP}} &= N_2 \Delta t_{\mathrm{EMT}} \end{aligned} \tag{6.4}$$

where N_1 and N_2 are integers. N_1 determines the time-step ratio when both solvers operate with the EMT solution. This is when the BFAST-EMT co-simulator runs different EMT segments at different time-steps. N_2 can be set based upon the maximum time-step allowed for the dynamic phasor solution, which is equal to the wave propagation delay, τ, of the transmission line interface.

Interaction when the BFAST Solver Operates with the EMT Solution

When the BFAST solver operates with the EMT solution method, the current and voltage values at the interface buses of each side are used to update the current sources of the other side of the interface after a delay of τ using (2.10) and (2.11) as shown in Figure 6.3, which is illustrated assuming $N_1 = 1$. If N_1 is chosen to be larger than unity, the intermediate values of the BFAST solver are interpolated to balance the granularity of data samples of both sides.

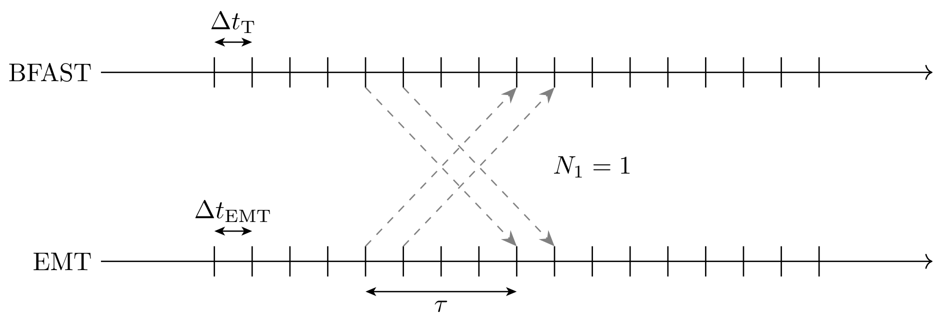

Figure 6.3: Co-simulator interaction when the BFAST solver operate with the EMT solution

Interaction when the BFAST Solver Operates with the Dynamic Phasor Solution

Once the BFAST solver switches to the dynamic phasor solution with a large time-step, one side of the interface is in dynamic phasor domain while the other side solution remains in time-domain; therefore, a sophisticated algorithm is required to (i) convert data between time-domain and frequency-domain signals, and (ii) balance the granularity of data samples.

The interface current source of the BFAST side, i.e., $\left\langle \mathrm{H_K} \right\rangle_{\mathrm{B}}(t)$, is updated with dynamic phasor values using (6.3). Values corresponding to $\left\langle \mathrm{V_K} \right\rangle_{\mathrm{B}}(t-2\tau)$ and $\left\langle \mathrm{H_K} \right\rangle_{\mathrm{B}}(t-2\tau)$ are available from prior time-steps of the BFAST solution. The base-frequency dynamic phasor quantity $\left\langle \mathrm{V_M} \right\rangle_{\mathrm{B}}(t-\tau)$ is readily extracted from sampled instantaneous values from the EMT-side of the interface. Calculation of the interface current source on the EMT side, i.e., $h_{\mathrm{M}}(t)$, can be done using (2.10) once the base-frequency dynamic phasor quantities are converted to natural time-domain values. Extracting base-frequency dynamic phasors and converting them to time-domain can be done as explained in section 3.4.

Once data conversion is established, the process of data communication between the solvers commences. Interpolation is enabled at the interface of the BFAST solver to acquire all the intermediate data points required for the EMT simulator to ensure an authentic data communication between two simulators.

Consider the case shown in the Figure 6.4, where Δt_{DP} is chosen to be the same as the travel time, τ, of the interfacing transmission line with $N_2 = 4$ and solutions corresponding to $t = t_{k-1}$ are known for both solvers. The following interaction algorithm takes place during $t \in (t_{k-1}, t_k]$.

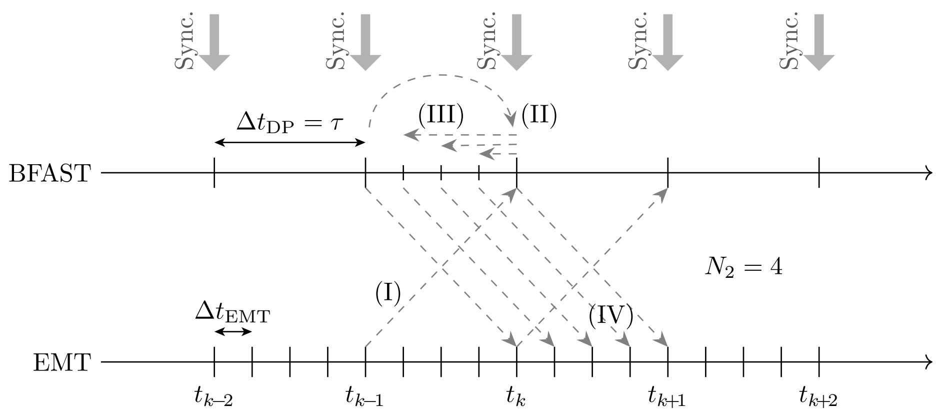

Figure 6.4: Co-simulator interaction when the BFAST solver operate with the DP solution

(I) BFAST interface is updated as in (6.3) using BFAST solver's history values and the EMT samples at $t = t_{k-1}$, which reach the BFAST solver after a delay of τ.

(II) The solution for the BFAST solver at $t = t_k$ is obtained. Simultaneously, the EMT solver is solved from $t = t_{k-1}$ to $t = t_k$. During this period, the EMT-side interface needs solved and interpolated values from the BFAST-side between $t = t_{k-2}$ and $t = t_{k-1}$ (see step IV).

(III) Intermediate values of interface currents and voltages between t_{k-1} and t_k of the BFAST solver are linearly interpolated.

(IV) Solved and interpolated interface values are converted and used to update the EMT solver's interface after a delay of τ.

It is apparent from the above sequence that the solution of one solver between t_{k-1} and t_k is not affected by the operations in the other solver during the same period. As such, the constituent simulators can operate in parallel solving the subsystems simultaneously as long as Δt_{DP} is kept less than or equal to τ.

Figure 6.5 illustrates the flow chart of the overall BFAST-EMT co-simulation algorithm. The simulation procedure starts with partitioning the network and assigning resultant subsystems into BFAST and EMT solvers. Then the nodal admittance matrices corresponding to each subsystem are built, inverted, and stored before the start of the main simulation-loop. Note that, for BFAST solver, two nodal admittance matrices are found with $\omega_{\mathrm{s}} = 0$ and $\omega_{\mathrm{s}} = \omega_0$. The rest of the simulation in the BFAST solver is as described in Chapter 5 while communication between the two simulators occurs after the network solution in each time-step.

6.1.3 Illustrative Validation

The partitioned test system shown in Figure 6.2 is simulated in the context of the BFAST-EMT co-simulator with $\Delta t_{\mathrm{T}} = 20$ μs, $\Delta t_{\mathrm{DP}} = \tau = 100$ μs, and $\Delta t_{\mathrm{EMT}} = 20$ μs, and its dynamic performance is examined by applying a line-to-ground fault to bus-6, which is inside the EMT solver, at $t = 0.5$ s for a duration of six cycles. Note that the dynamic phasor solution time-step of the external system, Δt_{DP}, is merely a limitation imposed by the wave propagation time through the transmission lines used to form the interface between the two solvers; a larger time-step size may be used in a system in which the interface is established using a long transmission line.

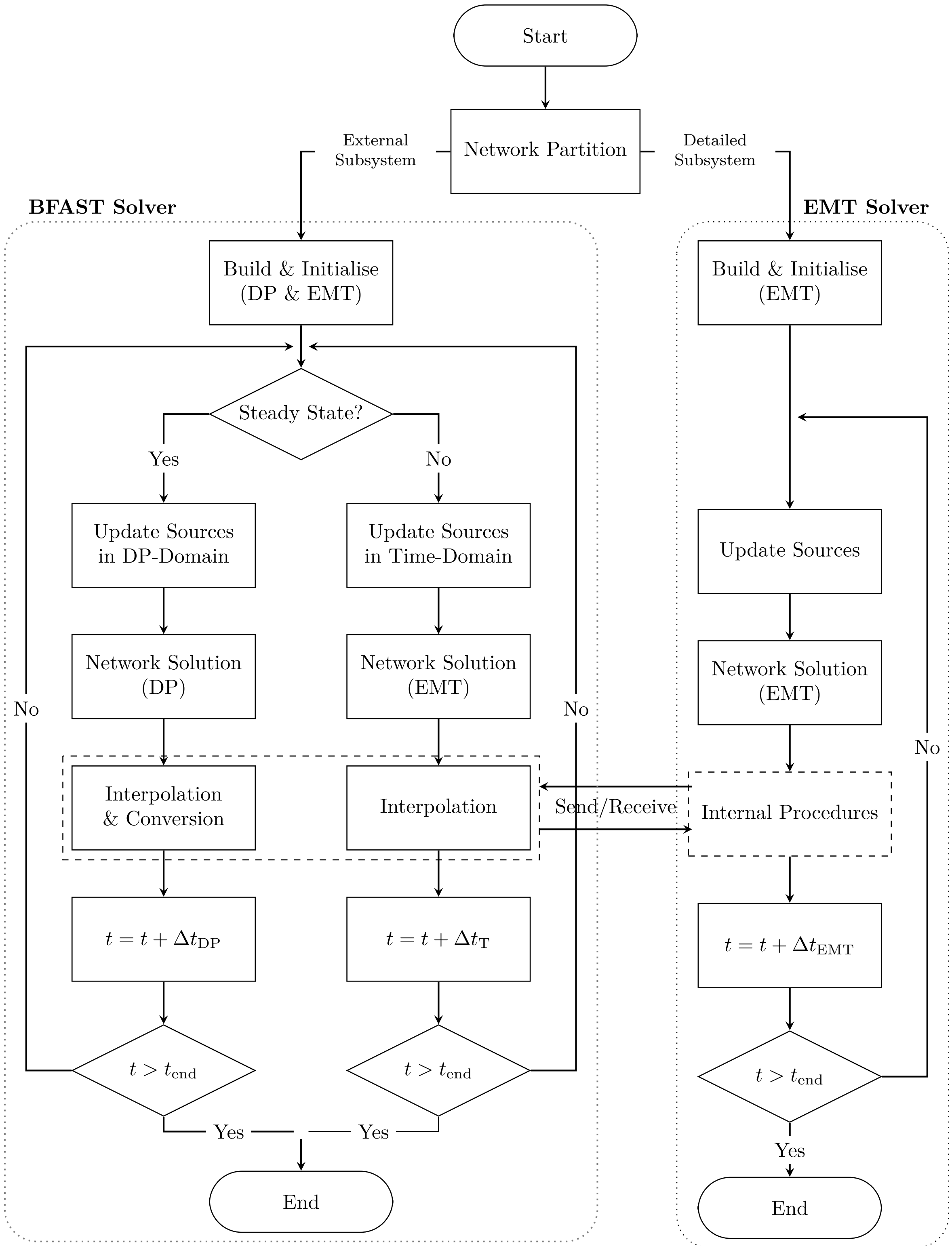

Figure 6.5: BFAST-EMT co-simulator flow chart

To validate the accuracy of co-simulation results, the entire system is also simulated in PSCAD/EMTDC with a 20 μs time-step, and its results serve as the baseline for comparison. In the shown waveforms, similar to Chapter 5, portions where the dynamic phasor solution is obtained are presented with the envelope of the waveform and the natural waveforms are displayed for the parts where the EMT solution is found.

Figure 6.6 is a comparison of the current waveforms of the interface transmission line (π_4) as seen from both ends of the line. As it can be seen from Figure 6.6a, the current going into node M is entirely simulated in the time-domain since this node belongs to the detailed EMT

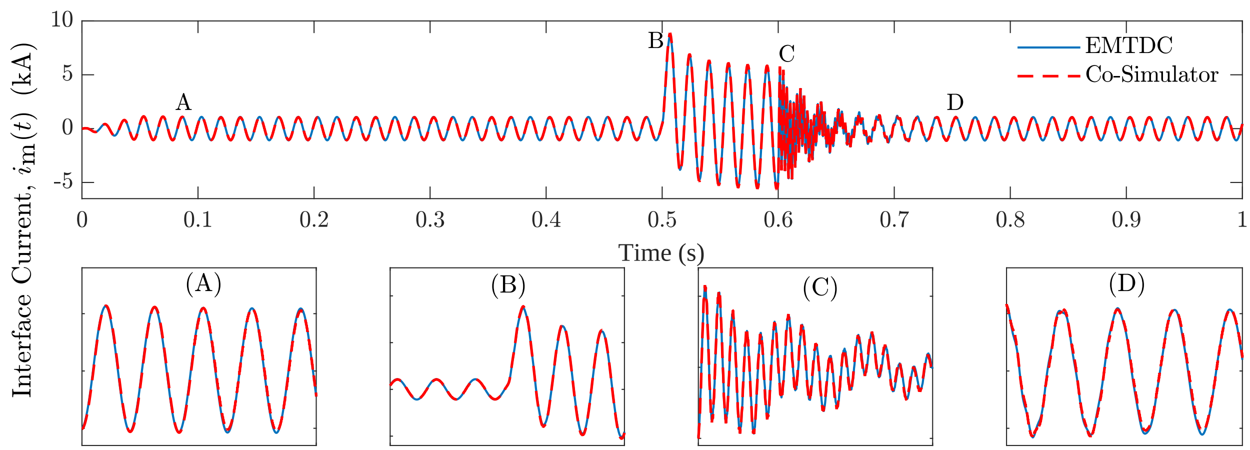

(a)

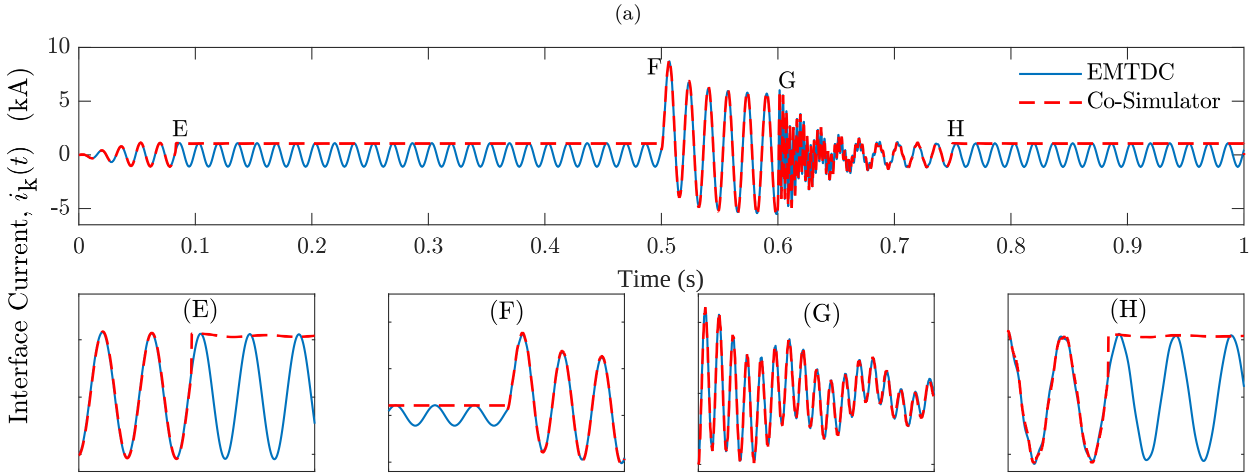

(b)

Figure 6.6: Interface transmission line current of BFAST-EMT co-simulation test system (a) as seen from the EMT solver (node M); (b) as seen from the BFAST solver (node K)

subsystem of the co-simulation. However, the current flowing into the node K, which is a part of the external subsystem and solved in the BFAST solver, changes its solution technique between dynamic phasor and EMT as shown in the Figure 6.6b. Both waveforms verify that the transient details of the BFAST-EMT co-simulator waveforms are identical to those of EMTDC. Enlarged views of the waveform at locations (A)-(H) are displayed at the bottom of each figure confirm that the BFAST-EMT co-simulator is able to alter its solution technique without losing the accuracy or fast transients details of the simulation.

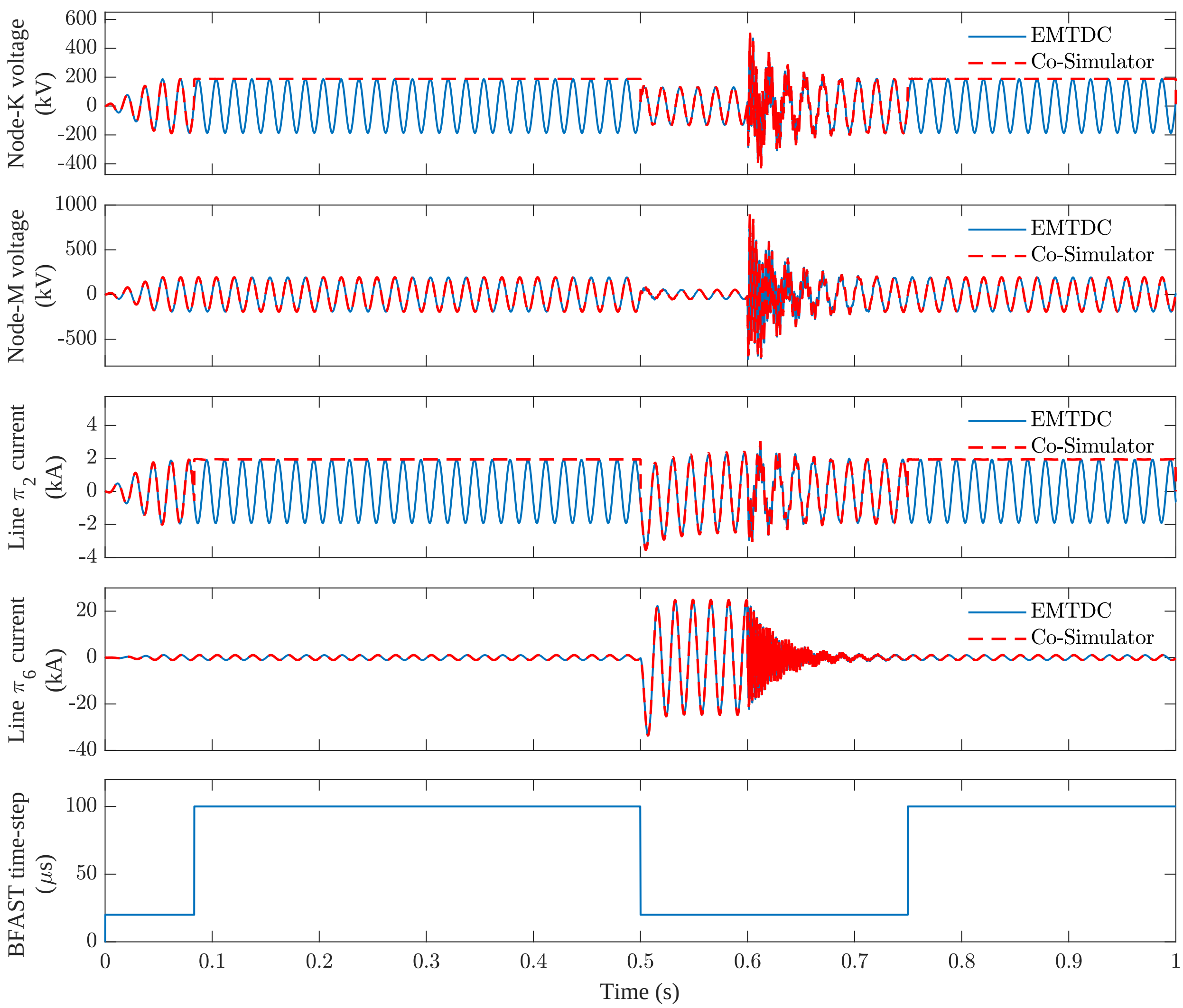

Figure 6.7: Waveform comparison for BFAST-EMT co-simulation test system

To further illustrate the accuracy of the co-simulator, a few selected waveforms from subsystem-1 and the subsystem-2, and the change of the time-step of the BFAST solver during the simulation are presented in the Figure 6.7. Identical dynamic and steady state behaviours demonstrated in both co-simulation and the EMTDC waveforms firmly attests the accuracy of the proposed co-simulation algorithm.

6.1.4 Modes of Operations of BFAST-EMT Co-Simulator

The adaptive solution in the BFAST solver implies that the proposed BFAST-EMT co-simulator lends itself to several simulation modes as described follows.

Mode 1. **BFAST-EMT multi-rate co-simulator:** In this mode, as illustrated in Figure 6.8a, the solution method and the time-step in the external system switches between dynamic phasor and EMT based upon the dynamics of the subsystem's waveforms. The detailed subsystem is simulated with the EMT solution using a small time step. This mode can be used when the simulations require retention of both the accuracy of dynamics and improved speed. Note that this mode is a superset of the other two, and once implemented other two modes can be readily derived.

Mode 2. **DP-EMT multi-rate co-simulator:** In this mode the external subsystem is simulated using dynamic phasors with a large time-step and the detailed subsystem is simulated with the EMT method using a small time step as illustrated in Figure 6.8b. This mode can be used if the external subsystem dynamics are very slow.

Mode 3. **EMT-EMT multi-rate co-simulator:** In this mode both external and detailed subsystems are simulated with the EMT method. The two sides may use different time-steps (larger in the external subsystem). This is shown in Figure 6.8c. This mode is useful when the external subsystem consists of fast - but comparatively slower - dynamics compared to the detailed subsystem. For example, with a switching converter, only the electrical vicinity of the converter may need a small time-step.

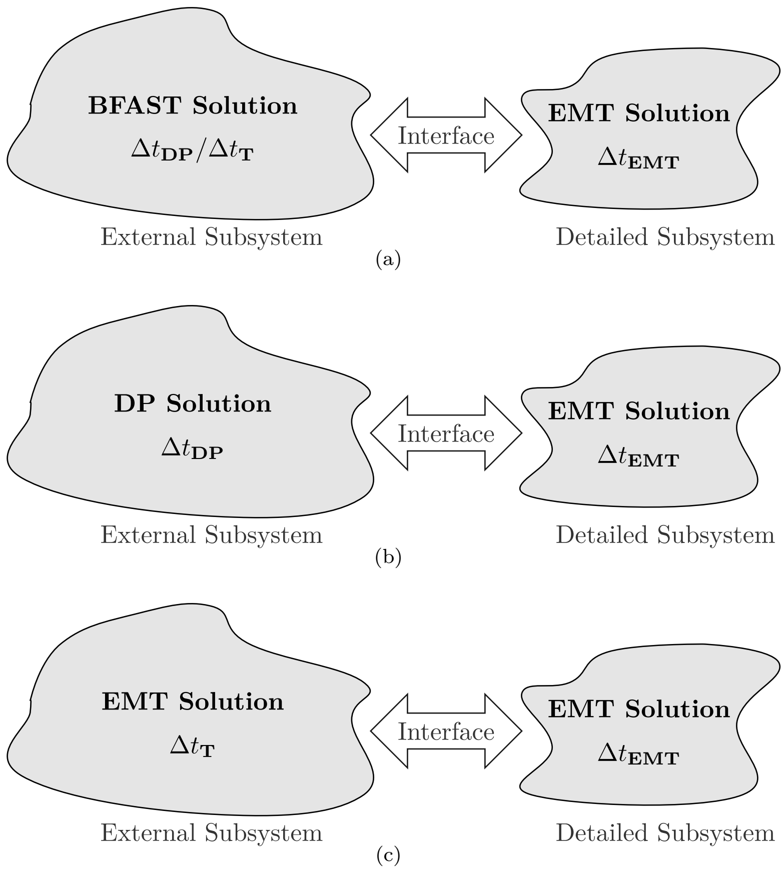

Figure 6.8: Modes of operations of the BFAST-EMT co-simulator (a) multi-rate BFAST-EMT (mode 1), (b) multi-rate DP-EMT (mode 2), (c) multi-rate EMT-EMT (mode 3)

6.2 BFAST-EMT Co-Simulation Cases

Compared to a standalone EMT solver, the effectiveness of the proposed co-simulator is expected to be increased as the network size and the length of the simulation increase. To validate this statement, co-simulation results of two power systems, a 12-bus system [89] and the IEEE's 118-bus system [90], using the proposed BFAST-EMT platform are shown in this section. Data for both test systems are given in Appendix E.

6.2.1 Co-Simulation Setup

In following co-simulation cases, the co-simulation setup is developed by integrating the BFAST solver to an industrial-grade EMT simulator. The detailed subsystem in each case is implemented in PSCAD/EMTDC using standard library components. PSCAD/EMTDC is an industrial-grade EMT simulator and includes a library of electrical and control components. The external subsystem, which is solved using the BFAST method, is implemented in an external integrated development environment using C++. A library of system components are build incorporating the models discussed in Chapter 5. The systems are decoupled using the transmission line interface; interaction between PSCAD/EMTDC and the BFAST simulator is established via an inbuilt co-simulation component in PSCAD/EMTDC. The co-simulation component allows each of the parts of a simulation to communicate with third-party applications such as the BFAST solver developed in this thesis in order to co-simulate in parallel with PSCAD/EMTDC (simultaneous solution).

Following simulations are performed in a computer with a 3.20 GHz clock speed, Intel Core i7-8700M processor, and 16 GB RAM. For each case, the entire system is also simulated in PSCAD/EMTDC using a small time-step; the results of this simulations are used to benchmark the co-simulation results.

6.2.2 Case I: IEEE 12-Bus Network

The single-line diagram of the segmented twelve-bus system [89] is shown in Figure 6.9. Generators and transformers in the external system are modeled as voltage sources and inductances, respectively, while the detailed subsystem is developed with standard EMT generator and transformer models. The network is partitioned at the 100 km line connecting buses 1 and 2 and the 300 km line connecting buses 4 and 5. Each interface line, i.e., $\mathrm{B1_m}$-$\mathrm{B1_k}$

and $B5_m$-$B5_k$, is 60 km long. The remaining 40 km portion of the original B1-B2 line is modeled in the detailed subsystem and the remaining 240 km portion of the original B4-B5 line is included in the external subsystem to be simulated with the BFAST solver. The characteristic impedance, (Z_C), and the wave propagation delay, (τ), of the interface lines are computed as 368.5 Ω and 200 μs, respectively.

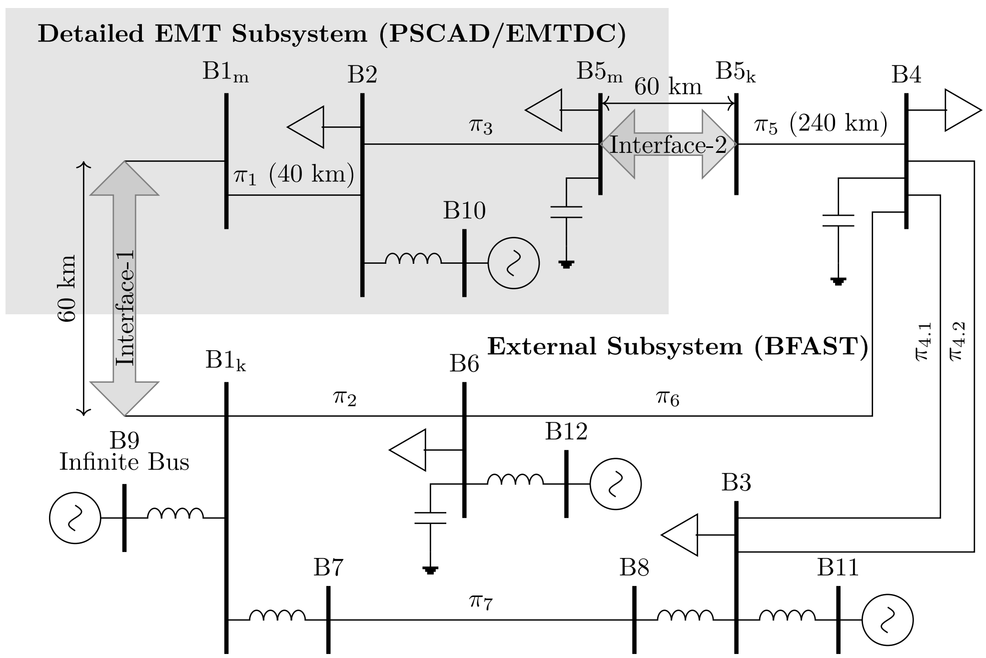

Figure 6.9: Decoupled representation of IEEE twelve-bus network

Transients in the systems are generated by applying disturbances into sybsystems in both the EMT and BFAST solvers. Solution time-steps are chosen as $\Delta t_{\mathrm{T}} = 10\ \mu$s, $\Delta t_{\mathrm{DP}} = 200\ \mu$s, and $\Delta t_{\mathrm{EMT}} = 10\ \mu$s. The maximum time-step in this case is restricted to 200 μs due to the length of the interface transmission lines.

Simulation Results for a Disturbance in the Detailed Subsystem

A solid line-to-ground fault is applied to bus-2 at $t = 2.0$ s. The fault is intentionally cleared at a non-zero crossing point of the fault current after six cycles (0.1 s) in order to assess the co-simulator's performance under high-frequency transients. The transient behaviour of interface transmission line currents from both sides are shown in Figure 6.10; BFAST and EMT subsystem waveforms during the fault are shown in Figure 6.11.

The comparison shows that the co-simulation waveforms are essentially identical to those from standalone PSCAD/EMTDC (i.e., the benchmark); most notably, the co-simulator is able to capture high-frequency contents of waveforms after the fault is cleared without losing accuracy. The entire frequency band of the transient are conveyed to the external system via the interface. This is a major gain compared to other co-simulation models available in the literature, and is achieved due to adaptive usage of both time-step and shift-frequency in the BFAST solver.

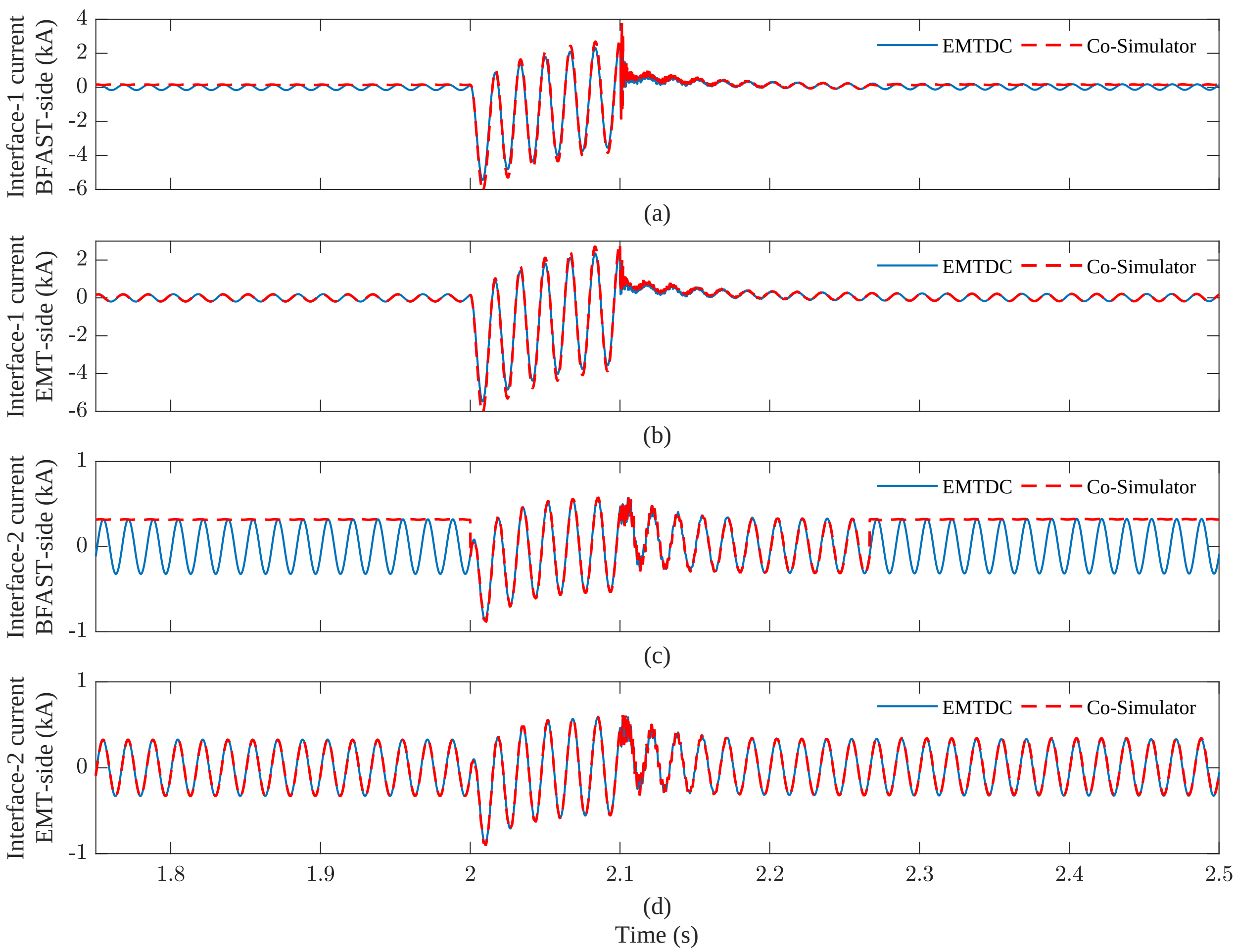

Figure 6.10: Line currents of 12-bus system for (a) interface-1 as seen from BFAST side; (b) interface-1 as seen from EMT side; (c) interface-2 as seen from BFAST side; (d) interface-2 as seen from EMT side.

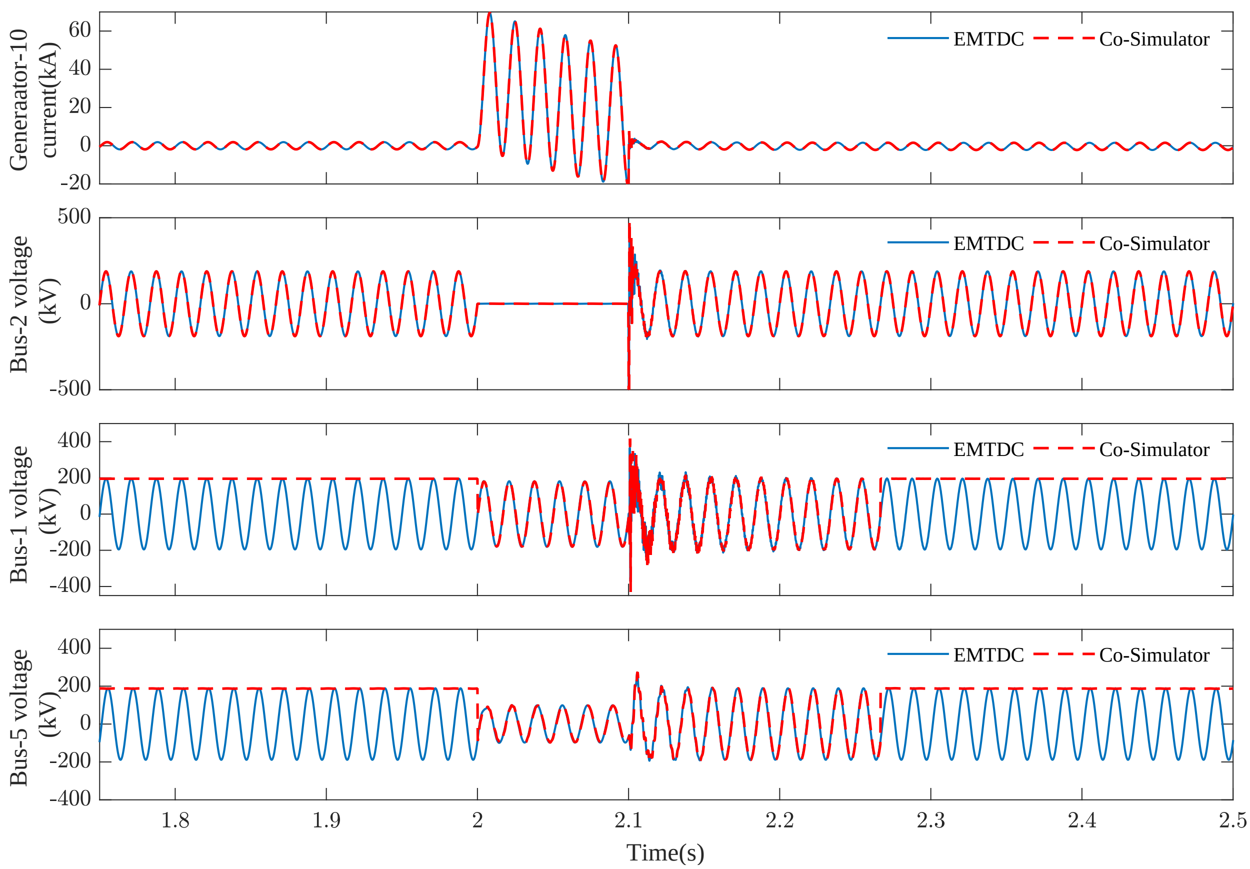

Figure 6.11: Co-simulation waveforms of 12-bus system for line-to ground fault at bus-2

Simulation Results Under Different Modes of Operations

Waveforms of interface-2 line current simulated by the BFAST solver for mode-2 and mode-3 operations of the co-simulator are shown in Figure 6.12. The mode-2 operation gives an exact replica of waveform's envelop during steady state, and captures most of the transients in shifted-frequency domain due to the harmonic-rich base-frequency dynamic phasor modeling. This, however, hinders the ability to use an extensively large simulation time-step for the external subsystem if a fixed time-step is used. It can be observed that the mode-3 simulation provides essentially identical results to the benchmark case as both subsystems are solved using the detailed EMT method.

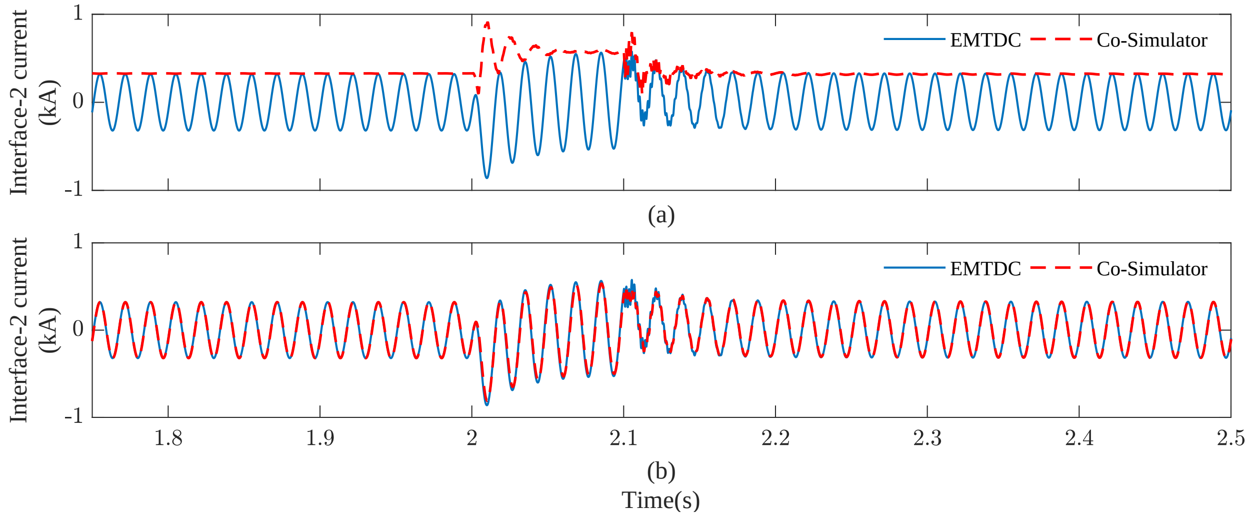

Figure 6.12: Interface-2 current waveforms generated by BFAST solver for (a) mode-2 and (b) mode-3 operations of the co-simulator

Simulation Results for a Disturbance in the External Subsystem

A solid line-to-ground fault is applied to bus-1 in the external subsystem to assess the impact of the external system dynamics on the EMT subsystem. It is seen from Figure 6.13 that the co-simulator produces results that are in good agreement with EMTDC simulation waveforms. The dynamic details are accurately conveyed into the EMT subsystem through the interface.

Computational Gain Comparisons

A comparison of computational gains is done to demonstrate the efficiency of the novel co-simulation algorithm against standalone EMT simulation. The PSCAD/EMTDC (i.e., the standalone EMT solver) took 81 s to complete a 10-s long simulation of the 12-bus system with a 10 μs time-step while the co-simulation shows noticeable computational gain as given in Table 6.2, for different time-step ratios and different modes of operations. The results show a nearly two-fold acceleration. Note that the 12-bus system is a small network, and co-simulation is not expected to provide massive gains here as the EMT subsystem constitutes a noticeable portion of the overall system.

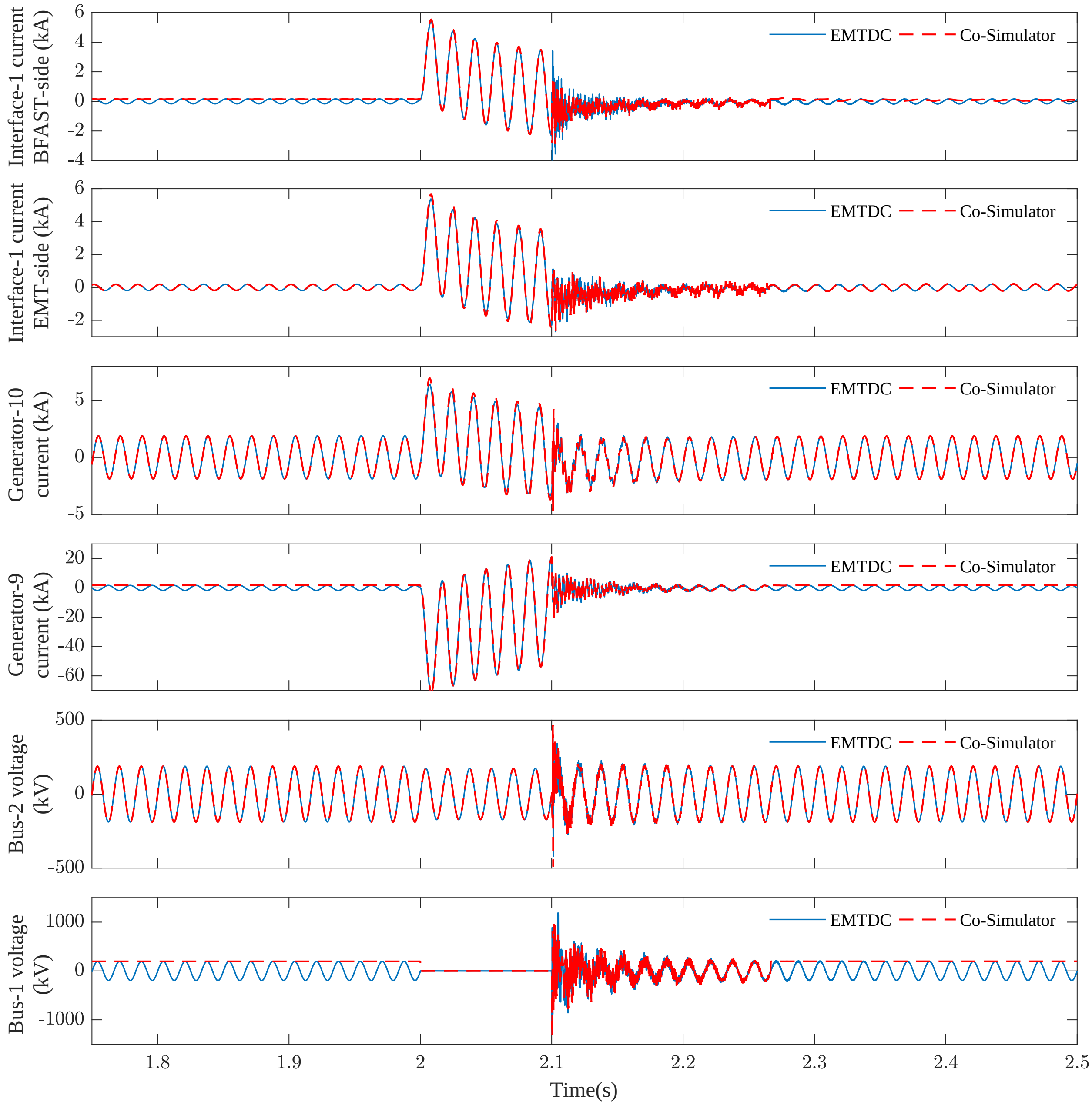

Figure 6.13: Co-simulation waveforms of 12-bus system for line-to ground fault at bus-1 (external subsystem)

It is also important to mention at this point that network co-simulations involves several types of computational and communication overheads. These includes computations of interface variable, domain conversions of signals, and data exchange between simulators. For a small system, co-simulation overhead may takes a significant proportion of the overall simulation time. However, such overheads are imperceptible when the size of the network increases.

Table 6.2: Co-simulation time comparison for 12-bus system

	Time-steps (μs)			Simulation time (s)
	Δt_{DP}	Δt_{T}	Δt_{EMT}	
Mode-1	200	20	10	44
	200	50	10	44
Mode-2	100	-	10	45
	200	-	10	44
Mode-3	-	20	10	46
	-	50	10	45

6.2.3 Case II: IEEE 118-Bus Network

IEEE's 118-bus system is a relatively larger system that is modeled and simulated using the developed BFAST-EMT co-simulator. In this example, similar to the 12-bus case, all the generators and transformers are modeled as voltage sources and inductances, respectively. The system data for the test system are based on [90]. Bus numbers 98 to 112, the chosen detailed part of the system, are implemented in detail in PSCAD/EMTDC using standard library components. The remaining buses are included in the BFAST solver. As in the 12-bus case, the interface between detailed subsystem and the external subsystem is formed assuming 60 km length of interfaced transmission lines. Parameters of five interface lines are given in Table 6.3.

Table 6.3: IEEE 118-bus co-simulation interface parameters

Interface Transmission Line	Characteristic Impedance (Z_c)	Propagation time (τ)
Line 80-98	1028 Ω	200 μs
Line 80-99	1028 Ω	200 μs
Line 92-100	1322 Ω	200 μs
Line 92-102	1034 Ω	200 μs
Line 94-100	518 Ω	200 μs

Simulation Results

Several tests similar to the previous example are performed on the system including application of faults in the detailed and external subsystems. It is observed that co-simulator produced results that are in good agreement with the benchmark results, and therefore, confirm the accuracy of the co-simulator in response to disturbances in both subsystems. For brevity, only a few waveforms are shown in Figure 6.14, for a line-to-ground fault applied at bus-106. Solution time-steps are chosen as $\Delta t_{\mathrm{T}} = 50\ \mu$s, $\Delta t_{\mathrm{DP}} = 200\ \mu$s, and $\Delta t_{\mathrm{EMT}} = 10\ \mu$s.

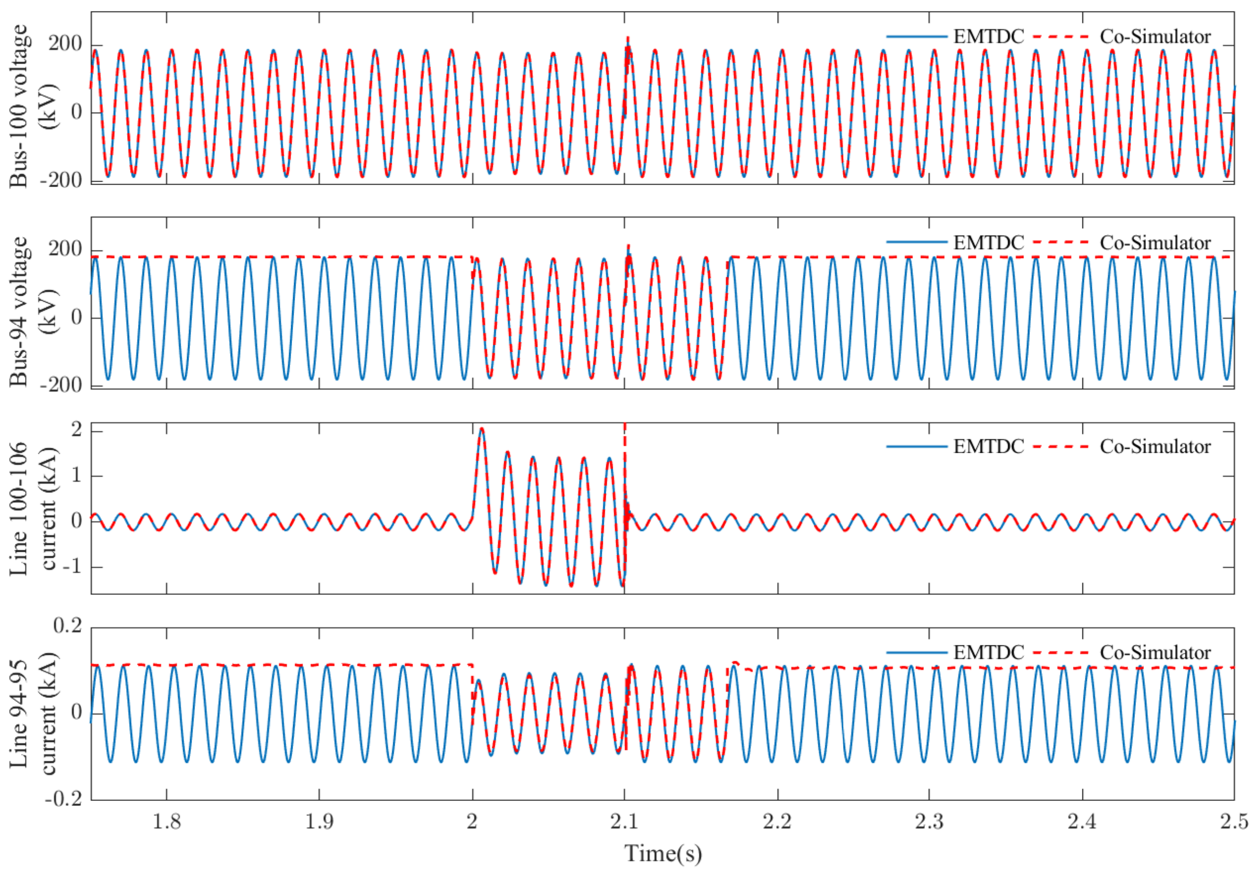

Figure 6.14: Co-simulation waveforms for line-to-ground fault at bus-106 of the 118-bus system

Computational Gain Comparisons

Simulations of the 118-bus system are performed for a 10-s duration. The standalone EMT simulator (PSCAD/EMTDC) took 740 s to complete the simulation with a 10 μs time-step while the co-simulation shows noticeable computational gain as given in Table 6.4, for different time-step ratios and different modes of operations.

It is clear that the computational gain in this example is much larger than what was observed in the 12-bus system. This is due to the fact that in this co-simulation example, the EMT subsystem is a smaller portion of the overall system. Relieving the rest of the system from having to use a small time-step contributes to a large reduction in the computing time needed for the whole simulation. Larger computational gains are expected from co-simulations of larger systems, in which the EMT subsystems are a small proportion of the entire system. Also, computational gain can be further improved by using a larger time-step ratio provided that the BFAST-EMT interface is not imposing any restriction on the maximum solution time-step that can be used in the external solver.

Table 6.4: Co-simulation time comparison for 118-bus system

	Time-steps (μs)			Simulation time (s)
	Δt_{DP}	Δt_{T}	Δt_{EMT}	
Mode-1	200	20	10	84
	200	50	10	81
Mode-2	100	-	10	96
	200	-	10	76
Mode-3	-	20	10	138
	-	50	10	102

6.3 Modeling and Controlling MMCs in the Context of the External Subsystem of Co-simulation

Modular multilevel converters have become the de facto topology in many high- and medium-voltage applications due to their superior performance compared with other converter topologies. Modeling MMCs in simulation studies is challenging due to the large number of switching devices these converters are built upon. This is exacerbated by the need to use small simulation time-steps to capture the switching transients. It is well-known that detailed switching models of MMCs are impractical for the above reasons; this has given rise to a great deal of research and development effort in efficient and accurate modeling of MMCs for transient simulation [51, 91–94].

Co-simulation is used as an effective solution to the problem of modeling and simulation of large, converter-intensive ac-dc hybrid power systems [22, 95, 96]. The established practice at the present time is to include MMCs in the detailed EMT subsystem of a co-simulated model assuming that the information of interest lies within a small vicinity of the MMCs. However, when multiple MMCs are present, as it is in multi-terminal HVDC or renewable energy systems, it will be inevitable to have to include MMCs in the external subsystems of the network.

This section employ the MMC model discussed in section 5.4.4 and builds a platform to interface and simulate MMCs in the context of the external subsystem in co-simulation environment. It also proposes a method for accurate modeling of MMC controls, which are immensely difficult to implement in co-simulation settings.

6.3.1 MMC Co-simulation Test System

The twelve-bus system [89] is simulated in the context of the developed BFAST-EMT co-simulator. For simplicity, only the mode-2, i.e. DP-EMT co-simulation, operation of the co-simulator is considered. The MMC replaces the original generator connected at bus-11 inside the external subsystem using the MMC interface provided in section 5.4.4, and it is controlled to provide the required active power and voltage level at the bus. The test system and the MMC parameters are given in Figure 6.15 and Table 6.5, respectively. Similar to early examples, the network in the EMT subsystems is implemented in the context of PSCAD/EMTDC using built-in library components.

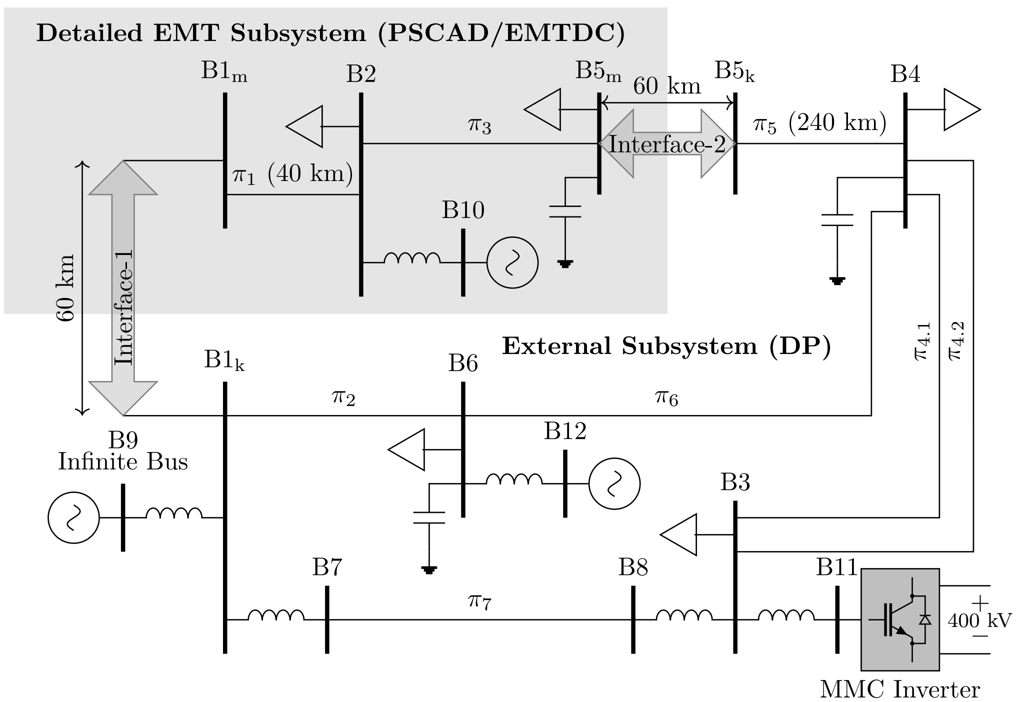

Figure 6.15: Twelve-bus system co-simulation with an MMC feeding bus-11.

6.3.2 Control of MMCs in the Context of the Co-Simulator

Control and synchronization units for the MMC need to be included and it is paramount that their characteristics such as controller limits and other non-linear functions be preserved to create a realistic representation of the converter even though it is a non-EMT model. These controllers are difficult to implement in the co-simulation settings due to difficulties in modeling non-linearities in

Table 6.5: MMC parameters

	Notation	Value
Number of SMs per arm	N_{arm}	50
Dc-bus voltage	V_{dc}	400 kV
SM capacitance	C_{sm}	10 mF
Arm inductance	L_{a}	0.001 H
Arm resistance	R_{a}	0.025 Ω
Rated ac voltage	V_{rat}	230 kV
Rated power	P_{rat}	300 MW

the phasor environment, lack of instantaneous details of waveforms, and requirement of devising feedback measuring techniques. As such, a sophisticated control mechanisms needs to be put in place in order to realize control objectives of the DP-MMC model. Controllers of an MMC can be basically separated to three categories.

1. Primary controller, which regulates system-level variables such as real and reactive power output or the converter bus voltage. These behaviours of the DP-MMC use in this thesis (see Appendix D) can be directly set by controlling the modulation index, m, and the power angle, δ of the capacitor switching function.

2. Secondary controller, which is in charge of internal dynamics of the MMC such as capacitor ripples and circulating current. Implementation of this category of control schemes for the DP-MMC model requires modifications to the switching function to include details that come from secondary control signals. This approach is well-explained in [97].

3. Balancing controller, which ensures that all SM voltages are kept approximately equal and around the nominal value. Enforcing a balancing control scheme is of no use in connection to the DP-MMC model as it is modeled under the assumption that all the submodule voltages are balanced and equal to $V_{\text{dc}}/N_{\text{arm}}$.

In the developed co-simulation platform the phase locked loop (PLL) and converter controllers are implemented in the PSCAD/EMTDC (EMT solver) using build-in EMT control blocks and the time-domain details of controllers are combined with dynamic phasors to obtain accurate control and dynamic results. This approach enables not only access to non-linear models in an EMT solver but also inclusion of manufacturers' proprietary converter control models that may be black-boxed and will be impossible to replicate in the dynamic phasor environment. Since the primary intention of this paper is to embed the DP-MMC in the external system for large time-step simulation, only the controllers at the system level are considered. The controller interfacing scheme to the MMC is shown in Figure 6.16.

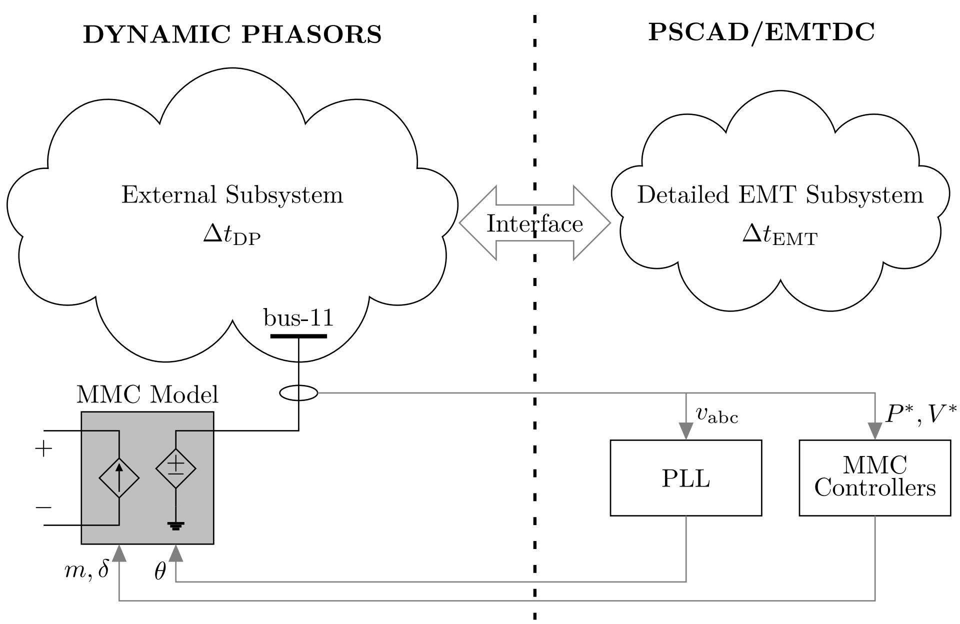

Figure 6.16: Block diagram of the MMC control scheme and controller interface.

The real power output of the MMC and the voltage magnitude of the bus-11 are controlled via direct controllers. Feedbacks taken from the dynamic phasor side are fed to controllers at each time-step after transforming them to time-domain. Instantaneous control parameters that are generated by the control system based on those feedback are communicated back to the DP solver for use in the MMC solution. The MMC output is synchronized with the ac network by tracking the phase angle, θ, via a PLL locked onto bus 3 (point of common coupling (PCC) of the MMC) of the twelve-bus network. Note that the solutions of DP solver and the EMT solver are obtained simultaneously (parallel solution); therefore, small time-delays may appear in controlled parameters when communicating values back and forth. This is a trivial matter as those delays are negligible compared to time-constants associated with system-level controllers.

6.3.3 Simulation Results

The controller parameters of the MMC are set to deliver 200 MW of real power and to maintain bus-3 (PCC) voltage at 0.99 pu. The EMT subsystem is simulated with a small time-step of $\Delta t_{\mathrm{EMT}} = 20\mu\mathrm{s}$ while the external system, including the MMC, is simulated using $\Delta t_{\mathrm{DP}} = 200\mu\mathrm{s}$ time-step. The entire system is also simulated without partitioning in PSCAD/EMTDC with a time-step of $20\mu s$ and its results are used for benchmarking the co-simulation results. In the benchmark case, the detailed equivalent MMC model [91] is used to feed bus-11.

MMC Response During a Disturbance

As the first scenario, a solid three-phase to ground fault is applied at $t = 10$ s to bus-2 to generate transients in the EMT subsystem; the fault is cleared after six cycles (100 ms). The comparative waveforms for network and MMC dynamics during the disturbance are given in Figure 6.17. In following figures, the co-simulator MMC waveforms, which are in fact complex phasor values, are transformed back to time-domain before being compared.

The fault at bus-2 within the EMT subsystem does not have a major impact on the MMC's operation in the external system as the MMC is located far away from the fault location. It is seen that the waveforms of the external subsystem such as inverter's bus voltage and current are closely conforming with the benchmark results. The underlying reason for any mismatch is the

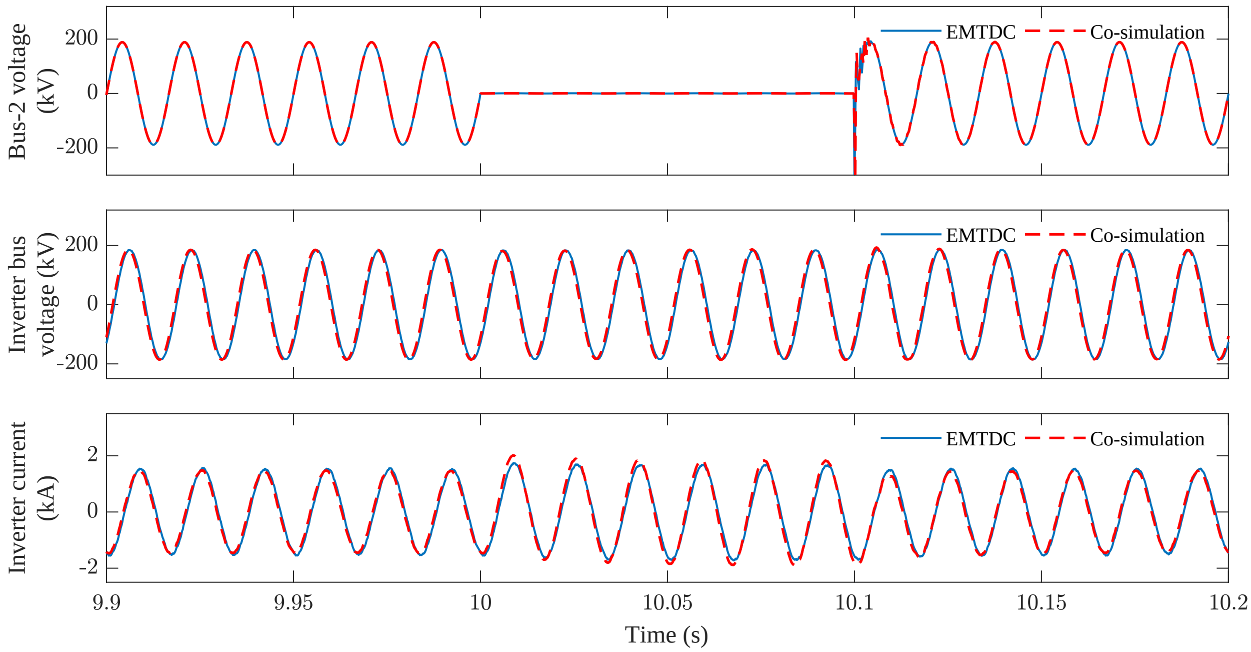

Figure 6.17: Network and MMC response to a three-phase fault applied at bus-2.

ignored harmonic details and the averaging nature of dynamic phasor waveforms of the MMC output. However, these errors are very small and imperceptible in large network simulations.

A distinct feature of the implemented DP-MMC model is that it can accurately replicates behaviours of internal MMC waveforms such as arm currents and average capacitor voltages. Figure 6.18 illustrates those waveforms during the three-phase fault applied in the EMT subsystem.

In the DP-MMC model, the internal dynamics are modeled considering only the predominant harmonics of each waveform. The comparison in Figure 6.18 shows that it is a reasonable assumption as the DP-MMC model is capable of delivering great accuracy compared to the benchmark PSCAD/EMTDC waveforms.

MMC Control Response

Figure 6.19 shows the response of the MMC to a step change in the real power order from 200 MW to 250 MW at $t = 7.5$ s. Similar dynamic responses are observed in both the DP-MMC

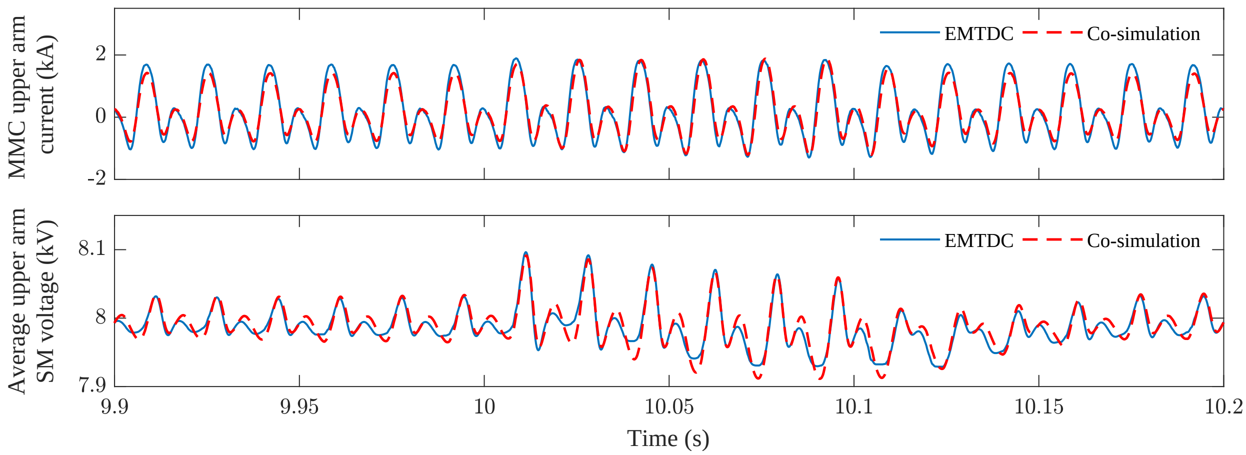

Figure 6.18: Internal response of MMC to a three-phase fault applied at bus-2.

model (co-simulation) and the PSCAD/EMTDC; slowly varying transients in the external system initiated by the power order change are well replicated by the DP-MMC and the proposed control strategy. Some minor oscillations are ignored in the DP simulation due to the large time-step used and the averaged nature of MMC waveforms.

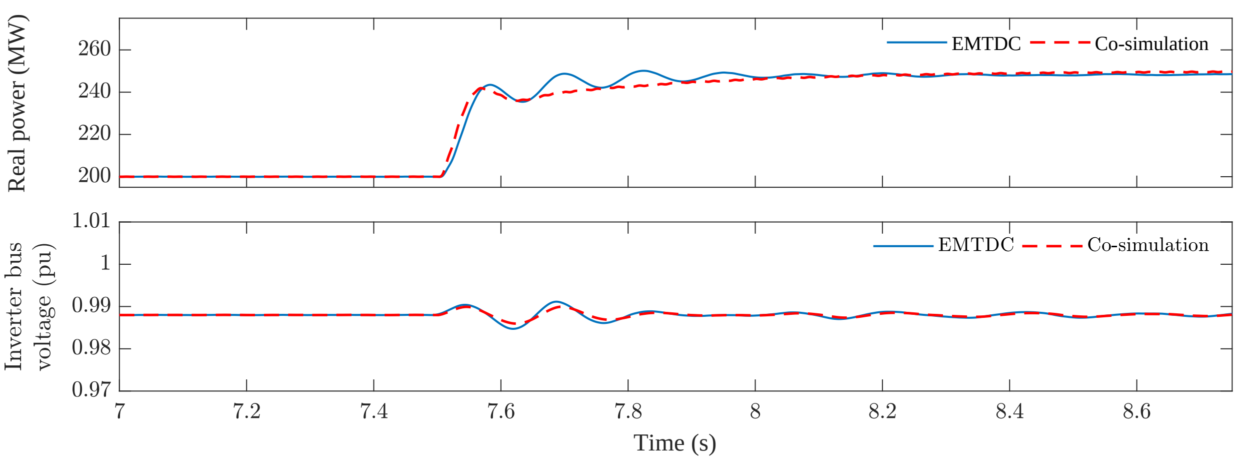

Figure 6.19: MMC's response to a step change in the real power reference.

The controller's response is further validated by applying a step change to the voltage controller reference. Initially, the system is set to maintain the inverter's bus voltage at 0.99 pu and then the reference is changed to 0.95 at $t = 7.5$ s. As illustrated in Figure 6.20, both the co-simulation and the benchmark simulation results predict similar transient response.

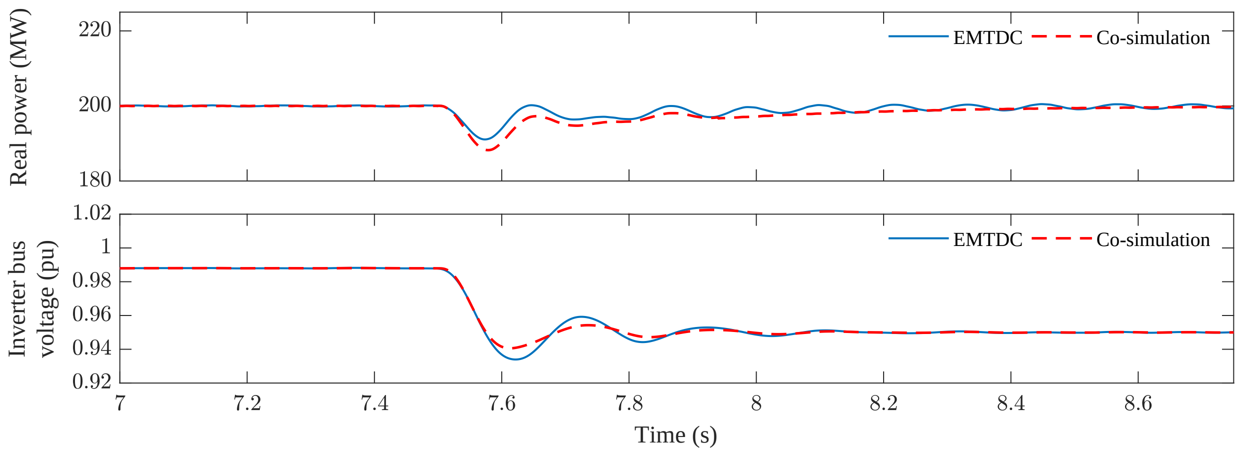

Figure 6.20: MMC's response to a step change in the voltage reference.

Computational Gain Comparison

The time taken to simulate the network for 20 s in a standalone EMT simulator (PSCAD/EMTDC) and the co-simulator is compared. The comparison results are listed in Table 6.6.

Table 6.6: Co-simulation time comparison for MMC embedded 12-bus system

	Time-steps (μs)		Simulation time (s)
	Δt_{EMT}	Δt_{DP}	
Benchmark simulation	20	N/A	167
DP-EMT Co-simulation with DP-MMC Model	20	40	57
	20	200	22

A marked gain of nearly three times can be observed from the co-simulator with DP-MMC model even for a time-step ratio of two; dramatically increases up to around eight when the ratio is increased to ten. A larger speed-up factor can be expected (i) when the number of submodules per MMC's arm increases, (ii) when the size of the overall network increases, and (iii) when a larger time-step ratio is used given no restriction is imposed by the co-simulator interface.

6.4 Summary of Contributions and Conclusions

In this chapter, an advanced adaptive multi-rate co-simulation platform was developed for accurate and accelerated simulation of transients in large power systems using the BFAST and EMT solvers. The BFAST-EMT co-simulator enables parallel processing and the ability to use large time-step ratios between the two solvers when the system is in normal operation adds considerable computational advantage. Its ability to operate in three different modes is a major benefit compared to standalone solvers and other co-simulators. Implementation of the co-simulator using a commercial-grade EMT solver interfaced with the BFAST algorithm readily enables usage of standard library components as well as custom models developed for sophisticated components such as converters.

The algorithm is demonstrated by co-simulating a 12-bus system and a 118-bus system. Simulation results were observed to be giving essentially identical results for both the EMT and the BFAST systems compared to those of standalone PSCAD/EMTDC simulation. The example systems studied showed that for larger networks wherein the EMT subsystem is relatively small, large computational gains are to be expected from the developed co-simulator.

This chapter also proposed a mechanism to model and test MMCs in the context of the external subsystem of the co-simulator. A novel control mechanism was also proposed to control the MMC model using control blocks available in the EMT solver. This permits to test any given MMC control scheme, which may be difficult to implement in the context of the dynamic phasor environment. Simulations demonstrated that this approach can provide a large computational gain while maintaining a sufficient level of accuracy. Therefore, it is expected that the proposed approach may be useful in accelerated simulation of large networks consisting of many MMCs.

Chapter 7

Co-simulation of Power System Transients Using Multi-Domain Solvers

In transient simulation of large power systems, it is often noted that disturbances that occur at a given location generate dissimilar levels of dynamic response in different parts of the network. The vicinity of the disturbance often experiences a great amount of fast electromagnetic transients while the rest of the network experiences far less or no noticeable dynamics depending on the distance from the disturbance location. On top of that, there may be areas of the network that constantly undergo fast dynamics, such as the ones generated by power electronic systems. Therefore, it is desirable to develop methods for multi-domain simulation combining the features of EMT simulation with those of other solvers such as dynamic phasor-based algorithms. Additionally, at far enough vicinities a conventional phasor solution is obtained in which fast network transients are essentially non-existing.

This chapter provides insight and guidelines to a novel multi-domain co-simulation framework that can be used for accurate and accelerated simulation of large power systems. The algorithm combines an EMT solver, the proposed BFAST solver with its different modes, and a TS solver to model and simulate different parts of the network by interfacing them to one another.

7.1 Multi-Solver Co-Simulation Framework

7.1.1 Co-Simulation Subsystems

In the proposed multi-domain co-simulator, EMT models provide the highest level of accuracy; thus, the study area of interest is implemented in an EMT simulator. The EMT simulator is chosen to be the core of the entire simulation. The rest of the network is segmented based on the expected dynamic behaviour, connected devices, the level of detail required for the study, and the distance from the areas where fast transients occur. Therefore, the subsystems of the multi-domain co-simulator are defined as follows.

1. **EMT Subsystem 1:** This is the area of the network that undergoes continuous transients. This area may include HVDC systems or other high frequency devices; thus, this subsystem needs to be solved using a very small simulation time-step.

2. **EMT Subsystem 2:** This area of the network is subjected to continuous or intermittent fast transients; however, they are not as severe as in the EMT subsystem 1. Therefore, this subsystem is simulated using a time-step larger than the EMT subsystem 1.

3. **BFAST Subsystem:** In this subsystem, fast dynamics occur intermittently. For example, a fault in one of the EMT subsystems may affect adjacent areas for a short period, and for the rest of the time this subsystem operates in steady-state or with relatively slow dynamics. Therefore, this subsystem is simulated with the BFAST method, changing its simulation method and the solution time-step depending on whether fast transients are present or not.

4. **DP Subsystem:** In this subsystem of the network, transients are slower than those observed in EMT subsystems. Disturbances applied at the EMT subsystems have low dynamic impact on this area. Therefore it is simulated with dynamic phasors using a large

simulation time-step for the entire duration. DP subsystem(s) can be used as a buffer region between EMT and TS solvers.

5. **TS Subsystem:** Areas of the network that operate in steady-state or near steady-state throughout the simulation are assigned to this subsystem. Typically, these subsystems fall electrically far from EMT subsystems where fast transients take place. For these subsystems, only the positive sequence solution is obtained using conventional phasor models. Therefore, any unbalanced condition is essentially ignored and a large simulation time-step is used.

Note that for a given simulation, the network may consist of no or more than one subsystem of a particular type. The selection is depends on such factors as the size of the network, presence of high frequency and non-linear devices, expected dynamic details of various sub-regions of the network, and the requirement of simulation accuracy and speed.

7.1.2 Multiple Interfacing and Interactions

In the proposed multi-domain simulator, more than two solvers are interfaced, each with distinctive numerical features and algorithms. Therefore, multiple interfacing schemes are necessary. Interfacing schemes can be classified as *core-type*, *chain-type*, and *loop-type* [48]. In a core-type interface, all simulators are interfaced to a common simulator, which act as the center of the entire simulation. In the chain-type interface, all solvers are connected in a chain. A loop interface is special type of a chain-type interface, in which the simulators form a loop.

The proposed multi-domain co-simulator uses a combination of core- and chain-type interfaces as illustrated in Figure 7.1. The EMT subsystems are implemented inside PSCAD/EMTDC software; therefore, it serves as the core of the overall simulation. Any solver that needs to be interfaced to the EMT simulator is connected to PSCAD/EMTDC via an external interface as users do not have access to the software's internal algorithm.

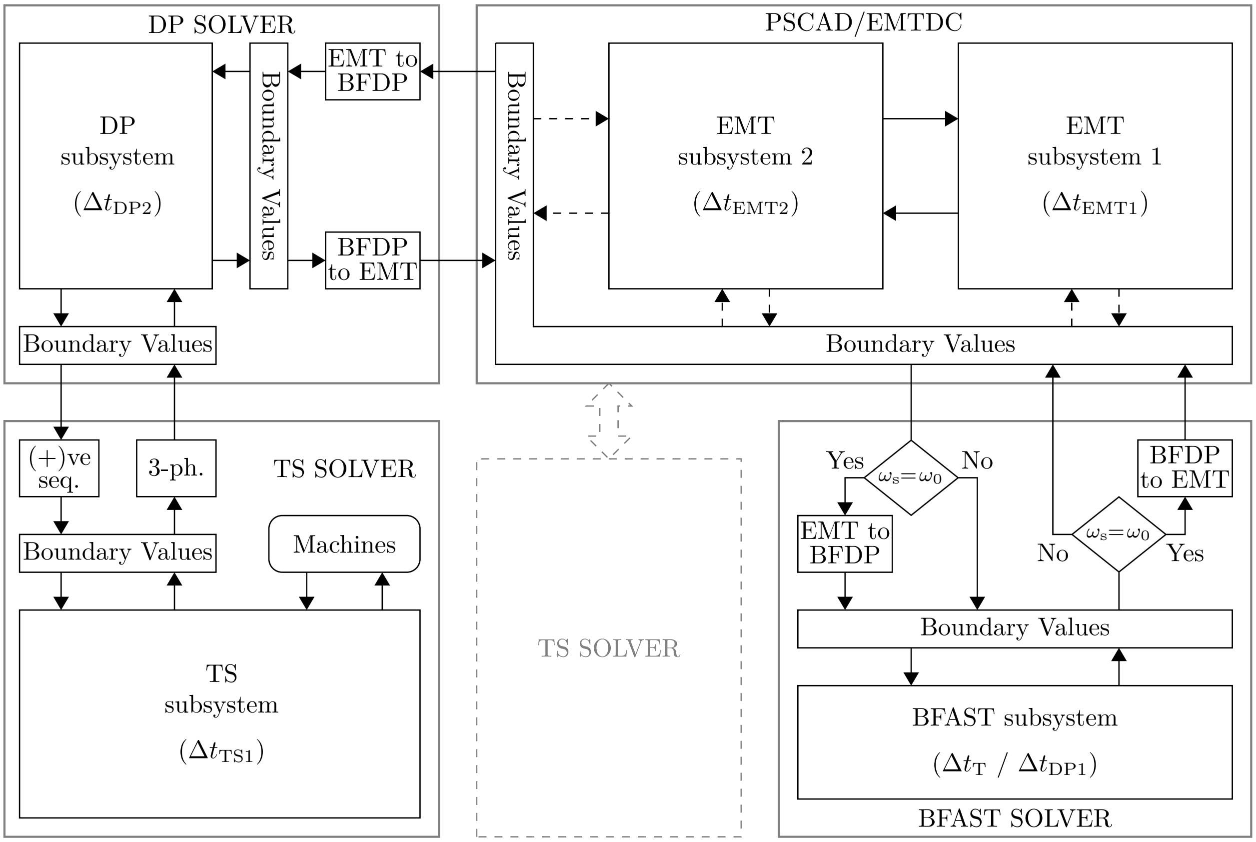

Figure 7.1: Multi-domain co-simulation architecture

Note that the composition of subsystems changes from one network to another. Therefore, the interface configuration illustrated in Figure 7.1 is only one possibility and not a universal arrangement. Different interface formations can be used depending on the dynamics of the network. The following is a description of the interactions and interfaces of the multi-domain configuration presented in Figure 7.1.

EMT-EMT Interface and Interaction

In the proposed multi-domain simulator, all EMT subsystems are implemented in PSCAD/EMTDC software. PSCAD/EMTDC allows to simulate different subsystems of a single network simultaneously as dependent projects and with multiple time-steps. Interaction between these subsystems are established via the electrical network interface (ENI) [81] in which boundaries of each subsystem are defined using transmission lines. The segmentation of EMT subsystems in the proposed multi-domain framework using ENI is illustrated in Figure 7.2.

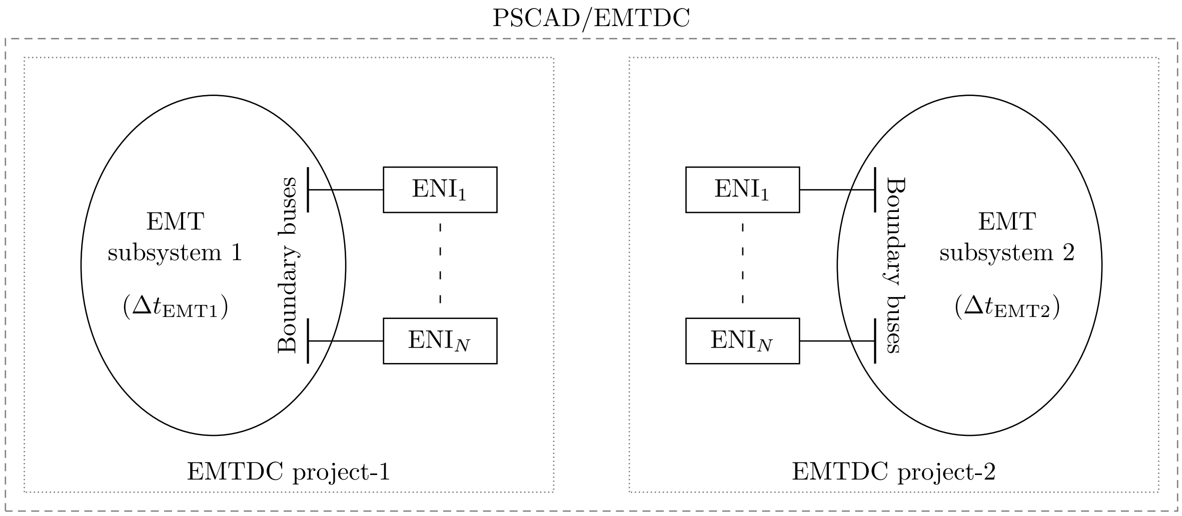

Figure 7.2: EMT-EMT multi-rate interaction using PSCAD/EMTDC electrical network interface

EMT-BFAST Interface and Interaction

The interface between the EMT and BFAST subsystems is formed using the lossless Bergeron's transmission line model, and follows the interaction algorithm explained in section 6.1. The maximum time-step for the BFAST simulation is set based on the wave propagation time of the interface lines.

EMT-DP Interface and Interaction

The EMT-DP co-simulation is based on the mode-2 operation of the proposed BFAST-EMT co-simulator in Chapter 6. Therefore, the EMT and DP subsystems are also divided at transmission lines, and follow the same interaction procedure.

DP-TS Interface and Interaction

The segmentation of the transient stability subsystem from the dynamic phasor subsystem permits to solve the regions of the network that are always operating in steady-state using a large simulation time-step of the order of a few milliseconds and only with positive sequence components. Therefore, a sophisticated interface that does not impose limitations on the transient stability simulation time-step is a necessity between the DP and TS subsystems.

In the proposed multi-domain framework, the interface between DP and TS subsystems is established using the MATE method, whose mathematical foundation is described in section 2.3.3. Note that the MATE interface is an internal mechanism, which needs the knowledge of admittance matrices of both subsystem; thus, if the user does not have access to the internal algorithms, an external interface is required.

In the DP-TS MATE algorithm, the admittance matrices and the Thévenin impedances of each subsystem and the linking branch impedance matrix are calculated before the start of the simulation to ensure a minimum amount of run-time computation. Consider the case illustrated in Figure 7.3, for which the simulation time-step ratio between TS and DP solvers is assumed to be N_{T} and the solutions at $t = t_{k-1}$ corresponding to both subsystems are obtained. Then the following algorithm takes place between DP and TS solvers.

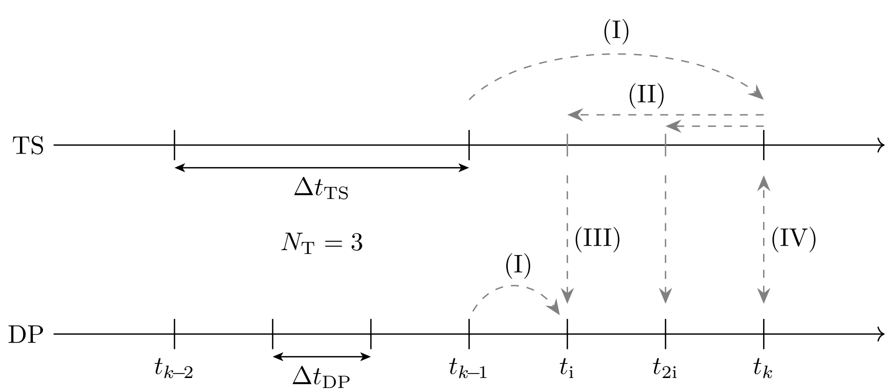

Figure 7.3: TS-DP interaction using MATE technique

(I) Partial solutions of TS subsystem at $t = t_k$ and DP subsystem at $t = t_\mathrm{i}$ are obtained simultaneously by solving them independently.

(II) The transient stability's partial solution is linearly interpolated to intermediate instants corresponding to DP solver's time steps. The interpolated positive sequence solution is transformed to a three-phase one in order to aid the interfacing with the three-phase DP subsystem as $[\vec{\mathrm{V}}, \vec{\mathrm{V}}\mathrm{e}^{-\mathrm{j}2\pi/3}, \vec{\mathrm{V}}\mathrm{e}^{\mathrm{j}2\pi/3}]^\mathrm{T}$.

(III) Using DP subsystem's partial solution at $t = t_\mathrm{i}$ and the interpolated TS subsystems' partial solution (three-phase), the Thévenin equivalent voltages are computed for each subsystem. Then the interface branch current vector, $I_\alpha(t_\mathrm{i})$, is computed. The complete solution for DP subsystem at $t = t_\mathrm{i}$ is obtained by injecting $I_\alpha(t_\mathrm{i})$ to interface nodes of the subsystem and solving it independently. The same process is repeated at all other intermediate instances of the DP subsystem.

(IV) At $t = t_k$, the interface branch current vector is calculated in the same manner. However, contrary to intermediate points, interface branch currents are injected to the both DP and TS subsystems, and complete solutions of both are acquired simultaneously.

In the preceding algorithm, once the partial solution at $t = t_k$ is obtained for the TS subsystem, barring minor computations such as interpolations, it essentially stays idle until the DP subsystem is solved for all intermediate points. Once the DP solver reaches $t = t_k$, both subsystems are solved simultaneously to find the final solution for the particular instance. Therefore, it is accurate to say that the DP-TS interaction algorithm is partially parallel when $N_\mathrm{T} > 1$. Nonetheless, it does not insert any restriction to the TS solver's simulation time-step; thus, an appropriately large step-size can be used to solve the regions consistently operating in steady-state.

EMT-TS Interface and Interaction

The interface between the EMT simulator (PSCAD/EMTDC) and a TS solver [98] is a well-established one at an industrial level. In a situation where an EMT subsystem should be directly connected to a transient stability subsystem in the proposed multi-domain co-simulator, such an interface [45] may be readily used. However, this scenario is not considered in the following simulation examples in this chapter.

7.2 Simulations and Results

7.2.1 Test System and Simulation Setup

The IEEE 118-bus system [90] with some minor modifications to the network is simulated in the context of the proposed multi-domain co-simulation framework. The system is divided into five subsystems and assigned to different solvers as given in Table 7.1. The data pertaining to the whole IEEE 118 bus system are given in Appendix E.2.

Table 7.1: Subsystem allocation of 118-bus test system for multi-domain co-simulation

Subsystem Name	Composition	Simulation Time-Step
EMT subsystem 1	Buses 59-67	$\Delta t_{\mathrm{EMT1}} = 10\,\mu$s
EMT subsystem 2	Buses 24, 33-58, 68-75, 116	$\Delta t_{\mathrm{EMT2}} = 50\,\mu$s
BFAST subsystem	Buses 76-112, 118	$\Delta t_{\mathrm{T}} = 50\,\mu$s, $\Delta t_{\mathrm{DP}} = 200\,\mu$s
DP subsystem	Buses 13-23, 25-32, 113-115	$\Delta t_{\mathrm{DP}} = 250\,\mu$s
TS subsystem	Buses 1-12, 117	$\Delta t_{\mathrm{TS}} = 5$ ms

In the EMT subsystem 1, the generator connected to bus 62 is replaced by an MMC-HVDC system as shown in Figure 7.4, and it is controlled to maintain the same active power and bus voltage as the generator. The converter has the same parameters as given in Table 6.5. The MMC and network buses in close vicinity of the MMC are solved with a small 10 μs time-step. The area around this subsystem is included in EMT subsystem 2, and simulated using a comparably larger

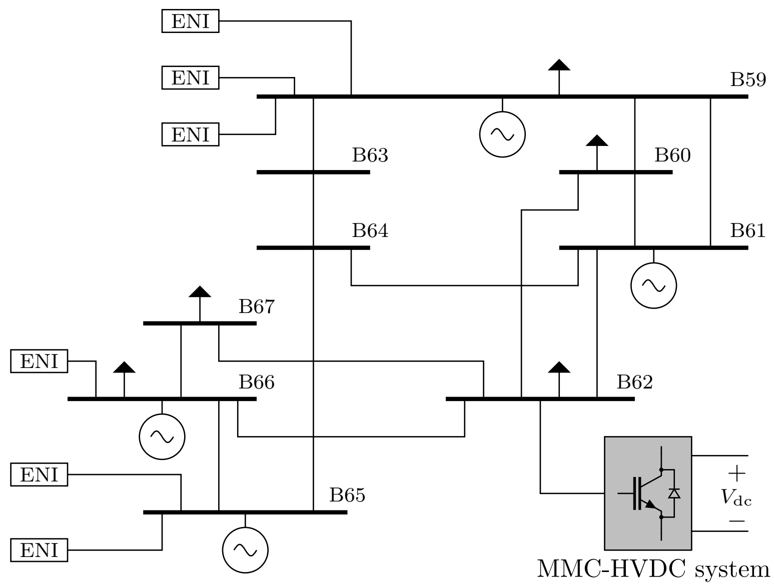

Figure 7.4: EMT subsystem 1 of 118-bus test system

50 μs time-step. This subsystem is chosen as the interested study area of the simulation, i.e., the area wherein the disturbances are applied. The rest of the network is segmented as follows: the presumed regions that can be highly affected by the EMT subsystem 2 disturbances in the BFAST subsystem, moderately affected area in the DP subsystem, and undisturbed area in the TS subsystem. The simulation time-step(s) of each solver/subsystem is also listed in Table 7.1.

The DP and BFAST subsystems are developed as two external independent simulation projects, which are programmed using C++. Run-time communication between those projects and PSCAD/EMTDC is established via the built-in *cosimulation* component. The TS subsystem is also separately programmed and linked to the dynamic phasor project using the MATE method. The details of transmission lines, which are used to form interfaces between subsystems, are listed in Table 7.2. For the entire system, all generators and transformers are modeled as voltage sources and inductors, respectively. Therefore, the test system may not exactly represent the aspects of a real world power system; however, it altogether serves the purpose of multi-domain simulation framework proposed in this thesis.

Table 7.2: Interface line details of partitioned 118-bus network

Subsystem 1	Subsystem 2	Interface Line	Line Data
EMT subsystem 1	EMT subsystem 2	line 38-65	R=4.7663 Ω; L=0.1384 H; C=5.2450 μF
		line 49-66	R=9.5220 Ω; L=0.1290 H; C=0.1244 μF
		line 54-59	R=26.6087 Ω; L=0.3218 H; C=0.2999 μF
		line 55-59	R=25.0693 Ω; L=0.3028 H; C=0.2831 μF
		line 56-59	R=42.4787 Ω; L=0.3354 H; C=0.2688 μF
		line 65-68	R=0.7300 Ω; L=0.0225 H; C=3.1991 μF
EMT subsystem 2	BFAST subsystem	line 69-77	Z_{C}=522 Ω; τ=0.0002 s
		line 75-77	Z_{C}=1060 Ω; τ=0.0002 s
		line 68-81	Z_{C}=592 Ω; τ=0.0002 s
		line 75-118	Z_{C}=1060 Ω; τ=0.0002 s
EMT subsystem 2	DP subsystem	line 15-33	Z_{C}=1044 Ω; τ=0.00025 s
		line 19-34	Z_{C}=1046 Ω; τ=0.00025 s
		line 23-24	Z_{C}=526 Ω; τ=0.00025 s
		line 30-38	Z_{C}=598 Ω; τ=0.00025 s
DP subsystem	TS subsystem	line 8-30	R=2.2800 Ω; L=0.0707 H; C=2.5774 μF
		line 11-13	R=11.7703 Ω; L=0.1026 H; C=0.0941 μF
		line 12-14	R=11.3735 Ω; L=0.0992 H; C=0.0911 μF
		line 12-16	R=11.2148 Ω; L=0.1170 H; C=0.1073 μF

R=resistance; L=inductance; C=capacitance; Z_{C}= surge impedance; τ=wave propagation time

7.2.2 Simulation Results

A solid line-to-ground unbalanced fault is applied at bus 47 at $t = 5$ s and cleared after 0.2 s. The following provides the result of the simulation as observed from each subsystem. To validate the accuracy of the co-simulated results, they are compared with the waveforms obtained from a single-rate simulation of the entire 118-bus system in PSCAD/EMTDC with a 10-μs time-step.

Figure 7.5 contains the waveforms of the study area, i.e., EMT subsystem 2, of the 118 bus network. As it can be observed, dynamic results of the multi-domain solver are identical to the those of PSCAD/EMTDC. Solving the network in different domains and using different time-steps has no perceptible implications on the accuracy of fault waveforms.

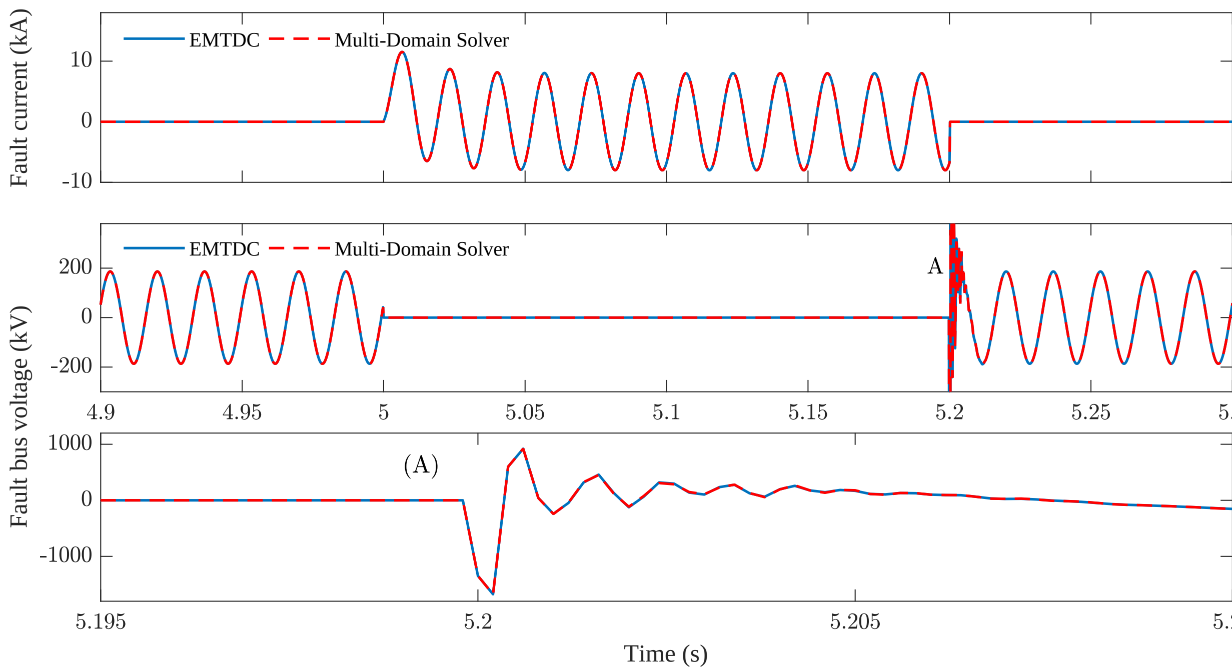

Figure 7.5: Waveforms from EMT subsystem 2

Figure 7.6 shows waveforms of the EMT subsystem, which includes the MMC-HVDC system. The MMC's output waveforms exhibit a slight amount of harmonics. The fault applied at bus 47 seemingly has no major impact on the operation of the MMC. Nevertheless, this subsystems has to be simulated with a small time-step considering the number of switching events taking place in the MMC. The MMC's output waveforms and control variables simulated by the multi-domain solver agree with the benchmark simulation results.

The current through the interface line 69-77 and the corresponding boundary bus voltages as simulated by the BFAST solver are shown in Figure 7.7. It changes its solution method from dynamic phasor to EMT just before the transient begins as they are pre-specified, and changes back to dynamic phasor solution after detecting the end of the transient. As such, details of the transient caused by the fault are accurately replicated by the solver. A small oscillation is visible in the line current waveform just after it is changed to the dynamic phasor solution, which is due

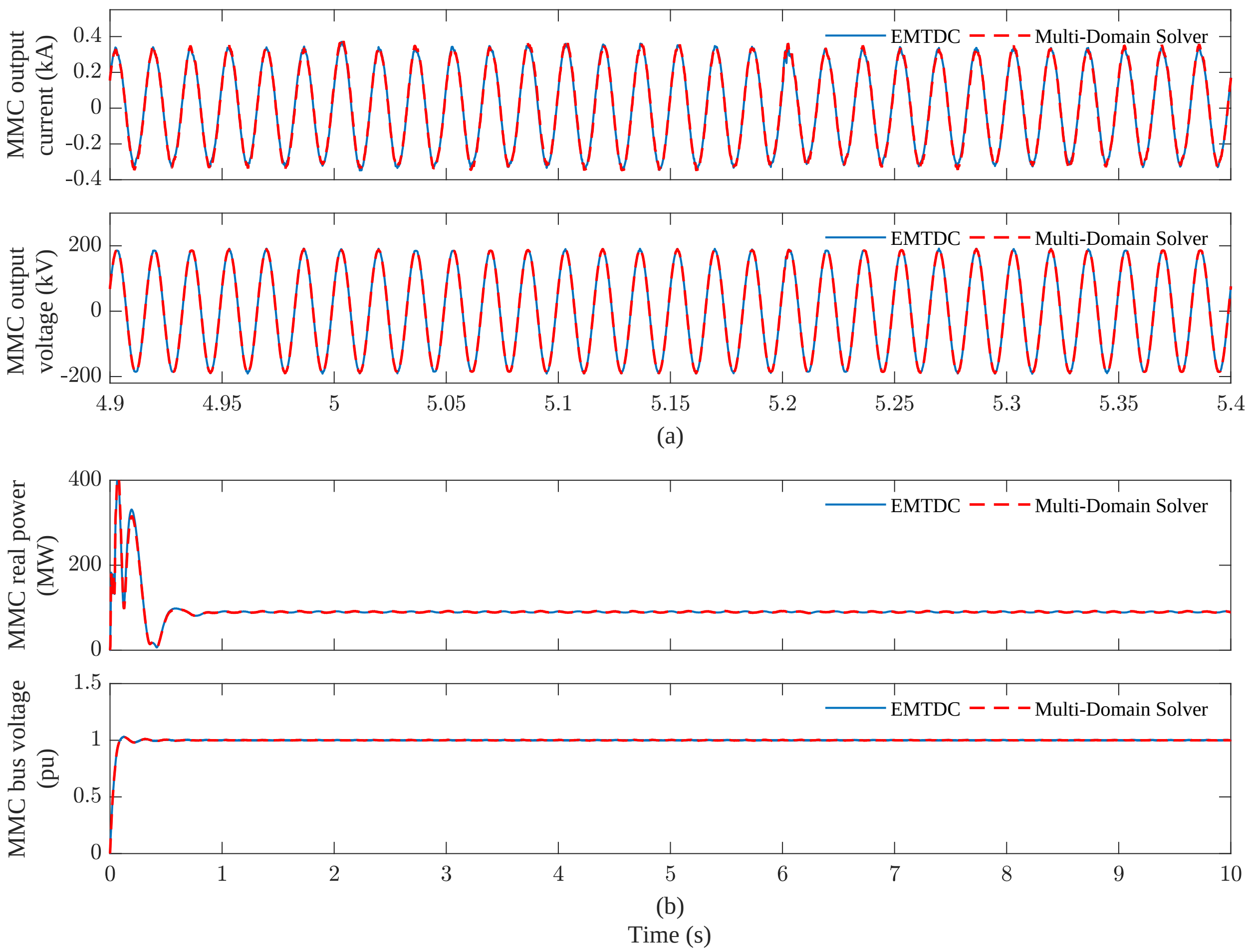

Figure 7.6: Waveforms from EMT subsystem 1; (a) MMC output waveforms, (b) MMC control variables

to a small dc offset in the waveform. The variation of the simulation time-step of the BFAST subsystem during the simulation is given in Figure 7.8.

Figure 7.9 shows the current of the transmission line 19-34, which forms one of DP-EMT interfaces, and the voltage of the corresponding dynamic phasor side interface bus. As expected, no fast transients are conveyed to this subsystem. A small level of dynamics can be visible in the current waveform during $t = 5 - 5.2$ s due to the fault and the fault clearing transients of the EMT subsystem 2. The harmonic-rich BFDPs capture this transient and follow the envelope of the waveform accurately. Recall that the BFDPs combine all frequency components of a waveform and shift them to a lower frequency band.

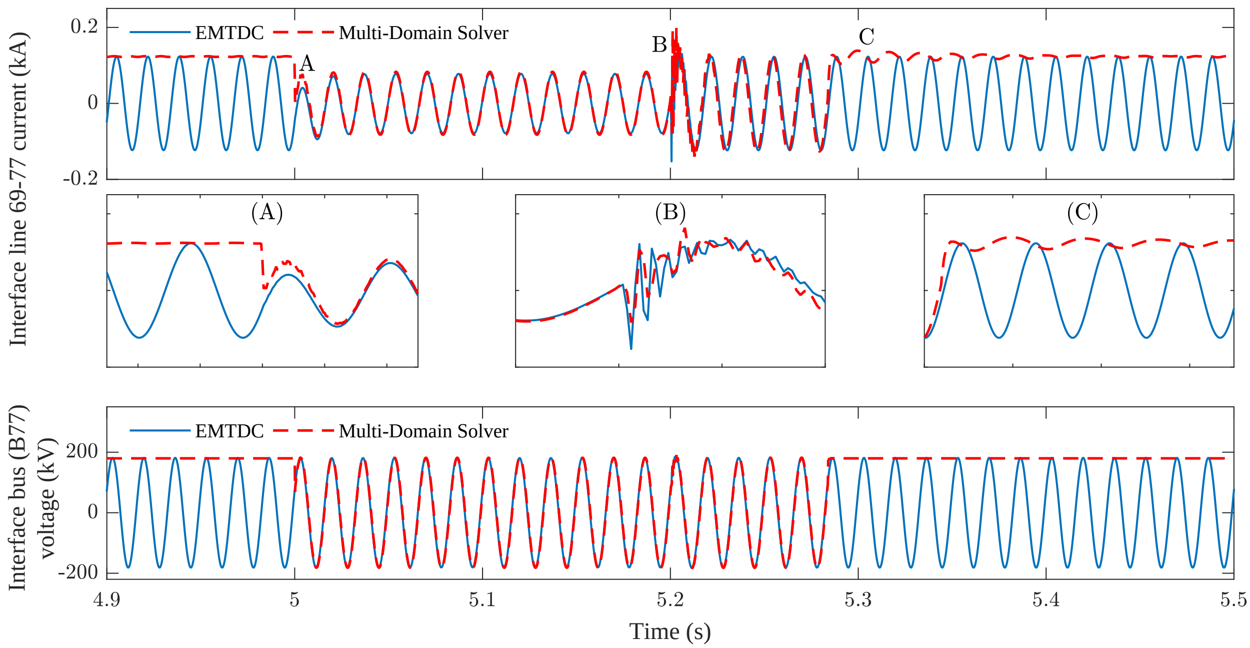

Figure 7.7: Waveforms from the BFAST subsystem

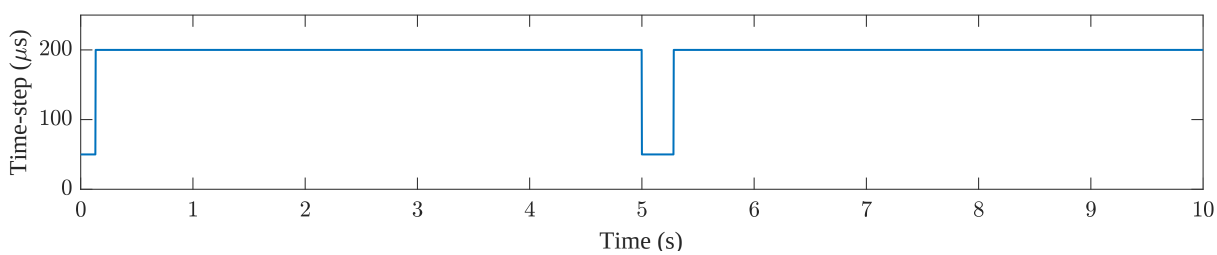

Figure 7.8: Simulation time-step variation of the BFAST subsystem

Several waveforms associated with the TS subsystem are given in Figure 7.10. The solution in the TS solver is based on steady-state phasors. As such, and for comparison purposes, benchmark waveforms are also given using per unit values. As it can be seen from the figure, the TS solver uses a large step size (5 ms) and provides the same accuracy level as standalone EMT simulation since the subsystem is operating in steady-state. Inclusion of rotating plants may bring electromechanical dynamics to the subsystem; however, they are unlikely to cause any complication to the simulation or the time-step as those dynamics are much slower than the power system frequency.

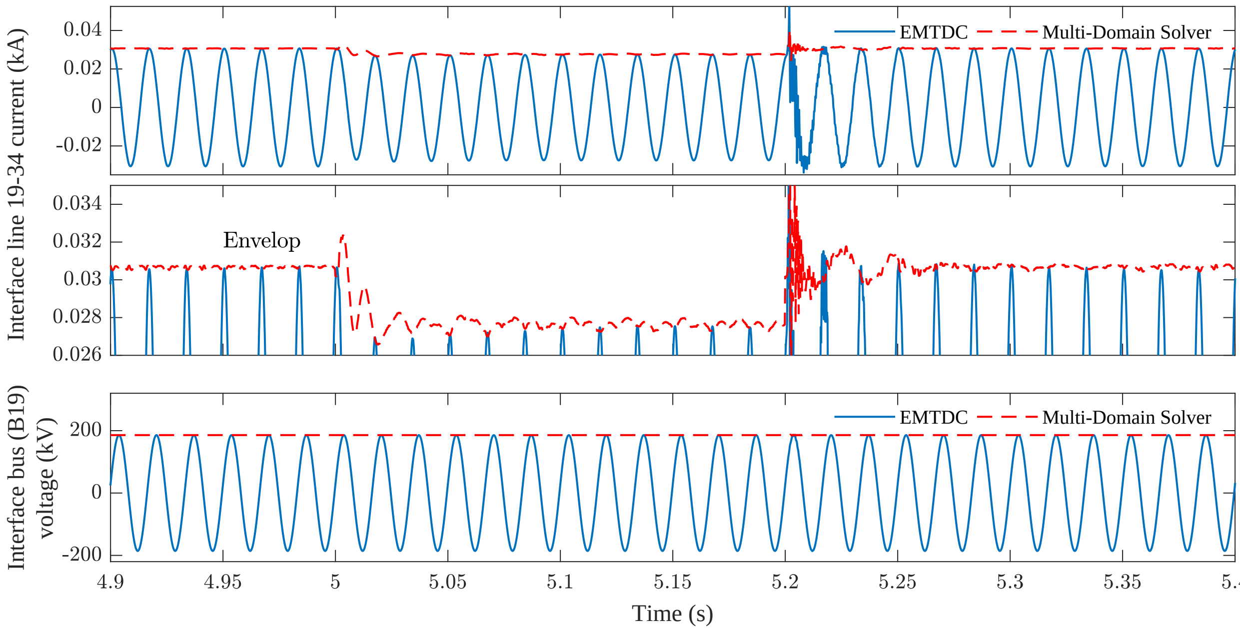

Figure 7.9: Waveforms from the DP subsystem

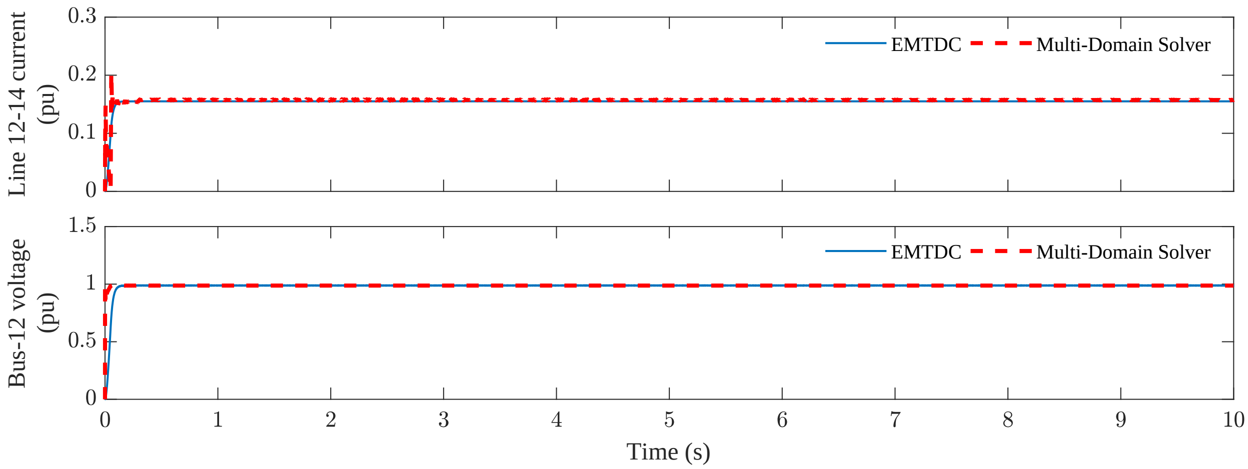

Figure 7.10: Waveforms from the TS subsystem

7.2.3 Computational Gain

Fast acting devices such as MMCs force standalone EMT simulators to solve the entire network employing a very small time-step. However, the proposed multi-domain co-simulation framework greatly enhances the simulation speed by simulating different segments with larger steps, using computationally efficient modeling techniques, and allowing simultaneous solutions of subsystems. For example, in the 118-bus example, the TS subsystem uses a 5-ms time-step for its phasor solution, which is 500 times larger than the one used for the standalone EMT solver.

For the 118-bus example, the single-rate EMT simulation (PSCAD/EMTDC) took 1314 s to run a 10-s long simulation. Meanwhile, the multi-domain solver was able to perform the same simulation in 112 s. The computational advantage provided by the multi-domain solver is clearly reflected through this measured simulation time. Note that this example is relatively small in size; therefore, it can be anticipated that the proposed multi-domain co-simulation framework will allow to perform simulations of very large electric networks with greatly reduced simulation time compared to standalone EMT simulators.

7.3 Summary of Contributions and Conclusions

This chapter proposed a novel multi-domain co-simulation framework combining a EMT solver, the BFAST solver with its different modes, and a TS solver. The solver handles several types of subsystems of a given network based upon the connected devices, required level of accuracy of dynamics details, and distances from location of disturbances; they are then assigned to respective solvers to simulate with an appropriately large time-step. Multiple interfacing mechanisms and interaction algorithms were explained. Simulations carried out using a 118-bus network, which included a MMC-HVDC system, in the context of the proposed multi-domain framework manifested great accuracy and promising improvements to the simulation speed.

Chapter 8

Contributions, Conclusions, and Future Work

8.1 Contributions

This research developed methods, models, and algorithms for the next generation of power system transients co-simulation engines. The following provides a summary of major contributions made throughout this work.

1. The underlying theory of several dynamic phasor extraction methods was presented. Through novel, in-depth analysis the merits and drawbacks of each method were assessed and demonstrated based on its ability to replicate wide range of power system conditions.
2. Criteria for numerically stable solution of interfaced co-simulation were derived based upon time delay of interaction, sequence of the solution, and physical structure of the network. A method to improve the stability of some systems were presented.
3. A novel dynamic phasor-based simulator for frequency-adaptive simulation of transient (BFAST solver) was developed and validated. A novel changeover algorithm was implemented to ensure a smooth and accurate transition between solution techniques.

4. A library of system components and interfacing mechanisms to the proposed BFAST solver was implemented. These include models of synchronous machines, transformers, transmission lines, and a modular multilevel converter.

5. A novel multi-rate co-simulation algorithm combining the BFAST simulator with an industrial EMT simulator was developed and validated.

6. A novel method to model and test modular multilevel converters and their controls in the context of the external subsystem of a co-simulation environment was implemented.

7. A multi-domain co-simulation platform combining the models of BFAST, DP, TS, and EMT simulators was implemented and validated. Special guidelines for subsystem partitioning and multiple interfacing were established.

8. The following publications are made based on the contribution of this thesis.

   - J. Rupasinghe, S. Filizadeh, A.M. Gole, and K. Strunz, "Multi-rate co-simulation of power system transients using dynamic phasor and EMT solvers," *The Journal of Engineering*, vol. 2020, no. 10, pp. 854–862, 2020.
   - J. Rupasinghe, S. Filizadeh, and D. Muthumuni, "A method for modeling and testing modular multilevel converters and their controls in large power system simulation studies," in *2020 CIGRE Canada Conference & Expo*, pp. 1–9, 2020.
   - J. Rupasinghe, S. Filizadeh, and D. Muthumuni, "A co-simulation platform for modeling and testing modular multilevel converters and their controls in large networks," in *IEEE Workshop on Control and Modeling for Power Electronics (COMPEL 2020)*, Denmark, 2020.
   - J. Rupasinghe, S. Filizadeh, and K. Strunz, "Assessment of dynamic phasor extraction methods for power system co-simulation applications," *Electric Power Systems Research*, vol. 197, 2021.

- J. Rupasinghe, S. Filizadeh, and D. Muthumuni, “A multi-solver framework for co-simulation of transients in modern power systems,” *IEEE Open Access Journal of Power and Energy*, submitted for publication.

8.2 Conclusions

- The requirement of a trade-off between accuracy and speed of transient simulations of modern power system has spurred development of hybrid algorithms to co-simulate electric networks using multiple solvers. In such an implementation, there are several important aspects that need investigations such as interfacing topology, interaction, stability, domain conversion, and control over speed and accuracy. Besides, the inability of the traditional phasor-based approach to model rapid transients encourages development of methods such as dynamic phasor modeling and frequency-adaptive simulations of transients. These methods have their own merits; however, sometimes face difficulties when performing standalone simulations.

- Domain transformation of signals is one of the main requirements in co-simulations. Several techniques are used to extract dynamic phasors from time-domain instantaneous signals in DP-EMT co-simulation applications, namely, fast time-varying phasors, generalized averaging, shifted-frequency analysis, and a recent concept referred to as base-frequency dynamic phasors. They have different capabilities when representing dc offsets, harmonics, imbalances, electromechanical oscillations, and fast transients in waveforms. These merits and limitations need to be considered carefully before selecting a appropriate extraction method for a given application.

- The stability analysis carried out in this thesis identified that the time delay introduced by the partitioning process causes inaccuracies and instabilities if the network does not satisfy certain conditions. For a resistive network, this condition depends only on the conductances of the network. However, in the presence of inductors and capacitors, stability criteria also depend on the size of the time-step. Moreover, the interaction delay makes complications in history terms of inductors' and capacitors' difference equations. As such, a resistive network can be made stable by supporting the interface, but doing so is much more challenging in RLC networks.

- The novel BFAST simulator combines the benefits of harmonic-rich, base-frequency dynamic phasors and frequency-adaptive simulation of transients. By developing methods to incorporate and interface a large set of system components such as the machine model and the converter model, this thesis was able to develop a professional-quality simulator that can be used to study a large set of modern power systems. Simulations performed using the novel BFAST solver confirmed its capabilities to capture all the details of transients and to accelerate the simulation during normal operation. This simulator is expected to show more efficacy in long simulations.

- The BFAST-EMT co-simulation combines the benefits of dynamic phasors, frequency-adaptive simulation of transients, multi-rate technique, parallel processing, and accuracy of EMT solvers. Its ability to operate in three different modes makes it unique compared to other similar implementations. Simulation results were observed to be giving almost identical results for both the detailed and the external subsystems compared to the standalone EMT simulation. This allows the co-simulator to keep the detailed subsystem as small as possible. Therefore, co-simulation of a power system model by integrating the BFAST solver to an industrial-grade EMT simulator can be concluded as successful.

- In the development of a multi-domain co-simulation platform, it is understood that a mixed-solver environment requires multiple interfacing topologies and interaction methods. This comes with the need for special guidelines and insights as to which locations are most suited for segmentation given the network topology and study purposes. The illustrative simulations performed using the proposed multi-domain co-simulator demonstrated a great deal of accuracy and efficiency; hence, the legitimacy of methods and guideline developed for mixed BFAST-DP-TS-EMT algorithm was confirmed.

It is anticipated that the outcomes of this research will contribute to the development of new co-simulation platforms that, compared with existing EMT simulators, are able to simulate networks of a size at least 1-2 orders of magnitude larger with greatly reduced computational burden.

8.3 Limitations and Recommended Future Work

During the implementations and validation process, several limitations of the proposed methods that need further research and improvements were identified. For a more all-encompassing co-simulation platform, the following can be proposed as potential directions for future work.

1. The transmission line interface used to couple BFAST and EMT simulators greatly restricted the maximum simulation time-step that can be used in the external subsystem. Methods such as MATE relieve such limitation, but may rule out the possibility of interfacing with an industrial EMT solver wherein internal algorithms are inaccessible to the user. Therefore, implementation of an accurate and stable explicit coupling technique(s) needs further investigations. This interface should allow simulators to execute independently without interaction delays and should allow simulation time-steps up to several milliseconds.

2. This research developed criteria and methods to analyse and improve stability in interfaced simulation of resistive networks. However, it was unable to derive a general criteria to examine the stability of networks consisting of inductors and capacitors. Development of such a method will indeed enhance the ability to come up with new procedures to improve the stability of simulations in partitioned environments. Therefore, this topic needs future investigations.

3. The proposed multi solver co-simulator combines BFAST, DP, TS, and EMT solution techniques to simulate a large power system. Although this served the purpose of this thesis, it did not look into the electromechanical behaviours of synchronous machines in the network. Connecting machine models to each solver will create an all-purpose muti-domain simulator. In such an implementation, the TS solver may have to rely on iterations to find its solution.

4. The largest power system co-simulated in this thesis had only 118 network buses. Investigating speed gains of the BFAST-EMT and multi-domain algorithms in large networks consisting tens of thousands nodes is a recommended future work.

5. Both EMT- and TS-type solvers are well established in power system industry. In this research, only the EMT sub-networks were executed in an industrial grade simulator. Therefore, it is recommended to develop industrial-grade multi-domain co-simulator prototypes combining the BFAST simulator with industrial TS and EMT solvers.

Bibliography

[1] D. M. Falcao, E. Kaszkurewicz, and H. L. S. Almeida, "Application of parallel processing techniques to the simulation of power system electromagnetic transients," *IEEE Transactions on Power Systems*, vol. 8, no. 1, pp. 90–96, 1993.

[2] G. D. Irwin, C. Amarasinghe, N. Kroeker, and D. Woodford, "Parallel processing and hybrid simulation for HVDCNSC PSCAD studies," in *10th IET International Conference on AC and DC Power Transmission (ACDC 2012)*, pp. 1–6, 2012.

[3] B. Jayasekara, R. Jayasinghe, D. Muthumuni, M. Pielahn, J. De Silva, and R. Singh, "Parallel EMT simulation of electrical networks on multiple processors," in *2018 IEEE Power and Energy Conference at Illinois (PECI)*, pp. 1–5, 2018.

[4] U. D. Annakkage, N. K. C. Nair, Y. Liang, A. M. Gole, V. Dinavahi, B. Gustavsen, T. Noda, H. Ghasemi, A. Monti, M. Matar, R. Iravani, and J. A. Martinez, "Dynamic system equivalents: A survey of available techniques," *IEEE Transactions on Power Delivery*, vol. 27, no. 1, pp. 411–420, 2012.

[5] A. S. Morched, J. H. Ottevangers, and L. Marti, "Multi-port frequency dependent network equivalents for the EMTP," *IEEE Transactions on Power Delivery*, vol. 8, no. 3, pp. 1402–1412, 1993.

[6] X. Lin, A. M. Gole, and M. Yu, "A wide-band multi-port system equivalent for real-time digital power system simulators," *IEEE Transactions on Power Systems*, vol. 24, no. 1, pp. 237–249, 2009.

[7] S. R. Sanders, J. M. Noworolski, X. Z. Liu, and G. C. Verghese, "Generalized averaging method for power conversion circuits," *IEEE Transactions on Power Electronics*, vol. 6, no. 2, pp. 251–259, 1991.

[8] V. Venkatasubramanian, "Tools for dynamic analysis of the general large power system using time-varying phasors," *International Journal of Electrical Power & Energy Systems*, vol. 16, no. 6, pp. 365 – 376, 1994.

[9] P. Zhang, J. R. Marti, and H. W. Dommel, "Shifted-frequency analysis for EMTP simulation of power-system dynamics," *IEEE Transactions on Circuits and Systems I: Regular Papers*, vol. 57, no. 9, pp. 2564–2574, 2010.

[10] M. Kulasza, "Generalized dynamic phasor-based simulation for power systems," Master's thesis, University of Manitoba, Winnipeg, Canada, Jan. 2015.

[11] A. T. J. Martí, "The application of shifted frequency analysis in power system transient stability studies," Master's thesis, University of British Columbia, Vancouver, Canada, 2018.

[12] A. M. Stankovic, S. R. Sanders, and T. Aydin, "Dynamic phasors in modeling and analysis of unbalanced polyphase AC machines," *IEEE Transactions on Energy Conversion*, vol. 17, no. 1, pp. 107–113, 2002.

[13] K. Strunz, R. Shintaku, and F. Gao, "Frequency-adaptive network modeling for integrative simulation of natural and envelope waveforms in power systems and circuits," *IEEE Transactions on Circuits and Systems I: Regular Papers*, vol. 53, no. 12, pp. 2788–2803, 2006.

[14] A. Semlyen and M. R. Iravani, "Frequency domain modeling of external systems in an electromagnetic transients program," *IEEE Transactions on Power Systems*, vol. 8, no. 2, pp. 527–533, 1993.

[15] G. W. J. Anderson, N. R. Watson, N. P. Arnold, and J. Arrillaga, "A new hybrid algorithm for analysis of HVDC and FACTS systems," in *Proceedings 1995 International Conference on Energy Management and Power Delivery EMPD '95*, vol. 2, pp. 462–467 vol.2, 1995.

[16] V. Jalili-Marandi, V. Dinavahi, K. Strunz, J. A. Martinez, and A. Ramirez, "Interfacing techniques for transient stability and electromagnetic transient programs IEEE task force on interfacing

techniques for simulation tools," *IEEE Transactions on Power Delivery*, vol. 24, no. 4, pp. 2385–2395, 2009.

[17] P. Zadkhast, X. Lin, F. Howell, B. Ko, and K. Hur, "Practical challenges in hybrid simulation studies interfacing transient stability and electro-magnetic transient simulations," *Electric Power Systems Research*, vol. 190, p. 106596, 2021.

[18] M. L. Crow and J. G. Chen, "The multirate method for simulation of power system dynamics," *IEEE Transactions on Power Systems*, vol. 9, no. 3, pp. 1684–1690, 1994.

[19] A. Semlyen and F. de Leon, "Computation of electromagnetic transients using dual or multiple time steps," *IEEE Transactions on Power Systems*, vol. 8, no. 3, pp. 1274–1281, 1993.

[20] F. A. Moreira, J. R. Marti, L. C. Zanetta, and L. R. Linares, "Multirate simulations with simultaneous-solution using direct integration methods in a partitioned network environment," *IEEE Transactions on Circuits and Systems I: Regular Papers*, vol. 53, no. 12, pp. 2765–2778, 2006.

[21] P. Le-Huy, G. Sybille, P. Giroux, L. Loud, J. Huang, and I. Kamwa, "Real-time electromagnetic transient and transient stability co-simulation based on hybrid line modelling," *IET Generation, Transmission Distribution*, vol. 11, no. 12, pp. 2983–2990, 2017.

[22] X. Meng and L. Wang, "Interfacing an EMT-type modular multilevel converter HVDC model in transient stability simulation," *IET Generation, Transmission Distribution*, vol. 11, no. 12, pp. 3002–3008, 2017.

[23] A. A. van der Meer, M. Gibescu, M. A. M. M. van der Meijden, W. L. Kling, and J. A. Ferreira, "Advanced hybrid transient stability and EMT simulation for VSC-HVDC systems," *IEEE Transactions on Power Delivery*, vol. 30, no. 3, pp. 1057–1066, 2015.

[24] F. Plumier, P. Aristidou, C. Geuzaine, and T. Van Cutsem, "Co-simulation of electromagnetic transients and phasor models: A relaxation approach," *IEEE Transactions on Power Delivery*, vol. 31, no. 5, pp. 2360–2369, 2016.

[25] D. Shu, X. Xie, Q. Jiang, Q. Huang, and C. Zhang, “A novel interfacing technique for distributed hybrid simulations combining EMT and transient stability models,” *IEEE Transactions on Power Delivery*, vol. 33, no. 1, pp. 130–140, 2018.

[26] Y. Li, D. Shu, F. Shi, Z. Yan, Y. Zhu, and N. Tai, “A multi-rate co-simulation of combined phasor-domain and time-domain models for large-scale wind farms,” *IEEE Transactions on Energy Conversion*, vol. 35, no. 1, pp. 324–335, 2020.

[27] C. Tian, H. Zhao, J. Diao, and B. Li, “Electromagnetic and electromechanical hybrid simulation based on Mosaik framework,” in *2020 IEEE/IAS Industrial and Commercial Power System Asia (I CPS Asia)*, pp. 887–891, 2020.

[28] K. Mudunkotuwa, S. Filizadeh, and U. Annakkage, “Development of a hybrid simulator by interfacing dynamic phasors with electromagnetic transient simulation,” *IET Generation, Transmission Distribution*, vol. 11, no. 12, pp. 2991–3001, 2017.

[29] D. Shu, X. Xie, Z. Yan, V. Dinavahi, and K. Strunz, “A multi-domain co-simulation method for comprehensive shifted-frequency phasor DC-grid models and EMT AC-grid models,” *IEEE Transactions on Power Electronics*, vol. 34, no. 11, pp. 10557–10574, 2019.

[30] H. Konara, U. Annakkage, and C. Karawita, “Real-time co-simulation model using electromagnetic transient and dynamic phasor simulations,” *CIGRE Science & Engineering*, pp. 86–95, June 2019.

[31] D. Shu, X. Xie, V. Dinavahi, C. Zhang, X. Ye, and Q. Jiang, “Dynamic phasor based interface model for EMT and transient stability hybrid simulations,” *IEEE Transactions on Power Systems*, vol. 33, no. 4, pp. 3930–3939, 2018.

[32] D. shu, Z. Ouyang, and Z. Yan, “Multi-rate and mixed solver based co-simulation of combined transient stability, shifted-frequency phasor and electro-magnetic models: A practical LCC HVDC simulation study,” *IEEE Transactions on Industrial Electronics*, pp. 1–1, 2020.

[33] K. M. H. K. Konara, *“Interfacing a transient stability model to a real-time electromagnetic transient simulation using dynamic phasors”*. PhD thesis, University of Manitoba, Winnipeg, Canada, 2020.

[34] N. Watson and J. Arrillaga, *Power Systems Electromagnetic Transients Simulation.* London, UK: IET Digital Library, 1st ed., Jan. 2003.

[35] A. E. Kennelly, "Vector power in alternating-current circuits," *Proceedings of the American Institute of Electrical Engineers*, vol. 29, no. 7, pp. 1023–1057, 1910.

[36] B. Stott, "Power system dynamic response calculations," *Proceedings of the IEEE*, vol. 67, no. 2, pp. 219–241, 1979.

[37] P. Kundur, *Power System Stability and Control.* NY, USA: McGraw-Hill Education, 1st ed., Jan. 1994.

[38] J. S. Chai, N. Zhu, A. Bose, and D. J. Tylavsky, "Parallel newton type methods for power system stability analysis using local and shared memory multiprocessors," *IEEE Transactions on Power Systems*, vol. 6, no. 4, pp. 1539–1545, 1991.

[39] H. W. Dommel, "Digital computer solution of electromagnetic transients in single-and multiphase networks," *IEEE Transactions on Power Apparatus and Systems*, vol. PAS-88, no. 4, pp. 388–399, 1969.

[40] F. L. Alvarado, "Parallel solution of transient problems by trapezoidal integration," *IEEE Transactions on Power Apparatus and Systems*, vol. PAS-98, no. 3, pp. 1080–1090, 1979.

[41] J. Mahseredjian, V. Dinavahi, and J. A. Martinez, "Simulation tools for electromagnetic transients in power systems: Overview and challenges," *IEEE Transactions on Power Delivery*, vol. 24, no. 3, pp. 1657–1669, 2009.

[42] M. D. Heffernan, K. Turner, J. Arrillaga, and C. P. Arnold, "Computation of A.C.-D.C. system disturbances - part i, ii, and iii," *IEEE Transactions on Power Apparatus and Systems*, vol. PAS-100, pp. 4341–4363, Nov. 1981.

[43] A. A. van der Meer, R. L. Hendriks, M. Gibescu, and W. L. Kling, "Interfacing methods for combined stability and electromagnetic transient simulations applied to VSC-HVDC," in *International Conference on Power System Transients (IPST)*, pp. 1–9, 2011.

[44] H. Su, K. W. Chan, L. A. Snider, and J. C. Soumagne, "Advancements on the integration of electromagnetic transients simulator and transient stability simulator," in *International Conference on Power System Transients (IPST)*, pp. 1–6, 2005.

[45] Xuegong Wang, P. Wilson, and D. Woodford, "Interfacing transient stability program to EMTDC program," in *Proceedings. International Conference on Power System Technology*, vol. 2, pp. 1264–1269 vol.2, 2002.

[46] W. Ren, M. Steurer, and T. L. Baldwin, "Improve the stability and the accuracy of power hardware-in-the-loop simulation by selecting appropriate interface algorithms," *IEEE Transactions on Industry Applications*, vol. 44, no. 4, pp. 1286–1294, 2008.

[47] H. Konara, U. D. Annakkage, and C. Karawita, "Stability criterion for interfacing a transient stability model to a dynamic phasor model," in *2018 IEEE/PES Transmission and Distribution Conference and Exposition (T D)*, pp. 1–5, 2018.

[48] S. Filizadeh, "Interfacing Methods for Electromagnetic Transient Simulation: New Possibilities for Analysis and Design," in *Transient Analysis of Power Systems*, pp. 552–567, John Wiley & Sons, Ltd, 2015. Section: 13.

[49] F. J. Plumier, C. Geuzaine, and T. Van Cutsem, "On the convergence of relaxation schemes to couple phasor-mode and electromagnetic transients simulations," in *2014 IEEE PES General Meeting | Conference Exposition*, pp. 1–5, 2014.

[50] F. Plumier, C. Geuzaine, and T. Van Cutsem, "A multirate approach to combine electromagnetic transients and fundamental-frequency simulations," in *International Conference on Power System Transients (IPST)*, pp. 1–7, 2013.

[51] J. Rupasinghe, S. Filizadeh, and L. Wang, "A dynamic phasor model of an MMC with extended frequency range for EMT simulations," *IEEE Journal of Emerging and Selected Topics in Power Electronics*, vol. 7, no. 1, pp. 30–40, 2019.

[52] S. Oh and S. Chae, "A co-simulation framework for power system analysis," *Energies*, vol. 9, pp. 131–145, Feb 2016.

[53] G. Kron, *Diakoptics; The piecewise solution of large-scale systems.* London: Macdonald, 1st ed., 1963. OCLC: 1155582.

[54] J. R. Marti, L. R. Linares, J. Calvino, H. W. Dommel, and J. Lin, "OVNI: an object approach to real-time power system simulators," in *POWERCON '98. 1998 International Conference on Power System Technology. Proceedings (Cat. No.98EX151)*, vol. 2, pp. 977–981 vol.2, 1998.

[55] M. Armstrong, J. R. Marti, L. R. Linares, and P. Kundur, "Multilevel MATE for efficient simultaneous solution of control systems and nonlinearities in the OVNI simulator," *IEEE Transactions on Power Systems*, vol. 21, no. 3, pp. 1250–1259, 2006.

[56] M. A. Tomim, J. R. Martí, and J. A. Passos Filho, "Parallel transient stability simulation based on multi-area thévenin equivalents," *IEEE Transactions on Smart Grid*, vol. 8, no. 3, pp. 1366–1377, 2017.

[57] H. T. Su, K. W. Chan, and L. A. Snider, "Parallel interaction protocol for electromagnetic and electromechanical hybrid simulation," *IEE Proceedings - Generation, Transmission and Distribution*, vol. 152, no. 3, pp. 406–414, 2005.

[58] J. Jardim, K. C. de Oliveira Salim, P. H. L. dos Santos, C. A. da Silva Neto, M. G. dos Santos, H. M. de Barros, and G. N. Taranto, "Variable time step application on hybrid eletromechanical–eletromagnetic simulation," *IET Generation, Transmission & Distribution*, vol. 11, pp. 2968–2973, August 2017.

[59] D. Gabor, "Theory of communication - part 1, part 3, part 3," *Journal of the Institution of Electrical Engineers - Part III: Radio and Communication Engineering*, vol. 93, no. 26, pp. 429–457, 1946.

[60] V. Venkatasubramanian, H. Schättler, and J. Zaborszky, "On the dynamics of differential-algebraic systems such as the balanced large electric power system," 1995.

[61] S. R. Sanders and G. C. Verghese, "Synthesis of averaged circuit models for switched power converters," *IEEE Transactions on Circuits and Systems*, vol. 38, no. 8, pp. 905–915, 1991.

[62] V. Venkatasubramanian, H. Schattler, and J. Zaborszky, "Fast time-varying phasor analysis in the balanced three-phase large electric power system," *IEEE Transactions on Automatic Control*, vol. 40, no. 11, pp. 1975–1982, 1995.

[63] C. J. O'Rourke, M. M. Qasim, M. R. Overlin, and J. L. Kirtley, "A geometric interpretation of reference frames and transformations: dq0, Clarke, and Park," *IEEE Transactions on Energy Conversion*, vol. 34, no. 4, pp. 2070–2083, 2019.

[64] A. Bagheri-Vandaei and S. Filizadeh, "Generalised extended-frequency dynamic phasor model of LCC-HVDC systems for electromagnetic transient simulations," *IET Generation, Transmission Distribution*, vol. 12, no. 12, pp. 3061–3069, 2018.

[65] M. Daryabak, S. Filizadeh, J. Jatskevich, A. Davoudi, M. Saeedifard, V. K. Sood, J. A. Martinez, D. Aliprantis, J. Cano, and A. Mehrizi-Sani, "Modeling of LCC-HVDC systems using dynamic phasors," *IEEE Transactions on Power Delivery*, vol. 29, no. 4, pp. 1989–1998, 2014.

[66] D. Maksimovic, A. M. Stankovic, V. J. Thottuvelil, and G. C. Verghese, "Modeling and simulation of power electronic converters," *Proceedings of the IEEE*, vol. 89, no. 6, pp. 898–912, 2001.

[67] S. Henschel, *"Analysis of electromagnetic and electromechanical power system transients with dynamic phasors".* PhD thesis, University of British Columbia, Vancouver, Canada, 1999.

[68] J. R. Martí, H. W. Dommel, B. D. Bonatto, and A. F. R. Barrete, "Shifted frequency analysis (SFA) concepts for EMTP modelling and simulation of power system dynamics," in *2014 Power Systems Computation Conference*, pp. 1–8, 2014.

[69] A. D. Poularikas, *The Transforms and Applications Handbook.* CRC Press, 2nd ed., Feb. 2000.

[70] E. Gengel and A. Pikovsky, "Phase demodulation with iterative Hilbert transform embeddings," *Signal Processing*, vol. 165, pp. 115–127, 2019.

[71] J. Rupasinghe, S. Filizadeh, A. Gole, and K. Strunz, "Multi-rate co-simulation of power system transients using dynamic phasor and EMT solvers," *The Journal of Engineering*, pp. 854–862, 2020.

[72] E. J. Candes and M. B. Wakin, "An introduction to compressive sampling," *IEEE Signal Processing Magazine*, vol. 25, no. 2, pp. 21–30, 2008.

[73] B. Lathi, *Linear Systems and Signals*. Oxford University Press, 4th ed., 2004.

[74] R. Shintaku and K. Strunz, "Branch companion modeling for diverse simulation of electromagnetic and electromechanical transients," *Electric Power Systems Research*, vol. 77, no. 11, pp. 1501 – 1505, 2007. Selected Topics in Power System Transients - Part II.

[75] F. Gao and K. Strunz, "Frequency-adaptive power system modeling for multiscale simulation of transients," *IEEE Transactions on Power Systems*, vol. 24, no. 2, pp. 561–571, 2009.

[76] L. Wang, J. Jatskevich, V. Dinavahi, H. W. Dommel, J. A. Martinez, K. Strunz, M. Rioual, G. W. Chang, and R. Iravani, "Methods of interfacing rotating machine models in transient simulation programs," *IEEE Transactions on Power Delivery*, vol. 25, no. 2, pp. 891–903, 2010.

[77] L. Wang, J. Jatskevich, and H. W. Dommel, "Re-examination of synchronous machine modeling techniques for electromagnetic transient simulations," *IEEE Transactions on Power Systems*, vol. 22, no. 3, pp. 1221–1230, 2007.

[78] H. Ye, F. Gao, K. Strunz, and Y. Xia, "Multi-scale modeling and simulation of synchronous machine in phase-domain," in *2012 3rd IEEE PES Innovative Smart Grid Technologies Europe (ISGT Europe)*, pp. 1–6, 2012.

[79] J. R. Marti and K. W. Louie, "A phase-domain synchronous generator model including saturation effects," *IEEE Transactions on Power Systems*, vol. 12, no. 1, pp. 222–229, 1997.

[80] P. Zhang, J. R. Marti, and H. W. Dommel, "Synchronous machine modeling based on shifted frequency analysis," *IEEE Transactions on Power Systems*, vol. 22, no. 3, pp. 1139–1147, 2007.

[81] Manitoba HVDC Research Center, Winnipeg, MB, Canada, *PSCAD/EMTDC User's Guide*.

[82] S. D. Pekarek, O. Wasynczuk, and H. J. Hegner, "An efficient and accurate model for the simulation and analysis of synchronous machine/converter systems," *IEEE Transactions on Energy Conversion*, vol. 13, no. 1, pp. 42–48, 1998.

[83] M. Chapariha, F. Therrien, J. Jatskevich, and H. W. Dommel, "Explicit formulations for constant-parameter voltage-behind-reactance interfacing of synchronous machine models," *IEEE Transactions on Energy Conversion*, vol. 28, no. 4, pp. 1053–1063, 2013.

[84] Y. Huang, M. Chapariha, F. Therrien, J. Jatskevich, and J. R. Martí, "A constant-parameter voltage-behind-reactance synchronous machine model based on shifted-frequency analysis," *IEEE Transactions on Energy Conversion*, vol. 30, no. 2, pp. 761–771, 2015.

[85] J. R. Marti, "Accurate modelling of frequency-dependent transmission lines in electromagnetic transient simulations," *IEEE Transactions on Power Apparatus and Systems*, vol. PAS-101, no. 1, pp. 147–157, 1982.

[86] Feng Gao and K. Strunz, "Modeling of constant distributed parameter transmission line for simulation of natural and envelope waveforms in power electric networks," in *Proceedings of the 37th Annual North American Power Symposium, 2005.*, pp. 247–252, 2005.

[87] K. Mudunkotuwa and S. Filizadeh, "Co-simulation of electrical networks by interfacing EMT and dynamic-phasor simulators," *Electric Power Systems Research*, vol. 163, pp. 423 – 429, 2018.

[88] P. Le-Huy, G. Sybille, P. Giroux, L. Loud, J. Huang, and I. Kamwa, "Real-time electromagnetic transient and transient stability co-simulation based on hybrid line modelling," *IET Generation, Transmission Distribution*, vol. 11, no. 12, pp. 2983–2990, 2017.

[89] Shan Jiang, U. D. Annakkage, and A. M. Gole, "A platform for validation of FACTS models," *IEEE Transactions on Power Delivery*, vol. 21, no. 1, pp. 484–491, 2006.

[90] "IEEE 118-bus system - Illinois Center for a Smarter Electric Grid (ICSEG)."

[91] U. N. Gnanarathna, A. M. Gole, and R. P. Jayasinghe, "Efficient modeling of modular multilevel HVDC converters (MMC) on electromagnetic transient simulation programs," *IEEE Transactions on Power Delivery*, vol. 26, no. 1, pp. 316–324, 2011.

[92] H. Saad, S. Dennetière, J. Mahseredjian, P. Delarue, X. Guillaud, J. Peralta, and S. Nguefeu, "Modular multilevel converter models for electromagnetic transients," *IEEE Transactions on Power Delivery*, vol. 29, no. 3, pp. 1481–1489, 2014.

[93] J. Xu, A. M. Gole, and C. Zhao, “The use of averaged-value model of modular multilevel converter in DC grid,” *IEEE Transactions on Power Delivery*, vol. 30, no. 2, pp. 519–528, 2015.

[94] J. Peralta, H. Saad, S. Dennetiere, J. Mahseredjian, and S. Nguefeu, “Detailed and averaged models for a 401-level MMC–HVDC system,” *IEEE Transactions on Power Delivery*, vol. 27, no. 3, pp. 1501–1508, 2012.

[95] D. Shu, X. Xie, Q. Jiang, G. Guo, and K. Wang, “A multirate EMT co-simulation of large AC and MMC-based MTDC systems,” *IEEE Transactions on Power Systems*, vol. 33, no. 2, pp. 1252–1263, 2018.

[96] D. Shu, Y. Wei, V. Dinavahi, K. Wang, Z. Yan, and X. Li, “Cosimulation of shifted-frequency/dynamic phasor and electromagnetic transient models of hybrid LCC-MMC DC grids on integrated CPU–GPUs,” *IEEE Transactions on Industrial Electronics*, vol. 67, no. 8, pp. 6517–6530, 2020.

[97] J. Rupasinghe, S. Filizadeh, and D. Muthumuni, “A method for modeling and testing modular multilevel converters and their controls in large power system simulation studies,” in *2020 CIGRE Canada Conference & Expo*, pp. 1–9, 2020.

[98] Siemens Power Technologies International, New York, USA, *Model Library PSS®E 33.12.1*.

Appendix A

Synchronous Machine Model

A.1 Parameter Derivation

Consider the equivalent circuits given in Figure A.1, which illustrates flux linkage and current relationships of a synchronous machine with one d-axis and two q-axis damper windings [37].

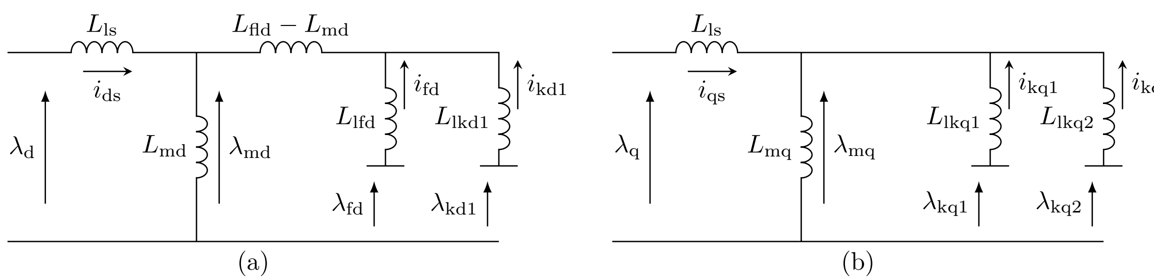

Figure A.1: Circuit illustrating flux linkage-current relationship of a synchronous machine; (a) d-axis, (b) q-axis

Using Figure A.1, relationships for magnetizing fluxes are derived as:

$$\lambda_{\mathrm{mq}} = L''_{\mathrm{mq}} i_{\mathrm{qs}} + \lambda''_{\mathrm{q}}, \qquad \lambda_{\mathrm{md}} = L''_{\mathrm{md}} i_{\mathrm{ds}} + \lambda''_{\mathrm{d}} \tag{A.1}$$

wherein λ_{mq} and λ_{md} are the sub-transient inductances, and λ''_{q} and λ''_{d} are the sub-transient flux linkages. The sub-transient inductances are defined as:

$$L''_{\mathrm{mq}} = \left(\frac{1}{L_{\mathrm{mq}}} + \sum_{j=1}^{2} \frac{1}{L_{\mathrm{lkq}j}} \right)^{-1}, \qquad L''_{\mathrm{md}} = \left(\frac{1}{L_{\mathrm{md}}} + \frac{1}{L_{\mathrm{lfd}}} + \frac{1}{L_{\mathrm{lkd1}}} \right)^{-1} \tag{A.2}$$

and the sub-transient flux linkages are defined as

$$\lambda''_{\mathrm{q}} = L''_{\mathrm{mq}}\left(\sum_{j=1}^{2}\frac{\lambda_{\mathrm{kq}j}}{L_{\mathrm{lkq}j}}\right), \qquad \lambda''_{\mathrm{d}} = L''_{\mathrm{md}}\left(\frac{\lambda_{\mathrm{fd}}}{L_{\mathrm{lfd}}} + \frac{\lambda_{\mathrm{kd1}}}{L_{\mathrm{lkd1}}}\right) \tag{A.3}$$

The state equations for flux linkages of rotor windings are derived using the d- and q-axis equivalent circuits of a synchronous machine, which are shown in Figure A.1 [37]. The corresponding state equations model is given in (A.4)-(A.7).

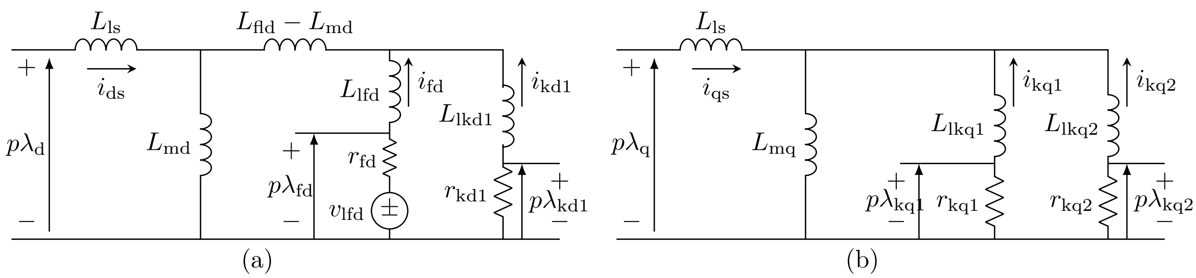

Figure A.2: Equivalent circuits of a synchronous machine; (a) d-axis, (b) q-axis

$$\frac{\mathrm{d}}{\mathrm{d}t}\lambda_{\mathrm{kq1}} = -\frac{r_{\mathrm{kq1}}}{L_{\mathrm{lkq1}}}(\lambda_{\mathrm{kq1}} - \lambda_{\mathrm{mq}}) \tag{A.4}$$

$$\frac{\mathrm{d}}{\mathrm{d}t}\lambda_{\mathrm{kq2}} = -\frac{r_{\mathrm{kq2}}}{L_{\mathrm{lkq2}}}(\lambda_{\mathrm{kq2}} - \lambda_{\mathrm{mq}}) \tag{A.5}$$

$$\frac{\mathrm{d}}{\mathrm{d}t}\lambda_{\mathrm{fd}} = -\frac{r_{\mathrm{fd}}}{L_{\mathrm{lfd}}}(\lambda_{\mathrm{fd}} - \lambda_{\mathrm{md}}) + v_{\mathrm{fd}} \tag{A.6}$$

$$\frac{\mathrm{d}}{\mathrm{d}t}\lambda_{\mathrm{kd1}} = -\frac{r_{\mathrm{kd1}}}{L_{\mathrm{lkd1}}}(\lambda_{\mathrm{kd1}} - \lambda_{\mathrm{md}}) \tag{A.7}$$

The electromechanical model of a synchronous machine is given by

$$\frac{\mathrm{d}}{\mathrm{d}t}\Delta\omega_{\mathrm{r}} = \frac{1}{J}(T_{\mathrm{mech}} - T_{\mathrm{elec}} - D\Delta\omega_{\mathrm{r}}); \qquad \omega_{\mathrm{r}} = \omega_0 + \Delta\omega_{\mathrm{r}} \tag{A.8}$$

$$\frac{\mathrm{d}}{\mathrm{d}t}\theta_{\mathrm{r}} = \omega_{\mathrm{r}} \tag{A.9}$$

where, T_{mech}, T_{elec}, ω_{r}, θ_{r}, J, and D are mechanical torque, electric torque, rotor speed, rotor angle, angular moment of inertia, and damping constant, respectively. The electric torque of a machine consisting p number of poles is given by

$$T_{\mathrm{elec}} = \frac{3p}{4}(\lambda_{\mathrm{md}} i_{\mathrm{qs}} - \lambda_{\mathrm{mq}} i_{\mathrm{ds}}) \tag{A.10}$$

A.2 Constant-Parameter Voltage-Behind-Reactance Synchronous Machine Model

The stator interface equation for synchronous machine represented as a voltage source behind constant impedance is given as follows.

$$\underline{\mathbf{v}}_{\mathrm{abcs}}(t) = \mathbf{R}_{\mathrm{s}} \underline{\mathbf{i}}_{\mathrm{abcs}}(t) + \mathbf{L}'' \frac{\mathrm{d}}{\mathrm{d}t} \underline{\mathbf{i}}_{\mathrm{abcs}}(t) + \underline{\mathbf{e}}''_{\mathrm{abc}}(t) \tag{A.11}$$

where

$$\mathbf{R}_{\mathrm{s}} = \begin{pmatrix} r_{\mathrm{S}} & 0 & 0 \\ 0 & r_{\mathrm{S}} & 0 \\ 0 & 0 & r_{\mathrm{S}} \end{pmatrix} \tag{A.12}$$

is the stator resistance matrix and

$$\mathbf{L}'' = \begin{pmatrix} L''_{\mathrm{S}} & L''_{\mathrm{M}} & L''_{\mathrm{M}} \\ L''_{\mathrm{M}} & L''_{\mathrm{S}} & L''_{\mathrm{M}} \\ L''_{\mathrm{M}} & L''_{\mathrm{M}} & L''_{\mathrm{S}} \end{pmatrix} \tag{A.13}$$

is a constant inductance matrix. The entries of $\mathbf{L}''$ are found as below.

$$L''_{\mathrm{S}} = L_{\mathrm{ls}} + \frac{2L''_{\mathrm{md}}}{3} \tag{A.14}$$

$$L''_{\mathrm{M}} = -\frac{L''_{\mathrm{md}}}{3} \tag{A.15}$$

The sub-transient voltages in (A.11) are calculated in the qd-domain and then transformed to the phase-domain as

$$\underline{\mathbf{e}}''_{\mathrm{abc}}(t) = \mathbf{K}_{\mathrm{s}}^{r\,-1}(\theta_{\mathrm{r}}) \begin{pmatrix} e''_{\mathrm{q}}(t) & e''_{\mathrm{d}}(t) & 0 \end{pmatrix}^{\mathrm{T}} \tag{A.16}$$

where $\mathbf{K}_{\mathrm{s}}^{r}(\theta_{\mathrm{r}})$ is the Park's transformation matrix (see Appendix A.4) and

$$e''_{\mathrm{q}} = \frac{L''_{\mathrm{d}}}{L''_{\mathrm{q}}}\left(\omega_{\mathrm{r}}\left(\lambda''_{\mathrm{d}} - (L''_{\mathrm{q}} - L''_{\mathrm{d}})i_{\mathrm{ds}}\right) + \sum_{j=1}^{2}\frac{L''_{\mathrm{mq}} r_{\mathrm{kq}j}}{L^2_{\mathrm{lkq}j}}(\lambda_{\mathrm{mq}} - \lambda_{\mathrm{kq}j})\right) + \frac{(L''_{\mathrm{q}} - L''_{\mathrm{d}})}{L''_{\mathrm{q}}}(\tilde{v}_{\mathrm{qs}} - r_{\mathrm{s}} i_{\mathrm{qs}}) \quad \text{(A.17)}$$

$$e''_{\mathrm{d}} = -\omega_{\mathrm{r}}\left(\lambda''_{\mathrm{q}} + (L''_{\mathrm{q}} - L''_{\mathrm{d}})i_{\mathrm{qs}}\right) + \frac{L''_{\mathrm{md}} r_{\mathrm{fd}}}{L^2_{\mathrm{lfd}}}(\lambda_{\mathrm{md}} - \lambda_{\mathrm{fd}}) + \frac{L''_{\mathrm{md}} r_{\mathrm{kd1}}}{L^2_{\mathrm{lkd1}}}(\lambda_{\mathrm{md}} - \lambda_{\mathrm{kd1}}) + \frac{L''_{\mathrm{md}}}{L_{\mathrm{fd}}} v_{\mathrm{fd}} \quad \text{(A.18)}$$

$\tilde{v}_{\mathrm{qs}}$ denotes the approximated value of v_{qs} for explicit implementation. The inductances L''_{q} and L''_{d} are given by

$$L''_{\mathrm{q}} = L_{\mathrm{ls}} + L''_{\mathrm{mq}}, \qquad L''_{\mathrm{d}} = L_{\mathrm{ls}} + L''_{\mathrm{md}} \quad \text{(A.19)}$$

A.3 Synchronous Machine Model Interface to the BFAST Solver

Figure A.3 illustrates the equivalent interfacing circuit, which is derived from (A.11), of the constant-parameter voltage behind reactance synchronous machine model [83].

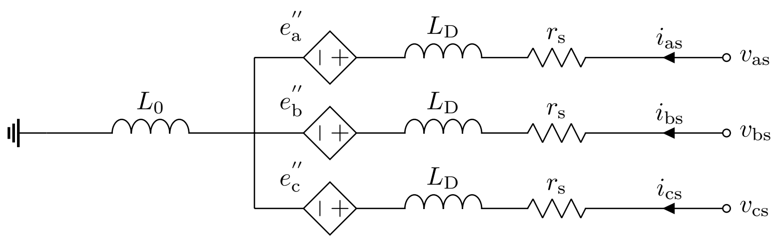

Figure A.3: Interface circuit for constant-parameter voltage behind reactance synchronous machine model

The inductances of Figure A.3 are

$$L_{\mathrm{D}} = L_{\mathrm{ls}} + L''_{\mathrm{md}}, \qquad L_0 = -\frac{L''_{\mathrm{md}}}{3} \quad \text{(A.20)}$$

In this interface circuit, the sub-transient voltage sources are recomputed and updated at each time-step. The inductors and resistors are discretized and then incorporated in the network nodal admittance matrix. Refer section 5.1 for development of discretized equivalents of resistors and inductors with dynamic phasors.

A.4 *qd*0-*abc* and *qd*0-DP Transformations

In the synchronous machine model, the following transformations are used.

1. Conversion from phase-domain quantities to $qd0$-domain quantities and vice versa are done using the following transformations [82].

$$\underline{\mathbf{x}}_{\mathrm{qd0}} = \mathbf{K}_{\mathrm{s}}^{r}(\theta_{\mathrm{r}}) \cdot \underline{\mathbf{x}}_{\mathrm{abc}} \tag{A.21}$$

$$\underline{\mathbf{x}}_{\mathrm{abc}} = \mathbf{K}_{\mathrm{s}}^{r-1}(\theta_{\mathrm{r}}) \cdot \underline{\mathbf{x}}_{\mathrm{qd0}} \tag{A.22}$$

where $\mathbf{K}_{\mathrm{s}}^{r}(\theta_{\mathrm{r}})$ is the Park's transformation matrix [63], and is defined as

$$\mathbf{K}_{\mathrm{s}}^{r}(\theta_{\mathrm{r}}) = \frac{2}{3}\begin{pmatrix} \cos\left(\theta_{\mathrm{r}}\right) & \cos\left(\theta_{\mathrm{r}} - 2\pi/3\right) & \cos\left(\theta_{\mathrm{r}} + 2\pi/3\right) \\ \sin\left(\theta_{\mathrm{r}}\right) & \sin\left(\theta_{\mathrm{r}} - 2\pi/3\right) & \sin\left(\theta_{\mathrm{r}} + 2\pi/3\right) \\ 1/2 & 1/2 & 1/2 \end{pmatrix} \tag{A.23}$$

2. Conversion from dynamic phasors quantities to $qd0$-domain quantities and vice versa are done using the following transformations [84].

$$\underline{\mathbf{x}}_{\mathrm{qd0}} = \mathbf{K}_{\mathrm{s}}^{r}(\theta_{\mathrm{r}}) \cdot \mathfrak{Re}\left\{\left\langle \mathrm{X}_{\mathrm{abc}} \right\rangle_{\mathrm{B}}(t)\mathrm{e}^{\mathrm{j}\omega_0 t}\right\} \tag{A.24}$$

$$\left\langle \mathrm{X}_{\mathrm{abc}} \right\rangle_{\mathrm{B}}(t) = \mathbf{K}_{\mathrm{u,qd}}^{\mathrm{U,abc}}(\theta_{\mathrm{r}}) \cdot \underline{\mathbf{x}}_{\mathrm{qd}} \tag{A.25}$$

where

$$\mathbf{K}_{\mathrm{u,qd}}^{\mathrm{U,abc}}(\theta_{\mathrm{r}}) = \begin{pmatrix} \mathrm{e}^{\mathrm{j}(\theta_{\mathrm{r}} - \omega_{\mathrm{s}} t)} & \mathrm{e}^{\mathrm{j}(\theta_{\mathrm{r}} - \frac{\pi}{2} - \omega_{\mathrm{s}} t)} \\ \mathrm{e}^{\mathrm{j}(\theta_{\mathrm{r}} - \frac{2\pi}{3} - \omega_{\mathrm{s}} t)} & \mathrm{e}^{\mathrm{j}(\theta_{\mathrm{r}} - \frac{\pi}{2} - \frac{2\pi}{3} - \omega_{\mathrm{s}} t)} \\ \mathrm{e}^{\mathrm{j}(\theta_{\mathrm{r}} + \frac{2\pi}{3} - \omega_{\mathrm{s}} t)} & \mathrm{e}^{\mathrm{j}(\theta_{\mathrm{r}} - \frac{\pi}{2} + \frac{2\pi}{3} - \omega_{\mathrm{s}} t)} \end{pmatrix} \tag{A.26}$$

Appendix B

Transformer Model

B.1 Parameter Derivation

The equivalent circuit of the basic two-winding transformer model is given in Figure B.1 [34, 81]. Consider that it has a leakage reactance of X_{l} (pu), magnetization current of I_{m} (pu), power rating of S_{base} (MVA), and turn ratio of a.

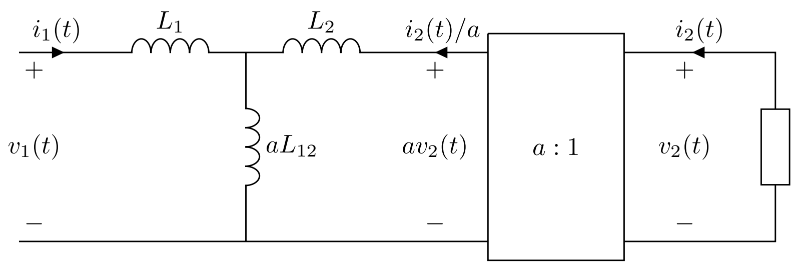

Figure B.1: Equivalent circuit of two-winding transformer

The voltage across two windings are given by

$$\begin{pmatrix} v_1 \\ v_2 \end{pmatrix} = \begin{pmatrix} L_{11} & L_{12} \\ L_{12} & L_{22} \end{pmatrix} \frac{\mathrm{d}}{\mathrm{d}t} \begin{pmatrix} i_1 \\ i_2 \end{pmatrix} \tag{B.1}$$

where

$$L_{11} = L_1 + aL_{12} \tag{B.2}$$

$$L_{22} = \frac{L_2 + aL_{12}}{a^2} \tag{B.3}$$

Inductances L_1, L_1, and L_{12} are calculated as

$$L_1 = L_2 = \frac{1}{2}\frac{X_l}{\omega_0} z_{1,\mathrm{base}} \tag{B.4}$$

$$L_{12} = \frac{1}{a}\left(\frac{1}{\omega_0 I_\mathrm{m}}\frac{v_{1,\mathrm{base}}}{i_{1,\mathrm{base}}} - L_1\right) \tag{B.5}$$

where subscript '$_{base}$' denotes the base quantities.

B.2 Numerical Implementation of Basic Transformer Model with Base-Frequency Dynamic Phasors

Equation (B.1) can be written as

$$\frac{\mathrm{d}}{\mathrm{d}t}\begin{pmatrix} i_1 \\ i_2 \end{pmatrix} = \frac{1}{D}\begin{pmatrix} L_{22} & -L_{12} \\ -L_{12} & L_{11} \end{pmatrix}\begin{pmatrix} v_1 \\ v_2 \end{pmatrix} \tag{B.6}$$

where $D = L_{11}L_{22} - L_{12}^2$. The base-frequency dynamic phasor representation of (B.6) is

$$\frac{\mathrm{d}}{\mathrm{d}t}\begin{pmatrix} \left\langle \mathrm{I}_1 \right\rangle_\mathrm{B} \\ \left\langle \mathrm{I}_2 \right\rangle_\mathrm{B} \end{pmatrix} = \frac{1}{D}\begin{pmatrix} L_{22} & -L_{12} \\ -L_{12} & L_{11} \end{pmatrix}\begin{pmatrix} \left\langle \mathrm{V}_1 \right\rangle_\mathrm{B} \\ \left\langle \mathrm{V}_2 \right\rangle_\mathrm{B} \end{pmatrix} - \mathrm{j}\omega_\mathrm{s}\begin{pmatrix} \left\langle \mathrm{I}_1 \right\rangle_\mathrm{B} \\ \left\langle \mathrm{I}_2 \right\rangle_\mathrm{B} \end{pmatrix} \tag{B.7}$$

By discretizing individual equation of (B.7) using the trapezoidal integration rule, the following expressions are obtained.

$$\left\langle \mathrm{I}_1 \right\rangle_\mathrm{B}(t) = y_1\left\langle \mathrm{V}_1 \right\rangle_\mathrm{B}(t) + y_{12}\left(\left\langle \mathrm{V}_1 \right\rangle_\mathrm{B}(t) - \left\langle \mathrm{V}_2 \right\rangle_\mathrm{B}(t)\right) + I_{\mathrm{h}1}(t) \tag{B.8}$$

$$\left\langle \mathrm{I}_2 \right\rangle_\mathrm{B}(t) = y_2\left\langle \mathrm{V}_2 \right\rangle_\mathrm{B}(t) - y_{12}\left(\left\langle \mathrm{V}_1 \right\rangle_\mathrm{B}(t) - \left\langle \mathrm{V}_2 \right\rangle_\mathrm{B}(t)\right) + I_{\mathrm{h}2}(t) \tag{B.9}$$

where

$$y_1 = \frac{(L_{22} - L_{12})\Delta t}{D(2 + \mathrm{j}\omega_\mathrm{s}\Delta t)} \tag{B.10}$$

$$y_2 = \frac{(L_{11} - L_{12})\Delta t}{D(2 + \mathrm{j}\omega_\mathrm{s}\Delta t)} \tag{B.11}$$

$$y_{12} = \frac{L_{12}\Delta t}{D(2 + \mathrm{j}\omega_{\mathrm{s}}\Delta t)} \tag{B.12}$$

$$\begin{aligned} I_{\mathrm{h1}}(t) = &\left(\frac{1 - \mathrm{j}\omega_{\mathrm{s}}\Delta t/2}{1 + \mathrm{j}\omega_{\mathrm{s}}\Delta t/2}\right)\Big\langle \mathrm{I}_1 \Big\rangle_{\mathrm{B}}(t - \Delta t) \\ &+ y_1\Big\langle \mathrm{V}_1 \Big\rangle_{\mathrm{B}}(t - \Delta t) + y_{12}\left(\Big\langle \mathrm{V}_1 \Big\rangle_{\mathrm{B}}(t - \Delta t) - \Big\langle \mathrm{V}_2 \Big\rangle_{\mathrm{B}}(t - \Delta t)\right) \end{aligned} \tag{B.13}$$

$$\begin{aligned} I_{\mathrm{h2}}(t) = &\left(\frac{1 - \mathrm{j}\omega_{\mathrm{s}}\Delta t/2}{1 + \mathrm{j}\omega_{\mathrm{s}}\Delta t/2}\right)\Big\langle \mathrm{I}_2 \Big\rangle_{\mathrm{B}}(t - \Delta t) \\ &+ y_2\Big\langle \mathrm{V}_2 \Big\rangle_{\mathrm{B}}(t - \Delta t) - y_{12}\left(\Big\langle \mathrm{V}_1 \Big\rangle_{\mathrm{B}}(t - \Delta t) - \Big\langle \mathrm{V}_2 \Big\rangle_{\mathrm{B}}(t - \Delta t)\right) \end{aligned} \tag{B.14}$$

Equations (B.8) and (B.9) are represented using the equivalent circuit shown in Figure B.2

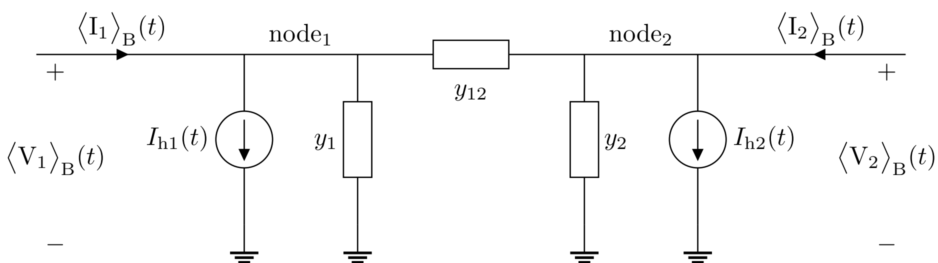

Figure B.2: Discretized equivalent circuit of basic transformer model with BFDPs

Appendix C

Transmission Line Model

The π-section transmission line model used in the BFAST solver is shown in Figure C.1.

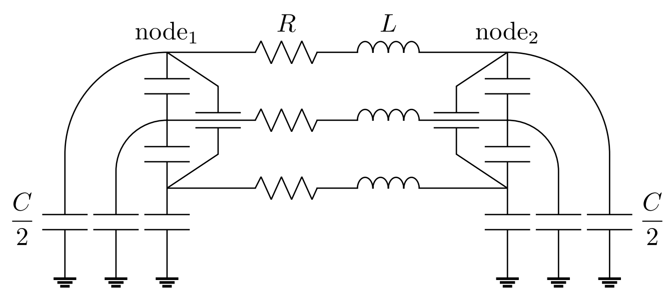

Figure C.1: Three phase π-section model of a transmission line

Elements in Figure C.1 are discretized as explain in section 5.1 and then included in the network nodal admittance matrix. The line resistance and inductance are combined to form a single Norton equivalent in order to reduce the number of nodes as given in Figure C.2 [34].

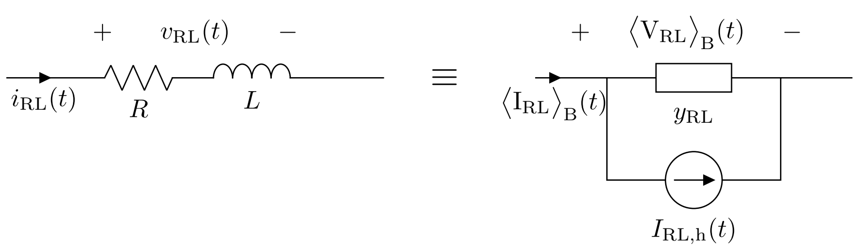

Figure C.2: Node reduction of a RL branch

$$y_{\mathrm{RL}} = \frac{1}{\frac{2L}{\Delta t}\left(1 + \mathrm{j}\omega_{\mathrm{s}}\Delta t/2\right) + R} \tag{C.1}$$

$$I_{\mathrm{RL,h}}(t) = y_{\mathrm{RL}}\left(\frac{2L}{\Delta t}(1 - \mathrm{j}\omega_{\mathrm{s}}\Delta t/2) - R\right)\left\langle \mathrm{I}_{\mathrm{RL}}\right\rangle_{\mathrm{B}}(t - \Delta t) + y_{\mathrm{RL}}\left\langle \mathrm{V}_{\mathrm{RL}}\right\rangle_{\mathrm{B}}(t - \Delta t) \tag{C.2}$$

Appendix D

Modular Multilevel Converter Model

Consider an arbitrary phase of an MMC with N_{arm} half-bridge sub-modules (SMs) per arm as shown in Figure D.1, where $j = \mathrm{a, b, c}$ refers to a phase.

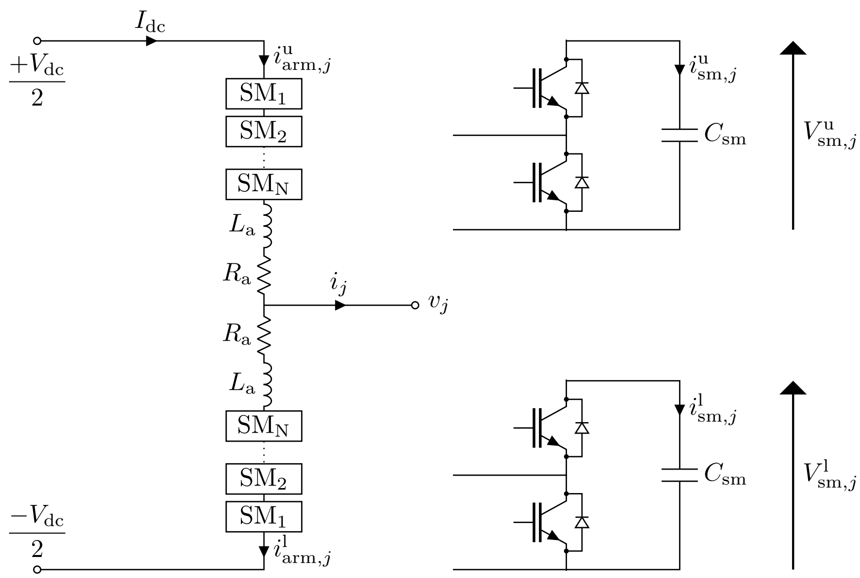

Figure D.1: Arm and SM configuration of an MMC

The expressions that describe the upper (u) and lower (l) SM voltages and arm currents are given below.

$$\frac{\mathrm{d}}{\mathrm{d}t}V^{\mathrm{u}}_{\mathrm{sm},j} = \frac{\lambda^{\mathrm{u}}_j}{C_{\mathrm{sm}}N_{\mathrm{arm}}} i^{\mathrm{u}}_{\mathrm{arm},j} \tag{D.1}$$

$$\frac{\mathrm{d}}{\mathrm{d}t}V^{\mathrm{l}}_{\mathrm{sm},j} = \frac{\lambda^{\mathrm{l}}_j}{C_{\mathrm{sm}}N_{\mathrm{arm}}} i^{\mathrm{l}}_{\mathrm{arm},j} \tag{D.2}$$

$$\frac{\mathrm{d}}{\mathrm{d}t}i^{\mathrm{u}}_{\mathrm{arm},j} = \frac{V_{\mathrm{dc}}}{2L_{\mathrm{a}}} - \frac{1}{L_{\mathrm{a}}}\lambda^{\mathrm{u}}_j V^{\mathrm{u}}_{\mathrm{sm},j} - \frac{R_{\mathrm{a}}}{L_{\mathrm{a}}} i^{\mathrm{u}}_{\mathrm{arm},j} - \frac{1}{L_{\mathrm{a}}} v_j \tag{D.3}$$

$$\frac{\mathrm{d}}{\mathrm{d}t}i^{\mathrm{l}}_{\mathrm{arm},j} = \frac{V_{\mathrm{dc}}}{2L_{\mathrm{a}}} - \frac{1}{L_{\mathrm{a}}}\lambda^{\mathrm{l}}_j V^{\mathrm{l}}_{\mathrm{sm},j} - \frac{R_{\mathrm{a}}}{L_{\mathrm{a}}} i^{\mathrm{l}}_{\mathrm{arm},j} + \frac{1}{L_{\mathrm{a}}} v_j \tag{D.4}$$

The switching functions λ^{u}_j and λ^{l}_j yields the number of inserted SMs in the arm during each switching state as follows:

$$\lambda^{\mathrm{u}}_j = \frac{N_{\mathrm{arm}}}{2}\Big(1 - m\sin(\theta+\delta)\Big), \qquad \lambda^{\mathrm{l}}_j = \frac{N_{\mathrm{arm}}}{2}\Big(1 + m\sin(\theta+\delta)\Big) \tag{D.5}$$

where m, δ, and θ are the modulation index, power angle, and the phase angle at the PCC of the MMC, respectively. Equations (D.1)-(D.5) are rewritten in terms of new variables defined by taking the summation (s) and the difference (d) of the upper and lower arm variables as:

$$\frac{\mathrm{d}}{\mathrm{d}t}V^{\mathrm{s}}_{\mathrm{sm},j} = \frac{1}{2N_{\mathrm{arm},j}C_{\mathrm{sm}}}\Big(\lambda^{\mathrm{s}}_j i^{\mathrm{s}}_{\mathrm{arm},j} + \lambda^{\mathrm{d}}_j i^{\mathrm{d}}_{\mathrm{arm},j}\Big) \tag{D.6}$$

$$\frac{\mathrm{d}}{\mathrm{d}t}V^{\mathrm{d}}_{\mathrm{sm},j} = \frac{1}{2N_{\mathrm{arm},j}C_{\mathrm{sm}}}\Big(\lambda^{\mathrm{s}}_j i^{\mathrm{d}}_{\mathrm{arm},j} + \lambda^{\mathrm{d}}_j i^{\mathrm{s}}_{\mathrm{arm},j}\Big) \tag{D.7}$$

$$\frac{\mathrm{d}}{\mathrm{d}t}i^{\mathrm{s}}_{\mathrm{arm},j} = -\frac{1}{L_{\mathrm{a}}}\left(\frac{1}{2}\lambda^{\mathrm{s}}_j V^{\mathrm{s}}_{\mathrm{sm},j} + \frac{1}{2}\lambda^{\mathrm{d}}_j V^{\mathrm{d}}_{\mathrm{sm},j} + R_{\mathrm{a}} i^{\mathrm{s}}_{\mathrm{arm},j} + V_{\mathrm{dc}}\right) \tag{D.8}$$

$$\frac{\mathrm{d}}{\mathrm{d}t}i^{\mathrm{d}}_{\mathrm{arm},j} = -\frac{1}{L_{\mathrm{a}}}\left(\frac{1}{2}\lambda^{\mathrm{s}}_j V^{\mathrm{d}}_{\mathrm{sm},j} + \frac{1}{2}\lambda^{\mathrm{d}}_j V^{\mathrm{s}}_{\mathrm{sm},j} + R_{\mathrm{a}} i^{\mathrm{d}}_{\mathrm{arm},j} - v_j\right) \tag{D.9}$$

$$\lambda^{\mathrm{s}}_j = N_{\mathrm{arm}}, \qquad \lambda^{\mathrm{d}}_j = -mN_{\mathrm{arm}}\sin(\theta+\delta) \tag{D.10}$$

All sum variables comprise of dc and even harmonics, and all difference variables are made of odd harmonics. The difference of the arm currents, $i^{\mathrm{d}}_{\mathrm{arm},j}$, is equal to the MMC's output ac current i_j. The h^{th} order dynamic phasor model of the MMC is derived as

$$\frac{\mathrm{d}}{\mathrm{d}t}\left\langle V^{\mathrm{s}}_{\mathrm{sm},j}\right\rangle_h = \frac{1}{2N_{\mathrm{arm}}C_{\mathrm{sm}}}\left(\sum_{i=-\infty}^{+\infty}\left\langle\lambda^{\mathrm{s}}_j\right\rangle_{h-i}\left\langle i^{\mathrm{s}}_{\mathrm{arm},j}\right\rangle_i + \sum_{i=-\infty}^{+\infty}\left\langle\lambda^{\mathrm{d}}_j\right\rangle_{h-i}\left\langle i^{\mathrm{d}}_{\mathrm{arm},j}\right\rangle_i\right) - \mathrm{j}h\omega_0\left\langle V^{\mathrm{s}}_{\mathrm{sm},j}\right\rangle_h \quad \text{(D.11)}$$

$$\frac{\mathrm{d}}{\mathrm{d}t}\left\langle V^{\mathrm{d}}_{\mathrm{sm},j}\right\rangle_h = \frac{1}{2N_{\mathrm{arm}}C_{\mathrm{sm}}}\left(\sum_{i=-\infty}^{+\infty}\left\langle\lambda^{\mathrm{s}}_j\right\rangle_{h-i}\left\langle i^{\mathrm{d}}_{\mathrm{arm},j}\right\rangle_i + \sum_{i=-\infty}^{+\infty}\left\langle\lambda^{\mathrm{d}}_j\right\rangle_{h-i}\left\langle i^{\mathrm{s}}_{\mathrm{arm},j}\right\rangle_i\right) - \mathrm{j}h\omega_0\left\langle V^{\mathrm{d}}_{\mathrm{sm},j}\right\rangle_h \quad \text{(D.12)}$$

$$\frac{\mathrm{d}}{\mathrm{d}t}\left\langle i^{\mathrm{s}}_{\mathrm{arm},j}\right\rangle_h = -\frac{1}{2L_{\mathrm{a}}}\left(\sum_{i=-\infty}^{+\infty}\left\langle\lambda^{\mathrm{s}}_j\right\rangle_{h-i}\left\langle V^{\mathrm{s}}_{\mathrm{sm},j}\right\rangle_i + \sum_{i=-\infty}^{+\infty}\left\langle\lambda^{\mathrm{d}}_j\right\rangle_{h-i}\left\langle V^{\mathrm{d}}_{\mathrm{sm},j}\right\rangle_i\right) - \left(\frac{R_{\mathrm{a}}}{L_{\mathrm{a}}} + \mathrm{j}h\omega_0\right)\left\langle i^{\mathrm{s}}_{\mathrm{arm},j}\right\rangle_h + \frac{1}{L_{\mathrm{a}}}\left\langle V_{\mathrm{dc}}\right\rangle_h \quad \text{(D.13)}$$

$$\left\langle v_j\right\rangle_h = -\frac{1}{4}\left(\sum_{i=-\infty}^{+\infty}\left\langle\lambda^{\mathrm{s}}_j\right\rangle_{h-i}\left\langle V^{\mathrm{d}}_{\mathrm{sm},j}\right\rangle_i + \sum_{i=-\infty}^{+\infty}\left\langle\lambda^{\mathrm{d}}_j\right\rangle_{h-i}\left\langle V^{\mathrm{s}}_{\mathrm{sm},j}\right\rangle_i\right) - \left(\frac{R_{\mathrm{a}} + \mathrm{j}h\omega_0 L_{\mathrm{a}}}{2}\right)\left\langle i^{\mathrm{d}}_{\mathrm{arm},j}\right\rangle_h - \frac{L_{\mathrm{a}}}{2}\frac{\mathrm{d}}{\mathrm{d}t}\left\langle i^{\mathrm{d}}_{\mathrm{arm},j}\right\rangle_h \quad \text{(D.14)}$$

$$\left\langle\lambda^{\mathrm{s}}_j\right\rangle_h = \begin{cases} N_{\mathrm{arm}} & \text{if } h = 0 \\ 0 & \text{Otherwise} \end{cases}, \qquad \left\langle\lambda^{\mathrm{d}}_j\right\rangle_h = \begin{cases} \mathrm{j}\frac{1}{2}mN_{\mathrm{arm}}\mathrm{e}^{\mathrm{j}\delta} & \text{if } h = 1 \\ 0 & \text{Otherwise} \end{cases} \quad \text{(D.15)}$$

$$I_{\mathrm{dc}}(t) = \sum_{j=a,b,c}\left\langle i^{\mathrm{s}}_{\mathrm{arm},j}\right\rangle_0 / \, 2 \quad \text{(D.16)}$$

Equations (D.11)-(D.13) are solved as a state equation model in order to determine internal dynamics the MMC. The output ac voltages and dc current are calculated using (D.14) and (D.16), respectively. Calculated values are used to update the sources of the model's interface circuit (see Figure 5.10) to the system.

Appendix E

Test System Data

This thesis uses the data from [89] and [90] for simulations of the IEEE-12 bus system and the IEEE-118 bus system, respectively.

E.1 IEEE 12-Bus System Data

Table E.1: Voltage source data, IEEE 12-bus system (system base: 230 kV, 100 MVA)

Bus	R (pu)	X (pu)	$\|V\|$ (pu)	$\measuredangle$ (deg)
9	1.89E-05	-	1.04	0.0
10	1.89E-05	-	1.02	1.92
11	1.89E-05	-	1.01	-37.14
12	1.89E-05	-	1.02	-31.16

Table E.2: Transformer data, IEEE 12-bus system (system base: 230 kV, 100 MVA)

From	To	X_1 (pu)	From	To	X_1 (pu)
1	7	0.01	1	9	0.01
2	10	0.01	3	8	0.01
3	11	0.01	6	12	0.02

Table E.3: Transmission line data, IEEE 12-bus system (system base: 230 kV, 100 MVA)

From	To	R (pu)	X (pu)	B (pu)	From	To	R (pu)	X (pu)	B (pu)
1	2	0.01144	0.09111	0.18261	1	6	0.03356	0.26656	0.55477
2	5	0.03356	0.26656	0.55477	3	4	0.01144	0.09111	0.18261
3	4	0.01144	0.09111	0.18261	4	5	0.03356	0.26656	0.55477
4	6	0.03356	0.26656	0.55477	7	8	0.01595	0.17214	3.28530

Table E.4: Load data, IEEE 12-bus system

Bus	P (MW)	Q (MVAr)
2	280	200
3	320	240
4	320	240
5	100	60
6	440	300

Table E.5: Shunt reactors and capacitors, IEEE 12-bus system

Bus	Q_{L} (MVAr)	Q_{C} (MVAr)
4	-	160
5	-	80
6	-	180

E.2 IEEE 118-Bus System Data

Table E.6: Voltage source data, IEEE 118-bus system (system base: 230 kV, 100 MVA)

Bus	R (pu)	X (pu)	$\|V\|$ (pu)	$\measuredangle$ (deg)	Bus	R (pu)	X (pu)	$\|V\|$ (pu)	$\measuredangle$ (deg)
1	1.89E-06	0.02	0.974	8.66	4	1.89E-06	0.02	1.000	13.43
6	1.89E-06	0.02	1.000	11.07	8	1.89E-06	0.02	1.000	18.97
10	1.89E-06	0.02	1.000	34.96	12	1.89E-06	0.02	1.000	10.28
15	1.89E-06	0.02	0.996	9.07	18	1.89E-06	0.02	1.000	9.40
19	1.89E-06	0.02	0.995	8.81	24	1.89E-06	0.02	1.000	19.04
25	1.89E-06	0.02	1.025	26.32	26	1.89E-06	0.02	1.000	28.12
27	1.89E-06	0.02	1.000	13.14	31	1.89E-06	0.02	1.000	10.64
32	1.89E-06	0.02	1.000	12.55	34	1.89E-06	0.02	1.004	8.70
36	1.89E-06	0.02	1.000	8.26	40	1.89E-06	0.02	1.000	2.39
42	1.89E-06	0.02	1.000	1.34	46	1.89E-06	0.02	1.000	16.43
49	1.89E-06	0.02	1.000	19.29	54	1.89E-06	0.02	1.000	11.75
55	1.89E-06	0.02	0.995	11.71	56	1.89E-06	0.02	0.995	11.76
59	1.89E-06	0.02	1.000	18.81	61	1.89E-06	0.02	1.000	24.06
62	1.89E-06	0.02	1.000	23.68	65	1.89E-06	0.02	1.000	27.95
66	1.89E-06	0.02	1.031	29.01	69	1.89E-06	0.02	1.000	30.00
70	1.89E-06	0.02	0.983	21.22	72	1.89E-06	0.02	1.000	19.13
73	1.89E-06	0.02	1.000	20.42	74	1.89E-06	0.02	0.952	20.25
76	1.89E-06	0.02	0.932	20.17	77	1.89E-06	0.02	0.973	25.40
80	1.89E-06	0.02	1.000	29.54	85	1.89E-06	0.02	0.981	36.21
87	1.89E-06	0.02	1.000	35.22	89	1.89E-06	0.02	1.000	46.15
90	1.89E-06	0.02	1.000	33.63	91	1.89E-06	0.02	1.000	31.69
92	1.89E-06	0.02	0.974	29.98	99	1.89E-06	0.02	1.000	25.60

100	1.89E-06	0.02	1.000	26.11	103	1.89E-06	0.02	1.000	22.20
104	1.89E-06	0.02	0.994	19.16	105	1.89E-06	0.02	0.995	17.98
107	1.89E-06	0.02	1.000	14.85	110	1.89E-06	0.02	0.998	15.71
111	1.89E-06	0.02	1.000	17.37	112	1.89E-06	0.02	1.000	12.77
113	1.89E-06	0.02	1.000	11.92	116	1.89E-06	0.02	1.000	27.32

Table E.7: Transformer data, IEEE 118-bus system (system base: 230 kV, 100 MVA)

From	To	X_1 (pu)	From	To	X_1 (pu)
5	8	0.01903	17	30	0.02765
25	26	0.02722	37	38	0.02672
59	63	0.02751	61	64	0.01910
65	66	0.02637	68	69	0.02637
80	81	0.02637			

Table E.8: Transmission line data, IEEE 118-bus system (system base: 230 kV, 100 MVA)

From	To	R (pu)	X (pu)	B (pu)	From	To	R (pu)	X (pu)	B (pu)
1	2	0.03030	0.09990	0.02540	1	3	0.01290	0.04240	0.01082
2	12	0.01870	0.06160	0.01572	3	5	0.02410	0.10800	0.02840
3	12	0.04840	0.16000	0.04060	4	5	0.00176	0.00798	0.00210
4	11	0.02090	0.06880	0.01748	5	6	0.01190	0.05400	0.01426
5	11	0.02030	0.06820	0.01738	6	7	0.00459	0.02080	0.00550
7	12	0.00862	0.03400	0.00874	8	9	0.00244	0.03050	1.16200
8	30	0.00431	0.05040	0.51400	9	10	0.00258	0.03220	1.23000
11	12	0.00595	0.01960	0.00502	11	13	0.02225	0.07310	0.01876
12	14	0.02150	0.07070	0.01816	12	16	0.02120	0.08340	0.02140
12	117	0.03290	0.14000	0.03580	13	15	0.07440	0.24440	0.06268
14	15	0.05950	0.19500	0.05020	15	17	0.01320	0.04370	0.04440
15	19	0.01200	0.03940	0.01010	15	33	0.03800	0.12440	0.03194
16	17	0.04540	0.18010	0.04660	17	18	0.01230	0.05050	0.01298
17	31	0.04740	0.15630	0.03990	17	113	0.00913	0.03010	0.00768
18	19	0.01119	0.04930	0.01142	19	20	0.02520	0.11700	0.02980
19	34	0.07520	0.24700	0.06320	20	21	0.01830	0.08490	0.02160
21	22	0.02090	0.09700	0.02460	22	23	0.03420	0.15900	0.04040
23	24	0.01350	0.04920	0.04980	23	25	0.01560	0.08000	0.08640
23	32	0.03170	0.11530	0.11730	24	70	0.00221	0.41150	0.10198
24	72	0.04880	0.19600	0.04880	25	27	0.03180	0.16300	0.17640
26	30	0.00799	0.08600	0.90800	27	28	0.01913	0.08550	0.02160
27	32	0.02290	0.07550	0.01926	27	115	0.01640	0.07410	0.01972
28	29	0.02370	0.09430	0.02380	29	31	0.01080	0.03310	0.00830
30	38	0.00464	0.05400	0.04220	31	32	0.02980	0.09850	0.02510
32	113	0.06150	0.20300	0.05180	32	114	0.01350	0.06120	0.01628
33	37	0.04150	0.14200	0.03660	34	36	0.00871	0.02680	0.00568
34	37	0.00256	0.00940	0.00984	34	43	0.04130	0.16810	0.04226

35	36	0.00224	0.01020	0.00268	35	37	0.01100	0.04970	0.01318
37	39	0.03210	0.10600	0.02700	37	40	0.05930	0.16800	0.04200
38	65	0.00901	0.09860	1.04600	39	40	0.01840	0.06050	0.01552
40	41	0.01450	0.04870	0.01222	40	42	0.05550	0.18300	0.04660
41	42	0.04100	0.13500	0.03440	42	49	0.07150	0.32300	0.08600
43	44	0.06080	0.24540	0.06068	44	45	0.02240	0.09010	0.02240
45	46	0.04000	0.13560	0.03320	45	49	0.06840	0.18600	0.04440
46	47	0.03800	0.12700	0.03160	46	48	0.06010	0.18900	0.04720
47	49	0.01910	0.06250	0.01604	47	69	0.08440	0.27780	0.07092
48	49	0.01790	0.05050	0.01258	49	50	0.02670	0.07520	0.01874
49	51	0.04860	0.13700	0.03420	49	54	0.08690	0.29100	0.07300
49	66	0.01800	0.09190	0.02480	49	69	0.09850	0.32400	0.08280
50	57	0.04740	0.13400	0.03320	51	52	0.02030	0.05880	0.01396
51	58	0.02550	0.07190	0.01788	52	53	0.04050	0.16350	0.04058
53	54	0.02630	0.12200	0.03100	54	55	0.01690	0.07070	0.02020
54	56	0.00275	0.00955	0.00732	54	59	0.05030	0.22930	0.05980
55	56	0.00488	0.01510	0.00374	55	59	0.04739	0.21580	0.05646
56	57	0.03430	0.09660	0.02420	56	58	0.03430	0.09660	0.02420
56	59	0.08030	0.23900	0.05360	59	60	0.03170	0.14500	0.03760
59	61	0.03280	0.15000	0.03880	60	61	0.00264	0.01350	0.01456
60	62	0.01230	0.05610	0.01468	61	62	0.00824	0.03760	0.00980
62	66	0.04820	0.21800	0.05780	62	67	0.02580	0.11700	0.03100
63	64	0.00172	0.02000	0.21600	64	65	0.00269	0.03020	0.38000
65	68	0.00138	0.01600	0.63800	66	67	0.02240	0.10150	0.02682
68	81	0.00175	0.02020	0.01608	68	116	0.00034	0.00405	0.16400
69	70	0.03000	0.12700	0.12200	69	75	0.04050	0.12200	0.12400
69	77	0.03090	0.10100	0.10380	70	71	0.00882	0.03550	0.00878
70	74	0.04010	0.13230	0.03368	70	75	0.04280	0.14100	0.03600
71	72	0.04460	0.18000	0.04444	71	73	0.00866	0.04540	0.01178
74	75	0.01230	0.04060	0.01034	75	77	0.06010	0.19990	0.04978
75	118	0.01450	0.04810	0.01198	76	77	0.04440	0.14800	0.03680
76	118	0.01640	0.05440	0.01356	77	78	0.00376	0.01240	0.01264
77	80	0.02940	0.10500	0.02280	77	82	0.02980	0.08530	0.08174
78	79	0.00546	0.02440	0.00648	79	80	0.01560	0.07040	0.01870
80	96	0.03560	0.18200	0.04940	80	97	0.01830	0.09340	0.02540
80	98	0.02380	0.10800	0.02860	80	99	0.04540	0.20600	0.05460
82	83	0.01120	0.03665	0.03796	82	96	0.01620	0.05300	0.05440
83	84	0.06250	0.13200	0.02580	83	85	0.04300	0.14800	0.03480
84	85	0.03020	0.06410	0.01234	85	86	0.03500	0.12300	0.02760
85	88	0.02000	0.10200	0.02760	85	89	0.02390	0.17300	0.04700
86	87	0.02828	0.20740	0.04450	88	89	0.01390	0.07120	0.01934
89	90	0.02380	0.09970	0.10600	89	92	0.03930	0.15810	0.04140
90	91	0.02540	0.08360	0.02140	91	92	0.03870	0.12720	0.03268
92	93	0.02580	0.08480	0.02180	92	94	0.04810	0.15800	0.04060
92	100	0.06480	0.29500	0.04720	92	102	0.01230	0.05590	0.01464
93	94	0.02230	0.07320	0.01876	94	95	0.01320	0.04340	0.01110

94	96	0.02690	0.08690	0.02300	94	100	0.01780	0.05800	0.06040
95	96	0.01710	0.05470	0.01474	96	97	0.01730	0.08850	0.02400
98	100	0.03970	0.17900	0.04760	99	100	0.01800	0.08130	0.02160
100	101	0.02770	0.12620	0.03280	100	103	0.01600	0.05250	0.05360
100	104	0.04510	0.20400	0.05410	100	106	0.06050	0.22900	0.06200
101	102	0.02460	0.11200	0.02940	103	104	0.04660	0.15840	0.04070
103	105	0.05350	0.16250	0.04080	103	110	0.03906	0.18130	0.04610
104	105	0.00994	0.03780	0.00986	105	106	0.01400	0.05470	0.01434
105	107	0.05300	0.18300	0.04720	105	108	0.02610	0.07030	0.01844
106	107	0.05300	0.18300	0.04720	108	109	0.01050	0.02880	0.00760
109	110	0.02780	0.07620	0.02020	110	111	0.02200	0.07550	0.02000
110	112	0.02470	0.06400	0.06200	114	115	0.00230	0.01040	0.00276

Table E.9: Load data, IEEE 118-bus system

Bus	P (pu)	Q (MVAr)	Bus	P (MW)	Q (MVAr)
1	51	27	2	20	9
3	39	10	4	39	12
6	52	22	7	19	2
8	28	0	11	70	23
12	47	10	13	34	16
14	14	1	15	90	30
16	25	10	17	11	3
18	60	34	19	45	25
20	18	3	21	14	8
22	10	5	23	7	3
24	13	0	27	71	13
28	17	7	29	24	4
31	43	27	32	59	23
33	23	9	34	59	26
35	33	9	36	31	17
39	27	11	40	66	23
41	37	10	42	96	23
43	18	7	44	16	8
45	53	22	46	28	10
47	34	0	48	20	11
49	87	30	50	17	4
51	17	8	52	18	5
53	23	11	54	113	32
55	63	22	56	84	18
57	12	3	58	12	3
59	277	113	60	78	3
62	77	14	66	39	18
67	28	7	70	66	20
72	12	0	73	6	0
74	68	27	75	47	11
76	68	36	77	61	28

78	71	26	79	39	32
80	130	26	82	54	27
83	20	10	84	11	7
85	24	15	86	21	10
88	48	10	90	163	42
91	10	0	92	65	10
93	12	7	94	30	16
95	42	31	96	38	15
97	15	9	98	34	8
99	42	0	100	37	18
101	22	15	102	5	3
103	23	16	104	38	25
105	31	26	106	43	16
107	50	12	108	2	1
109	8	3	110	39	30
112	68	13	113	6	0
114	8	3	115	22	7
116	184	0	117	20	8
118	33	15			

Table E.10: Shunt reactors and capacitors, IEEE 12-bus system

Bus	Q_{L} (MVAr)	Q_{C} (MVAr)	Bus	Q_{L} (MVAr)	Q_{C} (MVAr)
5	40	-	34	-	14
37	25	-	44	-	10
45	-	10	46	-	10
48	-	15	74	-	12
79	-	20	82	-	20
83	-	10	105	-	20
107	-	6	110	-	6